Mathematical modelling of bioreactors in the MELiSSA regenerative life support system

Laura Alemany Juvanteny

Advisors:

Prof. Francesc Gòdia Casablancas
PhD Carolina Arnau Jiménez

Title: Mathematical modelling of bioreactors in the MELiSSA regenerative life support system.

Títol: Modelització matemàtica de bioreactors del sistema regeneratiu de suport de vida MELiSSA.

Título: Modelización matemática de biorreactores del sistema regenerativo de soporte de vida MELiSSA.

Keywords: MELiSSA (Micro Ecological Life Support System Alternative), System modeling, Photobioreactor operation, Packed-bed bioreactor operation, Nitrifification.

Author: Laura Alemany Juvanteny

Supervisors: Prof Francesc Godia Casablancas and PhD Carolina Arnau Jiménez

PhD program in Biotechnology
Departament d'Enginyeria Química, Biològica i Ambiental
Escola d'Enginyeria
Universitat Autònoma de Barcelona
June 2022

El Dr. Francesc Gòdia Casablancas, Catedràtic d'Enginyeria i la Dra Carolina Arnau Jiménez, Coordinadora Tècnica a la Planta Pilot del projecte MELiSSA del Departament d'Enginyeria Química, Biològica i Ambiental de la Universitat Autònoma de Barcelona

Certifiquen:

Que la graduada en Biotecnologia Laura Alemany Juvanteny ha dut a terme al Departament d'Enginyeria Química, Biològica i Ambiental de la Universitat Autònoma de Barcelona i amb la nostra direcció, la tesis titulada "Modelització matemàtica de bioreactors del sistema regeneratiu de suport de vida MELiSSA.".

La mateixa, es presenta en aquesta memòria i constitueix el manuscrit per optar al Grau de Doctora en Biotecnologia per a la Universitat Autònoma de Barcelona.

I per tal que se'n prengui coneixement i consti als efectes oportuns, signem aquest certificat a Bellaterra, a Juny de 2022

Laura Alemany Juvanteny   Francesc Gòdia Casablancas   Carolina Arnau Jiménez
(Autora)   (Co-director)   (Co-directora)

Per als meus avis i àvies

Perquè heu sigut i sou un exemple de superació

Us estimo molt

Agraïments

Com va dir el meu germà un dia, la vida, és com anar amb bicicleta. El camí es llarg i difícil i a vegades et trobes pujades i baixades. Però també a vegades és important parar, baixar de la bicicleta i contemplar el camí que has recorregut. I això faig jo avui.

Avui acabo la meva tesis doctoral. Un projecte que vaig començar amb il·lusió i que significava per a mi molt més que un simple treball acadèmic. Era un repte, d'aquells impossibles (dels que m'agraden a mi), i que no hagués sigut possible sense l'ajuda d'un bon amic. David, tu has sigut el meu company de bogeries d'aquesta aventura i per tant, aquest llibre va acompanyat d'un segell únic. Crec que no seria just començar aquests agraïments sense fer un brindis per tots aquells "fatal errors", totes aquelles nits fins a les 3 del matí revisant codis matemàtics o tots aquells caps de setmana on la idea de ser PhDs (i tu, futura eminència universitària) es van convertir en el nostre projecte comú. I tal i com vaig dir un dia, "hi ha un temps per a cada paraula i una paraula per a cada record". I avui, necessito tancar aquesta etapa fent un segon brindis en record a tots aquells moments que formen i formaran sempre trossos de mi.

Però a la vida, cal seguir pedalejant tot i les dificultats que trobes en el camí. I en aquest sentit, m'agradaria donar les gràcies al suport rebut del meu germà, la meva família, els meus amics i amigues, a tots els companys de Grifols i als meus directors de tesis per haver estat allà en moments molt complicats. Gràcies per haver-me entès, donat suport i insistit, quan tocava, amb que això calia acabar-ho i s'havia d'acabar bé. Aquí, papa, mama, heu tingut un paper clau. No podria haver tancat tot aquest capítol sense el vostre incansable i incondicional suport. Gràcies per a ser pesats, pesats, pesats, pesats i pesats. Vosaltres sou una peça clau en aquest i tots els meus èxits i heu sigut el motor que m'ha ajudat, com sempre, a tirar endavant. Us estimo molt.

I avui, després de tancar aquest capítol, com deia l'Ignasi, haurem de seguir pedalejant amb tot lo que hem après i guanyat de tota aquesta experiència. I és que és cert que la meva tesis doctoral va començar com un repte intel·lectualment impossible però es va tornar també en un verdader repte emocional. I enmig de tot el merder, he tingut la gran sort de trobar-me, tot pedalejant, amb el millor company de viatge que una pot desitjar. Gràcies Lluís per haver sabut calibrar la insistència amb el carinyo, per haver sabut entendre la importància que significava per a mi tancar aquesta etapa i per estimar-me tant. Perquè avui acaba un capítol però jo encaro el meu present i el futur amb il·lusió al teu costat. I per tant, abans de tornar a pujar a la bicicleta, brindem, junts, per les noves aventures que estan per arribar.

Summary

MELiSSA (Micro-Ecological Life Support System Alternative) is a project conceived to develop a closed regenerative life support system where the integration of six biological compartments in a loop can enable to provide life support functions in long-term human space missions. Each one of the compartments is first tested at laboratory scale and then scaled-up to in the MELiSSA Pilot Plant (MPP) to demonstrate and characterize its operation and robustness according to the requirements defined at the design stage. Only when the reactors are fully characterized in stand-alone, the operation of several integrated compartments in continuous mode is studied. All this process is performed in a stepwise approach that enables the generation of knowledge and expertise to be used as a basis to increase the autonomy of the global loop and its control system, critical in its operational robustness. In this context, the development of mathematical models describing each compartment dynamics is paramount to correctly understand the processes occurring in each one of them, the performance when they are connected one to each other and the development of knowledge-based control architecture.

The present thesis is focused on developing different models to describe the performance of some of the compartments in MELiSSA loop in stand-alone operation as well as considering the connection between different compartments in different gas liquid and solid phases.

In a first step, a model for the description of the operation of the packed-bed nitrifying compartment 3 has been developed. This reactor operates in axenic conditions with two nitrification strains *Nitrosomonas europaea* and *Nitrobacter winogradsky*. The model is structured in different levels: the global reactor hydrodynamics and the biofilm that considers the growth of the different species based on a simplified 1-D diffusion model and includes a simplified approach to simulate biofilm consolidation. The validity of this model has been tested by using experimental data from the bioreactor operation during a period of 2 years in which different concentrations and loads of ammonium have been tested to characterize the continuous operation of the reactor. The obtained results fit reasonably well the experimental data and final biomass concentration profiles observed at the end of the operational period.

This is especially relevant considering the limitation to obtain biofilm samples during the long-term operation in order not to perturbate the packed-bed structure.

In a second phase, a model has been also created to describe the operation of the external loop air-lift photobioreactor colonized with *Limnospira indica*, corresponding to compartment 4a in the MPP. This model integrates existing knowledge on light transfer in the photobioreactor liquid, gas-liquid mass transfer of oxygen and carbon dioxide and the growth kinetics of microalgae.

In a third phase, a simplified model has also been developed for the oxygen consumption and carbon dioxide production in the gas phase of the crew compartment. This compartment is configured in the MPP by an animal isolator with a cohort of rats. To develop the model, the consumption coefficients have been calculated based on experimental data. Then, the knowledge generated in the development of these last two models has been integrated with the MPP control system to support the gas-phase integration of these two compartments (the photobioreactor and the animal compartment) in continuous operation. Given an oxygen set point in the animal compartment, the control system increases the illumination in the photobioreactor to reach the necessary oxygen production in order to maintain the oxygen level in the animal compartment.

Finally, the complete set of models has been validated by using two series of long-term operation experimental data of the complete system (photobioreactor and animal compartment) in closed gas loop. The developed models reproduce with high accuracy the experimental profile of the photobioreactor and the global system dynamics associated to the introduction of a real living crew in the gas close loop. This provides a proof of concept of the high potential of mathematical models to understand and support such type of complex systems dynamics.

The results obtained in the present thesis represent a step forward in the development of the MELiSSA loop. The knowledge generated in the formulation of the proposed models can be used for the definition of simplified knowledge-based control systems critical for future development steps as well as their use in the study of future integration scenarios as a tool to simulate the performance of different loop architecture options and operational conditions.

Resum

El projecte MELiSSA (Micro-Ecological Life Support System Alternative) es va concebre per a desenvolupar un sistema tancat de suport de vida regeneratiu basat en la integració de sis compartiments biològics en un circuit tancat pensat per missions humanes de llarga duració. Cada un dels compartiments es desenvolupa primer al laboratori i posteriorment s'escala a la MELiSSA Pilot Plant (MPP) per a demostrar i caracteritzar la seva operació i robustesa d'acord als requeriments definits a la etapa de disseny. Només quan els reactors estan completament caracteritzats en la operació en solitari s'estudia la operació de diferents compartiments en continu. Tot aquest procés es realitza de forma ordenada per a permetre generar coneixement i experiència que s'usaran com a base per incrementar l'autonomia del circuit global i els seus sistemes de control, crítics per a la robustesa operacional. En aquest context, el desenvolupament de models matemàtics que permetin descriure les dinàmiques de cada compartiment és indispensable per entendre de forma correcta els processos que succeeixen a dins de cada un, la resposta quan es connectin els compartiments entre ells i el desenvolupament d'una arquitectura de control basada en coneixement.

La present tesis es focalitza en desenvolupar diferents models per descriure el comportament d'alguns dels compartiments del MELiSSA en operació en solitari i també en la connexió entre diferents compartiments i diferents fases de gas, líquid i sòlid.

En una primera etapa, s'ha desenvolupat un model que descriu la operació del reactor nitrificant de llit empacat. Aquest reactor opera en condicions axèniques amb dues soques de nitrificació *Nitrosomonas europaea* i *Nitrobacter winogradsky*. El model s'estructura en diferents nivells: la descripció de la hidrodinàmica del reactor i la descripció del creixement del biofilm. Aquest últim està basat en la consideració del creixement de les diferents espècies basat en un model de difusió 1-D simplificat i inclou una aproximació simplificada per simular la consolidació del biofilm. La validesa d'aquest model s'ha testejat usant dades experimentals del bioreactor durant un període d'operació de 2 anys en el que diferents concentracions i càrregues d'amoni s'han usat per a caracteritzar la seva operació en continu. Els resultats obtinguts encaixen bastant bé amb les dades experimentals i els perfils de

concentració de biomassa observats al final del període operacional analitzat. Això és rellevant en aquest cas, considerant les limitacions existents en mostreig durant la operació de llarga duració per a no pertorbar la estructura del llit empacat.

En una segona fase, s'ha creat un model que descriu la operació d'un fotobioreactor tipus air-lift de loop extern colonitzat amb *Limnospira indica.* (commpartiment 4a de la MPP). Aquest model integra coneixement existent en transferència de llum en el líquid, la transferència gas-líquid d'oxigen i diòxid de carboni i cinètiques de creixement de les microalgues.

En una tercera fase, s'ha desenvolupat també un model simplificat per a la consumició d'oxigen i la producció de diòxid de carboni a la fase gas del compartiment de la tripulació. Aquest compartiment està configurat per un aïllador d'animals on hi viuen un conjunt de rates. Per a desenvolupar el model, s'han calculat els coeficients de consum d'acord amb dades experimentals existents. Després, el coneixement generat en el desenvolupament d'aquests dos últims models s'ha integrat amb el sistema de control de la MPP per a simular la integració en fase gas d'aquests dos compartiments (el fotobioreactor i el compartiment dels animals) en continu. A partir d'un objectiu específic d'oxigen al compartiment dels animals, el sistema de control incrementa la il·luminació en el fotobioreactor per a assolir el nivell necessari d'oxigen per a mantenir el nivell desitjat en el compartiment dels animals.

Finalment, el conjunt de models creats s'han validat usant dades experimentals de dues series llargues d'operació del sistema complet (fotobioreactor i tripulació) en loop de gas tancat. El desenvolupament dels models permet reproduir amb precisió els resultats i les dinàmiques del sistema global associades a la introducció d'una tripulació real en el loop tancat de gas. Aquests resultats són una prova de concepte de l'alt potencial dels models matemàtics per entendre i donar suport a la operació de sistemes d'operació complexos com aquest.

Els resultats obtinguts en aquesta tesis representen un pas endavant en el desenvolupament del loop MELiSSA. El coneixement generat en la formulació dels models proposats pot ser usat per a la definició de un sistema de control simplificat basat en coneixement que serà crític per a les etapes de desenvolupament futur i l'estudi d'escenaris d'integració com una eina per a simular el comportament de l'arquitectura del loop en diferents condicions operacionals.

Resumen

El proyecto MELiSSA (Micro-Ecological Life Support System Alternative) se concibió para desarrollar un sistema cerrado de soporte de vida regenerativo basado en la integración de seis compartimentos biológicos en un circuito cerrado. Cada uno de los compartimentos se desarrolla primero al laboratorio y posteriormente se escala en la MELiSSA Pilot Plant (MPP) para demostrar y caracterizar su operación y robustez en base a los requerimientos de la etapa de diseño. Sólo cuando los reactores están completamente caracterizados en su operación en solitario se estudia la operación de los distintos compartimentos en continuo. Todo este proceso se realiza de forma ordenada, permitiendo generar conocimiento y experiencia, base para incrementar la autonomía del sistema y sus sistemas de control, críticos para la robustez operacional. En este contexto, el desarrollo de modelos matemáticos para describir las dinámicas de cada compartimento es indispensable para entender los procesos de suceden dentro de cada uno, la respuesta cuando se conecten los compartimentos entre ellos y el desarrollo de una arquitectura de control basada en conocimiento.

La presente tesis se focaliza en el desarrollo de distintos modelos para describir el comportamiento de algunos de los compartimentos del MELiSSA en operación en solitario y en la conexión entre distintos compartimentos y distintas fases de gas, líquido y sólido.

En una primera etapa, se ha desarrollado un modelo que describe la operación el reactor nitrificante de lecho empacado. Este reactor opera en condiciones axénicas con dos cepas de nitrificación *Nitrosomonas europaea* i *Nitrobacter winogradsky*. El modelo se estructura en distintos niveles: la descripción de la hidrodinámica del reactor y la descripción del crecimiento del biofilm. Este último está basado en la consideración del crecimiento de las distintas especies basadas en un modelo de difusión 1-D simplificado que incluye una aproximación simplificada para simular la consolidación del biofilm. La validez de este modelo se ha testeado usando datos experimentales del biorreactor durante un período de operación de 2 años en el que se han usado distintas concentraciones y cargas de amonio para caracterizar su operación en continuo. Los resultados obtenidos encajan bastante bien con los datos experimentales y los perfiles de concentración de biomasa observados al final del

período operacional analizado. Esto es relevante, considerando las limitaciones existentes en muestreo durante la operación para no perturbar la estructura del lecho empacado.

En una segunda fase, se ha creado un modelo para la operación de un fotobiorreactor tipo air-lift de loop externo colonizado con *Limnospira indica.* (compartimento 4a MPP). Este modelo integra el conocimiento en la transferencia de luz en el líquido, la transferencia gas-líquido de oxígeno y dióxido de carbono y las cinéticas de crecimiento de microalgas.

En una tercera fase, se ha desarrollado también un modelo simplificado para el consumo de oxígeno y la producción de dióxido de carbono en la fase gas del compartimento de la tripulación. Este compartimento está configurado para un aislador de animales donde viven un conjunto de ratas. Para desarrollar el modelo, se han calculado los coeficientes de consumo de acuerdo con datos experimentales existentes. Después, el conocimiento generado en el desarrollo de estos dos últimos modelos se ha integrado con el sistema de control de la MPP para simular la integración en fase gas de estos dos compartimentos (el fotobiorreactor y el compartimento de los animales) en continuo. A partir de un objetivo específico de oxígeno al compartimento de los animales, el sistema de control incrementa la iluminación en el fotobiorreactor para lograr el nivel necesario de oxígeno para mantener el nivel deseado en el compartimento de los animales.

Finalmente, el conjunto de modelos creados se ha validado usando datos experimentales de dos largas series de operación del sistema completo (fotobiorreactor y tripulación) en un circuito de gas cerrado. El desarrollo de los modelos permite reproducir con precisión los resultados y las dinámicas del sistema global asociadas a la introducción de una tripulación real en el circuito cerrado de gas. Los resultados demuestran el alto potencial de los modelos matemáticos para entender y dar soporte a la operación de sistemas de operación complejos.

Los resultados obtenidos en esta tesis representan un paso adelante en el desarrollo del MELiSSA. El conocimiento generado en la formulación de los modelos propuestos puede ser usado para la definición de un sistema de control basado en conocimiento que será crítico para las etapas de desarrollo futuro y estudio de escenarios de integración como una herramienta para simular el comportamiento de la arquitectura del circuito en diferentes condiciones operacionales.

Abbreviations

|	
Bo	Bodenstein number
BPC	Biomass Production Chamber
BR	Bibliographic references
C1	Compartment 1 of the MPP (first step in organic waste degradation)
C2	Compartment 2 of the MPP (second step in organic waste degradation)
C3	Compartment 3 of the MPP (nitrification)
C4a	Compartment 4a of the MPP (photobioreactor)
C4b	Compartment 4b of the MPP (higher plants chamber (HPC))
C5	Compartment 5 of the MPP (crew compartment)
CEEF	Closed Ecological Experiment Facility
CELSS	Closed Ecological Life Support Systems
CNSA	China National Space Administration
DMT	Dimensionless mixing time
ECLSS	Environmental control and life-support systems
EHTI	Early Human Testing Initiative
ESA	European Space Agency
EU	European Union
EXP	Experimental data
FISH	Fluorescence in situ hybridization
FOP	Fixed operational parameters
HPC	Higher Plant Chamber
IOV	Input operational variable
ISS	International Space Station
JAXA	Japanese Space Agency
LED	Light-emitting diode
LEO	Low Earth Orbit
MELiSSA	Micro-Ecological Life Support System Alternative
MPP	MELiSSA Pilot Plant
NASA	National Aeronautics and Space Administration
OCV	Operation condition variable
PALACE	Permanent Astrobase Life-support Artificial Closed Ecosystem
PBR	Photobioreactor
PBVs	Packed-bed compartment volumes
Q-PCR	Quantitative polymerase chain reaction
RQ	Respiratory Quotient
TIC	Total inorganic carbon
UAB	Universitat Autònoma de Barcelona
US	United States
VFA	Volatile Fatty Acids
WP	Work Package

THESIS INDEX SUMMARY

CHAPTER 1

Introduction

1.1. Environmental control and Life Support Systems in human Space missions
1.2. CELSS. State of the art
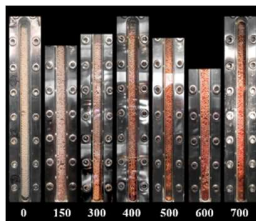*1.3. The MELiSSA Project*

CHAPTER 2

Objectives

CHAPTER 3
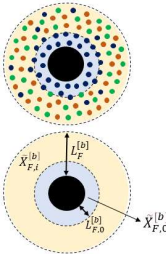
C3. Packed-bed nitrifying reactor modelling. Model description

3.1. Introduction
3.2. Materials and methods
3.3. Assumptions for model development
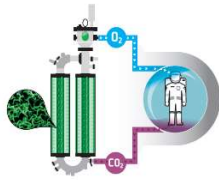*3.4. Model equations development*
3.5. Conclusions

CHAPTER 4

C3: Packed-bed nitrifying reactor modelling. Application of the model to a long duration experimental campaign

4.1. Introduction
4.2. Materials and methods
4.3. Experimental results
4.4. Estimation of model parameters and manipulable variables
4.5. Model validation
4.6. Conclusions

CHAPTER 5

Integration of the photobioreactor and animal compartment in gas close loop. Model description

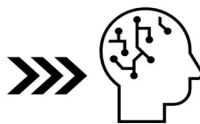# CHAPTER 6

Integration of the photobioreactor and the animal compartment in gas close loop: Experimental results and model validation
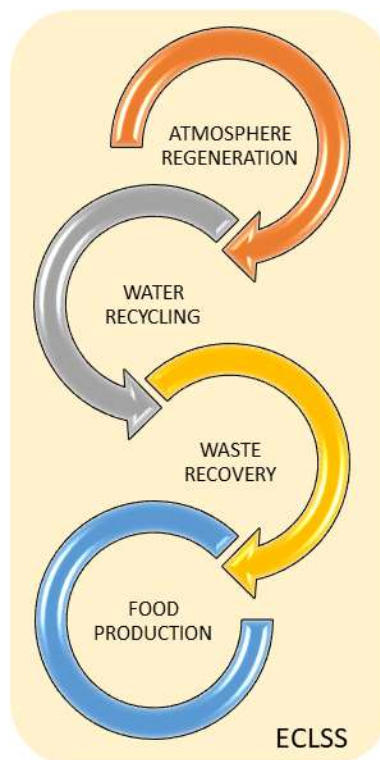
CHAPTER 7

Overall conclusions and future work

CHAPTER 1
Introduction

1.1. Environmental control and Life Support Systems in human Space missions

The concept of Space missions has changed radically over time. Initial human exploration missions (i.e., Apollo missions to the Moon) were of short duration (approx. 10 days) and at what can be considered a reasonable distance from Earth. Since then, the technology advances in fields such as environmental control and life-support systems (ECLSS) design have allowed the extension of human exploration missions duration, making possible the permanent human presence in space in the International Space Station (ISS). However, this permanent human presence is only possible due to the proximity of the ISS to Earth, allowing the evacuation of astronauts in case of emergency or the periodic resupply of food and goods, and the collection of wastes at reasonable cost and frequency. Thus, the next challenge in space-travel is nowadays the performance of long-duration Space missions beyond Low Earth Orbit (LEO). This is a common goal of most Space agencies that would expect to perform manned missions to the Moon or Mars by the first half of 21th century as defined in the Global Exploration Roadmap (International Space Exploration Coordination Group, 2007 [1]). Certainly, this may be considered and ambitious goal, and may need some more decades to be achieved, but the determination of achieving this target is out of doubt. The non-ceasing robotic missions that nowadays are being deployed are a strong sign of Space exploration interest revitalization and the intention of making humans an interplanetary species. International collaboration and public-private partnerships will certainly play a key role in such a tremendous effort. The robotic Mars lander Perseverance, the development of Orion and Dragon spacecrafts, the preparation for the development of Gateway Station or the Chinese Space Station are prominent examples of this new Space era.

Needless to say, that the main challenges of theses missions are associated to the increased distance from Earth and duration, what makes the support to human life even more critical. In such a context, the performance of these type of missions implies several challenges, among them the higher launching effort associated to the increase of consumables required and the need to design a self-sufficient system that does not require quick-return or emergency resupply from Earth. For this reason, the correct

balance between maximum recycling efficiency and system mass optimization is critical for the design of the optimal ECLSS in these types of missions [2]. Other aspects to be considered when preparing such long duration missions are the development of advanced propulsion, the protection from radiation and the potential utilization of *in situ* resources.

An ECLSS needs to cover four main functions: Atmosphere regeneration, Water recycling, Food production and Waste recovery. On top, the environmental conditions in the Space base or vehicle should also be maintained and controlled to guaranty the appropriate conditions for habitability and safety. Based on a general blocks design, available systems are divided in four different categories as detailed in Table 1-1: open, physico-chemical, bioregenerative and hybrid systems [3].

Table 1-1. Description of the different existing types of ECLSS

Type of ECLSS system	Description
Open	All consumables provided directly from storage
Physico-chemical	Physical and chemical process used to recycle Oxygen and Water closed systems. Carbon cycle stays open since food needs to be provided
Bioregenerative	Completely closed systems that can provide food and use wastes
Hybrid	Combination of physico-chemical and bioregenerative processes.

As presented in Figure 1-1, the best option for a life support system depends on the duration of the mission. For short missions (weeks or up to few months), open systems are recommended, since the mass of such systems is low and compensates the mass of resources necessary for the mission. However, as the mission time increases, the requirement for mass increases significantly and regenerative technologies are then coming to play. Even that these systems have higher initial mass, they require lower mass of new resources during the mission. Depending of the mission duration, it will be

more attractive the use of other ECLSS like physico-chemical ones for mission durations of few years or directly bioregenerative systems for higher duration missions. Thus, the use of bioregenerative systems is mandatory in this new space-travel challenge for the 21th century [4]. The current thesis is focused on the study of specific Bioregenerative systems called from now on as Closed Ecological Life Support Systems (CELSS).
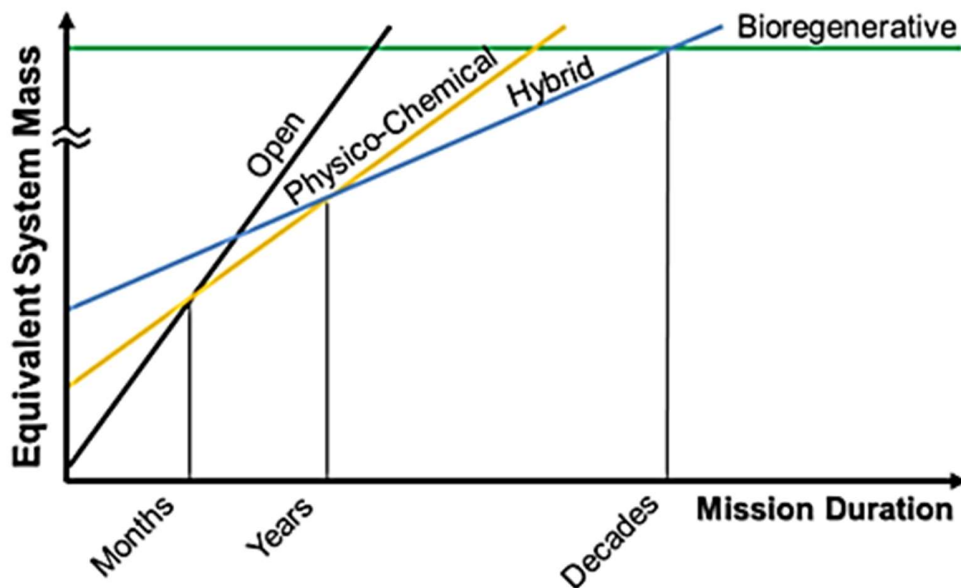
Figure 1-1. Relative mass of the ECLSS system depending on the space travel duration for the four main types of technologies (adapted from [4])

1.2. CELSS. State of the art

Interest for the use of biological systems in Space starts in early 20th century by the hand of the visionary Russian aerospace scientist, Konstantin Tsiolkovsky that envisioned closed space agricultural modules where humans and plants might co-exist [5]. Since then, several efforts have been performed in the last 60 years. In this section, a brief summary of the different research and findings performed as part of the different space agencies strategies up to now is highlighted.

6

The initial studies started with the use of unicellular algae (*Chlorella spp.*, the most studied, *Spirulina, Anacystis* and *Synechocystis* among others) [6–10] and provided predictions of power requirements ranging from 10 to 100 kW for lighting and a surface area of 5 to 50 m^2 to produce oxygen for one human [9]. These predictions became a reality in Russia where specific studies on human life support were started with real presence of humans in the system. The initial attempts implied the use of *Chlorella spp.* as the photosynthetic agent to allow for the gas exchange with human. This was the basis for the construction of Bios-1 facility, the first one of three main human life support trials performed. In this case, 8 m^2 of algae surface and 18 L of culture allowed a 20 % of closure in the ECLSS, with external introduction of water and food prior the start of the experiment. This facility was followed by the construction of Bios-2, where water cycle was closed in a loop with the algal culture and where the introduction and improvement of crops cultivation allowed for the 100 % closure of the air management (25% from higher plants and 75% from the microalgae). It should be noted that the introduction of crops implied additional advantages like the possibility of complementing the limited contribution of the microalgae to the diet balance of the crew [11].

The evolution of all this knowledge was translated into the construction of the Bios-3 facility, a body welded of stainless steel (14 x 9 x 2.5 m) separated in four equal compartments. Two of these compartments were occupied by the unit of higher plants (called phytotrons), the third was destined to unicellular seaweeds and the fourth was occupied by the crew and used for everyday needs [12] (see Table 1-2 for the main characteristics of each of the compartments). The particularity of this system was that, for the first time, the design allowed for a complete management of the system from the inside by a human crew. The final designed system was expected to completely provide the needs of three-man crew for oxygen, drinking water, sanitary water with partial (up to 20 %) supply of food in the form of bread and vegetables from higher plants.

Table 1-2. Bios-3 facility. Compartment characteristics

Compartment		Phytotrons (per unit)	Unicellular seaweeds	Crew
Composition		Wheat and other vegetable cultures	Chlorella vulgaris	3 humans
Surface		$31.5 \ m^2$ total $20.4 \ m^2$ cultivated ($14 \ m^2$ illuminated)	$31.5 \ m^2$ total 3 cultivators ($9.6 \ m^2$ illuminated)	$31.5 \ m^2$
Volume		$78.8 \ m^3$ total	$78.8 \ m^3$ total	$78.8 \ m^3$
Oxygen production capacity (L oxygen / 24h)		Estimated 1000 Possibility to increase it to 2300 with more intensive illumination	Estimated 1800	NA
Supply	Food supply (up to 20 %)	√	-	Responsible for the whole management of the plant
	Air management	√	√	
	Water management	√	√	
	Waste management	√	√	

The experiment performed in Bios-3 facility lasted for six months and included three stages (see Table 1-3 for a summarized description on the experiment details). First stage of the experiment was the implementation of a nearly closed ECLSS with humans and higher plants. The results obtained in this test were quite satisfactory, reaching 85% of closure of the ECLSS, allowing for a complete air management and an acceptable amount of edible biomass production according to the design.

This initial experiment ECLSS closure level was supposed to be increased up to an estimated 91 % by the introduction of the microalgae compartment during phases 2 and 3 of the experiment. However, in these stages, the generation of phytotoxic volatiles by the algae and cyanobacteria had a negative impact on the higher plant's growth. The production of edible biomass from the higher plants could not be achieved and the objective of these stages could not be fully assessed. In fact, these results compromised

the performance of more CELSS studies using algae and crops in Russia during years 60-70, that were performed entirely with only crops [11–13].

Finally, it should be noted that, although air management was fully complete in the first part of the trial, the levels of carbon dioxide were difficult to control during the whole operation and ranged from 2000 to 23000 ppm with an average concentration over 10000 ppm (1%) [12]. This raised the flag on the importance of non-optimal levels of carbon dioxide in large periods for humans that is now an area of concern in space biomedicine [14].

In parallel to these experiments in Russia, the importance of the balance diet in space missions using algae and/or crops was studied. Indeed, studies at that time concluded that most algae were too rich in protein and nucleic acids and many contained large amounts of indigestible cell wall materials [15,16]. For this reason, an assessment of potential crops to be used in space missions was performed by NASA in several workshops in 1980s, considering human nutritional needs, harvest index, food processing and horticultural requirements [17,18]. At the same time, other factors attracted research interest such as the effects of CO_2 enrichment, temperature and humidity conditions or even light spectral quality on crop growth and physiology [19] and lead to a huge increase on knowledge in this field. In fact, these investigations were initially focused on the implementation of CELSS in Space missions but some of them had a huge impact on a terrestrial level. A clear example is the use of LED lighting in controlled environment agriculture, that was initially implemented to be used in the Astroculture plant chamber for the Space Shuttle [20,21]. However, also research linked to the study of higher plants growing in Space conditions was also funded during these years, that lead to the creation of plant chambers for gravitational research [22]. All this knowledge was finally translated into the creation of the Biomass Production Chamber (BPC) at NASA's Kennedy Space Center that operated during the period 1988-2000 to study crops growth in space-like atmospheres in a 20 m^2 growing area. [23].

Table 1-3. Bios-3 facility. Experiments design characteristics

Stage		1	2	3
Period		2 months	4 months	
Compartments used	Phytotron I	√	√	-
	Phytotron II	√	-	√
	Microalgae	-	√	√
	Crew	√	√	√
Oxygen production capacity	Higher plants (per phytotron)	1500 L / 24h	Not feasible. Toxic effects to the plants that could not be reverted [1]	
	Microalgae	-	1830 L / 24h	1750 L / 24h
Food management	Classification	Wheat and 9 others vegetables cultures [2]	Wheat	Assortment of vegetable cultures
	Dry biological mass / 24h	1953 g	-	-
	Dry edible biological mass / 24h	624 g (32% total biomass) 200 g air-dry grain 388 g fresh vegetables	-	-
	Nutritional content (Percentage of the total required)	26% carbohydrates 14% proteins 2.3% fats vitamins	-	-
Air management	Oxygen resupply	Complete	Not detailed	
	Carbon dioxide	0.2-1.5%	0.4-1% with short peaks to 2.3%	
Closure of the system		80.4%	Estimated 91%	

1) Initial use of *Chlorella* culture in the system lead to the death of higher plants. For this reason, the third stage of the experiment was performed by initial regeneration of the air during 6 days. However, when higher plants and microalgae were again used together in the system, the toxic effect could not be avoided.

2) Bordeaux garden cabbage, chante carrots, dill, pretrovsky turnip, peking leaf cabbage, virovsky white radish, batun-onions, din-zo-on cucumbers and sorrel.

Due to all of this experimentation, the interest in ECLSS increased in NASA and this leaded to the construction of a facility in the Johnson Space Center. In this facility, NASA agency sponsored, for the first time, the creation of a ECLSS terrestrial level prototype designed to gain knowledge on ECLSS field. However, for the first time, the impact of introducing humans inside a closed facility was taken into consideration in this facility design. This program was called Advanced Life Support Program's Early Human Testing Initiative (EHTI) and was based on a three-step strategy to demonstrate three different methods for air management by combining (if required) the use of both physicochemical and biological processes. Table 1-4 details specific characteristics of each step of the program [24].

Table 1-4. EHTI program. Phases of the study

Phase		I	II	III
Number of crew members		1	4	4
Duration		15 days	15 days	90 days
LSS	Physicochemical	-	√	√
	Biological	√	-	√

As observed, the use of higher plants for the air management was studied in different conditions. The explanation provided here is essentially focused on the analysis of Phase I which is interesting since air recycling was done integrally by the use of a biological system (*Yecora Rojo* wheat). The facility designed for this test included a 27 m^2 chamber (11 m^2 cultivated) for wheat cultivation and a 19.2 m^3 (8.1 m^2 surface) airlock outfitted to be the accommodations of one person with air recirculation system. In this facility, variables such as temperature, humidity and levels of oxygen and carbon dioxide were monitored. The airlock chamber was specifically equipped with carbon dioxide emergency systems to be activated at levels higher than 1% in the airlock and additional oxygen supply mechanisms to be activated at a defined set point. This design assumed that a cultivated culture of 11 m^2 of this type of wheat should be capable of providing more than one human equivalent of oxygen production at the middle stage of

its life cycle with carbon dioxide maximum adsorption around 1.5 kg / day (equivalent to 1050 L of Oxygen per day at standard conditions of temperature and pressure) [25].

In the Phase I of the test, three mechanisms were studied to maintain air components concentration sequentially in the 15 days of the tests: a) the use of external gas supply to complement biological air revitalization, b) the performance of an active control of the incident light to determine the photosynthetic activity and c) the limitation of the available carbon dioxide to passively control the photosynthesis rate. Table 1-5 summarizes the main results obtained in each case.

Table 1-5. EHTI program. Phase I description and results

Phase		a)	b)	c)
Time (days)		6	6	3
Plants growth model		Optimal light conditions Pure CO_2 injections in the chamber	Variable PID control on light to maintain target CO_2 1200 ppm in the plant growth chamber	Light not limiting Carbon dioxide available provided only from human crew
General outline		Oxygen produced > required This oxygen was removed	Oxygen concentration maintained inside margins	
Airlock	Carbon dioxide (ppm)	1000-7500 (stable)	3500-7000 (stable)	6500-2000 (decrease)
	Oxygen (%)	21.0-21.5 (stable)	21.0-20.5 (decrease)	20.5-20.0 (decrease)
Plant chamber	Carbon dioxide (ppm)	1000-2000 (stable)	1000-1500 (stable)	1000-200 (decrease)
	Oxygen (%)	21.5-22.0 (stable)	21.5-21.0 (decrease)	21.0-20.5 (decrease)
Metabolic rate CO_2 (Human vs Plants)		Humans < Plants	Humans = plants	Humans < Plants

NOTE: Crops productivity detailed in previous paragraph (1050 L of Oxygen per 24h)

As observed, the levels of carbon dioxide during the whole trial varied from 1000-7500 ppm in the airlock and 200-2000 ppm in the plant chamber but they were maintained with a stable baseline in all cases. Thus, the global system (crew and higher plants) was able to convert all the carbon dioxide available to oxygen. However, oxygen levels could only be maintained stable in the first part of the test (a) where experimental conditions forced the generation of more oxygen than the one required. In the other cases (steps b and c), the system was not able to maintain a stable concentration of oxygen in both compartments. According to [24], this decrease is attributed to the difference in respiration quotient (moles of oxygen divided by moles of carbon dioxide) between wheat (0.95-1.00) and humans (0.805-1.0) that could be compensated in a completely closed ECLSS by recycling waste and inedible plant biomass.

The final values obtained at the end of the trial revealed a production of carbon dioxide of approximately 1.37 kg CO_2/day by the human subject and the production of 43.4 kg of dry biomass (1% edible, instead of the 35-40% expected according to previous experiments, see Table 1-3). Additionally, the analysis of trace contaminants revealed an accumulation of ethylene and methane in the system during the test. The other contaminants remained at undetectable levels [24].

These results were further analyzed with Phase III of the same experiment where these biological systems were used in combination with physicochemical life support system technologies to continuously recycle air, water and part of the solid waste steam generated by a 4-person crew for 91 days. In this facility, the regeneration needs of one human in the crew was performed by the biological system whereas the other three crew members air regeneration was performed by the physico-chemical life support. The combination of both systems allowed for a continuous recycle of air, water and part of the solid waste [26]. The next step in these sequence of experiments was supposed to be the building of a larger facility that could ultimately supply most of the life support needs for humans using crops but this building (BIO-Plex) was never completed [19].

However, NASA was not the only space agency trying to study the interaction of humans with crop-based life support system. At the same time the EHTI experiments were being

performed, the Japanese Space Agency (JAXA) developed the Closed Ecological Experiment Facility (CEEF) in Aomori Prefecture in Japan [27] that was also designed to allow for the co-existence of plants, animals and humans in the same CELSS by using two independent modules. The plant module included a total surface of 150 m^2 divided in 3 artificial light chambers of 30 m^2 each and one solar lighting chamber of 60 m^2. On the other hand, the Animal and human's module included two parallel chambers, one for each one. Based on this structure, the integration followed for the complete CELSS system evaluation was divided in two different phases: 1) Phase I: that considered the specific evaluation of both facility modules (Phase IA for plants and Phase IB for animals and humans) and 2) Phase II that included the integration between both modules. This integration was performed with a three one-week experiments where 2 humans, 2 goats and 23 crops coexisted in the same CELSS [28]. Levels of carbon dioxide during these experiments were under 4000 ppm with punctual carbon dioxide peaks in the first and second experiment. Estimated consumptions of oxygen of 56-63 mol/day (equivalent to approximately 1344 L/ 24 h) were obtained, with respiratory quotients around 0.86-0.89 mol CO_2/mol O_2. However, slightly higher production of carbon dioxide was detected in the animal and human compartment compared to the consumption in the plant compartment. This difference was due to the fact that the CELSS cycle was not completely closed and part of the carbon was lost [28–30].

As detailed in this brief summary, numerous developments of recycling technologies were initiated during the past 60 years. However, they typically consisted on recycling one product in a new consumable (i.e., water recycling, O_2 production) without a global overview of the complete life-support [31]. In this context, a new evolution on the concept of CELSS appeared when this global overview was approached in its bioregenerative side. In fact, a closed artificial system offers an extremely useful laboratory environment for the study of complex systems since they can, if correctly designed, allow for an acceleration of the elemental cycles already existing on Earth and allow to contribute to the understanding on how biogeochemical cycles are managed and balanced [32]. However, few examples can be found of this approximation including: Biosphere 2 in

Arizona (US, private initiative), the recently created Lunar Palace 1 (China, CNSA) and the MELiSSA project (EU, ESA).

Biosphere 2

The Biosphere 2 Consortium was created in the late 1980s in Tucson, Arizona (US) by private initiative and conceived as an American Earth system science research facility devoted to study Earth and its living systems (1990-1994). Biosphere-2 facility consisted on a 1.27-hectare system and was the first one designed with a diversity of biomes/ecosystem types with approximately 3800 species of plants and animals. It was specially designed to study Earth's biosphere and facility was created for the development of CELSS. This facility was used twice to perform experiments as an excellent prototype for manned space missions implying the co-habitancy of up to eight people in the facility for a period of up to two years. During these two years, a complete management of the water, wastewater and air was performed, with an internal production of 81% of the food. However, analysis of the whole experimental period revealed that progressive oxygen concentration decrease was observed due to the inherent facility leak (less than 10%) and light reduction due to the glass space frame that led to a low productivity of the crops [32].

Based on this experience, the same private initiative created the Laboratory Biosphere in 2002, a cylindrical steel chamber to continue studies on closed ecological system. Finally, and based on the knowledge acquired up to now, a next application in the context of this private ECLSS initiative will be the "Mars On Earth®" demonstration/research project. The main objective of this project will be to develop a system for maintaining 4 people in a sustainable (bioregenerative) life support system on Mars initially planned by end 2022, according to [32].

Lunar Palace 1

Lunar Palace 1 (from Permanent Astrobase Life-support Artificial Closed Ecosystem, PALACE) is a facility conceived as a CELSS that integrates atmospheric management, crop production, insect breeding, waster recovery and water-processing compartments.

One particularity of this experiment in comparison to the previous ones is that proposes a chemical system for urine nitrogen recycling and develops a strategy for the degradation of higher plants non edible material [33].

This facility, which has a leakage rate of 0.04% per day, comprises a comprehensive cabin (equipped with four private bedrooms, a living room, bathroom and room for waste treatment), one plant cultivation cabin with total crops growing area of 69 m^2 (a second plant cultivation cabin has been recently constructed) divided into two rooms dedicated to the culture of higher plants, a water treatment module and a solid waste conversion and an animal-rearing module.

In these conditions, a total of five volunteers were selected and trained to participate in a 105-day closed test experiment (2014) [33]. In this period, a total of 85.8% of straw powder was stored for fermentation with 2093 g oxygen / day production capacity in the plant cabin (equivalent to 1465 L oxygen /24h in standard conditions). This oxygen was destined to the crew consumption (92%) and also to wastes fermentation and animal rearing (8%). It should be noted that to maintain this mass balance, exogenous food and salts for the crew and higher plants were supplied and also part of solid waste was periodically sent out of the system. Thus, the carbon dioxide absorption capacity of the crops was equivalent to previous studies (see Table 1-3 for Bios-3 facility and Table 1-5 for EHTI project). In all cases, cultures of 20-25 m^2 of crops as single photosynthetic source proved not to be enough to supply sufficient oxygen for one human.

Additionally, the operation during this whole trial period was regulated by adjusting the facility conditions to maintain a limit of carbon dioxide maximum concentration of 5000 ppm. Final values obtained regarding both compounds air composition include variations of carbon dioxide in the system up to approximately 5000 ppm and also a global slow decrease of the average oxygen concentration related to the system leakage [33].
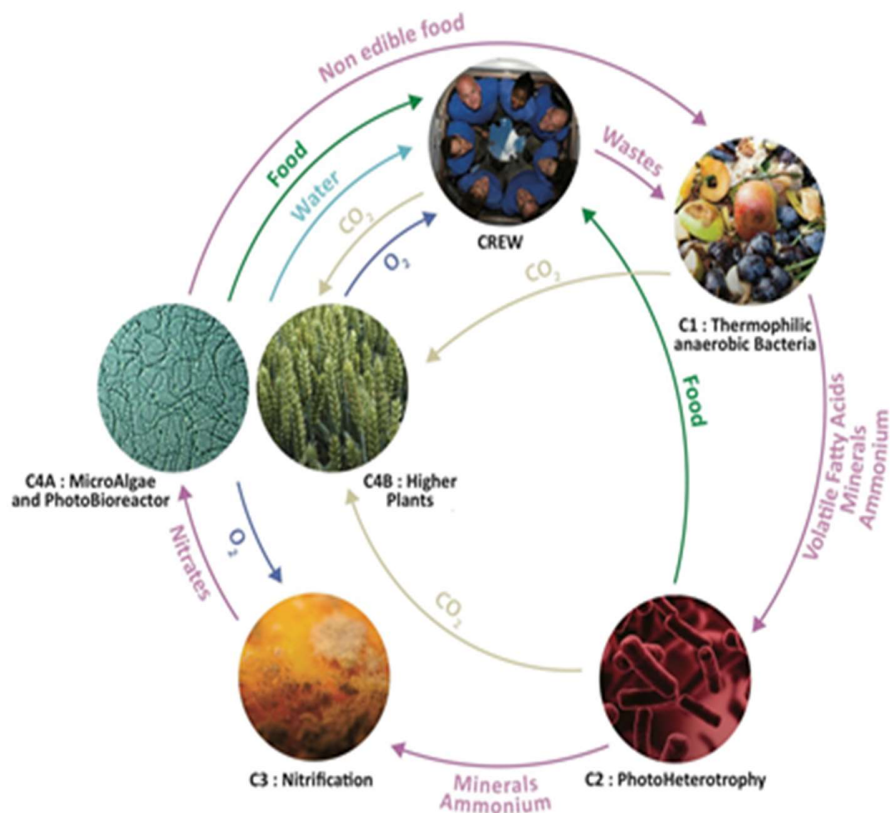
MELiSSA

The MELiSSA project was conceived by ESA in 1988 with the main objective of studying and developing biological life support considering all the basic functions of life support in an holistic and circular approach. Since the work performed in this thesis is under the scope of MELiSSA, an extended explanation is provided in the next section.

1.3. The MELiSSA project

The MELiSSA (Micro-Ecological Life Support System Alternative) project was conceived as a CELSS (Closed Ecological Life Support System) to provide life support technology in Space in 1988 [34] and was adopted by ESA, in the context of an international consortium [35]. The project concept is inspired in a terrestrial ecological system as detailed in Figure 1-2 by performing the main functions of a regenerative life support system, in specific microbiological or higher plant compartments, each one of them dedicated to a given function and all of them conforming the MELiSSA loop [36] (Figure 1-3).

Figure 1-2. Description of the MELiSSA concept. General scheme of a terrestrial ecosystem where the main biological transformations embraced in MELiSSA are highlighted.

Figure 1-3. The MELiSSA concept design, compartments and main interactions among them

The complete system is designed considering the combination of the main functions required in life support: production of food, recovery of water and regeneration of the atmosphere with a concomitant use of wastes (i.e. CO_2 and organic wastes) using light as a source of energy [35].

In order to achieve this objective, the main biological activities in the system are performed in six separated and independent compartments hosted by microbiological or higher plant organisms [36]. These compartments are connected one to each other in gas, liquid and solid phases, conforming a circular system [35] through various interfaces (filtration units, holding tanks, biomass harvesting, gas-phase enrichment units, etc). In this design, the operational conditions of each compartment should guarantee that only a given specific biological activity takes place and that this is done in the optimal

conditions for a given compartment and for the entire loop. Thus, the entire system should be capable of providing the essential functions of a life support system. This represents a unique effort in the development of life support systems enhancing the self-sustainability of human activities in Space.

In this biological loop design, the use of microalgae (Compartment 4a (C4a)) and higher plants (Compartment 4b (C4b)) is critical since they allow for the provision of food, oxygen and water purification to the rest of the biological loop. However, both microalgae and higher plant require, apart from light, a source of mineral nutrients, nitrogen sources and carbon dioxide to grow. In this global loop design, these mineral nutrients and nitrogen sources are obtained from the total loop organic and inorganic matter degradation. On one hand, carbon dioxide supply is attributed to the crew respiration (Compartment 5 (C5)) as part of the global design rationale. On the other hand, inorganic and organic matter degradation steps are designed to be performed by nitrification bacteria (inorganic matter degradation, Compartment 3 (C3)) whereas the degradation of organic matter is based on a continuous two-step biological transformation. The first step of the organic matter degradation is performed by thermophilic anaerobic bacteria (Compartment 1 (C1)) as a strategy to maximize the efficiency in the use of oxygen requirements for the global loop. The degradation of the organic matter in this initial step creates a mixture containing high amounts of volatile fatty acids (VFA). These VFA are eliminated in a second step by photoautotrophic/heterotrophic bacteria (Compartment 2 (C2)).

Table 1-6 details a description of the approach followed for the initial loop biological compartments design together with the selected species to perform each biological activity.

Table 1-6. Description of the compartments present in the MELiSSA loop design

Compartment	Function	Type of microorganism selected
C1	First step organic matter degradation	Thermophilic anaerobic bacteria
C2	Second step in organic matter degradation	Photoautotrophic/heterotrophic bacteria
C3	Nitrification	Nitrifying bacteria
C4a	Photosynthetic compound. Atmosphere regeneration Edible material	Microalgae
C4b	Photosynthetic compound. Atmosphere regeneration Edible material	Different crops
C5	Crew compartment	Humans or animals with equivalent oxygen consumption

The integration of such a complex system with full closure is challenging. Additionally, this complete loop closure becomes a real challenge when the space microgravity is also considered. For this reason, the development of this system requires a combined effort of experts in multiple disciplines, that conform the MELiSSA Consortium, with 15 partners from Europe and Canada, coordinated by ESA [35]. Researchers from universities and companies from the MELiSSA Consortium and additional teams associated to it participate in the conceptual design of each compartment and the experimentation to select the microorganisms/higher plants to perform the biological activity or develop the process behind the specific biological activity. Each one of the compartments is first tested at laboratory scale to generate the necessary knowledge on the biological system used, the growth kinetics, consumption and production dynamics, bioreactor design definition, mixing conditions, gas-liquid transfer rates, etc. In this step, initial mathematical models are developed on the different compartments. Noteworthy, the development of mathematical models of the different compartments is key for the complete understanding of such a complex system and represents a basic element to guide compartment operation, perform simulation of scenarios and develop the control architecture.

Once designed, the MELiSSA compartments requires two more steps for the final characterization:

- Studies in a higher process scale (pilot scale) to demonstrate and characterize their operation and robustness according to the corresponding design requirements during long operation periods. This approach allows for the generation of knowledge and expertise which is paramount to improve the future designed systems. Additionally, at this step, the initial mathematical models are further completed. In this scale, the mathematical models take a relevant role since they allow for the simulation and understanding of the interaction between the process conditions and the output from the biological system. This is basic for the prediction and analysis of the performance of the compartments under different operational conditions.

- Studies on the progressive integration of all the compartments in the loop. Indeed, the final operation of the complete loop requires the continuous operation of all the compartments under controlled conditions with interconnections between them in several phases (gas, liquid and solid) through various interfaces (filtration units, holding tanks, biomass harvesting, gas-phase enrichment units, etc.). In this case, a strategy to integrate, step by step, the different compartments is the only way for achieving a robust loop that tolerates and controls real fluctuations in final compartments continuous operation. The development of reliable mathematical models validated at pilot scale is the only way of assuring a final overall control system of the complete loop and an efficient and robust global loop performance for long periods of time.

For this reasons and considering this final scalability and integration complexity, the MELiSSA Consortium has developed a pilot plant with the main goal of demonstrating the long-term continuous operation feasibility of the loop under the supervision of a control system [37].

1.3.1. MELiSSA Pilot Plant

The MELiSSA Pilot Plant (from here MPP) is located at Universitat Autònoma de Barcelona (UAB) in Spain and considers the experimentation of the different reactor compartments at pilot scale. This reproduction in pilot scale test implies the use of higher volume reactors compared to previous development steps and the implementation of advanced control strategies. Finally, when this is achieved, an integration between the different reactors can be performed.

Thus, the final goal of this pilot plant is to achieve the connection of all the compartments of the MELiSSA system to provide a demonstration of the feasibility of the MELiSSA loop and its operation. The main characteristics and objectives of the MPP and the six related biological compartments [31] are described here.

1.3.1.1. MPP: Design objectives

The design objectives for the MPP definition at full capacity (with all compartments and connections implemented) in terms of CELSS closure are as follows [38]:

- Producing at least 100 % of the O_2 daily need for 1 human
- Producing at least 20-40 % concomitant production of the edible material daily need for 1 human
- Recycling of 100 % of the CO_2 daily produced by 1 human

1.3.1.2. MPP biological compartments description

The main characteristics of each one of the compartments in the MELiSSA loop is described below. Additionally, a summary of the main characteristics of each compartment can be found in Table 1-8 and Table 1-9.

C1: Waste degradation

The C1 compartment is a 90 L anaerobic thermophilic bioreactor, where a mixture of bacteria adapted to the degradation of the MELISSA waste material is used. This waste material includes a mixture of three plants material (lettuce, beet and wheat straw), toilet paper and human feces and is defined as representative of the real solid wastes generated by a crew using such a CELSS. In this compartment, the degradation is performed at pH conditions of 5.3 and at 55 ºC temperature. The main products of the waste degradation are Volatile Fatty Acids (VFA, mainly acetic, butyric and propionic), ammonium in the liquid phase and CO_2 in the gas phase.

C2: Recovery of organic carbon

The C2 compartment is designed to recover the organic carbon from the VFA generated in C1, and was originally conceived as an anaerobic photobioreactor working with the photoheterotrophic bacteria *Rhodospirilum Rubrum* in suspension in axenic pure culture. In this bioreactor, the volatile fatty acids from C1 are degraded to CO_2 whereas most of the ammonium is not metabolized. It should be mentioned though, that this part of the loop is currently extensively revisited, since new options to complete the degradation performed in C1 are being considered in several MELiSSA related activities and a different design will be adopted soon.

C3: Nitrification

The C3 compartment is devoted to the axenic co-culture of *Nitrosomonas europaea* and *Nitrobacter winogradskyi* autotrophic bacteria. The main objective of this 11.9 L packed bed reactor is to transform ammonium to nitrite and then to nitrate, the last one being a more assimilable form of nitrogen for the photosynthetic elements of the loop. This compartment has been initially tested with a synthetic rich ammonium medium as initial approximation. In a subsequent step, a more complex media will be treated, since Nitrogen in a life support system is mainly in the form of urea in urine.

This will be performed first by adapting C3 to treat a complex defined media simulating urine (so called synthetic urine) and then real human urine. To achieve this point, a reduced number of additional heterotrophic bacterial strain will be used in C3, together with the nitrifying strains, in order to archive urine hydrolysis and nitrification, also with reduction of the organic compounds found in urine. This work is already in progress in the MPP.

C4a: Oxygen and edible biomass production with microalgae

The C4a compartment is designed as a 83 L air-lift external loop photobioreactor working with an axenic pure culture of the cyanobacteria *Limnospira indica*. The main function of this compartment is to generate oxygen and edible biomass for the crew using the available CO_2 and light as energy source.

C4b: Oxygen and edible biomass production with higher plants

The C4b compartment is a Higher Plant Chamber (HPC) of 9000 L capacity. In this compartment, plants produce edible biomass and O_2 for the respiration of the crew using the available CO_2 and light as energy source. In the MPP three plants are used as models: lettuce, wheat and beet. The compartment operates as a hydroponic system and the plants are cultured in staggered mode (i.e., plants of different degree of maturation within the chamber) to achieve an averaged oxygen production.

C5: Crew compartment

The C5 compartment mimics the crew component in an ECLSS. In order to do that, the crew is represented in the MPP as a group of laboratory animals (Wistar rats) living in an isolator of 1600 L. In the MPP, this rats' isolator is connected in the gas phase with the rest of the loop to demonstrate the atmosphere regeneration capability to support breathing. The selection of Wistar rats as the animal to be used as mock of the crew was based on an easy animal accommodation [39] and the fact that these animals have a similar
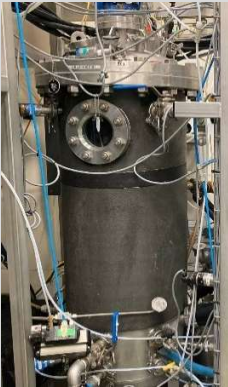
respiratory quotient (RQ) than humans in a controlled diet. However, differences are found regarding oxygen intake per weight between rats (13.71 mL/min/kg) and humans vs (3.51 mL/min/kg) [40,41]. These differences are typically related to the difference in weight and can be easily compensated by increasing the number of rats used in the experiment. For this reason, as detailed in Table 1-7, about 60 Wistar rats are required to reproduce the respiration capacity of one human.

Table 1-7. C5 sizing for the equivalent respiration of one human

	Rats	**Humans**
Age	14-30 weeks	20-50 years
Weight (approximate) (kg)	0.2-0.4	50-70
Oxygen intake (mL O_2/min/kg)	13.5	3.51
Oxygen consumption (mL O_2/min)	2.7-5.4 (1 rat)	175.5-245.7
	162.0-324.0 (60 rat)	

Based on this design rationale, Table 1-8 and Table 1-9 shows a description of the different reactors of the MPP with their main working characteristics.

Table 1-8. MELiSSA loop compartments description (1/2)

Compartment	C1	C2	C3
		Under investigation	
Microorganism/ Higher plant	Mixture of anaerobic thermophilic bacteria	Photoheterotrophic bacteria *Rhodospirilum Rubrum*	Nitrification bacteria *Nitrosomonas europaea* *Nitrobacter Winogradsky*
Function in the loop	Organic matter degradation (up to volatile fatty acids)	Organic matter degradation (up to carbon plant/algae assimilable forms)	Nitrification up to plant/algae assimilable nitrogen sources
Current status in MELiSSA project development	Compartment under characterization	Compartment under reconsideration: alternative technology will be used	Pilot Plant Integration
MPP Working Volume	90 L	NA	11.9 L
MPP reactor type	NA	NA	Packed-bed reactor
Comments	NA	NA	At the moment MPP do not consider the inclusion of real urine

Table 1-9. MELiSSA loop compartments description (continued 2/2)

Compartment	C4a	C4b	C5
Microorganism/ Higher plant	Microalgae *Limnospira indica* (also known as *Arthrospira platensis*)	Higher plants (Lettuce, wheat and beet)	Laboratory Wistar rats
Function in the loop	Photosynthetic compartment Air regeneration Food production	Photosynthetic compartment Air regeneration Food production	Mock of the human crew
Current status in MELiSSA project development	Pilot plant integration	Pilot plant integration	Pilot plant integration
MPP Working Volume	83 L	9000 L	1600 L
MPP reactor type	Air-lift external loop photobioreactor	Chamber for hydroponic culture	Max capacity 60 rats (Equivalent to one human)
Comments	NA	NA	NA

1.3.1.3. MPP integration strategy

The complex design structure of the MELiSSA loop, the challenges associated to perform a scale-up at representative scale and the difficulty to approach all multiple connections between the different compartments requires the design of a well-studied plan to achieve a solid implementation of the compartments included in the loop in the MPP. Additionally, this implementation needs to be done in parallel with the development of specific reliable mathematical models and control systems to regulate the operation of each compartment and the global high-level loop.

For this reason, an integration strategy was conceived, consisting in a total of 18 steps, called Work Packages (WPs) that approach separately the connections between different compartments to finally reach the complete MPP integration with the achievement of the MPP goals as described earlier. The final strategy presented here includes additional separation or storage units and is not sequential in time but subjected to the specific developments of each compartment.

Figure 1-4 summarizes a scheme of the MELiSSA compartments with the defined interfaces for their connection (gas, liquid and solid) in the final loop implementation, corresponding to the last integration package (WP18).

In this section, the global implementation strategy initially developed for the MPP integration is described. It should be considered that this initial strategy is a living document and is subjected to modifications in parallel to the generation of knowledge on different compartments or the inclusion of further design optimizations of the loop.
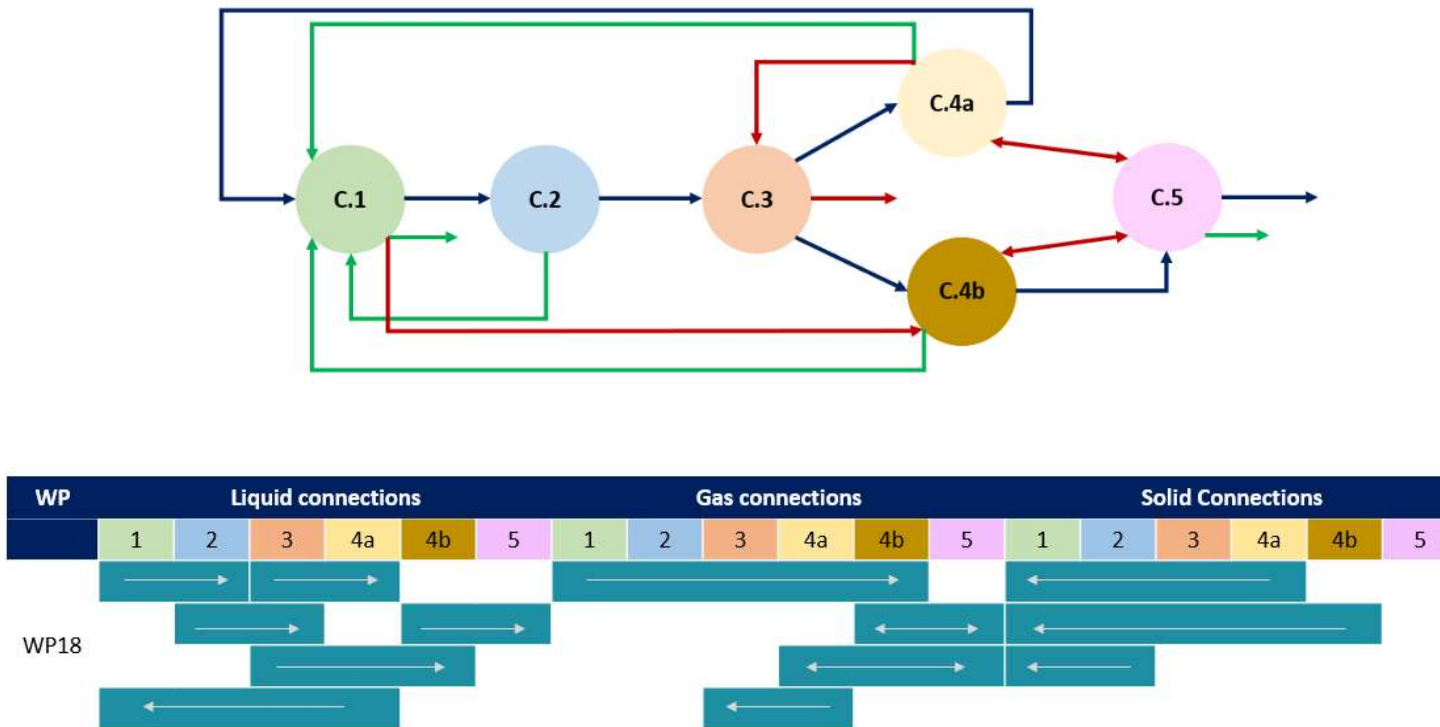
Figure 1-4. Description of the different MELiSSA compartments with the defined interphases connections. In the first part of the figure (Top), blue arrows indicate liquid interphase, green arrows indicate solid interphase and red lines indicate gas interphase. In the second part of the figure (bottom) these integrations are represented in a table-form for a simpler explanation.

First block: Oxygenic loop integration (WP1 to WP6)

The first steps in the integration of the different compartments are focused on the implementation and integration of the oxygenic loop centered in the compartments with photosynthetic activity (C4a, C4b) without considering the implementation of the global liquid interphase in these compartments (see Figure 1-5). In this context, specific integration steps are dedicated to the study of dynamics between these photosynthetic compartments and the crew (WP1 and WP5). Additionally, the liquid and gas dynamics between the nitrification and microalgae compartment are also addressed (WP3).

All of this knowledge should be further integrated sequentially in WP4 and WP6, achieving a first closure on the photosynthetic compartment air management with the crew. It should be noted that this initial strategy also includes an evaluation of the organic waste's degradation (integration of liquid phase in C2 and C3, WP2), that will be performed only when the final technology in C2 will be defined and the hardware installed.

Second block: Solid loop integration (WP7 to WP10)

The second block in the MPP integration strategy is focused on the connection of the different solid streams of the loop (see Figure 1-6). This is planned in a four-step strategy that considers, additionally to the solid connections, the gas connection between the first organic degradation compartment (C1) and the higher plants (C4b).

Third block: Linear liquid loop integration (WP11 to WP13)

Once the solid loop has been integrated, the third block of integration packages include the integration of the whole liquid loop from C1 to C4a. This is planned to be performed in a four-step strategy and includes as additional connections the entry of non-edible biomass (C4b) for degradation in C1, the return of the gas from this compartment (C1) to higher plants (C4b) and gas exchange between photosynthetic micro-algae (C4a) and nitrification compartment (C3) (See Figure 1-7).

Fourth block: Global integration

Once these three main blocks have been successfully performed, the final integration of the plant is planned in a four steps strategy. Initially, gas phase interactions in the crew compartment (C5) are included to previous WP14 integration package that considers complete liquid interaction. Then, sequential integration of the remaining liquid connections on WP14 scheme is performed in WP16 and WP17 without introducing the crew inside the loop. Once the implementations of all of these connections is considered successful, crew compartment is incorporated in the loop allowing for 100% closure of the loop (WP18) (See Figure 1-8).

Figure 1-5. Description of WP1 to WP6. Implementation of oxygenic loop. In this schematic representation, the different air-liquid-solid connections previewed for all compartments are summarized. Interphase's connections that are performed in a specific integration package are highlighted in blue whereas other interphases connections that are included as additional information are highlighted in light grey.

Figure 1-6. Description of WP7 to WP10. Solid loop integration. In this schematic representation, the different air-liquid-solid connections previewed for all compartments are summarized. Interphase's connections that are performed in a specific integration package are highlighted in blue whereas other interphases connections that are included as additional information are highlighted in light grey.

Figure 1-7. Description of WP11 to WP14. Linear liquid loop integration. In this schematic representation, the different air-liquid-solid connections previewed for all compartments are summarized. Interphase's connections that are performed in a specific integration package are highlighted in blue whereas other interphases connections that are included as additional information are highlighted in light grey.

Figure 1-8. Description of WP15 to WP18. Global plant integration strategy. In this schematic representation, the different air-liquid-solid connections previewed for all compartments are summarized. Interphase's connections that are performed in a specific integration package are highlighted in blue whereas other interphases connections that are included as additional information are highlighted in light grey.
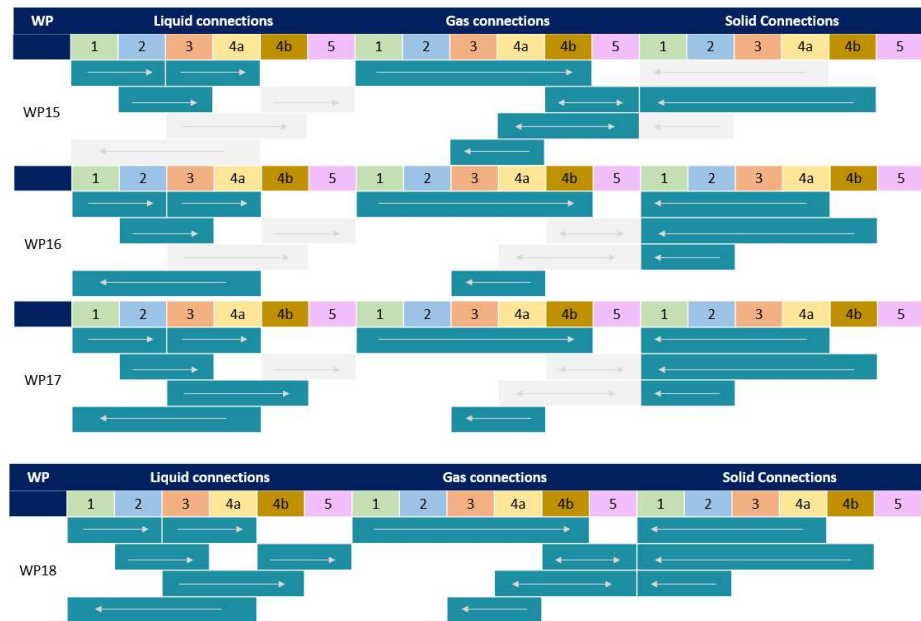
1.4. Bibliography

1.   Estec, E., Schade, B. & Zentrum, D. International Space Exploration Coordination Group: Annual Report 2013. *ISECG* 1–9 (2013). Available at: https://www.globalspaceexploration.org/. (Accessed: 31st October 2021)

2.   Detrell, G. Analysis and Simulation of a synergetic environmental control and life support sytem for long duration spaceflight. (Universitat Politècnica de Catalunya and University of Stuttgart, 2015).

3.   Messerschmid, E. & Bertrand, R. *Space stations: Systems and utilization. June* (Springer Verlag, 1999).

4.   Eckart, P. *Spaceflight Life Support and Biospherics.* (Microcosm Press, 1996).

5.   Tsiolkovskiy, K. *Study of outer space by reaction devices. In: NASA Technical Translation NASA TT F-15571 of "Issledovaniye mirovykh prostranstv reaktivnymi priborami".* (1975).

6.   Sorokin, C. & Myers, J. A High-Temperature Strain of *Chlorella. Science* 117, 330–331 (1953).

7.   Krall, A. & Kok, B. Studies on Algal Gas Exchangers with Reference to Space Flight. in *Developments in industrial microbiology* (ed. Rich, S.) 33–44 (Springer Science and Business Media, 1960).

8.   Taub, F. B. Closed Ecological Systems. *Annual Review of Ecology and Systems* 5, 139–160 (1974).

9.   Miller, R. & Ward CH. Algal Bioregenerative Systems. in *Atmosphere in Space Cabins and Closed Environments.* (ed. Kammermeyer, K.) 186–221 (Springer, Boston, MA, 1966).

10.   Matthern, R. & Kock, R. Developing an unconventional food, Algae, by continuous culture under high light intensity. *Food Technology.* 18, 58–65 (1964).

11.   Salisbury, F., Gitelson, J. & Lisovsky, G. Bios3: Siberian Experiments in Bioregenerative Life Support. *Bioscience* 47, 575–585 (1997).

12.   Gitelson, I. I. *et al.* Life support system with autonomous control employing plant photosynthesis. *Acta Astronautica* 3, 633–650 (1976).

13.   Gitelson, I. I. *et al.* Long-term experiments on Man's stay in biological life-support system. *Advanced Space Research* 9, 65–71 (1989).

14.   Law, J. *et al.* Relationship Between Carbon Dioxide Levels and Reported Headaches on the International Space Station. *Journal of Occupational and Environmental Medicine* 56, 477–483 (2014).

15.   Karel, M., Kamarei, A. & Nakhost, Z. *NASA internal report. Utilization of non-conventional systems for conversion of biomass to food components.* (1989).

16.   Golueke, C. G. & Oswald, W. J. Role of Plants in Closed Systems. *Annual Review of Plant Physiology* 15, 387–408 (1964).

17.   Hoff, J., Howe, J. & Mitchell, C. *NASA internal report: Nutritional and cultural aspects of plant species selection for a controlled ecological life support system.* (1982).

18.   Tibbitts, T. NASA Conference Publication 2231. Workshop at Ames Research Center, Moffett Field, California. in *Controlled Ecological Life-Support System. Use of Higher plants* (NASA, 1982).

19. Wheeler, R. Agriculture for Space: People and Places Paving the Way. *Open Agriculture De Gruyter open* 2, 14–32 (2017).

20. Barta, D. J., Tibbitts, T. W., Bula, R. J. & Morrow, R. C. Evaluation of light emitting diode characteristics for a space-based plant irradiation source. *Advanced Space Research* 12, 141–149 (1992).

21. Bula, R. J. *et al.* Light-emitting Diodes as a Radiation Source for Plants. *HortScience* 26, 203–205 (1991).

22. Zabel, P., Barnsey, M., Schubert, D. & Tajmar, M. Review and analysis of over 40 years of space plant growth systems. *Life Sciences in Space Research* 10, 1–16 (2016).

23. Prince, R. & Knott, W. CELSS Breadboard Project at the Kennedy Space Center. in *Lunar Base Agriculture: Soils for Plant Growth* (eds. Ming, D. W. & Henninger, D. L.) 155–163 (American Society of Agronomy, Inc. Crop Science Society of America, Inc, Soil Science Society of America, Inc., 1989).

24. Edeen, M., Dominick, J., Barta, D. & Packham, N. Control of Air Revitalization Using Plants: Results of the Early Human Testing Initiative Phase I Test. *J. Aerosp.* 105, 781–795 (1996).

25. Edeen, M. *'Early Human Testing Initiative - Phase I Human Simulation Wheat Growth Test Quick Look Test Report' JSC33232.* (1995).

26. Henninger, D. Overviews. Test Phases and Major Findings. in *Isolation - Nasa experiments in closed-environment living: EHTI System Final Report* (eds. Lane, H., Richard, S. & Feeback, D.) 34–52 (Amer Astronautical Society, 2002).

27. Nitta, K., Otsubo, K. & Ashida, A. Integration test project of CEEF - A test bed for Closed Ecological Life Support Systems. *Advanced Space Research* 26, 335–338 (2000).

28. Tako, Y. *et al.* One-week habitation of two humans in an airtight facility with two goats and 23 crops – Analysis of carbon, oxygen, and water circulation. *Advanced Space Research* 41, 714–724 (2008).

29. Masuda, T., Ogasawara, T., Harashima, E., Tako, Y. & Nitta, K. Evaluation and Implementation of an Advanced Life Support (ALS) Menu for Closed Ecology Experiment Facilities (CEEF). *Eco-Engineering* 17, 55–60 (2005).

30. Tako, Y. *et al.* CEEF: Closed Ecology Experiment Facilities. *Gravitational ans Space Biology* 23, 13–24 (2010).

31. Gòdia, F. *et al.* The MELISSA pilot plant facility as an integration test-bed for advanced life support systems. *Advanced Space Research* 34, 1483–1493 (2004).

32. Alling, A. *et al.* Lessons Learned from Biosphere 2 and Laboratory Biosphere Closed Systems Experiments for the Mars On Earth Project. *Biological Sciences in Space* 19, 250–260 (2005).

33. Fu, Y. *et al.* How to Establish a Bioregenerative Life Support System for Long-Term Crewed Missions to the Moon or Mars. *Astrobiology* 16, 925–936 (2016).

34. Mergeay, M. *et al.* MELiSSA. A microorganisms based model for CELSS development. in *3rd Symposium on Space Thermal Control and Life Support Systems.* 65–68 (1988).

35. Lasseur, C. *et al.* Melissa: The European project of closed life support system. *Gravitational and Space Biology* 23, 3–12 (2010).

36. Hendrickx, L. *et al.* Microbial ecology of the closed artificial ecosystem MELiSSA (Micro-Ecological Life Support System Alternative): Reinventing and compartmentalizing the Earth's food and oxygen regeneration system for long-haul space exploration missions. *Research in Microbiology* 157, 77–86 (2006).

37. Poughon, L., Farges, B., Dussap, C. G., Godia, F. & Lasseur, C. Simulation of the MELiSSA closed loop system as a tool to define its integration strategy. *Advanced. Space Research* 44, 1392–1403 (2009).

38. Poughon, L. MELiSSA *Technical Note: 83.11. Analysis of Working Packages for the MPP Integration Strategy*. (2008).

39. COE. *ETS 123: Protection of Vertebrate Animals, 18.III.1986. Cets* 123 (1986).

40. Vidal, S. & Vergara, P. *MELiSSA technical note (MPP-TN-08-5001): Animal model for MELiSSA pilot plant*. (2014).

41. Gonzalez, N. C. & Kuwahira, I. Systemic oxygen transport with Rest, Exercise and Hypoxia: A comparison of Humans, Rats and Mice. *Comprehensive Physiology* 8, 1537–1573 (2018).

CHAPTER 2
Objectives

The MELiSSA project implies the continuous operation of several bioreactor compartments with several solid, liquid and gas phase connections between them. In this context, the development of mathematical models describing each compartment dynamics is paramount to correctly understand the processes occurring in each one of them as well as the dynamics when they are connected one to each other, here referred as integration. Additionally, it is necessary to implement robust control system loops in the final design for the optimal operation of the loop in long term periods. This can only be efficiently achieved with the correct mathematical development enabling the generation of a robust control structure based on the fundamental mechanisms occurring in each reactor.

The main goal of this work is to generate knowledge on the definition of these mathematical models required for the complete loop operation. Specifically, this modelling effort will be focused on both: a) the reproduction of the dynamics inside different compartments by developing mathematical models that quantitatively and comprehensively describe the physical, chemical and biological processes occurring in each reactor and b) the reproduction of the dynamics observed in some of the integration packages performed in the MPP. In each case, the approach of this work starts from an analysis of the compartments to be modelled and previous knowledge in this field. Based on this analysis, specific models are developed taking into account the most critical phenomena occurring in the compartment. Finally, the models are validated with data from long-term operation series of experiments performed previously in the MPP.

This main objective is developed in more detailed ones as described below, with the mention of the chapters dedicated to each one of them:

- Development of a mathematical model for C3, a packed-bed bioreactor with an immobilized co-culture of *Nitrosomonas europaea and Nitrobacter winogradsky*, performing nitrification of ammonium to nitrate (Chapter 3)

- Implementation of the model developed in Chapter 3 to describe the performance of the axenic continuous operation of C3 for a period of 2 years. (Chapter 4)
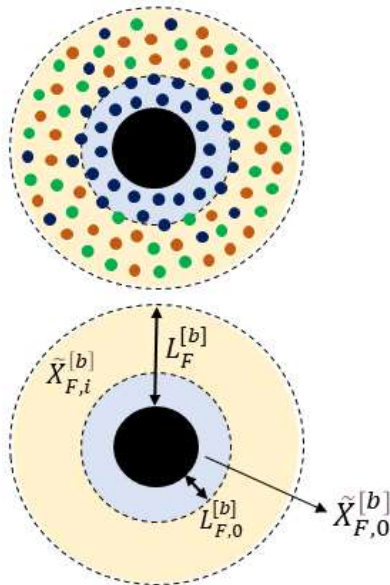
- Development of a mathematical model for C4a, an external loop air-lift photobioreactor with a suspension culture of *Limnospira indica*, capturing CO_2, performing photosynthesis and generating edible material and O_2 (Chapter 5)

- Development of a mathematical model for C5, an animal isolator with Wistar rats mimicking the crew respiration (Chapter 5)

- Implementation of the models developed for the C4a and C5 to describe the operation of both compartments integrated in the gas phase for periods of 30 and 50 days respectively. This study is performed by taking into consideration the existent dynamics between both compartments and the control system used for the operation of the integrated compartments. (See Chapter 6)

- Based on all the knowledge generated, the last chapter provides a discussion on the impact of these models on the final design of the loop and further integration steps (Chapter 7)

CHAPTER 3
C3. Packed-bed nitrifying reactor modelling. Model description

This manuscript is currently submitted to Journal of Theoretical Biology

3.1. Introduction

The work presented in this chapter is focused on the development of a mathematical model to describe the performance of one of the compartments in the MELiSSA loop, the packed-bed nitrifying reactor, corresponding to C3. This reactor is colonized with two nitrifying bacteria strains *Nitrosomonas europaea* ATCC 25978 and *Nitrobacter winogradsky* ATCC 25391 working in axenic conditions as a biofilm around polystyrene beads. Its main goal is to oxidize the ammonium derived from organic waste into nitrate and provide a more suitable nitrogen source to the photosynthetic compartments of the loop (culture of cyanobacteria and higher plants). It should be noted that this specific operation under axenic conditions implies an additional difficulty for the reactor modelling due to the lack of experimental data on the evolution of the immobilized biomass during operation caused by the need to preserve the packed-bed structure.

The development of biofilm mathematical models has been widely used in the literature as a tool to understand the mechanisms behind biofilm growth [1]. Indeed, a wide range of biofilm mathematical models are available in the literature with a range of complexity going from very simple correlations to sophisticated algorithms modelling the 3-D biofilm structure [2]. These biofilm models are classified into two main categories based on the biomass representation: discrete models that are more complex and treat differentially the interaction of the different biomass units and continuum models that treat biomass as a uniform distribution.

The specific application studied here aims to simulate the overall operation (reactor concentrations profile and general biofilm evolution description) of the axenic nitrifying packed-bed reactor during long periods of time at an acceptable computational cost. For this reason, a continuum model is considered to describe biofilm evolution at an appropriate level of detail. Specifically, this type of models is classified in two sub-categories according to the direction of biofilm expansion considered: one-dimensional (1-D, expansion perpendicular to the surface) and multidimensional models. The 1-D continuum model is the one adopted in the current study.

1-D continuum modelling started at the early 1970s with simple limited single-species biofilm models [3,4]. However, the progress of experimental methods allowed the development of more sophisticated multisubstrate and multispecies models [5–8]. In fact, the most known 1-D biofilm model [9] is probably the one currently implemented in the AQUASIM software [10] and widely used for industrial simulations. Additionally, recent advances in 1-D models based on differential equations from [9] have made possible the reproduction of biofilm aging as well as biofilm consolidation, referred as a structure realignment of the biofilm under dynamic conditions [11]. This realignment considers changes in space occupancy by the different particulate components present in the biofilm [12]. This enables to describe biofilm evolution more accurately. However, it should be noted that the increase of model complexity implies higher computational efforts, and therefore, increases modelling times. For this reason, proposals of 1-D models aiming to reduce computational efforts have been also developed [5,13–16]. These models are focused on reducing the computational load in transient-state biofilm modelling [14] or analytical simplified resolutions of the biofilm diffusion equations [5,13,15,16]. The analytical simplified resolutions proposed are based on the biofilm diffusion steady-state assumption and provide fast resolution but sufficiently accurate predictions avoiding the higher computational efforts necessary to solve the complete system of partial differential equations. However, these models are not able to reproduce consolidation phenomena and their capability for the linearization of the diffusion equations is highly dependent on the mathematical expression of the microbial growth equations [13]. Indeed, this simplification has been only successfully reproduced in cases with Monod like expressions in which a limiting substrate can be identified. It should be noted that in the case studied here, more complex kinetic formulation should be adopted.

Taking into account the previous considerations, the current chapter is focused on developing a model capable of reproducing the complete reactor evolution during a long-term operation period, with reduced computational effort. This model should enable to reproduce biofilm diffusion limitations with complex kinetics and biofilm consolidation phenomena. This is achieved by coupling a simplified 1-D diffusion and

reaction biofilm model of the quasi-static substrate diffusion with a hydrodynamic model regarding packed-bed bioreactor evolution and a biofilm model to reproduce global reactor biofilm growth.

3.2. Materials and methods

The integration of the equations of the model with respect to time has been implemented in MATLAB's Simulink, using the ode23tb solver with a variable timestep. This solver employs the TR-BDF2, a two-stage integration scheme: the first stage consists of an implicit Runge-Kutta algorithm with a trapezoidal rule step, while in the second stage, a backward differentiation formula of order two is used. This method is appropriate for solving stiff differential equations systems, and so it is used to model the reactor's bulk operation in order to determine its long-term evolution. Diffusion processes inside the biofilm are solved at each timestep of the global algorithm, under the assumption that equilibrium is reached at a much shorter time-scale (quasi-static approach). For this, a 1-D finite elements discretization in the radial direction of a representative bead is considered, and the resulting non-linear system of equations is solved using a Newton-Raphson scheme, as described in section 3.4.3 of this chapter

3.3. Assumptions for model development

The proposed model for the axenic packed-bed nitrifying reactor is based on a three-level approach. The simulation of the complete packed-bed reactor is achieved by coupling a diffusion and reaction model (used to describe internal biofilm parameters such as substrates and products diffusion and biochemical reactions) with a hydrodynamic model (used to describe the global behavior of the reactor) and a biofilm model (used to describe the global reactor bulk evolution).

Figure 3-1 describes the general structure of the proposed modelling strategy. As observed, the treatment of the packed-bed reactor is simplified in the hydrodynamic component by using a n-tanks in series approach where gas-liquid mass transfer as well as gas and liquid flow rates are considered. Additionally, a proposed biofilm model is linked to this hydrodynamic model in each n-tank. This biofilm model is based on a two-

phase structure, consisting of the bulk phase, where the substrates and the products are dissolved, and the biofilm phase, where the biomass concentration can be predicted as a function of the calculated biofilm volume. In this biofilm phase, the model adopts some simplifications to describe biofilm aging and consolidation phenomenon by considering the biomass detachment from the biofilm to the bulk liquid and the internal repositioning of the biomass units during biofilm consolidation. It should be noted that the presence of internal water content inside this biofilm phase (referred from here onwards as pore water [10,17]) is approached by taking into consideration an internal biofilm porosity as one of the model parameters. Finally, each iteration of the biofilm model is coupled to a diffusion and reaction model considering substrate and products diffusion in the specific biofilm thickness as well as biochemical reactions due to the growth of the biomass specifically attached to the packed-bed particles.
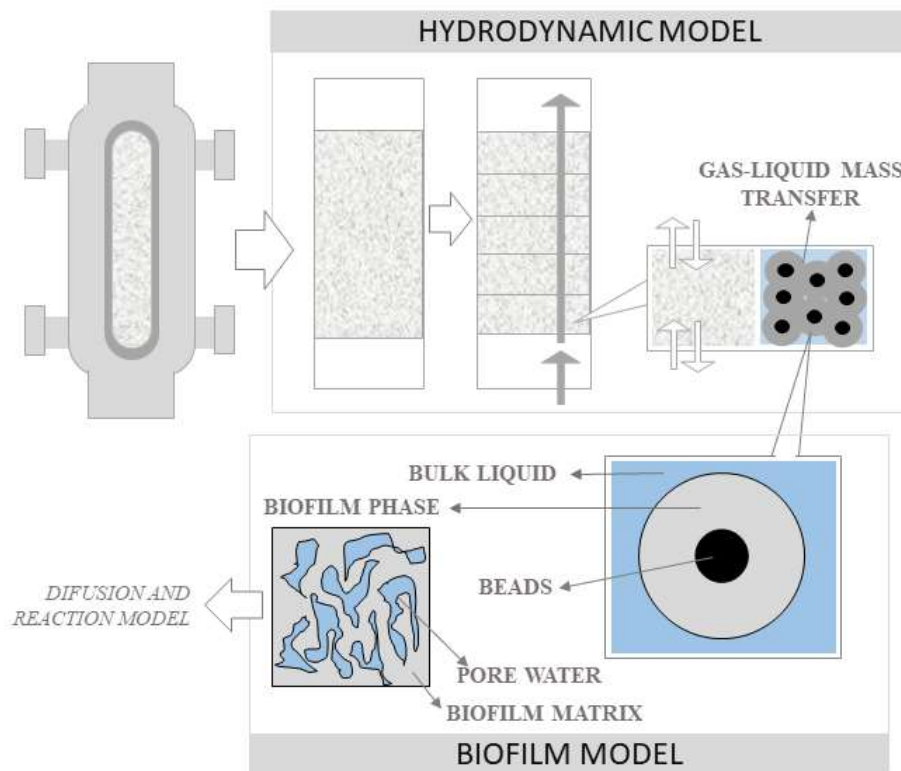

Figure 3-1. Global scheme of the proposed model approach.

The different sections below describe in detail the different blocks used to elaborate the model proposal in this three-level approach: hydrodynamic model, biofilm model and diffusion and reaction model.

3.3.1 Macroscopic hydrodynamic model assumptions

The hydrodynamic model implemented for the gas and bulk liquid is based on a model developed in previous publications [18,19] based on hydrodynamic characterization tests performed in the liquid phase.

According to these studies, the liquid phase of the reactor behaves as a perfectly mixed reactor in the operation ranges used, basically due to the effects of liquid recirculation and aeration. However, the packed-bed structure of the bioreactor and the biomass growth generating a biofilm surrounding the packed-bed particles has to be addressed as well in the global hydrodynamic model design since a gradient of biofilm thickness is observed during the operation along the packed-bed vertical axis. As described in [20], the high mixing time observed in the reactor (due to the high ratio height/diameter of the reactor) together with the high nitrification rate observed are the driving forces that produce this phenomena. Therefore, the model defined for the bulk phase considers the approximation of a perfectly mixed reactor observed in the hydrodynamic experimental tests and the biomass distribution along the reactor height. This is achieved by applying a scheme of n-tanks in series where a global one-direction flow (in terms of gas and liquid flow by considering the liquid and gas inlet flow and recirculation flow) is coupled with a back-mixing liquid flow between each tank and the ones located prior and after it. A global scheme of the liquid and gas fluxes in each one of the n-tank in series configuring the hydrodynamic model is summarized in Figure 3-2.
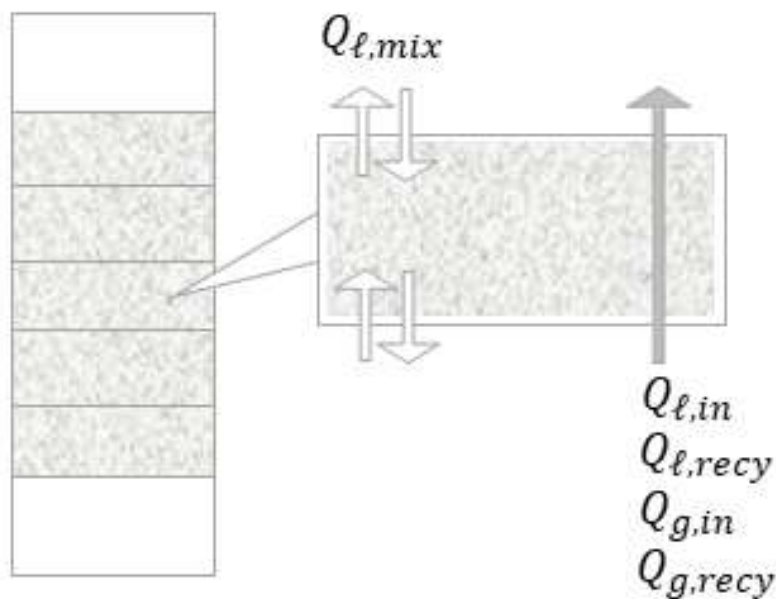
Figure 3-2. Description of the liquid (Q_l) and gas (Q_g) flow rates balance in a model n-tank compartment. Three types of fluxes are mentioned in the scheme: input flow rate (in), recirculation flow rate (recy) and back-mixing flow rate (mix).

With this general idea, the final approach proposed for the description of the packed-bed reactor considers the reactor as a cylinder with three different parts: the bottom and the top parts (part A and C in Figure 3-3, corresponding to the reactor volumes outside the packed bed) and the packed bed section (part B in Figure 3-3). Additionally, this packed-bed is considered to be divided in 5 tanks in series (b = 2 to b=6). In each tank (b), two phases are considered: the liquid bulk ($V_L^{[b]}$) and the solid phase ($V_S^{[b]}$). On one hand, the solid phase corresponds to the packed-bed particles volume ($V_b^{[b]}$) and the packed-bed material with the biofilm volume ($V_F^{[b]}$).

On the other hand, the bulk liquid phase contains as well, a gas phase ($V_G^{[b]}$) calculated as function of this total liquid volume by considering a constant gas hold-up factor (v).
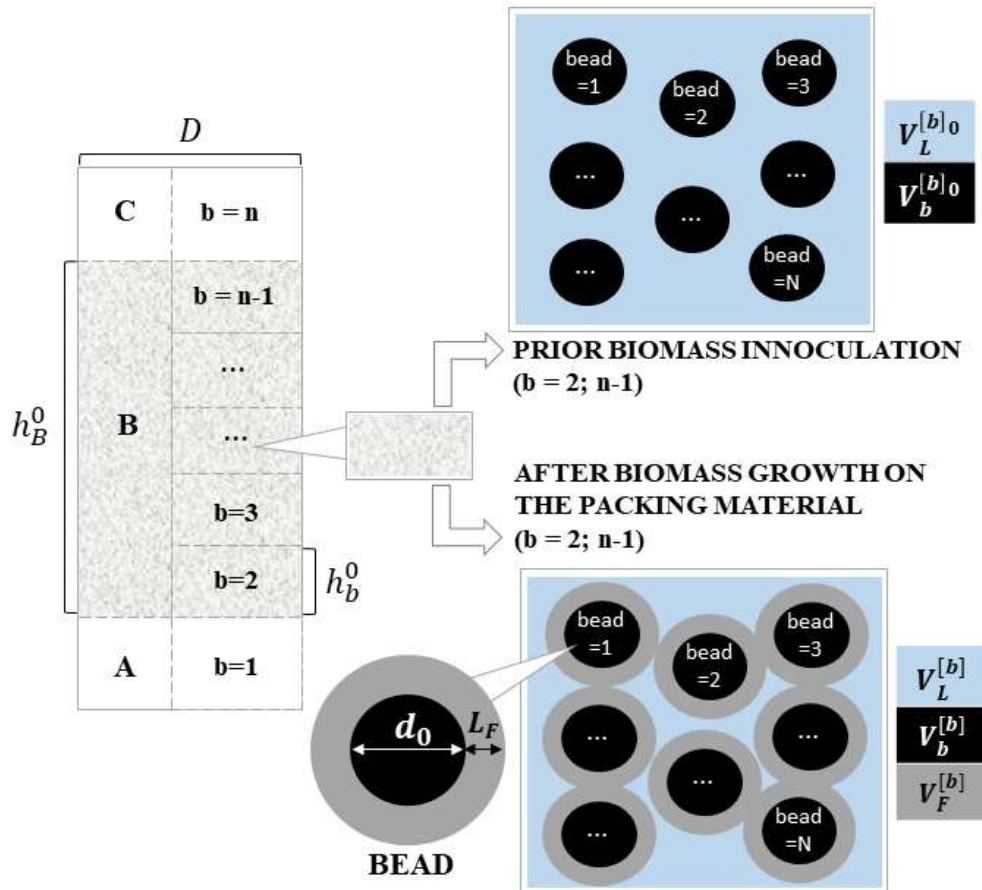
Figure 3-3. Definition of the main parameters in the hydrodynamic model for each n-tank in series (b, ranging from 2 to 6) corresponding to the packed bed section (B). In this figure, height of each tank in series (h_b^0) and total height of the packed-bed reactor (h_B^0) are also highlighted for the beginning of the operation. Hydrodynamic model is composed of a liquid bulk volume ($V_L^{[b]}$) and a solid volume ($V_S^{[b]}$) that consists of the volume of the packed-bed particlesl ($V_b^{[b]}$) and the biofilm growing on the surface of the beads ($V_F^{[b]}$)in a specific biofilm thickness (L_F). Specific details of the different model parameters and definitions are summarized in Table 3-1 and Table 3-2.

The model assumes that the number of beads in each n-tank ($N^{[b]}$) is constant (equal to Equation 3-9 specified in Table 3-1) and depends on the packed-bed reactor dimensions and the initial void fraction (η_l^0, referring to the ratio between the total liquid volume and the total volume in the packed-bed). Additionally, the model also considers the possible reduction of the packed-bed height as consequence of an increase of the packing efficiency due to the continuous up-flow applied in the reactor, also favored by the fact that the packed-bed particles have density lower than water. In this case, the volume of each n-tank in series is reduced proportionally to compensate the increase of volume in the first n-tank in the model that does not contain packing material. In that way, the decrease of the overall height of the packed-bed (h_B) is compensated. This packed bed n-tanks volume reduction is translated into a decrease of the void fraction up to the maximum theoretical sphere packing (corresponding to a 26% as detailed in [21]). In these conditions, the model assumes as a simplification that the reduction of liquid volume in the packed bed does not have an impact on the reactor hydrodynamics.

Additionally, gas-liquid mass transfer is also considered between gas and liquid phases for oxygen. This is calculated based on a mass transfer coefficient, the dissolved oxygen saturation concentration in the liquid calculated according to Henry's law and the specific partial pressure in the gas phase as described in Equation 3-1.

$$N_{O_2} = k_L a \cdot (C^* - C_L)$$
3-1

Where N_{O_2} is the oxygen mass transfer rate, C^* is the saturation concentration of dissolved oxygen in the liquid medium based on Henry's law and its partial pressure in the gas phase [22], C_L is the molar concentration of oxygen in the liquid phase and k_{La} is the mass transfer coefficient. For the top and bottom sections, fixed experimental values of k_{La} (32.4 h^{-1} for the top section and 54.0 h^{-1} for the bottom section) have been previously determined [23] whereas an experimental correlation of kla coefficient as function of the gas velocity (u_G), the reactor

48

diameter (D) and the packed-bed particles diameter (d_p) has been used for the packed bed according to previous tests (see Equation 3-2, [24]) by using the mass balance sulfite method [25].

$$k_{La}(h^{-1}) = 1481 \cdot u_G^{0.5979} \cdot \left(\frac{d_0}{D}\right)^{-0.1153}$$

3-2

Finally, the growth of biomass is also considered in the liquid phase. The model considers one variable for each species (*Nitrosomonas* ($X_{\ell,\text{Ns}}^{[b]}$), *Nitrobacter* ($X_{\ell,\text{Nb}}^{[b]}$)) and one additional variable for the inactive biomass in the liquid phase that are used for the kinetic calculations ($X_{\ell,0}^{[b]}$). The kinetic equations used for biomass growth in the liquid bulk are the same used in the specific model that describes biofilm growth and are summarized in Section 3.3.3.2.

The mathematical formulation of the hydrodynamic model basic concepts is summarized in Table 3-1 and Table 3-2.

Based on this hydrodynamic model parameters definition and the general design assumptions described, Table 3-3 summarizes the definition of the global input $M_{S_{phase}}^{in[b]}$ and output $M_{S_{phase}}^{out[b]}$ mass flow per each n-tank in series in the global reactor design in g/h for the liquid and gas phase. It should be noted that in these equations, S_{ℓ}^n corresponds to the specific concentration in each tank in series.

Table 3-1. Macroscopic hydrodynamic model: Definition of the main parameters (1/2)

Packed-bed status	Variable		Definition	
Prior addition of biomass	Total bed volume	V_T^0	$V_T^0 = \dfrac{\Pi}{4} D^2 \cdot h_B^0$	3-3
	n-tank total volume	$V_T^{[b]_0}$	$V_T^{[b]_0} = \dfrac{\Pi}{4} \dfrac{D^2 \cdot h_B^0}{(b-2)}$	3-4
	Liquid volume	$V_L^{[b]_0}$	$V_L^{[b]_0} = V_T^{[b]_0} \cdot \eta_l^0 = V_T^{[b]_0} \cdot \dfrac{V_L^{[b]_0}}{V_T^{[b]_0}} = V_T^{[b]_0} - V_b^{[b]_0}$	3-5
	Gas volume	$V_G^{[b]_0}$	$V_G^{[b]_0} = V_L^{[b]_0} \, \nu$	3-6
	Total solid volume	$V_S^{[b]_0}$	$V_S^{[b]_0} = V_b^{[b]_0}$	3-7
	Beads volume	$V_b^{[b]_0}$	$V_b^{[b]_0} = \dfrac{\Pi}{6} N^{[b]}(d^0)^3 = V_T^{[b]_0}(1 - \eta_l^0)$	3-8
	Number of beads per n-tank	$N^{[b]}$	$N^{[b]} = \dfrac{V_b^{[b]_0} \, 6}{\Pi \, (d_0)^3} = \dfrac{V_T^{[b]_0}(1 - \eta_l^0) \, 6}{\Pi \, (d_0)^3} = \dfrac{3}{2} \dfrac{D^2 h_B^0 (1 - \eta_l^0)}{(d_0)^3 \, (b-2)}$	3-9
	Beads area	$A_b^{[b]_0}$	$A_b^{[b]_0} = \Pi \, d_0^2 \, N^{[b]}$	3-10

Table 3-2. Macroscopic hydrodynamic model: Definition of the main parameters (2/2)

Packed-bed status	Variable		Definition	
After biofilm formation over the packing material	Total bed volume	V_T	$$V_T = \frac{\Pi}{4} D^2 \cdot h_B$$	3-11
	n-tank total volume	$V_T^{[b]}$	$$V_T^{[b]} = \frac{\Pi}{4} \frac{D^2 \cdot h_B}{(b-2)}$$	3-12
	Total solid volume	$V_S^{[b]}$	$$V_S^{[b]} = V_b^{[b]} + V_F^{[b]}$$	3-13
	Liquid volume	$V_L^{[b]}$	$$V_L^{[b]} = V_T^{[b]} \cdot \eta_l = V_T^{[b]} \cdot \frac{V_L^{[b]}}{V_T^{[b]}} = V_T^{[b]} - V_b^{[b]_0} - V_F^{[b]}$$	3-14
	Gas volume	$V_G^{[b]}$	$$V_G^{[b]} = V_L^{[b]} \nu$$	3-15
	Beads volume	$V_b^{[b]}$	$$V_b^{[b]} = \frac{\Pi}{6} N^{[b]} d^3 = V_T^{[b]} (1-\eta_l) - V_F^{[b]}$$	3-16
	Number of beads per n-tank	$N^{[b]}$	$$N^{[b]} = \frac{V_b^{[b]_0} 6}{\Pi (d_0)^3} = \frac{V_T^{[b]_0}(1-\eta_l^0) 6}{\Pi (d_0)^3} = \frac{3}{2} \frac{D^2 h_B^0 (1-\eta_l^0)}{(d_0)^3 (b-2)}$$	3-17
	Beads area	$A_b^{[b]}$	$$A_b^{[b]} = \Pi \, d^{[b]^2} N^{[b]}$$	3-18
	Biofilm volume	$V_F^{[b]}$	$$V_F^{[b]} = \frac{\Pi}{6} N^{[b]}[(d_0 + 2L_F^0)^3 - (d_0)^3]$$	3-19

Table 3-3. Definition of input and output mass flow for each n-tank (b 1 to 7)

Model phase	ID	Compartment (b)	Compartment mass flow description
Liquid[(1)]	$M_{l,C_l,j}^{in[b]}$	b=1	$Q_{\ell,in}S_\ell^{in} + Q_{\ell,recy}S_\ell^{[n]} + Q_{\ell,mix}S_\ell^{[2]}$
		b=7	$(Q_{\ell,in} + Q_{\ell,recy} + Q_{\ell,mix})S_\ell^{[n-1]}$
		b=2 to (n-1)	$(Q_{\ell,in} + Q_{\ell,recy} + Q_{\ell,mix})S_\ell^{[b-1]} + Q_{\ell,mix}S_\ell^{[b+1]}$
	$M_{l,C_l,j}^{out[b]}$	b=1 or 1	$(Q_{\ell,in} + Q_{\ell,recy} + Q_{\ell,mix})S_\ell^{[b]}$
		Otherwise	$(Q_{\ell,in} + Q_{\ell,recy} + 2Q_{\ell,mix})S_\ell^{[b]}$
Gas [(1)]	$M_{g,Cg,j}^{in[b]}$	b=1	$Q_{g,in}S_g^{in} + Q_{g,recy}S_g^{[n]}$
		Otherwise	$(Q_{g,in} + Q_{g,recy})S_g^{[b-1]}$
	$M_{g,Cg,j}^{out[b]}$	All cases	$(Q_{\ell,in} + Q_{\ell,recy})S_g^{[b]}$

(1) In order to obtain final units of g/h, the specific values need to be obtained from the original units (flow rates mL/min and concentrations g/L).

$Q_{g,in}$ defined as the pure gas (intended to be oxygen) flow rate to be added to the system to maintain the oxygen concentration in liquid to specific percentage of saturation.

3.3.2 Biofilm growth model assumptions

The model for the description of the biofilm growth is proposed on the basis of existing knowledge on this domain. Specifically, current available literature describes an initial growth of the biofilm in a fluffy structure (high water content or high porosity) up to the maximum biofilm thickness as an initial step of biofilm growth. Then, a second phase occurs, with an increase of the biomass concentration in the biofilm attributed to a reduction in its porosity (water content inside the biofilm) adjacent to the support material. This reduction of porosity is assumed/proposed to be related to the filling of void spaces by inert biomass produced in the external, more fluffy and active region of the biofilm [26,27]. Thus, this realignment of the biofilm leads to a final biomass distribution where external layers are more fluffy and with a higher presence of active biomass and internal layers are dominated by residual inert biomass [11]. In this context, the proposed macroscopic biofilm model, considers three simplifications in order to gain computational efficiency (See Figure 3-4A):

- The existence of only one variable for the concentration of each biomass species (*Nitrosomonas*, *Nitrobacter* and inactive biomass) inside the biofilm. This

variable is identified as $\bar{X}_{F,i}^{[b]}$ defined as the mass of the corresponding species (i) divided by the volume of the entire biofilm $V_F^{[b]}$.

- The consideration of a uniform biofilm porosity ($\varepsilon_{F,l}^{[b]}$) (existence of residual water inside the biofilm) in all biofilm depth. This porosity is considered as a variable in the biofilm modelling and therefore it increases in time as a consequence of biofilm aging.

- The assumption of a maximal biomass concentration in the biofilm of 270 g/L (ρ_{bio}) based on literature by considering that 1 mg of dry biomass is equivalent to an average of $3.7 \cdot 10^9$ cells and assuming a mean geometry for each cell of 1μm x 1μm x 1μm (1μm^3) [28]. Based on this assumption, the total biomass concentration in each compartment volume can be calculated considering the value of porosity in each simulation as $\rho_{bio}(1 - \varepsilon_{F,l}^{[b]})$.

However, the biofilm evolution is more complex, specifically when phenomena like biofilm aging and consolidation are considered (see Figure 3-4B). In order to take into account this time-increasing biofilm structure complexity, the model includes two additional variables to describe the expected increase of concentration and repositioning of the biomass: the global biofilm thickness ($L_F^{[b]}$) and the depth of the inactive layer of the biofilm or inactive biofilm thickness ($L_{F,0}^{[b]}$)). This allows for the consideration of an active and inactive layers of biomass inside the biofilm. As observed in Figure 3-4B, the internal layer grows adjacent to the support material with only inactive biomass as a consequence of biofilm aging and consolidation, whereas the active layer is composed by the three species present in the model.
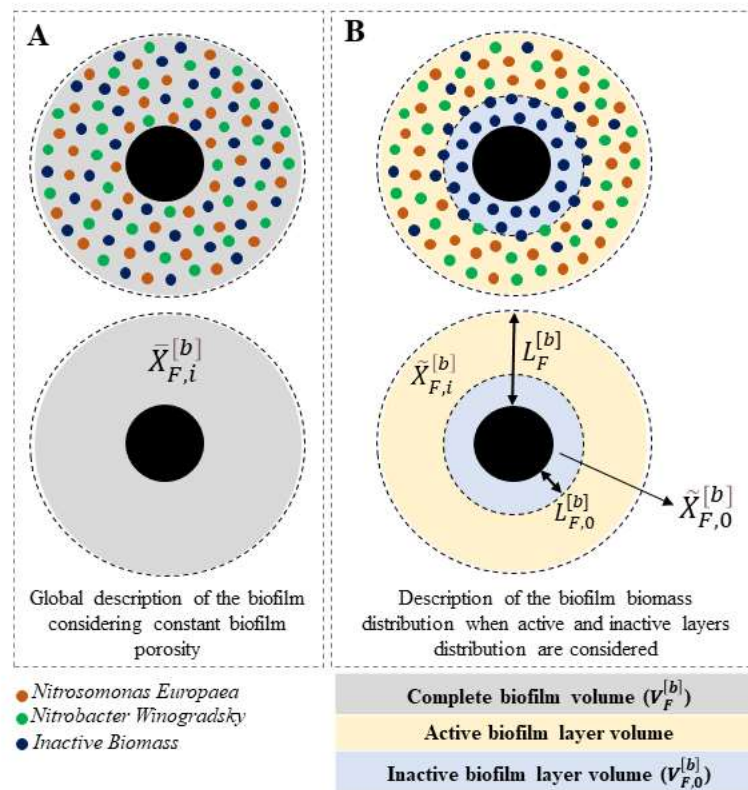
Figure 3-4. Description of simplified biofilm structure according to basic assumptions (A) and biofilm strucutre when active and inactive layers are considered (B).

When these two additional variables are considered, the model can recalculate the effective concentration of each biomass species (*Nitrosomonas*, *Nitrobacter* and inactive biomass) in the active layer of the biofilm. These effective concentrations in the active layer of the biofilm ($\tilde{X}_{F,i}^{[b]}$, where *i* is one of the two microorganism species (*Nitrosomonas*, *Nitrobacter*) present in the biofilm or $\tilde{X}_{F,0}^{[b]}$ when the inactive biomass is considered) are not specific model variables but are calculated by considering specific biofilm porosity ($\varepsilon_{F,l}^{[b]}$), complete biofilm thickness ($L_F^{[b]}$) and inactive biomass layer thickness ($L_{F,0}^{[b]}$) variables values in each iteration. Calculation of these effective concentrations is attained by Equation 3-20 and Equation 3-21 by considering a radial growth of the biofilm, specific simulation porosity and that inactive layer contains only inactive biomass. It should be noted

54

that $\phi_{F,0}^{[b]}$ corresponds to the ratio between the inactive $V_{F,0}^{[b]}$ and the total biofilm volume $V_F^{[b]}$ as $(\phi_{F,0}^{[b]} = \frac{V_{F,0}^{[b]}}{V_F^{[b]}})$.

$$\tilde{X}_{F,i}^{[b]} = \frac{1}{1 - \phi_{F,0}^{[b]}} \bar{X}_{F,i}^{[b]} \qquad\qquad 3\text{-}20$$

$$\tilde{X}_{F,0}^{[b]} = \rho_{bio} \left(1 - \varepsilon_{F,\ell}^{[b]}\right) - \sum_{i=1}^{n_x} \tilde{X}_{F,i}^{[b]} \qquad\qquad 3\text{-}21$$

In order to describe the biofilm aging and the final biofilm structure, the model postulates, apart from the specific kinetics, some driving forces to simulate biomass repositioning inside the biofilm. These driving forces are expressed as velocities and include the biomass detachment to the bulk liquid and the formation of an inactive layer of biomass in the surface of the beads. Figure 3-5 presents a general description of how the model considers this biomass repositioning phenomena during biofilm consolidation. Initially, the model considers a colonization of the packed-bed at low biofilm concentration to the maximum established biofilm thickness by only considering a proportional detachment of the three species present in the biofilm to the bulk phase. However, when this colonization arrives at the maximum biofilm thickness, the model allows for the biofilm porosity decrease and inactive layer formation to reflect biofilm aging and consolidation phenomena as a repositioning of the inactive biomass in the more internal layers of the biofilm.

On the basis of this rationale, the following subsections describe the approach followed for the calculation of the attachment and detachment velocities (m/h):

- Detachment velocities that transfer biomass from the biofilm to the bulk liquid
  - o Detachment of active biomass (*Nitrosomonas* and *Nitrobacter*) ($u_{det}^{[b]}$)
  - o Detachment of inactive biomass ($u_{det,0}^{[b]}$)
- Velocities to describe consolidation phenomena by using an attachment biomass velocity from the active part of the biofilm to the inactive part. ($u_{att,0}^{[b]}$)

These velocities are referred to the biofilm external area and can be incorporated to specific mass balances ($M_{\bar{X}_{F,i}}^{det[b]}$, $M_{\bar{X}_{F,0}}^{\text{det},0[b]}$ and $M_{\bar{X}_{F,0}}^{\text{att},0[b]}$ respectively) as g/h of a specific species detached or attached biomass by considering biofilm external area and specific biofilm concentration as detailed in Figure 3-6. With these velocities and considering the output of the microscopic model for biofilm growth (see section 3.3.3), specific mass balances can be performed for the biofilm phase
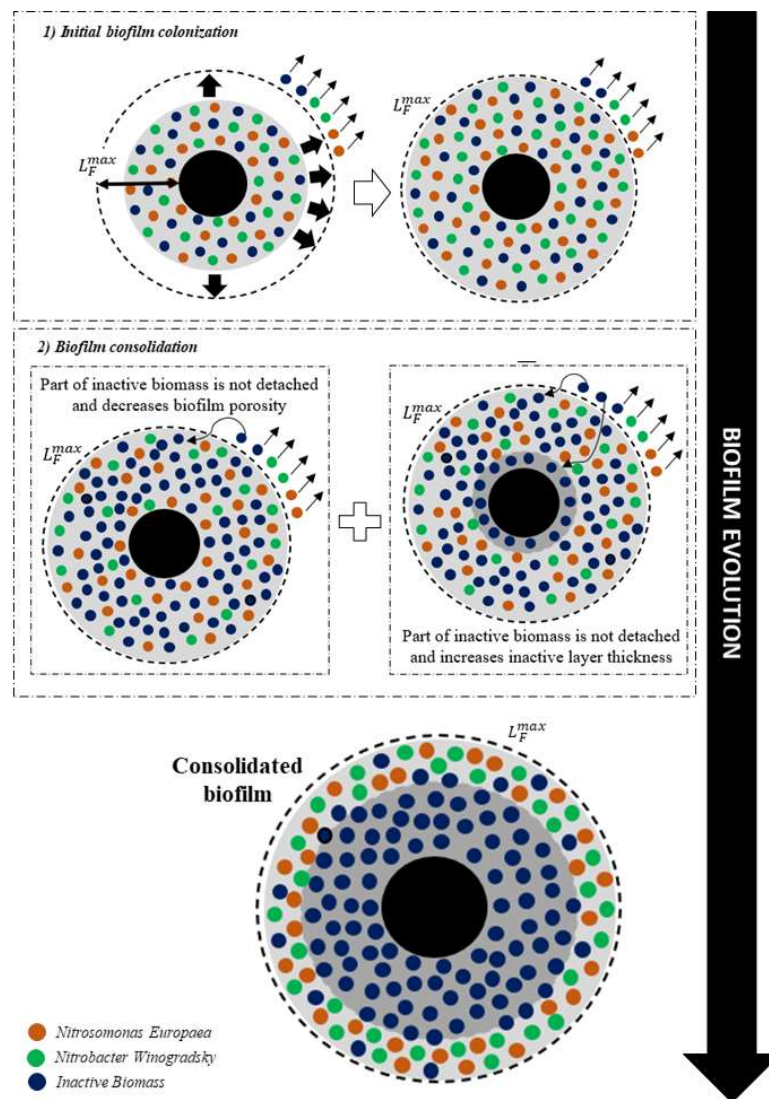
Figure 3-5. General description of specific biomass repositioning during biofilm consolidation..

56

$$u_{det}^{[b]}$$

$$M_{\tilde{X}_{F,i}}^{\mathrm{det}[b]} = u_{det}^{[b]} \cdot A_F \cdot \tilde{X}_{F,i}^{[b]}$$

$$u_{det,0}^{[b]}$$

$$M_{\tilde{X}_{F,0}}^{\mathrm{det,0}[b]} = u_{det,0}^{[b]} \cdot A_F \cdot \tilde{X}_{F,0}^{[b]}$$

$$u_{att,0}^{[b]}$$

$$M_{\tilde{X}_{F,0}}^{\mathrm{att0}[b]} = u_{att,0}^{[b]} \cdot A_{F_0} \cdot \tilde{X}_{F,0}^{[b]}$$

Inactive biomass concentration
in the active layer

$$\tilde{X}_{F,0}^{[b]} = \rho_{bio}\left(1 - \varepsilon_{F,\ell}^{[b]}\right) - \sum_{i=1}^{n_x} \tilde{X}_{F,i}^{[b]}$$

Active biomass concentration
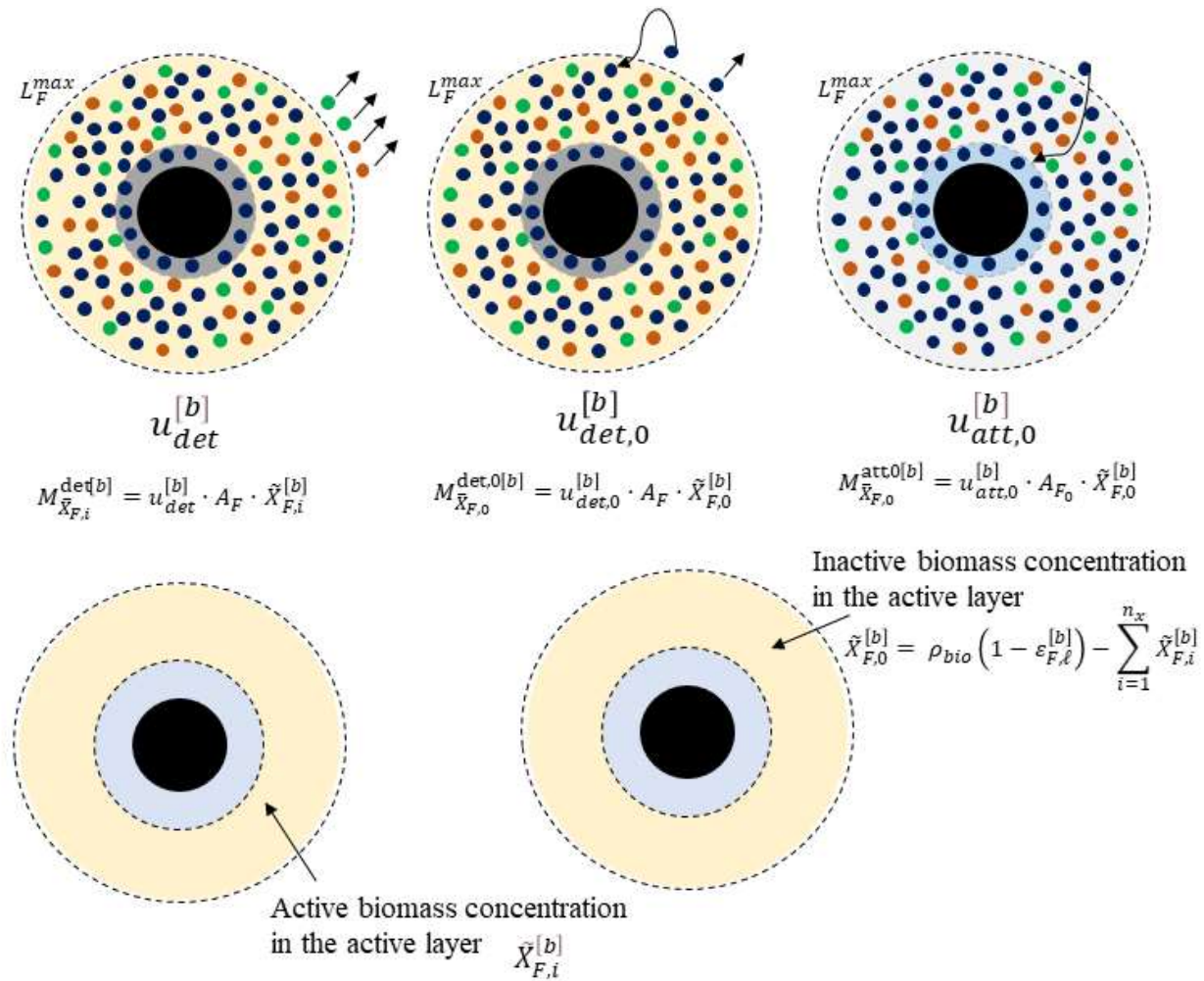in the active layer $\quad \tilde{X}_{F,i}^{[b]}$

Figure 3-6. Description of the mathematical transformation of repositioning velocities (m/h) in the specific mass balances.

57

3.3.2.1 Biomass detachment: biofilm to the liquid bulk

The model considers a detachment rate determined according to the biofilm maximum thickness as generally found in literature [26,27]. However, the model considers also a definition of a specific velocity for the detachment of active or inactive biomass in order to be able to reproduce the consolidation phenomena during biofilm growth.

On one hand, the general detachment velocity ($u_{det}^{[b]}$, m/h) for active biomass is determined as:

$$u_{det}^{[b]} = \alpha^{[b]} u_F^{[b]} = \left(\frac{L_F^{[b]}(t)}{L_F^{max}}\right)^2 \cdot \left(\frac{\sum_{i=1}^{n_x} R_{F,X_i}^{[b]}}{\rho_{bio}\left(1 - \varepsilon_{F,\ell}^{[b]}\right)A_F^{[b]}}\right) \qquad \text{3-22}$$

Where $\alpha^{[b]}$ is the active biomass detachment factor that depends on the current biofilm thickness ($L_F^{[b]}(t)$) and the final biofilm thickness (L_F^{max}) and $u_F^{[b]}$ is the biomass growth velocity calculated according to the simplified substrate diffusion microscopic model. This biomass growth velocity considers the biomass growth by using the microscopic model $\left(\sum_{i=1}^{n_x} R_{F,X_i}^{[b]} \text{ in g/h}\right)$, the biofilm density ($\rho_{bio}$), the biofilm current porosity $\left(\varepsilon_{F,\ell}^{[b]}\right)$ and the external biofilm surface area ($A_F^{[b]}$).

On the other hand, the general expression for the detachment of inactive biomass corresponds to the active detachment expression modified by the introduction of an additional factor, $\beta^{[b]}$. This factor corresponds to the fraction of the inactive biomass that remains in the biofilm allowing for the biofilm consolidation to occur by decreasing its porosity. Thus, the final inactive-biomass detachment velocity ($u_{det,0}^{[b]}$, m/h) reads as:

$$u_{det,0}^{[b]} = (1 - \beta^{[b]})u_{det}^{[b]} \quad \text{where } \beta^{[b]}(t) = max\left\{0, \varepsilon_{F,\ell}^{[b]}(t) - \varepsilon_{F,\ell}^{min}\right\} \qquad \text{3-23}$$

Where this additional factor $\beta^{[b]}$ depends on the difference between the current biofilm porosity and the minimum biofilm porosity ($\varepsilon_{F,\ell}^{[b]}(t)$ and $\varepsilon_{F,\ell}^{min}$ respectively)

3.3.2.2 Velocities to describe biofilm consolidation phenomena

Consolidation phenomena is modelled as a repositioning or attachment of inactive biomass from the biofilm active phase to an internal inactive layer of the biofilm. This repositioning of inactive biomass is governed by the inactive layer attachment velocity. This velocity (m/h) describes the attachment of inactive biomass to the inactive layer of biofilm and reads as:

$$u_{att,0}^{[b]} = \left(\gamma^{[b]} + \phi_{F,0}^{[b]} \beta^{[b]} \alpha^{[b]} \right) u_{F,0}^{[b]} \tag{3-24}$$

$$where \; u_{F,0}^{[b]} = \frac{A_F^{[b]}}{A_{F,0}^{[b]}} u_F^{[b]} \quad and \quad \gamma^{[b]}(t) = 0.01 \left[1 - \left(\frac{L_{F,0}^{[b]}(t)}{L_{F,0}^{max}} \right)^2 \right] \tag{3-25}$$

In this expression, the parameter $\gamma^{[b]}$ determines the growth of the inactive layer thickness. It should be noted that the growth of the inactive layer is limited by a specified maximum thickness $L_{F,0}^{max}$ (a value of $L_{F,0}^{max} = 0.2 \; L_F^{max}$,) established according to literature [11]. The rest of the equation determines the transfer of inactive biomass required for keeping the porosity constant throughout the biofilm. Note that $u_{F,0}^{[b]}$ is the equivalent $u_F^{[b]}$ for the active-inactive layer interface.

3.3.3 Microscopic model assumptions

This section includes the main assumptions for the definition of the substrate diffusion processes and the definition of the kinetic equations to be used inside the 1-D finite element discretization.

3.3.3.1 Assumptions used for the finite element discretization

A 1-D finite element discretization of the biofilm's active layer has been performed in order to account for substrate diffusion processes described by Fick's first and second laws (Equation 3-26 and Equation 3-27).

$$J_{F,j}^{[b]} = -D_j \frac{\partial C_{F,j}^{[b]}}{\partial z} \qquad\qquad 3\text{-}26$$

$$\frac{\partial C_{F,j}^{[b]}}{\partial t} + \frac{\partial J_{F,j}^{[b]}}{\partial z} = r_{F,j}^{[b]} \qquad\qquad 3\text{-}27$$

On one hand, Equation 3-26 defines the j-th substrate's diffusion flux $J_{F,j}^{[b]}$, with z referring to the biofilm's thickness coordinate (i.e. $z = r - d^{[b]}/2$ where r is the radius of the bead and the biofilm thickness and d is the beads diameter), D_j being the diffusivity of the corresponding substrate and $C_{F,j}^{[b]}$ its concentration (in g/m^3 of biofilm volume). On the other hand, Equation 3-27 gives the substrate balance equation, in which $r_{F,j}^{[b]}$ refers to the substrate production/consumption rate inside the biofilm. In this equation, $r_{F,j}^{[b]}$ depends on the biomass species concentration on each point of the biofilm which is considered when calculating the effective concentrations $\tilde{X}_{F,i}^{[b]}$. However, these global effective concentrations $\tilde{X}_{F,i}^{[b]}$ are only calculated as macroscopic parameters after each reaction-diffusion model iteration. For this reason, a uniform distribution of such biomass is considered for this reaction-diffusion analysis (i.e. $\tilde{X}_{F,i}^{[b]} =$ constant throughout the biofilm's active layer) as a simplification.

These expressions are given for the 1-D case under the assumption that the non-radial diffusion effects are negligible compared to radial diffusion. This hypothesis is very important in order to simplify the analysis of the biofilm, which is performed on each iteration step of the global macroscopic integration scheme, making the whole simulation computationally

60

affordable. Furthermore, the hypothesis that the biofilm's thickness is much smaller than the beads' diameter, $L_F^{[b]} \ll d^{[b]}$, is also considered to simplify some of the expressions.

The second main assumption considered here is regarding the time-dependency of Equation 3-27. In particular, since the time scale of the global simulation is much larger than the time scale at which diffusion processes occur, a quasi-static approach can be reasonably assumed [29]. This means that the biofilm system reaches its equilibrium state at each iteration step of the global simulation, with the corresponding biomass production rate used to model its growth and the flux of substrates between the bulk liquid and the biofilm. Finally, biofilm external transfer resistance is neglected for the calculation of diffusion inside the biofilm.

The application of all of these assumptions is explained in the next sections.

3.3.3.2 Kinetic equations

This section defines the kinetic equations used inside the 1-D finite element discretization. It should be noted that these same kinetic equations are also used for the calculation of the biomass growth in the bulk liquid phase. Kinetic equations describing the growth of both species as well as the parameters values used are described in Table 3-4 and Table 3-5.These kinetic equations used to define *Nitrosomonas europaea* and *Nitrobacter winogradsky* growth are equivalent to the ones applied in previous more simplified models of this reactor [19]. These equations consider the limitation by both the nitrogen source (NH_4^+ or NO_2^- respectively) and the dissolved oxygen concentration. Additionally, inhibition by the respective substrates and products has also been incorporated [30].

Table 3-4. Biomass growth kinetic equations used in the model

Species	Kinetic equations used
Nitrosomonas europaea	$$\mu_{max}^{Nts}\tilde{X}_{F,Ns}^{[b]}\;\frac{C_{\ell,\text{N-NH}_4^+}^{[b]}}{K_{NH_4^+}^{Nts}+C_{\ell,\text{N-NH}_4^+}^{[b]}+\dfrac{{C_{\ell,\text{N-NH}_4^+}^{[b]}}^{2}}{K_{FA}^{In,Nts}}}\;\frac{C_{\ell,\text{O}_2}^{[b]}}{K_{O_2}^{Nts}+C_{\ell,\text{O}_2}^{[b]}}$$ By considering the following recalculation of $K_{FA}^{In,Nts}$ by using the equivalence between $C_{\ell,\text{N-NH}_4^+}^{[b]}$ and $C_{FA}^{[b]}$ (free ammonia) in terms of pH and temperature: $$C_{FA}^{[b]}=\frac{\left(\dfrac{17}{14}\right)\cdot C_{\ell,\text{N-NH}_4^+}^{[b]}\cdot 10^{pH}}{\dfrac{K_b}{K_w}+10^{pH}}\;;where\;\frac{K_b}{K_w}=e^{\frac{6344}{273+T(^\circ C)}}$$
Nitrobacter winogradsky	$$\mu_{max}^{Ntb}\tilde{X}_{F,Nb}^{[b]}\;\frac{1}{K_{NO_2^-}^{Ntb}+C_{\ell,\text{N-NO}_2^-}^{[b]}+\dfrac{{C_{\ell,\text{N-NO}_2^-}^{[b]}}^{2}}{K_{FNA}^{In,Ntb}}}\;\frac{C_{\ell,\text{O}_2}^{[b]}}{K_{O_2}^{Ntb}+C_{\ell,\text{O}_2}^{[b]}}\cdot\frac{K_{FA}^{In,Ntb}}{K_{FA}^{In,Ntb}+C_{\ell,\text{N-NH}_4^+}^{[b]}}$$ By considering the following recalculation of $K_{FA}^{In,Nts}$ by using the equivalence between $C_{\ell,\text{N-NH}_4^+}^{[b]}$ and C_{FA} (free ammonia) in terms of pH and temperature: $$C_{FA}^{[b]}=\frac{\left(\dfrac{17}{14}\right)\cdot C_{\ell,\text{N-NH}_4^+}^{[b]}\cdot 10^{pH}}{\dfrac{K_b}{K_w}+10^{pH}}\;;where\;\frac{K_b}{K_w}=e^{\frac{6344}{273+T(^\circ C)}}$$ By considering the following recalculation of $K_{FNA}^{In,Ntb}$ by using the equivalence between $C_{NO_2^-}$ and $C_{FNA}^{[b]}$ (free ammonia) in terms of pH and temperature: $$C_{FNA}^{[b]}=\frac{\left(\dfrac{47}{14}\right)\cdot C_{\ell,\text{N-NO}_2^-}^{[b]}}{K_a\cdot 10^{pH}}\;;where\;K_a=e^{\frac{-2300}{273+T(^\circ C)}}$$

Note: Specific kinetic parameters values are summarized in

Table 3-5. Parameters of the kinetic equations used in the model

Parameter ID	Units	Nitrosomonas Europaea	Nitrobacter Winogradsky
$K_{NH_4^+}^{Nts}$	$\dfrac{g\,N-NH_4^+}{L}$	0.0175	-
$K_{NO_2^-}^{Ntb}$	$\dfrac{g\,N-NO_2^-}{L}$	-	$5.04\ 10^{-3}$
$K_{O_2}^{Nts}$	$\dfrac{g\,O_2}{L}$	$1.616\ 10^{-4}$	-
$K_{O_2}^{Ntb}$	$\dfrac{g\,O_2}{L}$	-	$5.44\ 10^{-4}$
$K_{FA}^{In,Nts}$	$\dfrac{g\,FA}{L}$	0.116	-
$K_{FA}^{In,Ntb}$	$\dfrac{g\,FA}{L}$	-	$5.2\ 10^{-4}$
$K_{FNA}^{In,Ntb}$	$\dfrac{g\,FNA}{L}$	-	$1.56\ 10^{-4}$
μ_{max}^{Nts}	d^{-1}	1.368	-
μ_{max}^{Ntb}	d^{-1}	-	0.864
$Y_{\frac{X}{S}}^{Nts}$	$\dfrac{g\,VSS}{g\,N-NH_4^+}$	0.119	-
$Y_{\frac{X}{S}}^{Ntb}$	$\dfrac{g\,VSS}{g\,N-NO_2^-}$	-	0.0414
m^{Nts}	$\dfrac{gN}{gVSS\,d}$	1.137	-
m^{Ntb}	$\dfrac{gN}{gVSS\,d}$	-	2.661

3.4. Model equations development

This section presents the mathematical development performed to determine specific equations describing the evolution of the different species proposed in the model. Final equations of the model are then summarized in Table 3-6 and Table 3-7.

3.4.1 Macroscopical model. Bulk Phase analytical development

This section presents the deduction of each of the equations describing the global bioreactor dynamics based on the evolution of the concentration in the bulk liquid of specific substrates, products and specific microorganisms' species.

In order to do that, the definition of the derivative of the mass (g) in each n-tank in series is considered for each substrate, product or microorganism. Since the volume is considered constant in this bulk phase, this derivative can be explained as the derivative of the concentration multiplied by the volume as explained in Equation 3-28:

$$\dot{M}_{S_\ell}^{[b]} = \frac{d}{dt}\left(S_\ell^{[b]}V_\ell^{[b]}\right) = \dot{S}_\ell^{[b]}V_\ell^{[b]}$$

3-28

Where $S_\ell^{[b]}$ is the substrate/product/species concentration of a compound in the liquid phase and $V_\ell^{[b]}$ is the specific volume of liquid. Thus, the equation defining the variation of specific substrate/product/species in the bulk liquid can be isolated as:

$$\dot{S}_\ell^{[b]} = \frac{\dot{M}_{S_\ell}^{[b]}}{V_\ell^{[b]}}$$

3-29

For this reason, in each case, a specific mass balance for a global compound (g/h) in each tank in series is performed as part of the deduction ($\dot{M}_{S_\ell}^{[b]}$). Then, this expression is applied to find the final proposed model equation defined in Equation 3-29.

3.4.1.1 Model equation for individual compounds in the liquid bulk phase.

The model considers four main compounds in the liquid phase: ammonium, nitrite, nitrate and oxygen.

The deduction of the model equations for any of these compounds is performed by defining the global mass balance in the liquid phase for each n-tank in series. $(\dot{M}^{[b]}_{C_{\ell,j}})$ as defined in Equation 3-30.

$$\dot{M}^{[b]}_{C_{\ell,j}} = M^{in[b]}_{\ell,C_{\ell,j}} - M^{out[b]}_{\ell,C_{\ell,j}} - M^{R[b]}_{C_{\ell,j}} - M^{g[b]}_{C_{\ell,j}} \text{(g/h)} \qquad 3\text{-}30$$

Where $M^{in[b]}_{\ell,C_{\ell,j}}$ and $M^{out[b]}_{\ell,C_{\ell,j}}$ are the mass balance inputs and outputs of each n-tank in series as defined in Table 3-3, $M^{R[b]}_{C_{\ell,j}}$ is the specific compound consumption/production by the biomass present in the biofilm (*Nitrosomonas* and *Nitrobacter*) defined in Equation 3-31 according to specific biomass growth in the bulk liquid $(R^{[b]}_{\ell,X_i})$, the biofilm phase $(R^{[b]}_{F,X_i})$ and kinetic equations for each species (i) and $M^{g[b]}_{C_{\ell,j}}$ is the rate of liquid-gas transfer of the substrate as described in Equation 3-32 (only applicable to oxygen in this case).

$$M^{R[b]}_{C_{\ell,j}} = -\sum_{i=1}^{n_x} \left(Y_{j/i} + Y^m_{j/i} \frac{m_i}{\mu_{max,i}} \right) \left(R^{[b]}_{\ell,X_i} + R^{[b]}_{F,X_i} \right) \text{[g/h]} \qquad 3\text{-}31$$

$$M^{g[b]}_{C_{\ell,j}} = k_{LA,j} \left(C^{[b]}_{\ell,j} - C^{*[b]}_{\ell,j} \right) V^{[b]}_{\ell} \quad \text{[g/h]} \qquad 3\text{-}32$$

If these mass balance equations are combined with Equation 3-29, the following final equation of a specific compound in the liquid is found:

$$\dot{C}^{[b]}_{\ell,j} = \frac{1}{V^{[b]}_{\ell}} \left(M^{in[b]}_{\ell,C_{\ell,j}} - M^{out[b]}_{\ell,C_{\ell,j}} + \sum_{i=1}^{n_x} \left(Y_{j/i} + Y^m_{j/i} \frac{m_i}{\mu_{max,i}} \right) \left(R^{[b]}_{\ell,X_i} + R^{[b]}_{F,X_i} \right) \right)$$
$$- k_{LA,j} \left(C^{[b]}_{\ell,j} - C^{*[b]}_{\ell,j} \right) \qquad 3\text{-}33$$

3.4.1.2 Biomass species model equations in the bulk liquid

As discussed previously, the model defines two active biomass species (*Nitrosomonas* and *Nitrobacter*) and a third additional variable describing the evolution of inactive biomass (accumulation of inactive biomass from both active species). In this case, specific equations need to be derived for the active and inactive biomass species. The corresponding mass balances are provided in Equation 3-34 and Equation 3-35.

$$\dot{M}_{X_{\ell,i}}^{[b]} = M_{l,X_{\ell,i}}^{in[b]} - M_{l,X_{\ell,i}}^{out[b]} + M_{X_{\ell,i}}^{R[b]} - M_{X_{\ell,i}}^{lethal[b]} + M_{\overline{X}_{F,i}}^{det[b]} \qquad \text{3-34}$$

$$\dot{M}_{X_{\ell,0}}^{[b]} = M_{l,X_{\ell,0}}^{in[b]} - M_{l,X_{\ell,0}}^{out[b]} + \sum_{i=1}^{n_x} M_{X_{\ell,0}}^{lethal[b]} + M_{\overline{X}_{F,0}}^{det[b]} \qquad \text{3-35}$$

As observed, the only difference between both mass balances is the reaction term in the active biomass balance, corresponding to the growth of the active species $(M_{X_{\ell,i}}^{R[b]})$ according to the specific biomass growth in liquid phase defined as function of specific kinetics. In all cases, however a mass input and output term $(M_{l,X_{\ell,i}}^{in[b]}$ and $M_{l,X_{\ell,i}}^{out[b]})$ is considered (as defined in Table 3-3), as well as a lethality term $\left(M_{X_{\ell,i}}^{lethal[b]} \right)$ corresponding to the flux of active biomass that dies and becomes inactive. Finally, a detachment term is considered for the active $(M_{\overline{X}_{F,i}}^{det[b]})$ and inactive biomass $(M_{\overline{X}_{F,0}}^{det[b]})$ with specific characteristics in each case as stated in Section 3.3.2.1.

When these mass balance equations are considered and linked to Equation 3-29, the following equation of a generic substrate/product in the liquid phase is found for active (Equation 3-36) and inactive (Equation 3-37) biomass:

$$\dot{X}_{\ell,i}^{[b]} = \frac{1}{V_{\ell}^{[b]}} \left(M_{\ell,X_{\ell,i}}^{in[b]} - M_{\ell,X_{\ell,i}}^{out[b]} + R_{\ell,X_i}^{[b]} + u_{det}^{[b]} A_F^{[b]} \tilde{X}_{F,i}^{[b]} \times \frac{1000\ \text{L}}{1\ \text{m}^3} \right)$$
$$- b_i^{lethal} X_{\ell,i}^{[b]} \qquad \text{3-36}$$

$$\dot{X}_{\ell,0}^{[b]} = \frac{1}{V_\ell^{[b]}} \left(M_{\ell,X_{\ell,0}}^{in[b]} - M_{\ell,X_{\ell,0}}^{out[b]} + u_{det,0}^{[b]} A_F^{[b]} \rho_{bio} \left(1 - \varepsilon_{F,\ell}^{[b]}\right) \varphi_{F,0}^{[b]} \times \frac{1000 \text{ L}}{1 \text{ m}^3} \right)$$
$$+ \sum_{i=1}^{n_x} b_i^{lethal} X_{\ell,i}^{[b]}$$

3-37

3.4.1.3 Specific compounds model equations in gas phase

The model considers the global mass balance of a specific compound (g/h, oxygen or carbon dioxide) in the gas phase as reflected in Equation 3-38 below.

$$\dot{M}_{C_g,j}^{[b]} = M_{g,C_g,j}^{in[b]} - M_{g,C_g,j}^{out[b]} + M_{C_\ell,j}^{g[b]}$$

3-38

In this expression, $\left(M_{g,C_g,j}^{in[b]}\right)$ and $\left(M_{g,C_g,j}^{out[b]}\right)$ correspond to the input and output mass terms respectively. These terms are defined in Equation 3-39 and Equation 3-40. It should be noted that the specific concentrations of the equation compound S in the gas phase are considered in this expression as a fraction of volume (%, S in the following equations) and converted by using the specific compound molecular weight (M_S) to general equations of flux (g/h).

$$M_{g,C_g,j}^{in[b]} = \frac{60 \text{ min}}{1 \text{ h}} \times \frac{M_S \text{ g } S}{1 \text{ mol } S} \times \frac{1 \text{ mol air}}{22.4 \text{ L air}}$$
$$\times \begin{cases} Q_{g,in} \dfrac{S_g^{in}}{100} + Q_{g,re} \dfrac{S_g^{[n]}}{100} & \text{for } b = 1 \\ (Q_{g,in} + Q_{g,recy}) \dfrac{S_g^{[b-1]}}{100} & \text{otherwise} \end{cases} \quad [\text{g/h}]$$

3-39

$$M_{g,C_g,j}^{out[b]} = \frac{60 \text{ min}}{1 \text{ h}} \times \frac{M_S \text{ g } S}{1 \text{ mol } S} \times \frac{1 \text{ mol air}}{22.4 \text{ L air}} \times (Q_{\ell,in} + Q_{\ell,recy}) \frac{S_g^{[b]}}{100} \text{ [g/h]}$$

3-40

Additionally, the specific term describing the internal variation of the compound (equivalent to Equation 3-28 but considering the conversion from fraction of volume to weight (g)) in the packed-bed due to gas-liquid mass transfer is detailed in Equation 3-41.

$$\dot{M}_{C_g}^{[b]} = \frac{d}{dt}\left(\frac{\dot{S}_g^{[b]}}{100}V_g^{[b]} \times \frac{M_S \text{ g } S}{1 \text{ mol } S} \times \frac{1 \text{ mol air}}{22.4 \text{ L air}}\right)$$

$$= \left(\frac{\dot{S}_g^{[b]}}{100}V_g^{[b]}\right) \times \frac{M_S \text{ g } S}{1 \text{ mol } S} \times \frac{1 \text{ mol air}}{22.4 \text{ L air}} \quad [\text{g/h}]$$

3-41

Thus, if we isolate $\dot{S}_g^{[b]}$, the model equation of this specific compound in the gas fraction is expressed by the Equation 3-42 below.

$$\dot{S}_g^{[b]} = \frac{1}{V_g^{[b]}}\left(\dot{M}_{C_g}^{[b]} \times \frac{1 \text{ mol } S}{M_S \text{ g } S} \times \frac{22.4 \text{ L air}}{1 \text{ mol air}} \times 100\right) \quad [\%/\text{h}]$$

3-42

When all these expressions are considered, the mass balance for a specific compound in the gas phase can be established by developing Equation 3-38, giving finally Equation 3-43 below.

$$\dot{C}_{g,j}^{[b]} = \frac{1}{V_g^{[b]}}\left(M_{g,C_g,j}^{in[b]} - M_{g,C_g,j}^{out[b]} + k_{LA,j}\left(C_{\ell,j}^{[b]} - C_{\ell,j}^{*[b]}\right)V_\ell^{[b]}\right) \times \frac{1 \text{ mol } S}{M_S \text{ g } S}$$

$$\times \frac{22.4 \text{ L air}}{1 \text{ mol air}} \times 100 \quad [\%]$$

3-43

3.4.1.4 Packed-bed height reduction

The packed-bed reactor considered in the model formulation assumes that the packing material will be beads of a specific diameter and density lower than water. In these conditions, the observed reduction of the packed-bed height due to the continuous flux in the reactor during long periods of time can be linked to a compression of these beads and therefore it needs to be included in the global model (see Chapter 4 of the present thesis for more details). This phenomenon will be termed from here on as packed-bed height reduction and this section details the mathematical development for the description of this phenomena in the model equations.

As explained in Section 3.3.1, the proposed model considers a constant number of beads per compartment and reproduces the packed-bed height reduction by considering an increase of the first compartment volume (initial volume of the packed-bed reactor without packing material) in

68

response to a decrease in the packed-bed compartment volumes due to the reduction of their void fraction. This is achieved by using an equation that describes the packed-bed height reduction as a function of liquid velocity and biofilm aging and consolidation as the most relevant factors, inspired on the Ergun equation definition [31] widely used for the description of packed bed columns as described in Equation 3-44.

$$\Delta \dot{h}^{[b]} = K \left(\frac{L_F^{[b]}(t - t_d)}{L_F^{max}} \right)^2 \left(\eta_\ell^{[b]} - \eta_\ell^{min} \right)^2 \frac{Q_{\ell,in} + Q_{\ell,recy}}{\frac{\pi}{4} D^2} \qquad \text{3-44}$$

Where $L_F^{[b]}$ and L_F^{max} are the current and maximal theoretical biofilm thickness, respectively, $\eta_\ell^{[b]}$ and η_ℓ^{min} are the current and minimal theoretical void fraction respectively, $Q_{\ell,in}$ and $Q_{\ell,recy}$ are the inlet and recirculation flow rates corrected by an experimental constant (K). It should be noted that a time delay t_d is considered to reflect the initial period when biomass attachment and adaptation to the packed-bed occurs and the packed-bed compression is not occurring, as indeed observed in the experimental data for pressure drop in the bioreactor.

3.4.2 Macroscopical model. Solid Phase analytical development

This section describes the development of each of the equations describing biofilm growth variables: microorganisms species concentration, biofilm thickness, inactive biomass layer thickness and biofilm porosity.

3.4.2.1 Concentration of microorganisms' species

As explained in Section 3.3.2, the proposed model considers only the existence of one variable for each species present in the biofilm (*Nitrosomonas*, *Nitrobacter* and inactive biomass).

In these conditions, the global mass balance for each species is performed by considering that biofilm is configured by an active and an inactive zone. Thus, for each species, the global balance for the total mass $(M_{\bar{X}_{F,i}}^{[b]})$ in the biofilm is described as:

$$M_{\bar{X}_{F,i}}^{[b]} = M_{\bar{X}_{F,i}}^{act[b]} + M_{\bar{X}_{F,i}}^{In[b]} = \bar{X}_{F,i}^{[b]} \cdot V_F^{[b]} \qquad \text{3-45}$$

Where $M_{\bar{X}_{F,i}}^{act[b]}$ and $M_{\bar{X}_{F,i}}^{In[b]}$ are the total mass of a specific specie (i) in the active or inactive layers of the biofilm respectively.

Thus, in order to calculate the evolution of mass of each species, it is necessary to consider the global influence of the detachment, attachment and biomass growth inside the active and the inactive layer of the biofilm and the impact on the whole biofilm evolution.

Figure 3-7 summarizes the analysis of the main mechanisms affecting the active, inactive and global biofilm biomass evolution for each of the species considered.

According to the results of this specific analysis, the total mass balances in the biofilm volume for active and inactive biomass species are summarized in Equation 3-46 (active biomass corresponding to both microorganisms species in the axenic culture) and Equation 3-47 (inactive biomass, corresponding to the accumulation of inactive biomass from both species).

$$\dot{M}_{\bar{X}_{F,i}}^{[b]} = M_{\bar{X}_{F,i}}^{R[b]} - M_{\bar{X}_{F,i}}^{lethal[b]} - M_{\bar{X}_{F,i}}^{det[b]} \qquad \text{(g/h)} \qquad \text{3-46}$$

$$\dot{M}_{\bar{X}_{F,0}}^{[b]} = \sum_{i=1}^{n_x} M_{\bar{X}_{F,i}}^{lethal\,[b]} - M_{\bar{X}_{F,0}}^{det\,[b]} \qquad \text{(g/h)} \qquad \text{3-47}$$
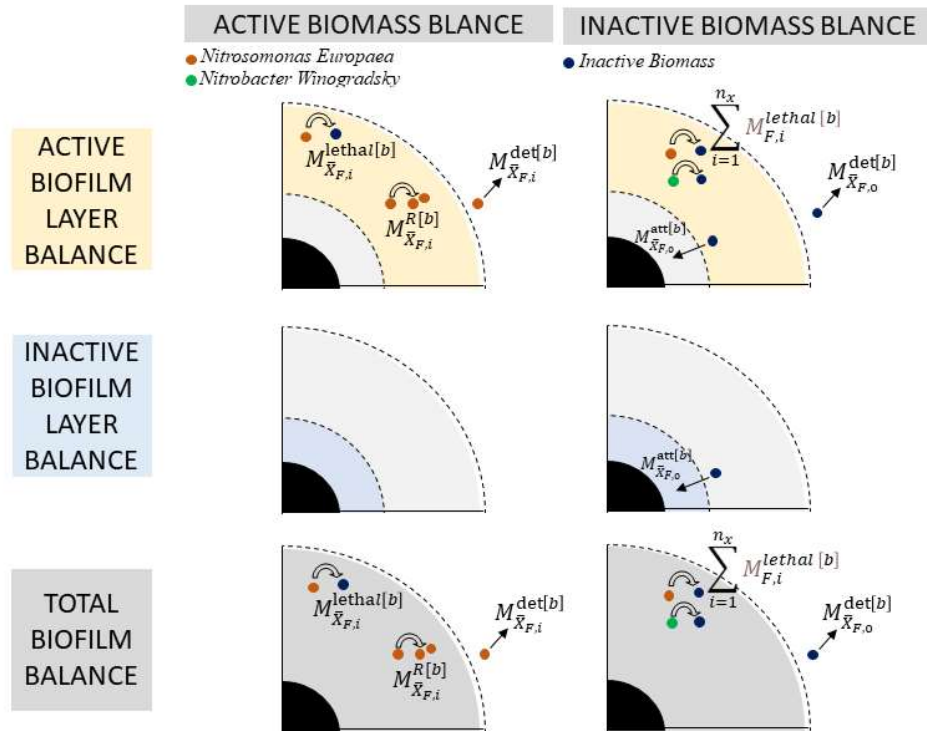
Figure 3-7. Description of mass balance for active biomass (left) or inactive biomass (right) according to the proposed model. This mass balance is performed in the active layer of the biofilm (yellow), the inactive layer of the biofilm (blue) and the total biofilm volume (grey) which is the one used in the model core equations. As observed, the generation of active and inactive biomass occurs in the active layer of the biofilm. Additionally, part of this active and inactive biomass is also detached to the bulk while part of the inactive can be attached to the internal inactive layer. This specific flux of inactive biomass to the inactive layer is also the only process taking place in the inactive biofilm layer area. However, if all of these pocesses are considered in a total biofilm balance overview, the transition processes of biomass from the active to the inactive layer do not need to be considered. Therefore, the final global model mass balances are the ones in grey.

Additionally, these mass balances of each species total active or inactive biomass can be also expressed by considering the definition of mass as concentration of the specific specie multiplied by the volume. In this case, the variation of biofilm volume cannot be negligible since it is growing on the surface of the beads.

$$\dot{M}_{\bar{X}_{F,i}}^{[b]} = \dot{\bar{X}}_{F,i}^{[b]} \cdot V_F^{[b]} + \bar{X}_{F,i}^{[b]} \cdot \dot{V}_F^{[b]}$$

3-48

If the definition performed in Equation 3-48 is considered together with the analysis presented in Equation 3-29, specific expressions to define the variation of each species concentrations in the global biofilm can be considered, resulting in in Equation 3-49 (active biomass concentration) and Equation 3-50 (inactive biomass concentration).

$$\dot{\bar{X}}_{F,i}^{[b]} = \frac{1}{V_F^{[b]}} \left(\dot{M}_{\bar{X}_{F,i}}^{[b]} - \bar{X}_{F,i}^{[b]} \cdot \dot{V}_F^{[b]} \right)$$

3-49

$$\dot{\bar{X}}_{F,0}^{[b]} = \frac{1}{V_F^{[b]}} \left(\dot{M}_{\bar{X}_{F,0}}^{[b]} - \bar{X}_{F,0}^{[b]} \cdot \dot{V}_F^{[b]} \right)$$

3-50

Combining Equation 3-46 with Equation 3-49 and combining Equation 3-47 with Equation 3-50, the final expressions to define the variation of the concentration of each species are detailed in Equation 3-51 and Equation 3-52.

$$\dot{\bar{X}}_{F,i}^{[b]} = \frac{1}{V_F^{[b]}} \left(\left(M_{\bar{X}_{F,i}}^{R[b]} - M_{\bar{X}_{F,i}}^{lethal[b]} - M_{\bar{X}_{F,i}}^{det[b]} \right) - \bar{X}_{F,i}^{[b]} \cdot \dot{V}_F^{[b]} \right)$$

3-51

$$\dot{\bar{X}}_{F,0}^{[b]} = \frac{1}{V_F^{[b]}} \left(\left(\sum_{i=1}^{n_x} M_{\bar{X}_{F,i}}^{lethal\,[b]} - M_{\bar{X}_{F,0}}^{det\,[b]} \right) - \bar{X}_{F,0}^{[b]} \cdot \dot{V}_F^{[b]} \right)$$

3-52

3.4.2.2 Biofilm thickness

The rate of change of the biofilm thickness (m/h) is obtained from the difference between the maximum potential biofilm growth if all resources were completely devoted to biofilm growth (reflected in the growth velocity $u_F^{[b]}$) and the detachment velocity that reflects how biomass is lost to the bulk liquid ($u_{det}^{[b]}$). Therefore, the final expression is described in Equation 3-53.

$$\dot{L}_F^{[b]} = u_F^{[b]} - u_{det}^{[b]}$$

3-53

3.4.2.3 Inactive biomass layer thickness

The rate of change of the inactive biomass layer thickness (m/h) is used to calculate the growth of the inactive biomass layer from the surface of the packing material as consequence of biofilm consolidation. To develop this expression, the fact that the growth of the total biomass in the inactive biofilm phase equals the total mass transfer of biomass from the active layer to the inactive layer is used (see Equation 3-54).

$$\dot{M}_{\bar{X}_{F,0}}^{inactive} = M_{\bar{X}_{F,0}}^{att\,[b]}$$

3-54

A complete deduction of the final equation (Equation 3-55) can be found in Supplementary materials Section 3.7.2.1.

$$\dot{L}_{F,0}^{[b]} = \left(u_{att,0}^{[b]} - \phi_{F,0}^{[b]} \frac{A_F^{[b]}}{A_{F,0}^{[b]}} \left(u_{det}^{[b]} - u_{det,0}^{[b]} \right) \right) \varphi_{F,0}^{[b]} \\ - \left(\frac{A_{F,0}^{[b]} - A_b^{[b]} - \phi_{F,0}^{[b]} \left(A_F^{[b]} - A_b^{[b]} \right)}{A_{F,0}^{[b]}} \right) \frac{\dot{d}^{[b]}}{2}$$

3-55

Where $\varphi_{F,0}^{[b]}$ corresponds to the fraction of inactive biomass in the active layer of the biofilm, expressed as:

$$\varphi_{F,0}^{[b]} = 1 - \frac{\sum_{i=1}^{n_x} \tilde{X}_{F,i}^{[b]}}{\rho_{bio} \left(1 - \varepsilon_{F,\ell}^{[b]} \right)}$$

3-56

3.4.2.4 Biofilm porosity

Biofilm porosity expression is deduced by considering the mass balance of global biomass (active and inactive species) in the global biofilm ($\dot{M}_{\overline{M}_F}$). This expression considers the addition of all the biomass species formation rate ($\sum_{i=1}^{n_x} M_{\overline{X}_{F,i}}^{R\ [b]}$) and inactive ($M_{\overline{X}_{F,0}}^{\det\ [b]}$) and active ($M_{\overline{X}_{F,i}}^{\det\ [b]}$) biomass detachment. Global mass balance reads as:

$$\dot{M}_{\overline{M}_F} = \sum_{i=1}^{n_x} M_{\overline{X}_{F,i}}^{R\ [b]} - M_{\overline{X}_{F,i}}^{\det\ [b]} - M_{\overline{X}_{F,0}}^{\det\ [b]} \qquad \text{3-57}$$

A complete deduction of the final equation (Equation 3-58) can be found in Supplementary materials Section 3.7.2.2.

$$\dot{\varepsilon}_{F,\ell}^{[b]} = -\frac{1 - \varepsilon_{F,\ell}^{[b]}}{V_F^{[b]}} \left[A_F^{[b]} \left(u_{det}^{[b]} - u_{det,0}^{[b]} \right) \varphi_{F,0}^{[b]} - \left(A_F^{[b]} - A_b^{[b]} \right) \frac{\dot{d}^{[b]}}{2} \right]$$
$$\times \frac{1000\ \text{L}}{1\ \text{m}^3} \qquad \text{3-58}$$

3.4.2.5 Void fraction

The void fraction is defined according to the volumes of the biofilm model described in Table 3-1 and Table 3-2 (see Equation 3-59).

$$V_T^{[b]} \eta_\ell^{[b]} = V_T^{[b]} - V_b^{[b]} - V_F^{[b]} \qquad \text{3-59}$$

If this expression is derived, the expression summarized in Equation 3-60 is shown:

$$\dot{V}_T^{[b]} \eta_\ell^{[b]} + V_T^{[b]} \dot{\eta}_\ell^{[b]} = \dot{V}_T^{[b]} - \dot{V}_b^{[b]} - \dot{V}_F^{[b]} \qquad \text{3-60}$$

If this equation is developed and the variation of void fraction is isolated, the final equation to describe the variation of this variable in the model reads as:

$$\dot{\eta}_\ell^{[b]} = -\frac{\dot{V}_b^{[b]} + \dot{V}_F^{[b]}}{V_T^{[b]}} + \left(1 - \eta_\ell^{[b]}\right)\frac{\dot{V}_T^{[b]}}{V_T^{[b]}}$$

$$\dot{\eta}_\ell^{[b]} = \frac{-2N^{[b]}}{D^2 h^{[b]}}\left(d^{[b]} + 2L_F^{[b]}\right)^2 \left(\dot{d}^{[b]} + 2\dot{L}_F^{[b]}\right) + \left(1 - \eta_\ell^{[b]}\right)\frac{\dot{h}^{[b]}}{h^{[b]}}$$

3-61

3.4.3 Microscopical model development

Under the specific assumptions detailed in Section 3.3.3, the resulting diffusion equation of the biofilm considering quasi static equilibrium assumption, becomes:

$$\frac{\partial}{\partial z}\left(-D_j \frac{\partial C_{F,j}^{[b]}}{\partial z}\right) = r_{F,j}^{[b]}$$

3-62

$$J_{F,j}^{[b]} = -D_j \frac{\partial C_{F,j}^{[b]}}{\partial z}$$

3-63

$$\frac{\partial C_{F,j}^{[b]}}{\partial t} + \frac{\partial J_{F,j}^{[b]}}{\partial z} = r_{F,j}^{[b]}$$

3-64

Where $r_{F,j}^{[b]}$ stands for the biomass species concentration on each point of the biofilm (i.e. $z = r - d^{[b]}/2$ where r is the radius of the bead and the biofilm thickness and d is the beads diameter), which is considered when calculating the effective concentrations $\tilde{X}_{F,i}^{[b]}$. D_j is the diffusivity of the corresponding compound and $C_{F,j}^{[b]}$ its concentration (in g/m³ of biofilm volume) in each specific point of the biofilm.

Additionally, it should be noted that Equation 3-62 is completed with the corresponding boundary conditions:

- The concentration of compounds (substrates and products) at the interface of the biofilm with the bulk liquid (at $z = L_F^{[b]}$) equals the concentration on the bulk liquid, $C_{\ell,j}^{[b]}$: Thus, neglecting the material external transfer resistance.

$$C_{F,j}^{[b]}\Big|_{z=L_F^{[b]}} = C_{\ell,j}^{[b]}$$

3-65

- Beads are considered to be inert. For this reason, the variation of the concentration in time of a specific compound in the surface of the bead is zero.

$$\frac{\partial C_{F,j}^{[b]}}{\partial z}\bigg|_{z=0} = 0 \qquad \text{3-66}$$

Upon performing a finite element discretization of Equation 3-62 into n concentric spherical layers of thickness $\Delta z = L_F^{[b]}/n$ (see Figure 3-8), a system can be obtained with equations of the form:

$$K_j^{(a,a-1)}\hat{C}_{F,j}^{(a-1)} + K_j^{(a,a)}\hat{C}_{F,j}^{(a)} + K_j^{(a,a+1)}\hat{C}_{F,j}^{(a+1)}$$
$$= B_j^{(a,a-1)}\hat{r}_{F,j}^{(a-1)} + B_j^{(a,a)}\hat{r}_{F,j}^{(a)} + B_j^{(a,a+1)}\hat{r}_{F,j}^{(a+1)} \qquad \text{3-67}$$

where $\hat{C}_{F,j}^{(a)}$ is the a-th nodal value of the corresponding substrate concentration and $\hat{r}_{F,j}^{(a)}$ is the equivalent of its consumption rate.
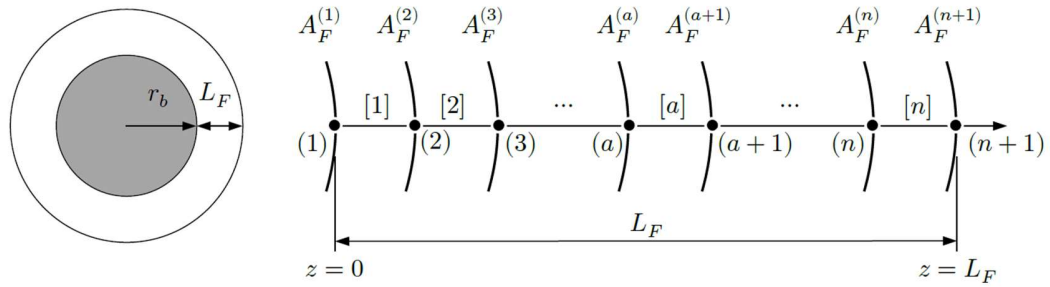
Figure 3-8. Discretization of the biofilm into n concetric spherical layers with constant thickness. In the picture, $A_F^{(a)}$ refers to each layer's surface area.

In this context, the coefficients in Equation 3-67 are defined as:

$$K_j^{(a,a-1)} = -\frac{\varepsilon_{F,\ell}D_j}{3}\left(\frac{\left(r^{(a)}\right)^3 - \left(r^{(a-1)}\right)^3}{\Delta z^2}\right)$$

$$K_j^{(a,a)} = \frac{\varepsilon_{F,\ell}D_j}{3}\left(\frac{\left(r^{(a+1)}\right)^3 - \left(r^{(a-1)}\right)^3}{\Delta z^2}\right) \qquad \text{3-68}$$

$$K_j^{(a,a+1)} = -\frac{\varepsilon_{F,\ell}D_j}{3}\left(\frac{\left(r^{(a+1)}\right)^3 - \left(r^{(a)}\right)^3}{\Delta z^2}\right)$$

$$B_j^{(a,a-1)} = \frac{1}{24}\left(r^{(a)} + r^{(a-1)}\right)^2 \Delta z$$

$$B_j^{(a,a)} = \frac{2}{3}\left(r^{(a)}\right)^2 \Delta z \qquad \qquad \text{3-69}$$

$$B_j^{(a,a+1)} = \frac{1}{24}\left(r^{(a+1)} + r^{(a)}\right)^2 \Delta z$$

In the above equations, $r^{(a)}$ refers to the radius corresponding to the a-th discretization node. It should be noticed that the porosity, $\varepsilon_{F,\ell}$, is added in the coefficients because the integrals are performed over the whole biofilm volume but the nodal concentrations $\hat{C}_{F,j}^{(a)}$ are referred to the bulk liquid volume.

In matrix form, the resulting system may be expressed as:

$$[K]\{C_F\} = [B]\{r_F\} \equiv \{R_F(C_F)\} \qquad \qquad \text{3-70}$$

where the matrices $[K]$ and $[B]$ are tri-diagonal, with their coefficients defined in Equation 3-68 and Equation 3-69, respectively, $\{C_F\}$ is the vector of unknown substrate concentrations in each biofilm layer and $\{r_F\}$ a vector containing the consumption rates. Each nodal consumption rate $\hat{r}_{F,j}^{(a)}$ is given by:

$$\hat{r}_{F,j}^{(a)} = \sum_{i=1}^{n_x} \left(Y_{j/i}\mu_{max,i} + Y_{j/i}^m m_i\right) \widetilde{X}_{F,i}^{[b]} \phi_i\left(C_{F,k}^{(a)}\right) \qquad \qquad \text{3-71}$$

with $\phi_i\left(C_{F,k}^{(a)}\right)$ referring to the growth inhibition parameter, which can be expressed, in general, as the product of polynomial fractions:

$$\phi_i\left(C_{F,k}^{(a)}\right) = \prod_{k=1}^{n_s} \frac{p_{k/i}^0 + p_{k/i}^1 C_{F,k}^{(a)}}{q_{k/i}^0 + q_{k/i}^1 C_{F,k}^{(a)} + q_{k/i}^2 \left(C_{F,k}^{(a)}\right)^2} \qquad \qquad \text{3-72}$$

Depending on the values given to the polynomial coefficients in Equation 3-72, the model can account for different kinetics and inhibition mechanisms, including Monod or Haldan-like expressions as detailed in specific kinetic equations required.

It is important to notice that Equation 3-72 introduces a non-linearity into the system of equations, because of its dependence on the concentrations of coumpounds. To deal with this issue, a Newton-Raphson scheme is used to solve the system (given in Figure 3-9). The concentrations of compounds in the bulk liquid $C_{\ell,j}^{[b]}$ are used as initial guess value. The computation of the Jacobian matrix ($[\mathcal{J}]$ in Figure 3-9), is performed explicitly at each iteration step, since it simply involves the derivatives of Equation 3-72 with respect to $C_{F,k}^{(a)}$, which can be obtained analytically. As a remark, since only positive-valued concentrations are physically possible, all $\hat{C}_{F,j}^{(a)} < 0$ resulting from each evaluation are forced to be zero before updating the solution vector for the next iteration step.

Finally, to improve the stability of the algorithm, the solution vector's update is carried out so that the initial guessed value of the next iteration step is the mean value between the results of the present iteration and the previous one, as depicted in the algorithm in Figure 3-9.

78
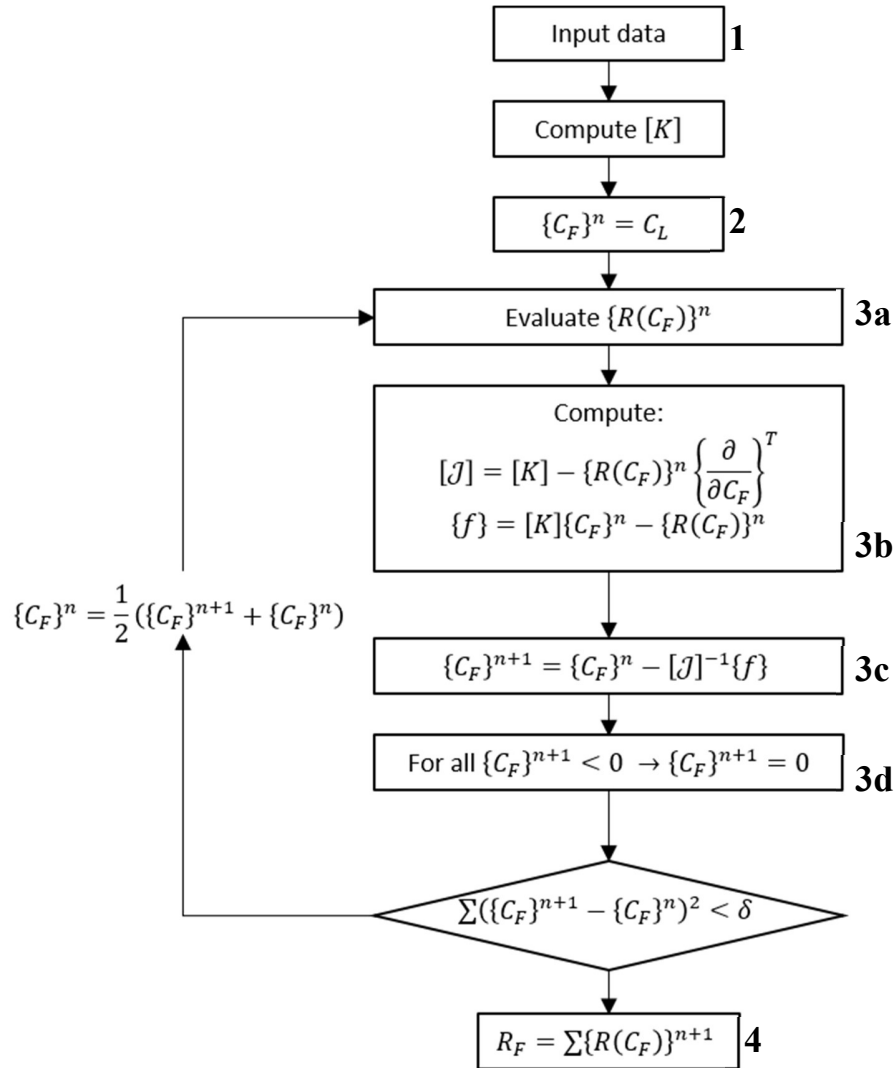
Figure 3-9. Algorithm to solve the biofilm system. With the input data, (1) the system matrix [K] is computed and (2) the substrate concentrations {CF} are initialized with the values of the bulk liquid concentrations CL (which are considered as initial guess). An iterative process then begins where, in each step, (3a) the right hand side vector {R} and the system derivatives ([J] matrix) are computed with the current values of {CF} and the Newton-Raphson scheme is used to evaluate the system residual {f}. (3b) This residual is used to update the substrate concentrations {CF}(n+1), and (3c) a correction is performed to force unphysical negative concentrations to 0. (3d) After evaluating the convergence criterion (comparing the difference between the current and updated solutions with a tolerance delta) the algorithm either goes back to step (3a) reevaluating the current substrate concentrations {CF}(n) assigning them the mean value between the current and updated solutions; or (4) it breaks the iteration loop and evaluates the total RF.

Table 3-6. Description of the proposed model final equations (1/2)

Phase	Variable		Reaction term	Gas-liquid mass transfer term	General derivative equation
Liquid bulk variable	N-NH$_4^+$	$C_{\ell,\text{N-NH}_4^+}^{[b]}$ [g/L]	YES	NO	$\dot{C}_{\ell,j}^{[b]} = \dfrac{1}{V_\ell^{[b]}} \left(M_{\ell,C_{\ell,j}}^{in[b]} - M_{\ell,C_{\ell,j}}^{out[b]} + \displaystyle\sum_{i=1}^{n_x} \left(Y_{j/i} + Y_{j/i}^m \dfrac{m_i}{\mu_{max,i}} \right) \left(R_{\ell,X_i}^{[b]} + R_{F,X_i}^{[b]} \right) \right) - k_{LA,j}\left(C_{\ell,j}^{[b]} - C_{\ell,j}^{*[b]} \right)$
	N-NO$_2^-$	$C_{\ell,\text{N-NO}_2^-}^{[b]}$ [g/L]	YES	NO	
	N-NO$_3^-$	$C_{\ell,\text{N-NO}_3^-}^{[b]}$ [g/L]	YES	NO	
	O$_2^{(l)}$	$C_{\ell,\text{O}_2}^{[b]}$ [g/L]	YES	YES	
	Nitrosomonas	$X_{\ell,\text{Ns}}^{[b]}$ [g/L]	YES	NO	$\dot{X}_{\ell,i}^{[b]} = \dfrac{1}{V_\ell^{[b]}} \left(M_{\ell,X_{\ell,i}}^{in[b]} - M_{\ell,X_{\ell,i}}^{out[b]} + R_{\ell,X_i}^{[b]} + u_{det}^{[b]} A_F^{[b]} \tilde{X}_{F,i}^{[b]} \times \dfrac{1000\ \text{L}}{1\ \text{m}^3} \right) - b_i^{letha}\ X_{\ell,i}^{[b]}$
	Nitrobacter	$X_{\ell,\text{Nb}}^{[b]}$ [g/L]	YES	NO	
	Inert biomass concentration	$X_{\ell,0}^{[b]}$ [g/L]	YES	NO	$\dot{X}_{\ell,0}^{[b]} = \dfrac{1}{V_\ell^{[b]}} \left(M_{\ell,X_{\ell,0}}^{in[b]} - M_{\ell,X_{\ell,0}}^{out[b]} + u_{det,0}^{[b]} A_F^{[b]} \rho_{bio} \left(1 - \varepsilon_{F,\ell}^{[b]} \right) \varphi_{F,0}^{[b]} \times \dfrac{1000\ \text{L}}{1\ \text{m}^3} \right) + \displaystyle\sum_{i=1}^{n_x} b_i^{lethal} X_{\ell,i}^{[b]}$
Gas bulk variable	O$_2^{(g)}$ fraction	$C_{g,\text{O}_2}^{[b]}$ [%]	NO	YES	$\dot{C}_{g,j}^{[b]} = \dfrac{1}{V_g^{[b]}} \left(M_{g,C_g,j}^{in[b]} - M_{g,C_g,j}^{out[b]} + k_{LA,j}\left(C_{\ell,j}^{[b]} - C_{\ell,j}^{*[b]} \right) V_\ell^{[b]} \right) \times \dfrac{1\ \text{mol}\ S}{M_S\ \text{g}\ S} \times \dfrac{22.4\ \text{L air}}{1\ \text{mol air}} \times 100\ [\%]$

Table 3-7. Description of the proposed model final equations (Continued 2/2)

Phase	Variable		Reaction term	Gas-liquid mass transfer term	General derivative equation
Biofilm variable	*Nitrosomonas*	$\bar{X}_{F,\text{Ns}}^{[b]}$ [g/L]	YES	NO	$\dot{\bar{X}}_{F,i}^{[b]} = \frac{1}{V_F^{[b]}}\left(\left(M_{\bar{X}_{F,i}}^{R[b]} - M_{\bar{X}_{F,i}}^{lethal[b]} - M_{\bar{X}_{F,i}}^{det[b]}\right) - \bar{X}_{F,i}^{[b]} \cdot \dot{V}_F^{[b]}\right)$
	Nitrobacter	$\bar{X}_{F,\text{Nb}}^{[b]}$ [g/L]	YES	NO	
	Inert biomass	$\bar{X}_{F,0}^{[b]}$ [g/L]	YES	NO	$\dot{\bar{X}}_{F,0}^{[b]} = \frac{1}{V_F^{[b]}}\left(\left(\sum_{i=1}^{n_x} M_{\bar{X}_{F,i}}^{lethal\,[b]} - M_{\bar{X}_{F,0}}^{det\,[b]}\right) - \bar{X}_{F,0}^{[b]} \cdot \dot{V}_F^{[b]}\right)$
	Biofilm thickness	$L_F^{[b]}$ [m]	-	-	$\dot{L}_F^{[b]} = u_F^{[b]} - u_{det}^{[b]}$
	Inactive biomass layer thickness	$L_{F,0}^{[b]}$ [m]	-	-	$\dot{L}_{F,0}^{[b]} = \left(u_{att,0}^{[b]} - \phi_{F,0}^{[b]}\frac{A_F^{[b]}}{A_{F,0}^{[b]}}\left(u_{det}^{[b]} - u_{det,0}^{[b]}\right)\right)\varphi_{F,0}^{[b]}$ $- \left(\frac{A_{F,0}^{[b]} - A_b^{[b]} - \phi_{F,0}^{[b]}\left(A_F^{[b]} - A_b^{[b]}\right)}{A_{F,0}^{[b]}}\right)\frac{\dot{d}^{[b]}}{2}$ Where $\varphi_{F,0}^{[b]} = 1 - \frac{\sum_{i=1}^{n_x}\tilde{X}_{F,i}^{[b]}}{\rho_{bio}\left(1-\varepsilon_{F,\ell}^{[b]}\right)}$
	Biofilm porosity	$\varepsilon_{F,\ell}^{[b]}$ [-]	-	-	$\dot{\varepsilon}_{F,\ell}^{[b]} = -\frac{1-\varepsilon_{F,\ell}^{[b]}}{V_F^{[b]}}\left[A_F^{[b]}\left(u_{det}^{[b]} - u_{det,0}^{[b]}\right)\varphi_{F,0}^{[b]} - \left(A_F^{[b]} - A_b^{[b]}\right)\frac{\dot{d}^{[b]}}{2}\right] \times \frac{1000\ \text{L}}{1\ \text{m}^3}$
Packed bed variables	Packed bed column lift	$\Delta h^{[b]}$ [m]	-	-	$\Delta\dot{h}^{[b]} = K\left(\frac{L_F^{[b]}(t-t_d)}{L_F^{max}}\right)^2\left(\eta_\ell^{[b]} - \eta_\ell^{min}\right)^2 \frac{Q_{\ell,in} + Q_{\ell,recy}}{\frac{\pi}{4}D^2}$
	Void fraction	$\eta_\ell^{[b]}$ [-]	-	-	$\dot{\eta}_\ell^{[b]} = \frac{-2N^{[b]}}{D^2 h^{[b]}}\left(d^{[b]} + 2L_F^{[b]}\right)^2\left(\dot{d}^{[b]} + 2\dot{L}_F^{[b]}\right) + \left(1 - \eta_\ell^{[b]}\right)\frac{\dot{h}^{[b]}}{h^{[b]}}$

3.5. Conclusions

A mathematical model to describe the operation of a packed-bed nitrifying reactor has been developed. Final equations are summarized in Table 3-6 and Table 3-7. The summary of complete model parameters identification can be found in supplementary materials, Section 3.7.1. In the next chapter, this model will be used to describe the operation of the nitrifying packed-bed bioreactor over a long period of continuous operation

3.6. Bibliography

1.	Picioreanu, C., Loosdrecht, M. & Heijnen, J. Modelling and predicting biofilm structure. in *Community structure and co-operation in biofilms. Published for the fifty-ninth symposium of the society for general microbiology.* 129–166 (2000).
2.	Mattei, M. *et al.* Continuum and discrete approach in modeling biofilm development and structure: a review. *Journal of Mathematical Biology.* 76, 945–1003 (2018).
3.	Williamson, K. & McCarty, P. A model of substrate utilization by bacterial films. *Water Pollution Control Federation* 48, 9–24 (1976).
4.	Atkinson, B. & Davies, I. The overall rate of substrate uptake (reaction) by microbial films. Part I-A biological rate equation. *Chemical Engineering Research and Design.* 52a, 260–268 (1974).
5.	Rauch, W., Vanhooren, H. & Vanrolleghem, P. A simplified mixed-culture biofilm model. *Water Research* 33, 2148–2162 (1999).
6.	D'Acunto, B. & Frunzo, L. Free boundary problem for an initial cell layer in multispecies biofilm formation. *Applied Mathematics Letters* 25, 20–26 (2012).
7.	D'Acunto, B. & Frunzo, L. Qualitative analysis and simulations of a free boundary problem for multispecies biofilm models. *Mathematical and Computer Modelling* 53, 1596–1606 (2011).
8.	Wanner, O. & Reichert, P. Mathematical modeling of mixed-culture biofilms. *Biotechnology and Bioengineering* 49, 172–184 (1996).
9.	Reichert, P. & Wanner, O. Movement of solids in biofilms: Significance of liquid phase transport. *Water Science and Technology* 36, 321–328 (1997).
10.	Reichert, P. Aquasim - A tool for simulation and data analysis of aquatic systems. *Water Science and Technology* 30, 21–30 (1994).
11.	Laspidou, C. & Rittmann, B. Evaluating trends in biofilm density using the UMCCA model. *Water Research* 38, 3362–3372 (2004).
12.	Lee, M. W. & Park, J. M. One-dimensional mixed-culture biofilm model considering different space occupancies of particulate components. *Water Research* 41, 4317–4328 (2007).
13.	Perez, J., Picioreanu, C. & Loosdrecht, M. Modeling biofilm and floc diffusion processes based on analytical solution of reaction-diffusion equations. *Water Research* 39, 1311–1323 (2005).

14. Rittmann, B., Stilwell, D. & Ohashi, A. The transient-state, multiple-species biofilm model for biofiltration processes. *Water Research* 36, 2342–2356 (2002).

15. Gonzo, E. E., Wuertz, S. & Rajal, V. B. The continuum heterogeneous biofilm model with multiple limiting substrate Monod kinetics. *Biotechnology and Bioengineering.* 111, 2252–2264 (2014).

16. Gonzo, E. E., Wuertz, S. & Rajal, V. B. Continuum heterogeneous biofilm model — A simple and accurate method for effectiveness factor determination. *Biotechnology and Bioengineering* 109, 1779–1790 (2012).

17. Reichert, P. Aquasim - A tool for simulation and data analysis of aquatic systems. *Water Science and Technology* 30, 21–30 (1994).

18. Poughon, L., Dussap, C., Perez, J., Montesinos, L. & Godia, F. Dynamics and steady state operation of a nitrifying fixed bed biofilm reactor: mathematical model based description. *Process Biochemistry* 40, 2359–2369 (2005).

19. Montras, A. *et al.* Distribution of Nitrosomonas europaea and Nitrobacter winogradskyi in an autotrophic nitrifying biofilm reactor as depicted by molecular analyses and mathematical modelling. *Water Research* 42, 1700–1714 (2008).

20. Pérez, J., Poughon, L., Dussap, C., Montesinos, J.L. & Godia, F. Dynamics and steady state operation of a nitrifying fixed bed biofilm reactor: mathematical model based description. *Process Biochemistry,* 40, 2359–2369 (2005).

21. Steinhaus, H. *Mathematical Snapshots*. (1999).

22. Wilhem, E., Battino, R. & Wilcok, R. J. Low-pressure solubility of gases in liquid water. *Chem. Rev. Chemical Reviews* 77, 219–262 (1977).

23. Arnau, C., Peiro, E. & Godia, F. *Test report for volumetric mass transfer coefficient (kLa) determination in C3 compartment (MELiSSA internal technical note TN 87.2.9.)*. (2012).

24. Poughon, L., Duchez, D., Cornet, J. F. & Dussap, C. G. *MELiSSA internal Technical note (TN-63.2)*. (2002).

25. Poughon, L., Duchez, D., Cornet, J. & Dussap, C. kLa determination: comparative study for a gas mass balance method. *Bioprocess Biosystems Engineering* 25, 341–348 (2003).

26. Xavier, J., Picioreanu, C. & Loosdrecht, M. C. M. A general description of detachment for multidimensional modelling of biofilms. *Biotechnoogy and Bioengineering* 91, 651–669 (2005).

27. Casey, E. Tracer measurements reveal experimental evidence of biofilm consolidation. *Biotechnology and Bioengineering* 98, 913–918 (2007).

28. Hunik, J., Bos, C., Van der Hoogen, D. G. C. & Tramper, J. Co-Immobilized Nitrosomonas europaea and Nitrobacter agilis cells: validation of a dynamic model for simultaneous substrate conversion and growth in K-carrageenan gel beads. *Biotechnology and Bioengineering* 43, 1153–63 (1994).

29. Morgenroth, E. *Biological Wastewater Treatment*. (2008).

30. Anthonisen, A., Loehr, R., Prakasam, T. & Srinath, E. Inhibition of nitrification by ammonia and nitrous acid. *Journal of Water Pollution Control* 48, 835–852 (1976).

31. Ergun, S. Fluid flow through packed columns. *Chemical Engineering Progress* 48, 89–94 (1952).

3.7. Supplementary materials

This supplementary material is composed of the following information

- Summary of model terminology

  o Model state variables, initial conditions and input variables identification

  o Other model parameters

  o General model terminology used in the chapter

- Additional model equations (biomass layer thickness and porosity)

3.7.1 Model variables and parameters definition summary

Table 3-8 summarizes the main state variables used in the model with its identification. This table also includes a definition of the model state variables at t=0 if applicable and terminology used to refer the possible input values of a specific variable into the system.

Table 3-8. Model state variables

Phase	$y_i^{[b]}$	Description	Variable identification	Initial conditions	Variable limitation	Input variables
Liquid	$y_1^{[b]}$	N-NH$_4^+$ concentration [1]	$C_{\ell,\text{N-NH}_4^+}^{[b]}$ [g/L]	$C_{\ell,\text{N-NH}_4^+}^0$	-	$C_{\ell,\text{N-NH}_4^+}^{in}(t)$
	$y_2^{[b]}$	N-NO$_2^-$ concentration[1]	$C_{\ell,\text{N-NO}_2^-}^{[b]}$ [g/L]	$C_{\ell,\text{N-NO}_2^-}^0$	-	$C_{\ell,\text{N-NO}_2^-}^{in}(t)$
	$y_3^{[b]}$	N-NO$_3^-$ concentration[1]	$C_{\ell,\text{N-NO}_3^-}^{[b]}$ [g/L]	$C_{\ell,\text{N-NO}_3^-}^0$	-	$C_{\ell,\text{N-NO}_3^-}^{in}(t)$
	$y_4^{[b]}$	O$_2^{(1)}$ concentration [1]	$C_{\ell,\text{O}_2}^{[b]}$ [g/L]	C_{ℓ,O_2}^0	-	$C_{\ell,\text{O}_2}^{in}(t)$
	$y_5^{[b]}$	Ns concentration [1]	$X_{\ell,\text{Ns}}^{[b]}$ [g/L]	$X_{\ell,\text{Ns}}^0$	-	NA
	$y_6^{[b]}$	Nb concentration [1]	$X_{\ell,\text{Nb}}^{[b]}$ [g/L]	$X_{\ell,\text{Nb}}^0$	-	NA
	$y_7^{[b]}$	Inert biomass concentration [1]	$X_{\ell,0}^{[b]}$ [g/L]	$X_{\ell,0}^0$	-	NA
Gas	$y_8^{[b]}$	O$_2^{(g)}$ fraction [2]	$C_{g,\text{O}_2}^{[b]}$ [%]	C_{g,O_2}^0	-	C_{g,O_2}^{in}
Biofilm	$y_9^{[b]}$	Ns concentration [3]	$\overline{X}_{F,\text{Ns}}^{[b]}$ [g/L]	$\overline{X}_{F,\text{Ns}}^0$	-	NA
	$y_{10}^{[b]}$	Nb concentration [3]	$\overline{X}_{F,\text{Nb}}^{[b]}$ [g/L]	$\overline{X}_{F,\text{Nb}}^0$	-	NA
	$y_{11}^{[b]}$	Inert biomass concentration [3]	$\overline{X}_{F,0}^{[b]}$ [g/L]	$\overline{X}_{F,0}^0$	-	NA
	$y_{12}^{[b]}$	Biofilm thickness	$L_F^{[b]}$ [m]	$L_F^0 = 0$	L_F^{max}	NA
	$y_{13}^{[b]}$	Inactive biomass layer thickness	$L_{F,0}^{[b]}$ [m]	$L_{F,0}^0 = 0$	$L_{F,0}^{max}$	NA
	$y_{14}^{[b]}$	Biofilm porosity	$\varepsilon_{F,\ell}^{[b]}$ [-]	$\varepsilon_{F,\ell}^0 = 1$	$\varepsilon_{F,\ell}^{min}$	NA
	$y_{15}^{[b]}$	Void fraction	$\eta_\ell^{[b]}$ [-]	η_ℓ^0	η_ℓ^{min}	NA
Others	$y_{16}^{[b]}$	Packed bed column lift	$\Delta h^{[b]}$ [m]	$\Delta h^0 = 0$		NA

(1) Referred to the mass of substance p.u. of bulk liquid volume.
(2) Referred to mols of gas contained in 100 mols of air.
(3) Referred to the mass of substance p.u. of biofilm volume. Based on this parameter and by considering specific biofilm thickness and inactive biomass layer thickness, specific concentrations of biomass for each species (i) in the active ($\tilde{X}_{F,i}^{[b]}$) or inactive ($\tilde{X}_{F,0}^{[b]}$) parts of the biofilm can be estimated.

Table 3-9 summarizes the main model parameters whereas Table 3-10 and Table 3-11 summarizes the different specific model terminology used in this chapter.

Table 3-9. Model main parameters

Category	Description	Symbol
Model definition	Number of compartments	$n=7$
	Number of beads (Nº)	$n^{\text{o}}\ beads = \dfrac{3}{2}\dfrac{D^2 h_B^0 (1-\eta_l^0)}{(d^0)^3\ (b-2)}$
Reactor hydrodynamics	Main input liquid flow rate	$Q_{\ell,in}(t)$ [mL/min]
	Recirculation liquid flow rate	$Q_{\ell,recy}(t)$ [mL/min]
	Main gas flow rate	$Q_{g,in}(t)$ [L/min]
	Recirculation gas flow rate	$Q_{g,recy}(t)$ [L/min]
	Back-mixing liquid flow rate	$Q_{l,mix}(t)$ [L/min]
Reactor physical and chemical conditions	Temperature	T [°C]
	Input pH setpoint	$\text{pH}^{in}(t)$
Reactor dimensions and characteristics and operation	Lower section reactor height (before packed bed)	h_A [m]
	Total packed bed height	h_B [m]
	Specific n-tank in series packed bed height	h_b [m]
	Upper section reactor height (after packed bed)	h_C [m]
	Column diameter	D [m]
	Reactor pressurization	P [atm]
	$O_2^{(l)}$ concentration	$C_{\ell,O_2}^{in}(t)$ [g/L]
	Input $O_2^{(g)}$ fraction	$C_{g,O_2}^{in}(t)$ [%]
Gas-liquid mass transfer	Mass transfer coefficient (Differential for sections A, B and C of the packed bed)	k_{La}
	Hold up (gas fraction)	v [L gas/L liq]
Packing material characteristics	Diameter of the packing material (initial)	d_0 [m]
Biofilm definition	Biofilm consolidation time	t_d [h]
	Experimental constant	K
	Biomass density	ρ_{bio} [g/L]
	Initial mass of Nitrosomonas (Ns)	M_{Ns}^0 [g]
	Initial mass of Nitrobacter (Nb)	M_{Nb}^0 [g]

Table 3-10. General model terminology

Category	Description	Symbol
Reactor hydrodynamics	Input liquid flow rate	$Q_{\ell,in}(t)$ [mL/min]
	Recirculation liquid flow rate	$Q_{\ell,recy}(t)$ [mL/min]
	Input gas flow rate	$Q_{g,in}(t)$ [L/min]
	Recirculation gas flow rate	$Q_{g,recy}(t)$ [L/min]
	Back-mixing liquid flow rate	$Q_{l,mix}(t)$ [L/min]
	Mass transfer coefficient (differential for sections A, B and C of the packed bed)	k_{La}
	Hold up (gas fraction)	ν [L gas/L liq]
	Number of beads per n-Tank	$N^{[b]}$
	Total bed volume	V_T^0 total bed volume at time=0 V_T total bed volume at specific time $V_T^{[b]}$ at specific time and n-Tank $V_T^{[b]0}$ at time=0 and specific n-Tank
	Volume of solid phase (beads and biomass)	V_S^0 total bed volume at time=0 V_S total bed volume at specific time $V_S^{[b]}$ at specific time and n-Tank $V_S^{[b]0}$ at time=0 and specific n-Tank
	Volume of beads	V_b^0 total bed volume at time=0 V_b total bed volume at specific time $V_b^{[b]}$ at specific time and n-Tank $V_b^{[b]0}$ at time=0 and specific n-Tank
	Volume of bulk liquid	V_L^0 total bed volume at time=0 V_L total bed volume at specific time $V_L^{[b]}$ at specific time and n-Tank $V_L^{[b]0}$ at time=0 and specific n-Tank
	Volume of gas	V_G^0 total bed volume at time=0 V_G total bed volume at specific time $V_G^{[b]}$ at specific time and n-Tank $V_G^{[b]0}$ at time=0 and specific n-Tank

Table 3-11. General model terminology (continued)

Category	Description	Symbol
Biofilm characterization	Volume of biofilm (active)	V_F^0 total bed volume at time=0 V_F total bed volume at specific time $V_F^{[b]}$ at specific time and n-Tank $V_F^{[b]0}$ at time=0 and specific n-Tank
	Volume of biofilm (inactive)	$V_{F,0}^0$ total bed volume at time=0 $V_{F,0}$ total bed volume at specific time $V_{F,0}^{[b]}$ at specific time and n-Tank $V_{F,0}^{[b]0}$ at time=0 and specific n-Tank
	Packing material area	$A_b^{[b]0}$ at time=0 and n-Tank $A_b^{[b]}$ at specific time and n-Tank
	Biofilm surface area	$A_F^{[b]}$ at specific time and n-Tank
	Biofilm inactive surface area	$A_{F,0}^{[b]}$ at specific time and n-Tank
General mass balance terminology	Derivative expression for global mass balance (g/h) of specific substrate/biomass j	$\dot{M}_{S,j}^{[b]}$
	Input flux in specific n-Tank in compound Sj and liquid or gas phase (g/h) in specific time step	$M_{\ell,S_j}^{in[b]} / M_{g,S_j}^{in[b]}$
	Output flux in specific n-Tank in compound Sj and liquid or gas phase (g/h) in specific time step	$M_{\ell,S_j}^{out[b]} / M_{g,S_j}^{out[b]}$
	Reaction production term in g/h of specific substrate (g/h) in specific time step	$M_{S_j}^{R[b]}$
	Flux derived from gas-liquid mass transfer in g/h of specific compound S (g/h) in specific time step	$M_{S_j}^{g[b]}$
	Flux of active biomass (i) that dies and becomes inactive (0) (g/h) in specific time step	$M_{X_{\ell,i}}^{lethal[b]} M_{X_{\ell,0}}^{lethal[b]}$
	Flux of active biomass (i) or inactive biomass (0) that is detached from the biofilm (g/h) in specific time step	$M_{\bar{X}_{F,i}}^{det[b]} M_{\bar{X}_{F,0}}^{det[b]}$
	Total mass of specific specie (i) in active layer of the biofilm	$M_{\bar{X}_{F,i}}^{act[b]}$
	Total mass of specific specie (i) in inactive layer of the biofilm	$M_{\bar{X}_{F,i}}^{In[b]}$
Effective biomass concentrations	Effective concentration in the active layer of the biofilm	$\tilde{X}_{F,i}^{[b]}$
	Effective concentration in the inactive layer of the biofilm	$\tilde{X}_{F,0}^{[b]}$
Biofilm growth velocities	Biofilm growth velocity	$u_F^{[b]}$
	Active biomass detachment velocity	$u_{det}^{[b]}$
	Inactive biomass detachment velocity	$u_{det,0}^{[b]}$
	Inactive biomass attachment in inactive layer	$u_{att,0}^{[b]}$

88

3.7.2 Additional model equations

This section includes specific details for the deduction of the final inactive biomass layer thickness and biofilm porosity derivatives.

3.7.2.1 Deduction of the biomass layer thickness derivative

Inactive biomass layer thickness derivative is used to calculate the growth of the inactive biomass layer from the surface of the packing material as consequence of biofilm consolidation. In order to do that, the fact that the variation of total biomass in the inactive biofilm phase equals to the total mass transfer of biomass from the active layer to the inactive layer is used.

$$\dot{M}_{F,0}^{inactive} = M_{F,0}^{att\,[b]} \qquad\qquad 3\text{-}73$$

On the other hand, if the expression of the variation of total biomass in the inactive layer of the biofilm is analytically developed, it can be also expressed by using the following expression:

$$M_{F,0}^{inactive} = \rho_{bio} \left(1 - \varepsilon_{F,l}^{[b]}\right) V_{F,0}^{[b]} \qquad\qquad 3\text{-}74$$

So, if this Equation 3-74 is derived, the following expression can be found:

$$
\begin{aligned}
\dot{M}_{F,0}^{inactive} = \rho_{bio}\left(1 - \varepsilon_{F,l}^{[b]}\right) \\
\cdot \left(A_{F,0}^{[b]}\dot{L}_{F,0}^{[b]} + \left(A_{F,0}^{[b]} - A_b^{[b]}\right)\frac{\dot{d}^{[b]}}{2}\right) x \frac{1000\,L}{m^3} \\
- \rho_{bio}\,\dot{\varepsilon}_{F,l}^{[b]}V_{F,0}^{[b]}
\end{aligned}
\qquad\qquad 3\text{-}75
$$

Then, if the same procedure is performed for definition of the inactive biomass attachment to the inactive biofilm layer and the expression is developed, the following expression is obtained:

$$M_{F,0}^{att\,[b]} = u_{att,0}^{[b]}\,A_{F,0}^{[b]}\left(\rho_{bio}\left(1 - \varepsilon_{F,l}^{[b]}\right) - \tilde{X}_{F,i}\right)\frac{1000\,L}{m^3} \qquad\qquad 3\text{-}76$$

At this point, if Equation 3-75 and Equation 3-76 are combined and we consider the definition of $\tilde{X}_{F,i}$ as $\tilde{X}_{F,i} = \left(1 - \varphi_{F,0}^{[b]}\right)\rho_{bio}(1 - \varepsilon_{F,l}^{[b]})$ isolated from Equation 3-56, we obtain an expression where $\dot{L}_{F,0}^{[b]}$ can be isolated:

$$\dot{L}_{F,0}^{[b]} = \left(u_{att,0}^{[b]} - \phi_{F,0}^{[b]} \frac{A_F^{[b]}}{A_{F,0}^{[b]}} \left(u_{det}^{[b]} - u_{det,0}^{[b]} \right) \right) \varphi_{F,0}^{[b]}$$
$$- \left(\frac{A_{F,0}^{[b]} - A_b^{[b]} - \phi_{F,0}^{[b]} \left(A_F^{[b]} - A_b^{[b]} \right)}{A_{F,0}^{[b]}} \right) \frac{\dot{d}^{[b]}}{2} \qquad\qquad \text{3-77}$$

3.7.2.2 Deduction of the biofilm porosity derivative

Biofilm porosity derivative is deduced by considering the global mass balance of biomass (active and inactive species) in the global biofilm ($\dot{M}_{\bar{M}_F}$). This derivative considers the addition of all the species biomass formation rate ($\sum_{i=1}^{n_x} M_{\bar{X}_{F,i}}^{R\ [b]}$) and inactive ($M_{\bar{X}_{F,0}}^{\det\ [b]}$) and active ($M_{\bar{X}_{F,i}}^{\det\ [b]}$) biomass detachment mass balance and reads as:

$$\dot{M}_{\bar{M}_F} = \sum_{i=1}^{n_x} M_{\bar{X}_{F,i}}^{R\ [b]} - M_{\bar{X}_{F,i}}^{det\ [b]} - M_{\bar{X}_{F,0}}^{det\ [b]} \qquad\qquad \text{3-78}$$

At the same time, derivative of the global mass balance in the biofilm can be defined as:

$$\dot{M}_F^{[b]} = \rho_{bio} \left(1 - \varepsilon_{F,\ell}^{[b]} \right) \left(A_F^{[b]} L_F^{[b]} + \left(A_F^{[b]} - A_b^{[b]} \right) \frac{\dot{d}^{[b]}}{2} \right)$$
$$\times \frac{1000\ L}{1\ m^3} - \rho_{bio} \dot{\varepsilon}_{F,\ell}^{[b]} V_F^{[b]} \qquad\qquad \text{3-79}$$

When the definition of these equations is developed considering the definition of $\tilde{X}_{F,i}^{[b]}$ as $\tilde{X}_{F,i}^{[b]} = \left(1 - \varphi_{F,0}^{[b]}\right)\rho_{bio}\left(1 - \varepsilon_{F,\ell}^{[b]}\right)$ and isolating $\dot{\varepsilon}_{F,\ell}^{[b]}$ we obtain the definition of the porosity derivative:

$$\dot{\varepsilon}_{F,\ell}^{[b]} = -\frac{1 - \varepsilon_{F,\ell}^{[b]}}{V_F^{[b]}} \left[A_F^{[b]} \left(u_{det}^{[b]} - u_{det,0}^{[b]} \right) \varphi_{F,0}^{[b]} - \left(A_F^{[b]} - A_b^{[b]} \right) \frac{\dot{d}^{[b]}}{2} \right] \times \frac{1000\ \text{L}}{1\ \text{m}^3} \qquad\qquad \text{3-80}$$

CHAPTER 4

C3: Packed-bed nitrifying reactor modelling. Application of the model to a long duration experimental campaign

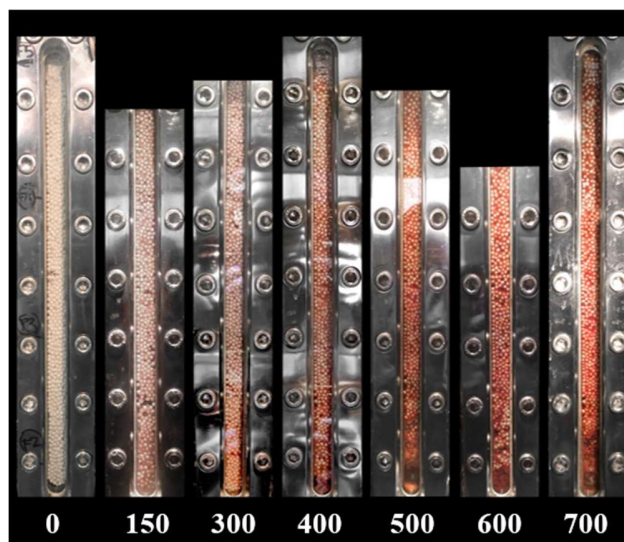This manuscript is currently submitted to Journal of Theoretical Biology

4.1. Introduction

The work presented in this chapter consists on the application of the model developed in Chapter 3 to a set of data corresponding to a long duration experimental campaign of operation of the nitrifying Compartment 3 (C3) in the MELiSSA Pilot Plant. This packed-bed reactor is colonized with two nitrifying bacteria strains, *Nitrosomonas europaea* ATCC 25978 and *Nitrobacter winogradsky* ATCC 25391, working in axenic conditions and immobilized on Biostyr® beads. Its main goal in the final MELiSSA loop is to oxidize the ammonium generated in the degradation of organic waste and urine into nitrate and provide a more assimilable nitrogen source to the photosynthetic compartments of the loop (culturing cyanobacteria (C4a) and higher plants (C4b)).

As explained in Chapter 1, the implementation of the different compartments in the MPP includes a two-stage process. First of all, initial tests are performed at bench scale to gain knowledge on the basic mechanisms and operational performance to obtain a detailed reactor characterization. Then, final operational and control strategies are developed and implemented at pilot-scale to latter perform the integration of the compartment with different interphases at the loop level. In the case of C3, bench-scale experiments were performed in bioreactors of approximately 0.7 L [1] based on previous work to define the general reactor configuration [2] and select the packing material [3,4]. In these bench-scale studies, the final design of the compartment was studied, with specific focus on reactor basic control, hydrodynamic characterization (residence time distribution and phase hold-up characterization studies). Then, initial pilot-scale reactor tests (8.1 L) were also used to gain knowledge on the implementation of this reactor in a higher process scale in an approximate 120 days period. Behavior of the reactor was characterized and used to create a first version of the model to describe its operation [5]. During this period of operational characterization, that included ammonium loads up to 1.35 kg N-NH_4^+/m^3/day, a stratification of the biomass along the bioreactor heigh was observed together with an accumulation of biomass that leaded to reactor clogging in some cases. Higher amounts of biomass were detected in the bottom part of the reactor (with the

correspondent reduction in void volume) whereas only in higher ammonium loads the upper part of the packed bed was colonized.

This aspect was also observed in a long-term experimental campaign of this reactor. In this case, a pilot scale reactor was operated for a period of 4.8 years [6]. Additionally, at the end of this long-term operation, a specific study of the population distribution using Q-PCR and FISH techniques was performed. Results showed a stratification of nitrification strains with higher proportion of *Nitrosomonas europaea* in the lower part of the reactor that decreased at higher reactor heights in contrast to *Nitrobacter winogradsky* proportion. Additionally, FISH analysis revealed also the presence of heterotrophic bacteria at the end of the operation [6]. Thus, axenicity of the culture could not be maintained during the whole operation. Axenicity is certainly of particular interest in the MELiSSA context where the control on the microbial components in the compartments is in the baseline for the development of a well characterized system that performs in a very reproducible, robust and controllable manner [1].

Finally, in both experimental series, an increase of the packed-bed differential pressure was detected in the bioreactor at long operation times, associated to the increase of biomass concentration at the lower parts of the packed bed and the compressible nature of the packing material. For this reason, the implementation of the so called "backwashing" (consisting to perform a media flushing through the packed bed at reverse flow with high flow rates) were performed to allow biomass removal and packed-bed decompression, avoiding reactor collapse due to clogging.

According to all the knowledge acquired, the design of the pilot-scale reactor was considered robust enough to start using it in the integration of this compartment in the complete MELiSSA loop according to the strategy defined in Chapter 1. Accordingly, a new 11.9 L pilot-scale reactor was designed, manufactured and installed in the MPP. This bioreactor included several improvements in comparison to the previous one, in terms of protection for axenicity, improved instrumentation, peripheral equipment, operations, control elements, etc. Indeed, this new bioreactor was installed in the new laboratory dedicated to the MPP, where substantial improvements were made at all

levels. This reactor was operated in three phases: a) start-up (an initial phase to allow the colonization of the particles in the packed-bed), b) stand-alone (a phase to characterize and challenge the nitrification performance of the reactor) [7] and c) integration (a phase where the reactor was operated connected to other elements of the MPP, particularly C4a, as part of the integration WP3 [8]. This implied a total continuous operation time of nearly two years in axenic conditions.

The strategy followed from the beginning of the reactor operation up to the integration WP3 consisted on the inoculation of the packed-bed reactor at low ammonium load with an axenic mixture of nitrifying bacteria. Initially, a fed-batch operation period was performed to enable the generation of the bacterial biofilm by the attachment of cells to the particles of the support material (polystyrene beads). Once biomass was attached to the beads, continuous operation was started with a stepwise increase of ammonium loads up to approximately 1.5 kg $N-NH_4^+/m^3/day$, to test the robustness of the reactor and increase biofilm growth. During this period, the identification of possible partial nitrification conditions, the global oxygen demand and the different stationary states reached were studied to characterize the global behavior of the compartment and detect possible improvements. Once this study was performed, WP3 integration package was initiated at more constant and lower ammonium loads (0.4-0.9 kg $N-NH4^+/m^3/day$) by connecting the liquid outlet of C3 to the entrance of the photosynthetic compartment (C4a). Although the initial integration strategy also included the connection of the two compartments in the liquid and gas phase, it was finally decided not to include the gas phase in WP3 and to test this gas connection latter in the integration strategy.

In this context, this chapter describes the validation of the model proposed for C3 (see Chapter 3) for long-term continuous operation period of approximately two years during the performance of the start-up, stand alone and integration WP3 in the MPP.

4.2. Materials and methods

This section summarizes the specific procedures and analysis used for the nitrifying reactor monitoring and operation.

4.2.1. Pure strains inoculum preparation

Pure cultures of *Nitrosomonas europaea* (ATCC 25978) and *Nitrobacter winogradsky* (ATCC 25391) were maintained in 500 mL T-Flasks for *Nitrosomonas europaea* (ThermoFisher Scientific, Waltham, USA) or Erlenmeyer Flasks for *Nitrobacter winogradsky*. Inoculum cultures were initiated by using 20 mL (*Nitrobacter winogradsky*) or 60 mL (*Nitrosomonas europaea*) of culture and expanded by performing dilutions 1:2 with fresh medium when the culture reached an optical value of 0.1-0.2 AU up to a final volume of 100 mL (*Nitrosomonas europaea*) or 240 mL (*Nitrobacter winogradsky*). During the inocula culture expansion, pulses of ammonium (*Nitrosomonas europaea*) or nitrite (*Nitrobacter winogradsky*) were added to each specific culture each week to reach a value of 100 ppm of $N-NH_4^+$ (*Nitrosomonas europaea*) or 1000 ppm of $N-NO_2^-$ (*Nitrobacter winogradsky*).

During both inocula preparation, temperature was maintained at 30ºC (*Nitrosomonas europaea*) or 28ºC (*Nitrobacter winogradsky*) and pH was maintained to the range 7.5-8.5 by using a 200 g/L solution of sodium carbonate. Axenic conditions of the culture were maintained during the complete inocula preparation. The media used for each culture is specified below:

Nitrosomonas europaea inoculum medium: $(NH_4)_2SO_4$ 3.2738 g/L, KH_2PO_4 0.4103 g/L, $MgSO_4 \cdot 7H_2O$ 0.1786 g/L, $CaCl_2 \cdot 2H_2O$ 0.0264 g/L, $CuSO_4 \cdot 5H_2O$ 0.1325 mg/L, $FeSO_4 \cdot 7H_2O$ 0.331 g/L, KH_2PO_4 5.4233 g/L, $NaH_2PO_4 \cdot 2H_2O$ 0.6018 g/L and Na_2CO_3 anhydrous 0.3968 g/L.

Nitrobacter winogradsky inoculum medium: $CaCl_2 \cdot 2H_2O$ 13.25 mg/L, $MgSO_4 \cdot 7H_2O$ 100 mg/L, $EDTA \cdot 2H_2O$ 1.54 mg/L, $FeSO_4 \cdot 7H_2O$ 5 mg/L, $NaNO_2$ 207 mg/L, $MnCl_2 \cdot 4H_2O$ 0.1 mg/L, $CoCl_2 \cdot 6H_2O$ 0.001 mg/L, $ZnSO_4 \cdot 7H_2O$ 0.05 mg/L, $CuSO_4 \cdot 5H_2O$ 0.01 mg/L, $Na_2MoO_4 \cdot 2H_2O$ 0.05 mg/L, K_2HPO_4 1.37 mg/L and H_2SO_4 0.0005 mg/L.

4.2.2. Packed-bed bioreactor

A pilot scale up-flow packed-bed reactor (SNC-Lavalin, Brussels, Belgium and Bioprocess Technologies, Madrid, Spain) with 0.125 m of diameter, 1.031 m height and a total volume of 11.9 L was used in this work. The support used in the packed-bed was Biostyr® (expanded polystyrene) beads with a mean diameter of 4.1 mm. Figure 4-1 shows a detailed description of the packed-bed reactor.
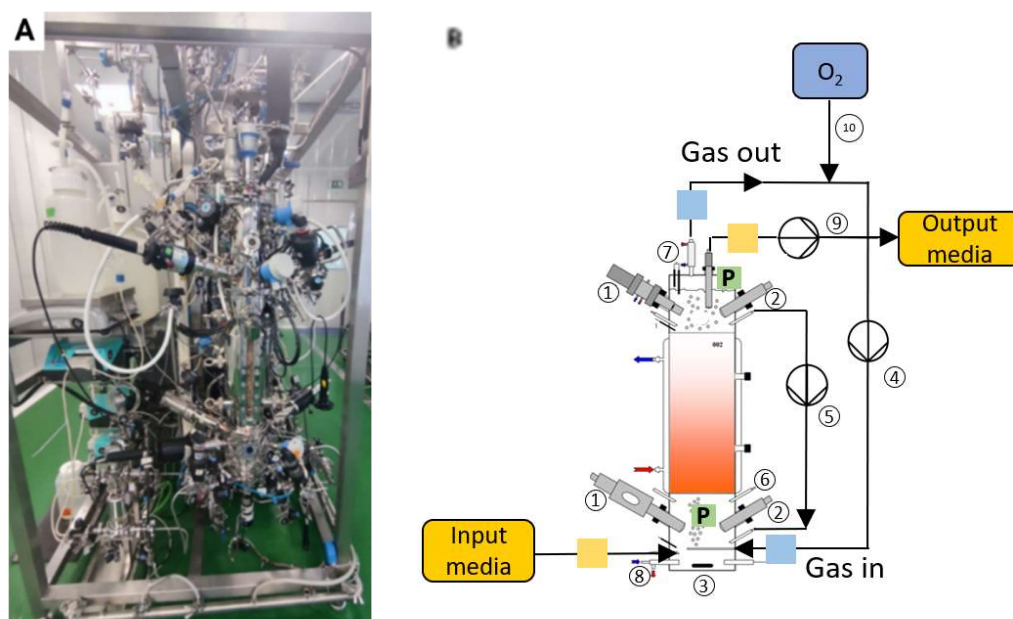
Figure 4-1. Picture of the nitrifying bioreactor (A) and scheme of the nitrifying bioreactor (B) where (1)- pO₂ sensor; (2)- pH sensor; (3)- Agitator; (4)-recirculating gas closed-loop; (5)-liquid recirculation loop; (6)- acid and base additions; (7); condenser; (8)- liquid influent line; (9)- liquid effluent line; (10)- O₂/N₂ inlet line. Yellow boxes correspond to liquid filters whereas blue boxes correspond to air filters. Finally, Green boxes with symbol P represents pressure probes to analyze the bioreactor differential pressure.

As it can be observed in Figure 4-1, the reactor has three different zones (from bottom to top): A first section with a height of 0.175 m without packing-support and mechanically stirred (marine type helix impeller) used for air sparging, liquid fresh medium and recirculation feeding and instrumentation hosting. A second packed-bed central section, with a height of 0.556 m and a third final section for

gas-liquid separation, liquid outlet and instrumentation hosting, with a height of 0.300 m.

In terms of flow rates, the bioreactor design also includes an up-flow liquid circulation in the reactor that incorporates a recirculation flow rate and an external flow with fresh medium. Additionally, the design also includes a gas recirculation up-flow rate with a PID control system in the return to add specific oxygen concentration to specific target (80% saturation in this case). Continuous control of liquid and gas flow rates is performed by the implementation of specific flow meters in the liquid recirculation (Endress Hauser Proline Promass F300, Reinach BL, Switzerland), liquid input (Endress Hauser Proline Promass F300, Reinach BL, Switzerland) and in the gas recirculation flowrate (Bronkhorst, F-202D-FA, Bronkhorst, Ruurlo, Netherlands).

Additionally, design of this pilot-plant reactor includes also a high degree of control of the physic-chemical variables of the system. Two sterilizable glass pH probes are located at the bottom and the top of the reactor and allow for on-line pH reading (Mettler, InPro 3253i/SG/325, Greifensee, Switzerland). Based on these measurements, pH is regulated by calculating the weighted average mean (80% weight of the bottom section pH probe and 20% weight of the top section pH probe) by the addition of 0.1 M sulfuric acid and 0.94 M sodium carbonate solution in the bottom part of the reactor. Oxygen is measured by two on-line Clark amperometric sensor (Mettler, InPro 6850i/12/320, Greifensee, Switzerland) located also in the top and bottom sections of the reactor. Oxygen set-point is controlled at 80% on the top amperometric sensor by adding pure oxygen when required. Lower oxygen sensor measurements are recorded for information but not considered for controlling of this variable. Temperature is also measured on-line with three different temperature probes (bottom, middle and upper part of the reactor, (Endress Hauser, TR45-BB5A1R2MA4GB0, Reinach BL, Switzerland). All of this continuous data collected is sent to specific control system specifically designed for the complete monitoring and control of the reactor operation. Additionally, an overpressure of 80 mbar as initial base value is assured in the

system based on the control of two pressure probes located at the bottom (liquid phase) and top (Gas phase) of the packed-bed reactor (Endress Hauser, Deltabar S FMD78-AB17HC1TC1BA, Reinach BL, Switzerland). Differential pressure from the lower and top section of the bioreactor is online monitored to characterize the status of the packed-bed by means of two pressure probes located at the bottom (liquid phase) and top (Gas phase) of the packed-bed reactor (Endress Hauser, Deltabar S FMD78-AB17HC1TC1BA, Reinach BL, Switzerland). Additionally, an overpressure of 80 mbar is maintained in the headspace of the packed-bed reactor.

Finally, requirement to maintain reactor axenicity implies also additional constrains in the bioreactor design. The reactor is operated in sterile-conditions and in a classified room (C-Class) as additional security to avoid contaminations. This sterile-operation conditions includes additional considerations, for example reactor air filtration (PALL, MCY4463PFRPH4, New York, US), fresh medium filtration (PALL, MCY4440DFLPH4, New York, US) or specific procedure designed to fill the bioreactor with the support material for the packed-bed (see section 4.2.3).

4.2.3. *Packed bed reactor inoculation*

<u>Inoculum preparation:</u> A co-culture of pure strains of *Nitrosomonas europaea* (ATCC 25978) and *Nitrobacter winogradsky* (ATCC 25391) was inoculated in a 2 L Biostat B bioreactor (Sartorius Stedim Biotech, Göttingen, Germany) by using pure cultures previously grown in axenic conditions (see section 4.2.1) at 50% proportion according to optical density. Specifically, 180 mL of inoculum were used for a final reactor volume of 1.9 L where fed-batch operation was performed with ammonium pulses to reach 100 ppm of $N-NH_4$ in the reactor, until a final optical density value of 0.3 AU. Temperature was maintained at 30ºC and pH was controlled at 7.5 value. pH was adjusted by sulfuric acid (0.5 M) and sodium carbonate 50 g/L solution addition. The axenicity of the reactor was maintained and checked weekly by plating 100 µL of sample in PCA (37ºC) and PDA (30ºC) media Petri dishes in triplicates.

The specific composition of the medium used for the inoculum growth at reactor culture was: $(NH_4)_2SO_4$ 1.32 g/L, $FeSO_4 \cdot 7H_2O$ 2.5 mg/L, Na_2HPO_4 0.71 g/L, KH_2PO_4 0.68 g/L, $(NH_4)_6Mo_7O_2 \cdot 4H_2O$ 0.177 g/L, $ZnSO_4 \cdot 7H_2O$ 0.0043 g/L, $CuSO_4 \cdot 5H_2O$ 0.004 g/L, $MgSO_4 \cdot 7H_2O$ 0.052 g/L, $CaCl_2 \cdot 2H_2O$ 0.74 g/L and $NaHCO_3$ 0.8 g/L.

Packed-bed reactor inoculation: Bioreactor inoculation requirements regarding packed-bed material sterilization and inoculum introduction were also restricted to specific sterile-operation conditions of the reactor. On one hand, packed-bed material used (Biosty® beads (expanded polystyrene) with 4.1 mm diameter) cannot be sterilized by heat. For this reason, the bioreactor was first sterilized empty by heat, together with all auxiliary lines. In parallel, the packing material was sterilized by gamma-irradiation at 30kGy in Aragogama S.L. (La Roca del Vallès, Barcelona) and then introduced by over-pressure to the reactor in sterile conditions through a dedicated line. At this point, the complete hardware was submitted to a 13 days sterility test in order to guarantee the sterility of the system prior to the inoculation. For this inoculation, the complete content of the Biostat bioreactor (approximately 1.9 L at an optical density of approximately 0.3 AU, see section 4.2.3) was transferred to a sterile 2L bottle and then introduced inside the packed-bed reactor in sterile conditions.

4.2.4. Packed-bed operation

An initial operation of the packed-bed reactor was performed in fed-batch mode during five days. In this period, pulses of ammonium up to final target concentration of 100 ppm $N-NH^+_4$ were added. After this period, a continuous culture operation mode was stablished in the packed-bed reactor. This packed-bed operation was divided in three different phases according to global MPP strategy: start-up (initial operation of the bioreactor), stand alone and integration WP3 (see Figure 4-2).

Start-up phase had a total duration of approximately 250 days. In this continuous phase, ammonium loads were progressively increased up to 0.6 kg/m^2/day to

facilitate the attachment and growth of the biomass in the packing material. In order to increase these charges, bioreactor liquid flow rate was increased from approximately 1.4 mL/min up to 10 mL/min at maximum final ammonium concentration of 300 ppm. After this initial period, the second continuous operation called stand-alone implied a challenge of the packed-bed reactor in terms of nitrification capacity. In this phase (operational days 250-477), a continuous increase of ammonium load from 0.6 kg/m^2/day to a maximum of 1.5 kg/m^2/day was tested by a consecutive increase of ammonium concentration in the reactor input flow up to values of 850 ppm at continuous liquid flow rate of 8.3 mL/min. Finally, the third period of continuous operation was part of the WP3 integration of C3 and C4a compartments. This period was liked to an operation of the C3 in the final conditions designed for the integration where ammonium charges were changed by testing different liquid flow rates (7-14 mL/min input flow).

During the complete operational period, temperature was maintained at 30ºC and pH was set initially to 7.5 and increased to 8.1 when the packed-bed was considered fully colonized by visual inspection. Oxygen in the liquid phase was maintained at 80% of the saturation with pulses of pure oxygen to the gas phase recirculation line by using a PID control system. Finally, minimum overpressure of the system of 80 mbar was assured during the complete operation. The differential pressure increased at the last part of the operation (500-700 days) due to biomass growth and packed bed compression due to continuous liquid flow rate in the upper direction.

Finally, medium composition during the first two phases was equal to the one used for the inoculum growth at reactor culture. However, culture media was modified in the third period (WP3) in order to include all the compounds and concentrations necessary for C3 and C4a in series operation. Thus, a combination of a modified Zarrouk medium regularly used for *Limnospira indica* (cyanobacteria used in C4a [9]) and the medium defined in the literature for nitrifying cultures [10] was used: 1.358 g·L^{-1} of $(NH_4)_2SO_4$, 1 g·L^{-1} of K_2SO_4, 1 g·L^{-1} of $NaCl$, 0.816 g·L^{-1} of $NaHCO_3$, 0.71 of Na_2HPO_4, 0.68 of KH_2PO_4, 0.5 of K_2HPO_4, 0.1 g·L^{-1} of

MgSO$_4$·7H$_2$O, 0.18 g·L^{-1} of (NH$_4$)$_6$Mo$_7$O$_2$·4H$_2$O, 0.08 g·L^{-1} EDTA-2Na·2H$_2$O, 0.01 g·L^{-1} of FeSO$_4$·7H$_2$O, 0.04 g·L^{-1} of CaCl$_2$·2H$_2$O, 1.81 mg·L^{-1} of MnCl$_2$·4H$_2$O, 0.22 mg·L^{-1} of ZnSO$_4$·7H$_2$O, and 0.079 mg·L^{-1} of CuSO$_4$·5H$_2$O
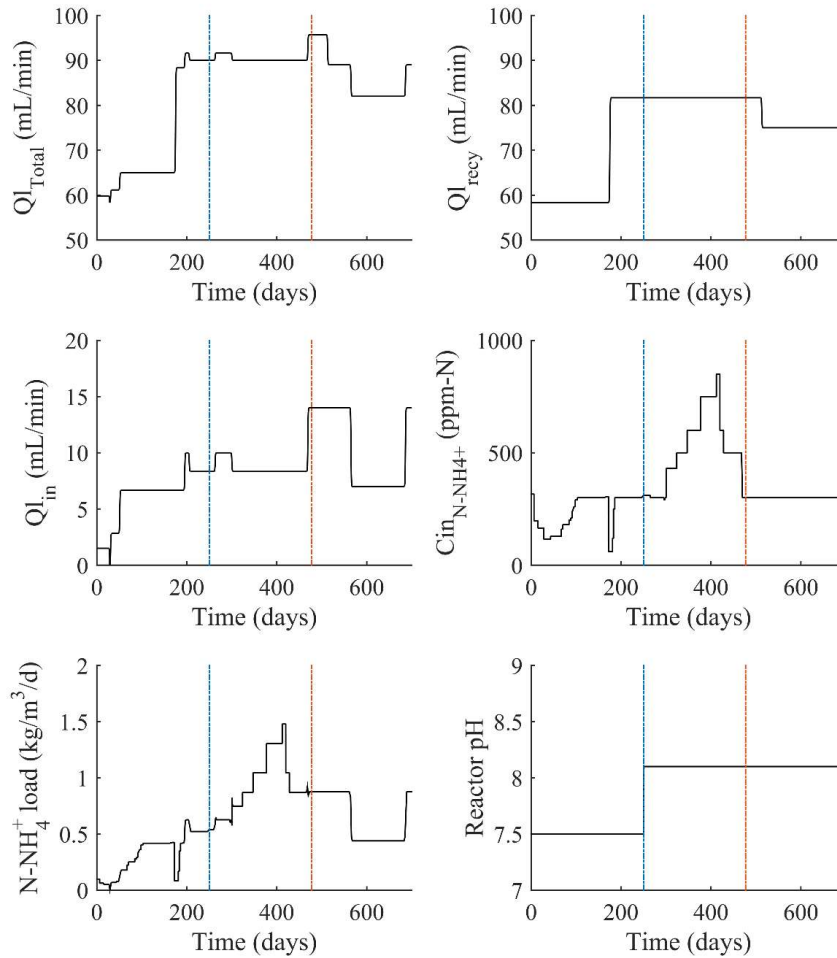
Figure 4-2. Evolution of the reactor operation conditions (liquid inlet and recirculation liquid flow rates, reactor pH and inlet ammonium concentration and load). The concentration of oxygen in the liquid phase was maintained at 80% liquid saturation during the complete period. In this picture, the specific time cultures where the different continuous phases were initiated are highlighted. Transition between start-up and stand-alone characterization phase is highlighted in blue whereas transition between stand-alone and WP3 is highlighted in red.

4.2.5. Analytical determination of N-species

Samples for the determination of the N-species concentration were taken from the packed-bed reactor during continuous operation, three times per week from the recirculation line of the reactor and once per week from the lower part of the reactor. In each case, analyses of ammonium, nitrite and nitrate were performed using the following kits (Hach_Lange GMBH, Düsseldorf, Germany): LCK 304 (2-47 $N-NH^+_4$ ppm) and LCK 303 (0.015-2 $N-NH^+_4$ ppm) for ammonium, LCK 341 (0.015-0.6 $N-NO^-_2$ ppm) and LCK 342 (0.6-6 $N-NO^-_2$ ppm) for nitrite and LCK 339 (0.23-13.5 $N-NO^-_3$ ppm) and LCK 340 (5-35 $N-NO^-_3$ ppm) for nitrate.

4.2.6. Determination of initial and final bioreactor void fraction

A known volume of beads colonized with biofilm (equivalent to 40 mL) was extracted after the reactor dismantling at the end of the complete operation period, once liquid had been drawn from the reactor. These amounts of beads colonized with biofilm were placed inside a 40 mL recipient without compressing the material. Once the beads including the biofilm were added, the amount of water that could be introduced to the recipient up to the defined final volume (40 mL) was determined. This amount of water was considered representative of the liquid inside the packed-bed structure at a specific point. This procedure could be performed only with new beads (representative of the initial state of the non-colonized packing material) and with real colonized beads at the end of the operation after the liquid was eliminated from the reactor, since it was not possible to extract samples of the packed-bed in a non-intrusive way during continuous operation. When the reactor was stopped, this procedure was performed at 5 different heights corresponding to the 5 compartments described in the proposed model (see Chapter 3). The values measured at the end of the operation are summarized in Supplementary materials section 0. Regarding the initial measurements for the non-colonized beads an experimental void fraction of 40% was determined.

4.2.7. Biofilm sampling and preparation

Total biomass concentration of the biofilm was determined at five different packed-bed heights by dry weight determination once the packed-bed reactor was dismantled after the whole operation period. According to the procedure, a minimum of two representative samples with a known total volume of 15 mL were submitted to stirring with 30 mL phosphate buffer saline solution (PBS: NaCl 9 g/L, KH_2PO_4 0.24 g/L, NA_2HPO_4 1.44 g/L, KCl 0.2 g/L) to allow for all the attached biomass to be detached from the packing material. This suspension-detachment procedure was performed twice using specific centrifugation conditions (4ºC and 10000 rpm for 15 minutes (Beckman A J2-21, Brea, California, USA)). Then, the obtained pellet was drained at 100ºC until constant weight and weighted.

Specific calculations of the final biofilm concentration (in grams of biomass per volume of biofilm) could be determined for each sample by considering the packing material properties (Supplementary materials section 4.8.4), the dry weight determination and the experimental void fraction at the beginning and end of operation (see section 4.2.6).

Supplementary materials section 0 provides a more detailed information on these calculations.

4.3. Experimental results

The experimental results obtained in the reactor during the two-years operation period are provided here, based on:

1) Nitrification profiles: ammonium, nitrite and nitrate concentrations over time at different operational conditions

2) Visual comparison of the biofilm evolution along the bioreactor height

3) Final estimated biomass concentration distribution profile in the different reactor heights

4) Increase in differential pressure of the reactor.

Based on the interpretation of the results, the experimental data will be used in a following step to validate the proposed model.

4.3.1. Nitrification profiles

Figure 4-3 and Figure 4-4 summarize the nitrification profiles obtained during the approximately 2 years operation period. The first figure shows the experimental values obtained from manual samples taken from the bioreactor recirculation line (equivalent to the top section of the bioreactor). The second figure shows the experimental values obtained from manual samples extracted during the same period of time from the bottom part of the packed bed reactor.

As detailed in Figure 4-3 and Figure 4-4, initial operation of the reactor included a first period corresponding to the start-up phase of the reactor (first 250 days of culture approximately) and a second period that included stand-alone characterization of the nitrification compartment as an initial set up of the conditions for the reactor continuous controlled operation (250-477 days of culture). Finally, the third period corresponded to the performance of WP3 integration package where liquid outlet of this compartment was introduced as feed for the C4a bioreactor (477 to the end of operation).

Operation of the nitrification compartment during this first period (start-up phase) started at lower ammonium loads up to a maximum of 0.6 $kg/m^2/day$ (see Figure 4-2). This procedure was performed by changing the input flow rates in low ammonium concentrations (< 100 ppm N-NH_4^+) and allowed for the biomass to attach to the packing material and adapt its characteristics for a consistent biofilm development. This biofilm development was probably the cause for the initial lower nitrification capacity (initially around 75%) detected, with presence of residual not converted ammonium in the output of the bioreactor. However, consistent biofilm development led to the reduction of these residual ammonium concentrations to nearly undetectable levels at culture time of 250 days and an increase in the nitrification capacity up to 98-99%. Thus, achieving a correct biofilm development.
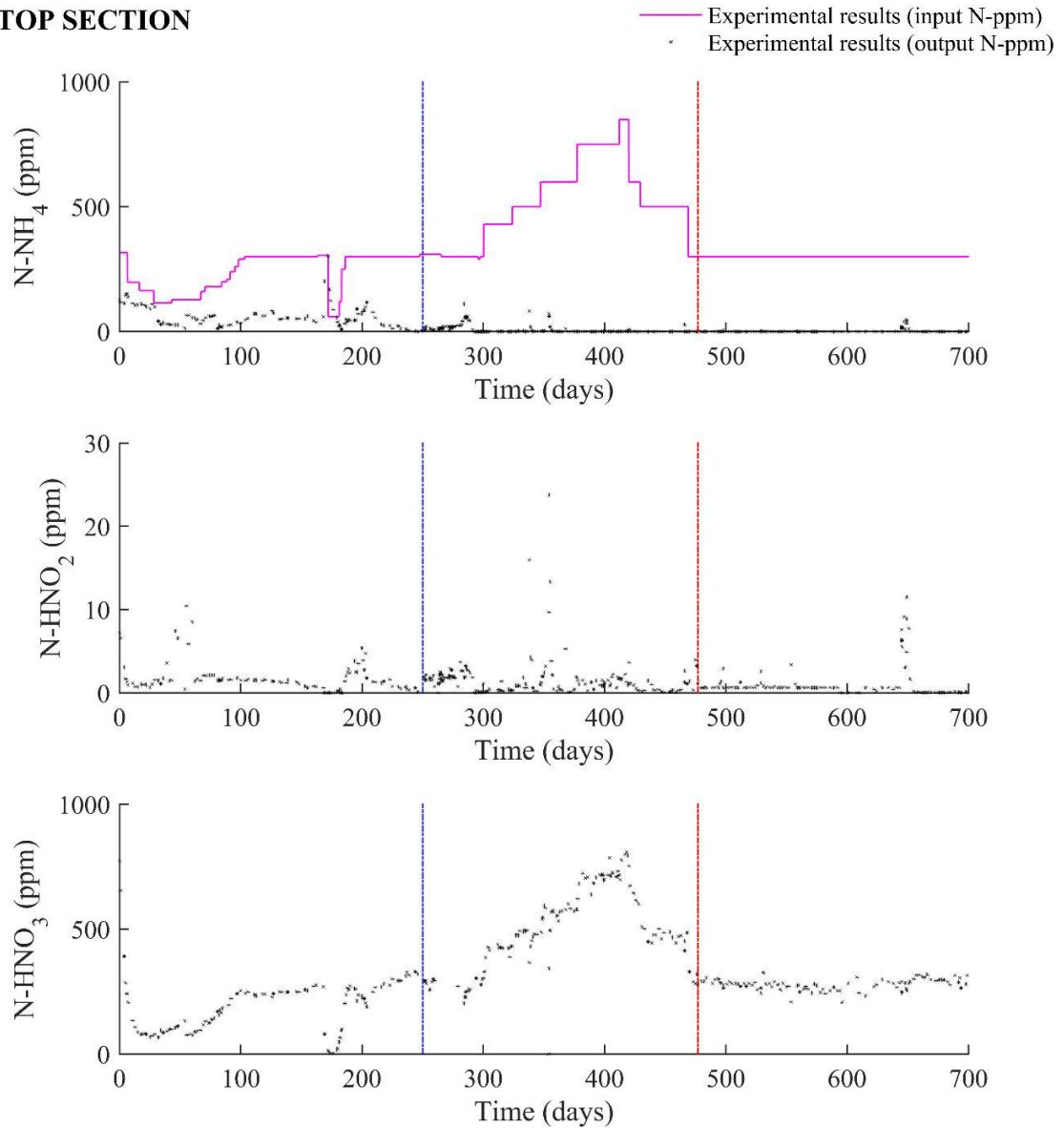
Figure 4-3. Nitrification experimental results obtained during the two years of operation in the pilot plant reactor. Grey dots correspond to experimental analytical values obtained at the top of the bioreactor whereas continuous pink line corresponds to experimental ammonium input in the bioreactor. In this figure, transition periods between start-up and stand-alone phases (blue) and stand-alone and WP3 phases (red) have been highlighted.
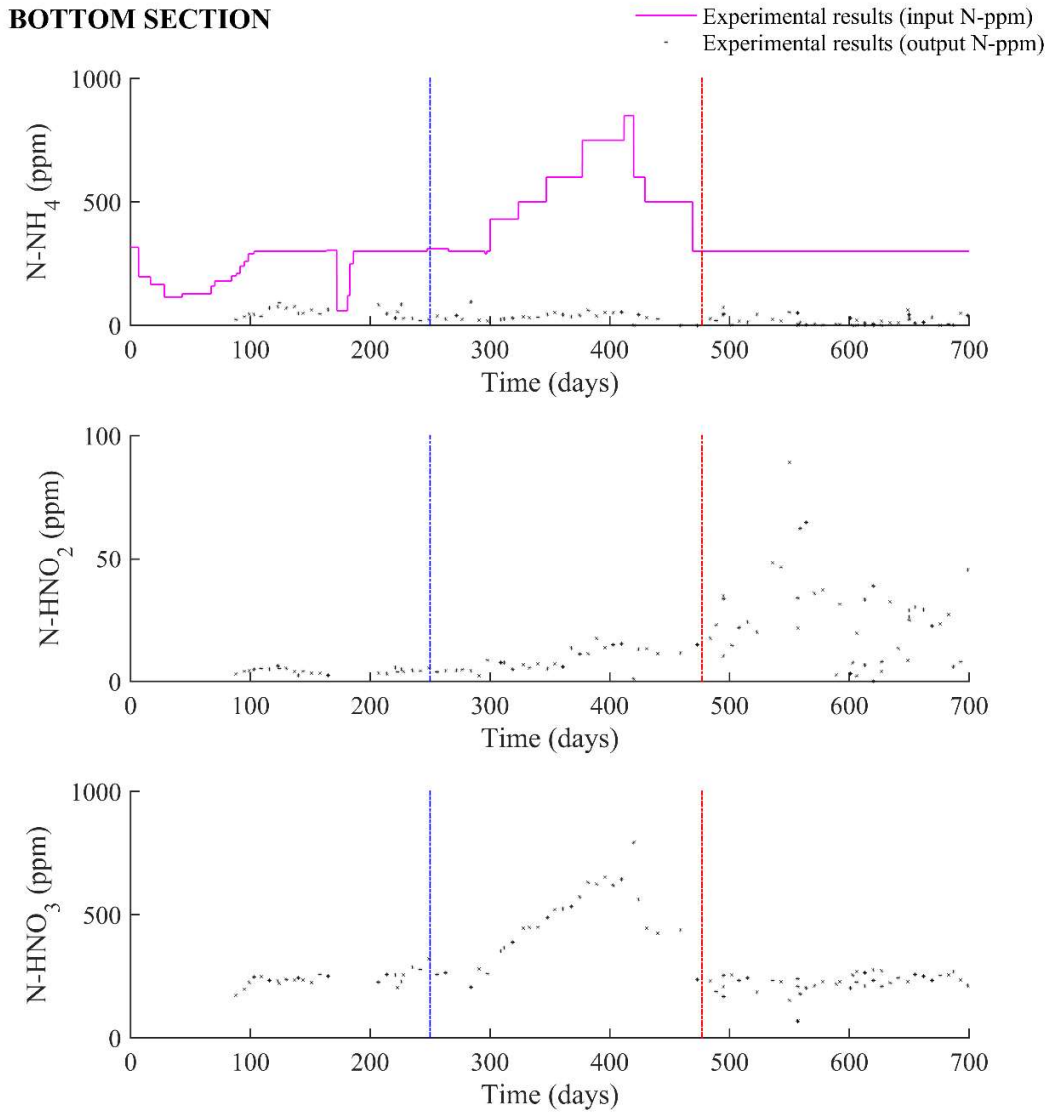
Figure 4-4. Nitrification experimental results obtained during the two years of operation in the pilot plant reactor. Grey dots correspond to experimental analytical values obtained at the bottom of the bioreactor whereas continuous pink line corresponds to experimental ammonium input in the bioreactor. In this figure, transition periods between start-up and stand-alone phases (blue) and stand-alone and WP3 phases (red) have been highlighted.

After this initial period, stand-alone characterization phase started. In this phase, nitrification of 100% was obtained at the output of the reactor (top section) even when the ammonium load was challenged (days 300-477) up to a high ammonium load of 1.5 kg/m^2/day. This was achieved by maintaining a constant residence time of 17 h and increasing ammonium concentration (> 300 ppm) in the inlet flow rate. In these conditions, the system was able to achieve 99% ammonium removal with a rapid adaptation to the new conditions whatever the load tested. Thus, these results corroborated a correct adaptation of the axenic culture, a solid biofilm formation and a high capability for ammonium assimilation.

Additionally, the evolution of intermediate nitrogen forms (nitrite) at the output of the reactor showed always low values (< 50 ppm) during the whole experiment. Thus, corroborating correct capability of the culture to convert the different ammonium loads tested. However, a few peaks of nitrite were observed. Some peaks of nitrite were related to the days following increases in the ammonium load but other were caused or amplified due to some operational incidences. This is the case, for example, of the nitrite peaks observed at approximately 50 and 350 days of culture where a specific misadjustment of pH due to operational problems during probes calibration was detected with additional aeration problems in the second case.

It should be noted additionally that initial stand-alone phase was also used to set up the control system for online oxygen control in the PID present in the gas loop. For this reason, oxygen limitation problems also occurred during this initial period. This could also be translated into to the apparition of additional/amplified intermediate forms peak concentration. A clear example in this case could be a potential peak of nitrite detected at approximately 200 days of culture. In this case, a contamination of the feed tank that required to stop the test and set up the system in open loop to reset gas phase concentrations occurred, causing a limitation of oxygen. However, once the connection between the feed tank and the reactor was recovered, the system could easily return to nominal operation. Nitrite peaked down and the ammonium load could be increased without any additional problems.

This is proof of the capacity of the reactor to overcome changes that could potentially affect nitrification capacity.

Finally, a nitrite peak was observed at approximately 650 days of operation. In the last part of the operational period studied (500-700 days), manual interventions to the bioreactor were performed as an attempted strategy to overcome a slight increase detected in the reactor differential pressure related to the biomass growth and packing material compression. This peak of nitrite is related to an incidence in the operation of the bioreactor during one of these manual interventions.

Finally, the monitoring of the bottom section concentrations was also initiated after 100 days of culture and provides additional evidence of the internal efficiency of the reactor. As observed, the levels of ammonium and nitrite in the bottom section were slightly higher than the output in most of the operation time. This is in agreement with the reactor design and would be consistent with previous results that showed a certain stratification of the two nitrification strains in the reactor height [6]: *Nitrosomonas europaea* distribution in the reactor would tend to be the more predominant bacteria at the bottom part of the reactor, causing slightly higher nitrite concentrations in this part of the reactor. For this reason, biofilm consolidation together with the manual interventions performed at the end of operation (500-700 days) could potentially be the cause for the higher difference in NO_2^- intermediate forms concentrations observed between top and bottom sections.

4.3.2. Biofilm structure visual evolution

Figure 4-5 provides examples of the observations made on the experimental evolution of the packed bed during the operational period considered. In these visual observations, increase of biomass forming the biofilm could be traced by the fact that the beads have white color while the bacterial biofilm has a pink-brown color that allows distinguishing how it is developing. Packed-bed operation started with a fluffy uniform colonization of the biofilm in all the reactor height. As Figure 4-5 shows, in pictures at 0 and 150 days of culture, the color of the beads is similar

in all reactor height. However, as detailed in the same figure, this uniformity in the reactor color is not maintained in the following days. The pink color related to the presence of biomass increases the intensity at the bottom part of the reactor compared to more upper parts. This is especially relevant for the picture corresponding to culture times higher than 400 days, where a dense biomass concentration at the bottom of the reactor can be visually observed. This reactor height distribution of the biomass was also seen in previous trials with this reactor [1,6] and is in agreement with previous reports on biofilm consolidation phenomenon that suggest a possible structure realignment of the biofilm under dynamic conditions as a relevant property in its development [11,12].

Also, as detailed in previous studies, in these conditions the performance of backwashing procedures can be a good option to avoid future reactor clogging. For these reasons, initial attempts to perform backwashing procedures (referred as manual interventions in section 4.3.1) were performed at the end of the operation (500-700 days of culture). However, these attempts did not show a clear effectiveness. In fact, the performance of these procedures could not avoid a packed bed height reduction linked to the continuous flow rates applied for long periods of time. This packed bed height reduction could be visually observed at the end of the operation (for example for the visual observation at 500, 600 and 700 days of operation (Figure 4-5)). Based on the reactor dimensions, this packed bed reduction is estimated to be of 13 cm.
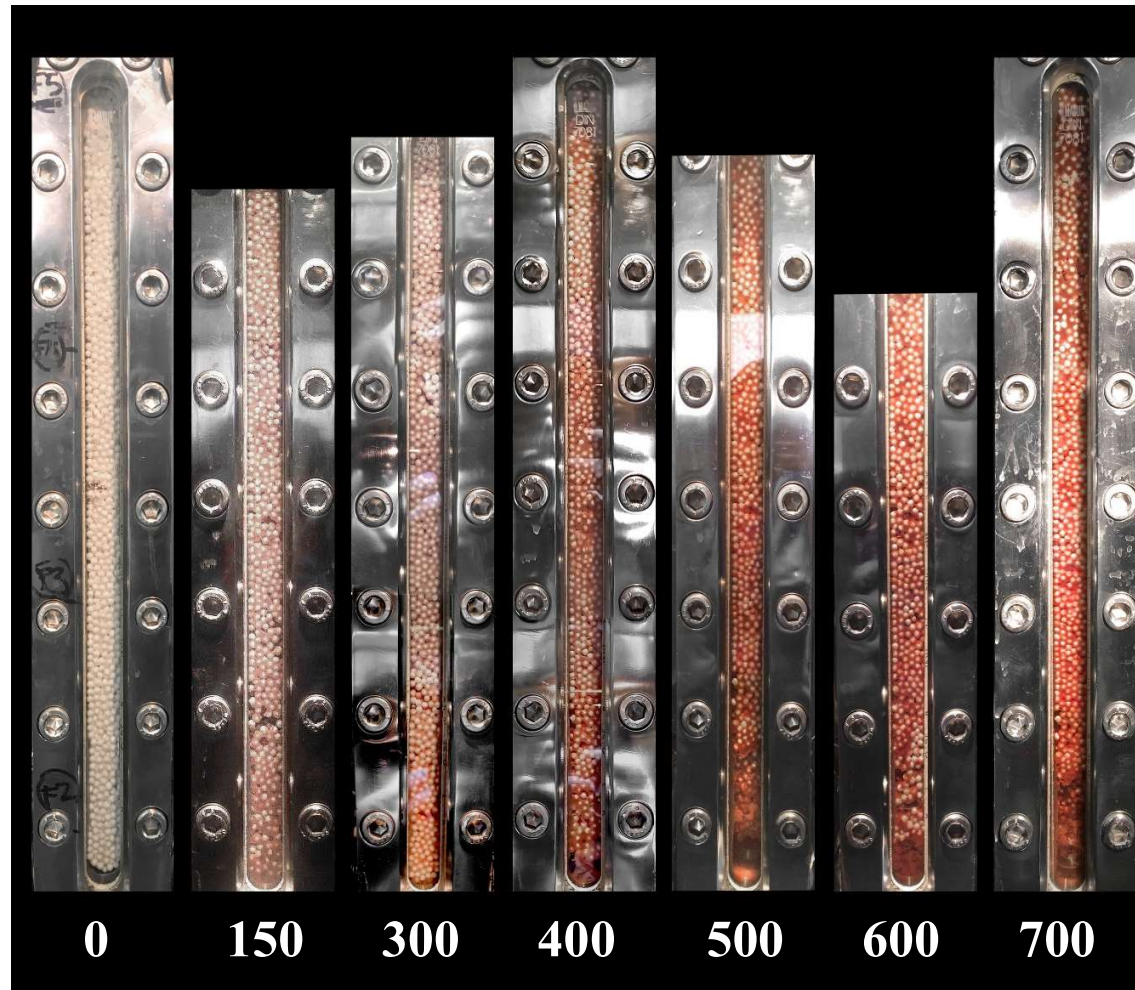
Figure 4-5. Packed bed visual evolution during the two-years operation. Numbers below the figure provide the days where each photograph was taken. All photographs have been normalized by considering the available information of the reactor height. If some part of the packed bed appears in black it means that no picture of this part was available.

4.3.3. Biomass concentration in the biofilm at the end of operation

Biomass concentration in the biofilm was determined at the end of the operation as described in section 4.2.7. This determination was performed at five different packed-bed compartment volumes (PBVs) corresponding to the number of n-tanks in series proposed to be implemented in the model description (see Chapter 3 for more information). Final experimental data with the mean and standard deviation, is presented in Figure 4-6. As observed in this figure, additional evidence of the reactor height distribution of the biomass at the end of the operation is also found when biofilm concentration is determined for the different heights. It should be noted that experimental determination of these kind of data implies multiple experimental measurements and this can be causing high variability. However, for the purpose of this analysis the results can be considered representative. Lower parts of the reactor are linked to higher biomass concentration near to the defined maximum biofilm concentration of 260 g/L and in accordance with previous results with this type of bioreactor [1,6] and in general theoretical biofilm consolidation hypotheses [11,12]. Thus, confirming the visual inspection evaluation shown during the whole culture period.
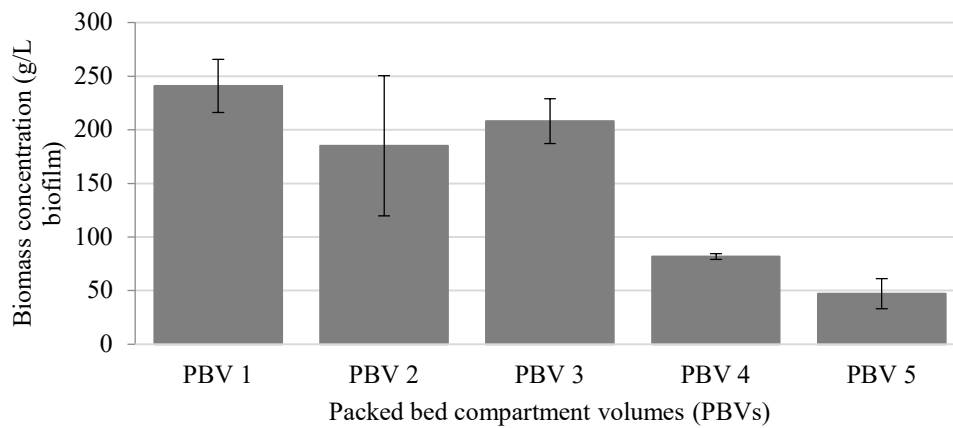

Figure 4-6. Experimental distribution of the biomass concentration in the biofilm for the different packed bed compartment volumes (PBVs) as proposed in the model. Values presented correspond to a minimum of 2 samples and are presented as the mean value with its standard deviation.

4.3.4. Bioreactor differential pressure profile during operation

The profile of the differential pressure of the packed bed measured during the two-years operation is presented in Figure 4-7.
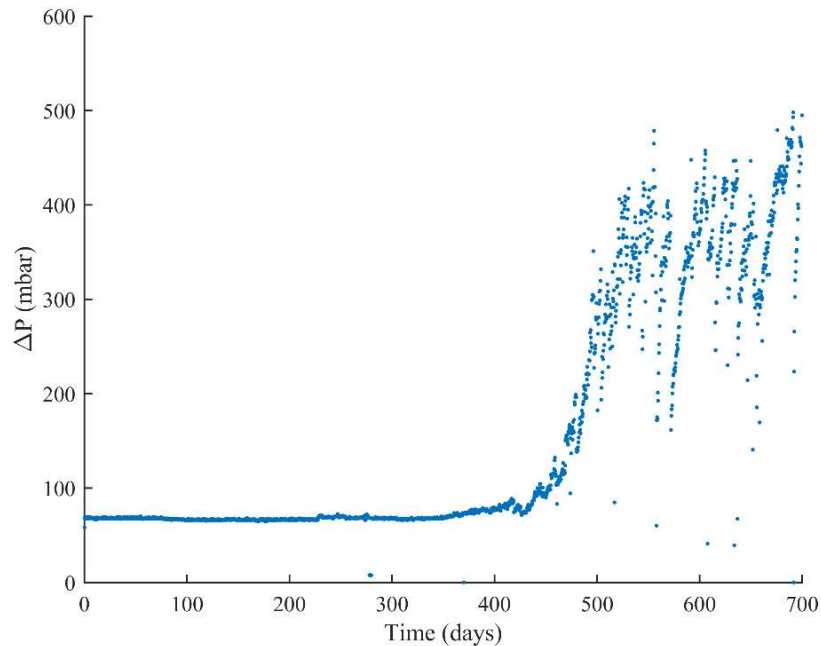
Figure 4-7. Packed bed experimental differential pressure profile during the two years of operation.

As observed, the packed-bed differential pressure was constant during the first period of operation up to approximately 400 days at 80 mbar, which is the working overpressure of the packed-bed reactor (see section 4.2.4). At this point, the biofilm is considered to be fully colonized and the biofilm starts its consolidation in the reactor, producing an increase in the reactor differential pressure. This observation is also in agreement with the visual increase of biomass observed at the bottom part of the reactor and a reduction of the packed bed height (see Figure 4-5) and aligned with previous studies [1,6] discussions on the importance of the performance of backwashing procedures after certain operation time to avoid future reactor collapse. In fact, as already mentioned in section 4.3.3, initial attempts of backwashing were performed at culture times higher than 500 days and can be

112

observed in the reactor differential pressure evolution. However, the effectiveness of these backwashing procedures was not high since reactor differential pressure reduction was only momentaneous. Based on the results, the implementation of the backwashing procedure in this reactor would require of an optimization to effectively remove biomass and return the reactor to differential pressure around 80 mbar.

4.4. Estimation of model parameters and manipulable variables

Table 4-1 describes the parameters used in the proposed mathematical model according to the description in Chapter 3. Then, this section summarizes the values given to each one of these parameters in the model simulation. As observed in the sixth column the model parameters are classified according to their origin:

a) Parameters obtained from bibliographic references (BR)

b) Fixed parameters in operation (FOP): Corresponding to physical parameters fixed due to the equipment design characteristics.

c) Parameters determined by specific calculations from experimental data (EXP): biological, chemical or physical parameters fixed during operation determined with experimental data.

d) Input operational variables (IOV): Corresponding to manipulable input variables adjusted as part of the test design.

e) Operation condition variables (OCV): Corresponding to specific instructions for operation set up in the control system of the reactor.

For the first three categories, the specific value given to each parameter and related justifications, if required, are summarized in this section.

Table 4-1. Main model parameters: categories, values and determination source

Category	Description	Symbol	Parameter classification	Value/ origin	Classification
Model definition	Number of compartments	n	7	Model definition	-
	Number of beads	$n^{\underline{o}}\ beads$	113445	Model definition	-
Reactor hydrodynamics	Main input liquid flow rate	$Q_{\ell,in}(t)$ [mL/min]	Input control parameter	Figure 4-2	IOV
	Recirculation liquid flow rate	$Q_{\ell,recy}(t)$ [mL/min]	Input control parameter		IOV
	Main gas flow rate	$Q_{g,in}(t)$ [L/min]	Input control parameter		IOV
	Recirculation gas flow rate	$Q_{g,recy}(t)$ [L/min]	Input control parameter		IOV
	Back-mixing liquid flow rate	$Q_{l,mix}(t)$ [L/min]	Input control parameter		IOV
Reactor physical and chemical conditions	Temperature	T [°C]	30	Chapter 4 Section 4.2.4	OCV
	Input pH setpoint	$pH^{in}(t)$	Control parameter	Figure 4-2	OCV
Reactor dimensions, characteristics and operation	Lower section reactor height (before packed bed)	h_A [m]	1.75	Supp. materials 4.8.3	FOP
	Total packed bed height	h_B [m]	5.56		FOP
	Specific n-tank in series packed bed height (t=0)	h_b^0 [m]	5.56/5		FOP
	Upper section reactor height (after packed bed)	h_C [m]	3.00		FOP
	Column diameter	D [m]	1.25		FOP
	Reactor pressurization	P [mBar]	80	Chapter 4 Section 4.2.4	OCV
	$O_2^{(l)}$ concentration	$C_{\ell,O_2}^{in}(t)$ [g/L]	0.008096 g/L 80 % air saturation	Chapter 4 Section 4.2.4	OCV
	Input $O_2^{(g)}$ fraction	$C_{g,O_2}^{in}(t)$ [%]	Pure O_2	Chapter 4 Section 4.2.4	OCV

BR: Bibliographic reference / IOV: Input operational variable / OCV: Operational condition variable
FOP: Fixed operational parameter / EXP: Calculated parameter based on experimental data

Table 4-2. Main model parameters: categories, values and determination source

Category	Description	Symbol	Parameter classification	Value/ origin	Classification
Gas-liquid mass transfer	Mass transfer coefficient (Differential for sections A, B and C of the packed bed)	k_{La}	32.4 (Top) 54.0 (Bottom) Correlation (Packed bed)	[13] [13] [14]	EXP
	Hold up (gas fraction)	v [L gas/L liq]	0.0846	[13]	EXP
Packing material characteristics	Diameter of the packing material (initial)	d_0 [m]	0.0041 m	Supp. materials 4.8.4	FOP
Biofilm definition	Biofilm consolidation time	t_d [d]	400	Estimation based on differential pressure profile. See Figure 4-7	EXP
	Experimental constant	K	100	-	EXP
	Biomass density	ρ_{bio} [g/L]	270	[15]	BR
	Initial mass of Nitrosomonas (Ns)	M_{Ns}^0 [g]	57	Chapter 4 Section 4.4.4	EXP
	Initial mass of Nitrobacter (Nb)	M_{Nb}^0 [g]	133		EXP
Model state variables limitations	Maximum biofilm thickness	L_F^{max} [m]	16.9×10^{-5} m	Chapter 4 Section 4.4.3	EXP
	Maximum inactive layer thickness	$L_{F,0}^{max}$ [m]	$0.2 \times L_F^{max}$	[11]	BR
	Initial void fraction	η_ℓ^0	40%	Chapter 4 Section 4.2.6	EXP
	Minimum void fraction	η_ℓ^{min}	5.7%	Chapter 4 Section 4.4.1	EXP
	Initial biofilm porosity	$\varepsilon_{F,\ell}^0$	100%	Porosity theoretical definition	BR
	Final biofilm porosity	$\varepsilon_{F,\ell}^{min}$	0%		BR

BR: Bibliographic reference
IOV: Input operational variable
OCV: Operational condition variable
FOP: Fixed operational parameter
EXP: Calculated parameter based on experimental data

4.4.1. Estimation of packed-bed void fraction at the end of operation

Packed-bed void fraction at the end of the operation was estimated by considering the differential pressure as a reference value. As observed in Equation 4-1 and Equation 4-2, the definition of the friction factor (f_P) for the packed bed can be defined as function of the Reynolds number (Re_P) or the specific differential pressure and packed bed characteristics such as final void fraction.

$$f_P = \frac{150}{Re_P} + 1.75 \; where \; Re_P = \frac{D_P V_S \rho}{(1-\varepsilon)\cdot\mu} \tag{4-1}$$

$$f_P = \frac{\Delta p}{L} \cdot \frac{D_P}{\rho V_S^2} \cdot \left(\frac{\varepsilon}{1-\varepsilon}\right) \tag{4-2}$$

Where D_P (m) is the equivalent spherical diameter of the particle defined as function of the particle volume ($V_P \; in \; m^3$) and its surface ($S_P \; in \; m^2$) as $D_P = 6\frac{V_P}{S_P}$; V_S is the superficial velocity (m/s) calculated as function of the volumetric flow rate (F) and real cross-sectional area of the bed (A); ρ and μ are the liquid density and viscosity in kg/m^3 and Pa·s, respectively (in this case approximated to water properties), ε is the specific packed bed void fraction linked to a specific differential pressure lecture (Δp in Pa); and L is the packed bed length (m) at the end of operation.

With this information, it is possible to determine the final void fraction as ratio of void volume/complete packed bed volume (ε) that matches with the experimental observed differential pressure at the end of operation (41400 Pascal equivalent to approx. 420 mBar) as expressed in Equation 4-3.

$$\Delta p = \left(\frac{150}{\frac{D_p V_S \rho}{(1-\epsilon)\mu}} + 1.75\right) \cdot \frac{\rho V_2^2}{D_P} \cdot \left(\frac{1-\varepsilon}{\varepsilon^3}\right) L \tag{4-3}$$

Therefore, experimental parameters at the end of the operation were used for the estimation of the final packed bed void fraction. According to the calculations performed, a final bed void fraction of approximately 5.7% was calculated. This low final void fraction calculated is in agreement with the experimental results

observed in the analysis of biomass concentration and the visual inspection of the packed-bed.

Table 4-3 summarizes the values used for the variables/parameters used in the determination of the void volume, as well as the specific rationale used in their determination.

Table 4-3. Variables/parameters used in the calculation of final void volume

Parameter/variable		Value	Units	Rationale
Liquid viscosity	μ	0.001	Pa·s	Estimated as water
Density	ρ	1000	kg/m³	Estimated as water
Packed bed height	L	0.426	m	Packed bed height at the end of operation. Approximately 13 cm reduction due to beads compression.
Total liquid flow rate	F	$1.51 \cdot 10^{-6}$	$\dfrac{m^3}{s}$	Input and recirculation flow rates
Packed bed section	A	0.012	m²	Packed bed section based on packed bed diameter (D)
Effective velocity	V_S	0.0001	m/s	Velocity considering real section in bed due to presence of biomass and beads
Bead diameter	D_P	0.0041	m	Value according to manufacturer (d^0)
Bead volume	V_P	$3.61 \cdot 10^{-8}$	m³	Considering beads as perfect spheres with diameter d^0
Bead surface	A_P	$5.28 \cdot 10^{-5}$	m²	Considering beads as perfect spheres with diameter d^0
RESULTS				
Estimated void fraction	ε	0.057	Void volume / total volume	Estimated parameter to adjust differential pressure
Differential pressure resultant	Δp	414	mBar	Calculated value to fit the experimental differential pressure of approx. 400 mBar

4.4.2. Estimation of packing material final diameter

As detailed in Chapter 3, the model considers a fixed number of packing beads in each reactor compartment and a packed bed height reduction due to the increase of beads packing up to a maximum theoretical packing efficiency of 26% [16].

In these conditions, the impact of beads diameter reduction was considered negligible based on the final packed bed height and theoretical final packing efficiency.

Table 4-4 summarizes the specific values regarding packed bed height at the beginning and the end of operation, estimated based on experimental evidences (approximately 13 cm reduction) and the specific dimensions of the reactor used for the calculations.

Table 4-4. Packed-bed conditions

Parameter	Initial conditions at the beginning of operation	Final conditions at the end of operation
Packed bed diameter (m)	0.125	
Packed bed height (m)	0.556	0.426 (13 cm height reduction)
Number of total beads (nº beads)	113445	
Packing efficiency (void fraction) (%)	40 (experimental)	26 (theoretical)

With this information, and considering a sphere packing efficiency is 26%, the volume occupied by the packing material at the end of the operation was estimated to be a 74% of the final volume. With this information and knowing the number of beads in the packed bed (constant at 113445 beads, Table 4-1), it was possible to calculate a final bead diameter of 0.0040 m. This value was considered equivalent to the one at the beginning of the operation (0.0041 m) and therefore, the diameter decrease due to beads compression was considered negligible in terms of the model implementation.

4.4.3. Estimation of maximum biofilm thickness

Once the volume occupied by the beads at the end of the operation (74% of the reactor volume, see section 4.4.2) and the final theoretical void fraction of the pached-bed (estimated at 5.7%, see section 4.4.1) was determined, the next step was to estimate the final biofilm thickness at the end of the operation. In this context, the specific volume of the biofilm was estimated as 20.3% of the total packed bed volume (1.06 L), corresponding to the total volume (100%) minus the beads volume (74%) and minus the real void volume (5.7%)). It should be noted that this total packed-bed reactor volume (estimated as 5.2 L) was estimated by considering a diameter of 0.125 m and a final packed bed height of 42.6 cm (See Table 4-4). With this information and considering the number of beads (nº beads = 113445) and the beads diameter (0.0041 m), biofilm thickness was estimated to be 169.3 μm. More details on the calculation of the biofilm final thickness are provided in Supplementary material 4.8.1.

4.4.4. Determination of initial quantity of biomass inoculated

In order to determine an estimation for the initial quantity (g) of biomass from each nitrifying species inoculated, specific equations that correlate the optical density of specific cell culture and number of bacterial cells in axenic cultures were used [17]. Specific correlations available in literature are summarized in Equation 4-4 and Equation 4-5.

$$\frac{N^{\underline{o}}\ Cells_{nitrosomonas}}{mL} = 1.01 \cdot 10^9 \; x \; O.D._{\cdot nitrosomonas} \qquad \text{4-4}$$

$$\frac{N^{\underline{o}}\ Cells_{nitrobacter}}{mL} = 1.779 \cdot 10^9 \; x \; O.D._{\cdot nitrobacter} \qquad \text{4-5}$$

Based on these correlations and assuming that the contribution of each species in the OD of the mixed culture is equivalent, a specific equation that correlates optical density of both species with the ratio between the number of cells of each one of the species as presented in Equation 4-6 can be developed.

$$O.D._{nitrosomonas} = \frac{1.779 \cdot 10^9}{1.01 \cdot 10^9} \; x \; O.D._{nitrobacter} \; x \; \frac{N^oCells_{nitrosomonas}}{N^oCells_{nitrobacter}} \qquad\qquad 4\text{-}6$$

As explained in section 4.2.3, inoculation was performed by using a co-culture of both species at approximately 50% contribution of each one of them in the final culture. For this reason, the ratio between the number of cells of *Nitrosomonas europaea* and *Nitrobacter winogradsky* in the inoculum can be estimated as 1. Therefore, Equation 4-6 reads now as:

$$O.D._{nitrosomonas} = \frac{1.779 \cdot 10^9}{1.01 \cdot 10^9} \; x \; O.D._{nitrobacter} \qquad\qquad 4\text{-}7$$

By taking into account the expression in Equation 4-7 and the fact that inoculum optical density was 0.43 AU (corresponding to the addition of $O.D._{nitrosomonas}$ and $O.D._{nitrobacter}$), specific O.D. contribution of each species can be estimated as 0.27 AU for *Nitrosomonas* and 0.15 AU for *Nitrobacter*.

With this information and using Equation 4-4, Equation 4-5 and the molecular weight of each species (1.6 g/cell for *Nitrosomonas* and 1.4 g/cell for *Nitrobacter* [17]), the specific cell concentration for each species can be determined as 0.03 g/L for *Nitrobacter* and 0.07 g/L for *Nitrosomonas*.

Finally, 1.9 L of this inoculum were added to 6.9 L of packed bed bioreactor (See section 4.2.3). Thus, the concentration of biomass from each species introduced in the reactor at the beginning of operation is estimated by considering 100% attachment and multiplying the concentration of each specie by the volume introduced.

Table 4-5. Specific biomass concentration at the beginning of the operation

Specie	*Nitrosomonas Europaea*	*Nitrobacter Winogradsky*
Concentration in the inoculum (g/L)	0.07	0.03
Volume of inoculum introduced (L)	1.9	1.9
Total biomass introduced in the packed bed reactor to be divided homogeneously (mg)	133	57
Concentration in the beginning of the operation (g/L)	*0.02*	*0.01*

4.5. Model validation

This section presents the results obtained during the validation of the model described in Chapter 3. In order to do that, the long-term operation of the pilot packed-bed reactor detailed in previous section (approximately 700 days operation) was used. Results obtained are presented here and consider four different aspects:

1) The fitting of nitrification profiles obtained by the model with real nitrification profiles.

2) The fitting of the visual comparison of the biofilm structure at different points during operation with results obtained with the model.

3) The fitting of the model final estimated biomass distribution profile at the end of operation in the different reactor heights with real experimental values.

4) The fitting of the reactor differential pressure profiles reproduced by the model compared to experimental evaluation.

The reliability of the model is analyzed in terms of the good fitting of the predicted values to the observed experimental data.

### *4.5.1. Nitrification profiles*

Figure 4-8 and Figure 4-9 present the experimental values of the different nitrogen-species concentrations at the top (Figure 4-8) and at the bottom (Figure 4-9) parts of the reactor previously discussed in section 4.3.1. These data are compared to the nitrogen-species concentrations predicted by the model in each case (results from n-Tank in series number 7 for Figure 4-8 and results from n-Tank in series number 1 for Figure 4-9). In all cases, a complete mass balance has been accomplished for the total nitrogen species.

The results suggest that in general terms, the model has a high capacity of describing the nitrification process pattern observed in the reactor since the fitting of predicted and experimental data at the input and output of the reactor is accurate, especially considering the long-term period considered and the different factors involved in the process. However, a certain lack of fit for the ammonium and nitrate
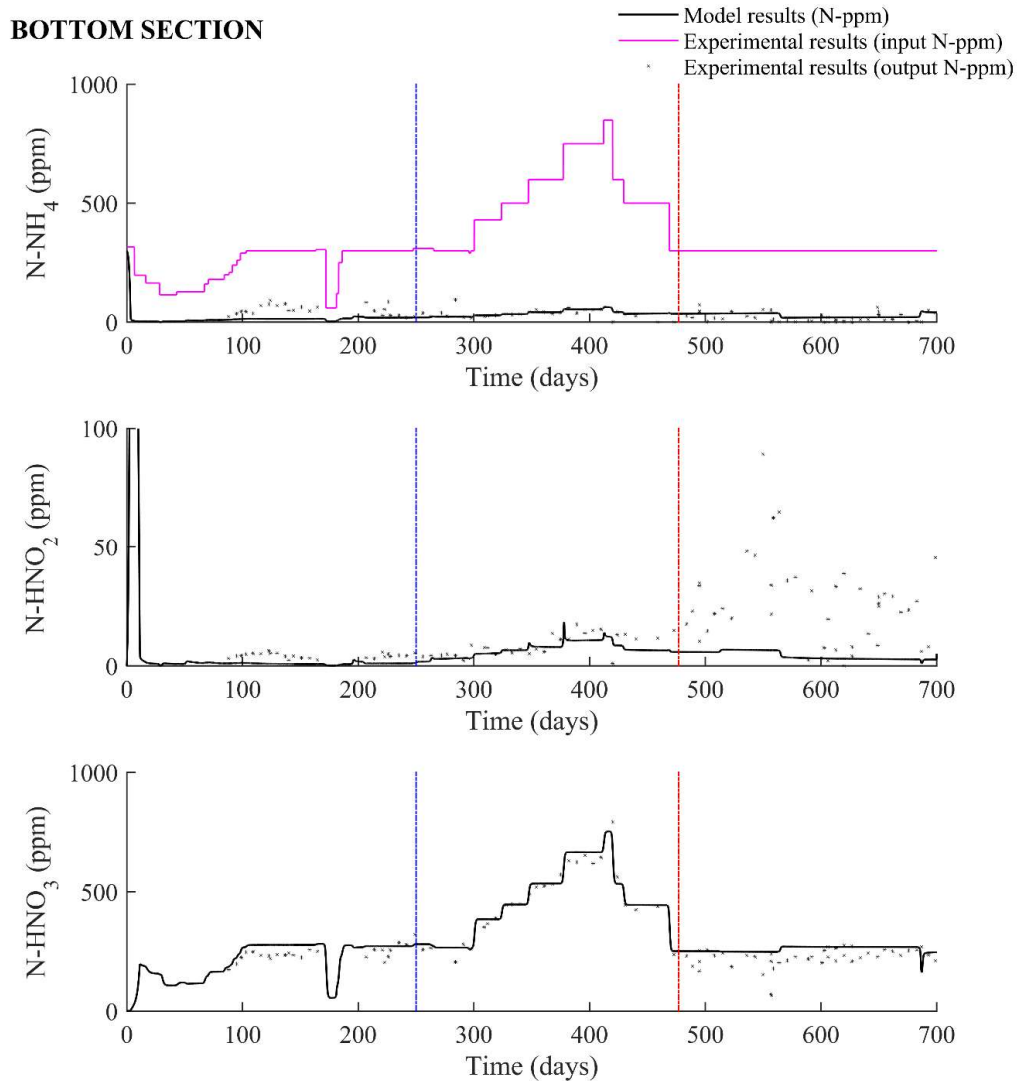
concentrations at the top of the reactor is observed in the initial period of operation. This tendency is also detected in the bottom part of the reactor. In this period (0 to 200 days), the results show that the model predicts a slightly higher nitrification capacity. This difference can be probably related to the initial attachment of the biomass into the packed-bed that is not reproduced with complete accuracy by the model.

Additionally, the model is able also to predict the presence of nitrite peaks when sudden changes of ammonium load are performed as detailed in these same figures at process culture time of 300-500 days. However, some misadjustments can be seen between the values predicted by the model and the experimental values at other culture times such as the ones corresponding to approximately 50, 200 or 650 days of culture. In this case, the peak is not predicted by the model or is predicted but with a lower value than the experimental one. This can be linked to several operational problems related to pH control and oxygen control during specially the first step of the culture (C3 compartment start-up and stand-alone characterization) where the global oxygen control system was being implemented and improved. Specific points with relevant operational incidences are mentioned in the figure caption and have been discussed in the experimental results part (see section 4.3.1). Finally, a slight misadjustment of nitrite concentration at the end of the simulation (days 500 to 700) is observed at the bottom part of the reactor. As detailed in the description of experimental data, this period is the one linked to a visually observed packed-bed height reduction and biomass accumulation on the bottom of the reactor. And also, the period where initial attempts of performing backwashing (without showing clear signs of effectivity) were initiated as a strategy to avoid possible reactor collapse. Thus, the performance of this additional manipulation of the reactor together with hydrodynamic simplifications applied to current model can be the responsible for this specific reduction in the model accuracy.

Thus, in this period of operation, the simplification implemented allows for an accurate reproduction of the global nitrification capacity but with less accuracy in the description of the reactor transition.

TOP SECTION
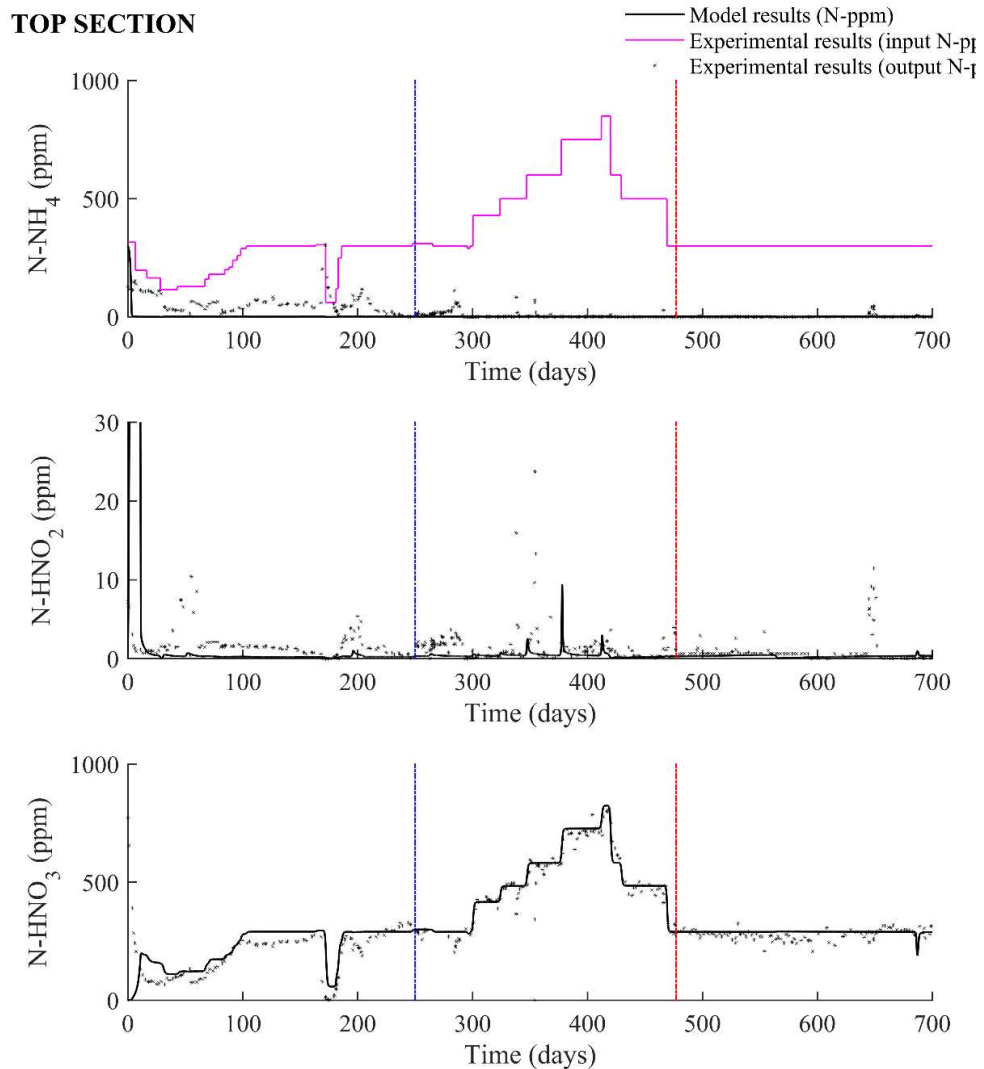
Figure 4-8. Nitrification experimental results (Top of the packed-bed) obtained during the approximately two years of operation in the pilot plant reactor compared with model predictions. In this figure, transition periods between start-up and stand-alone phases (blue) and stand-alone and WP3 phases (red) have been highlighted. In all cases, experimental results are presented in grey dots, model predicted results are shown in a black thick line. Additionally, the initial ammonium concentration at the input of the reactor is included in the ammonium top section figure with a thin pink line. Operational disturbances for the experimental data were attributed to time cultures of approximately 50, 200, 350 and 650 days. See Section 4.3.1 for a detailed explanation of these disturbances.

BOTTOM SECTION

Figure 4-9. Nitrification experimental results (Bottom of the packed-bed) obtained during the approximately two years of operation in the pilot plant reactor compared with model predictions. In this figure, transition periods between start-up and stand-alone phases (blue) and stand-alone and WP3 phases (red) have been highlighted. In all cases, experimental results are presented in grey dots, model predicted results are shown in a black thick line. Additionally, the initial ammonium concentration at the input of the reactor is included in the ammonium top section figure with a thin pink line. Operational disturbances for the experimental data were attributed to time cultures of approximately 50, 200, 350 and 650 days. See Section 4.3.1 for a detailed explanation of these disturbances.

### *4.5.2. Visual comparison on biofilm evolution*

The demonstration of the correct reproduction of the biofilm evolution in the packed-bed reactor is particularly difficult in this type of systems due to the lack of experimental data. Thus, experimental observations normally allow for a qualitatively comparison of the biofilm evolution as explained in section 4.3.2. With this objective, Figure 4-10 and Figure 4-11 summarize the model prediction of the total biomass concentrations profile in the different reactor heights during operation. These concentration profiles predictions have been compared with the real visual biomass distribution data at the same specific times.

As observed in the presented images, the profile of biomass accumulation predicted by the model is equivalent to the one visually observed during the two years operational period: initially, operation of the reactor starts with a fluffy colonization in all the available height. However, after a determined period of time, a stratification of the biomass occurs being more concentrated at the bottom part of the packed-bed. This is especially relevant at culture times higher than 500 days, as observed by experimental observation.

This visual evolution of the biofilm is in agreement with the description of the model parameters as detailed in Figure 4-11. Growth initially starts with an increase of the biofilm thickness at a low concentration (see Figure 4-11A). Once the complete biofilm thickness is reached, the model predicts a transition to a period where biofilm porosity decreases and the biofilm concentration increases up to its maximum level (see Figure 4-11B). This latter decrease of biofilm porosity is translated into a decrease of the inactive biomass detachment and the creation of an inactive layer at the internal part of the biofilm (see Figure 4-11C). This process is especially relevant in the bottom parts of the reactor.
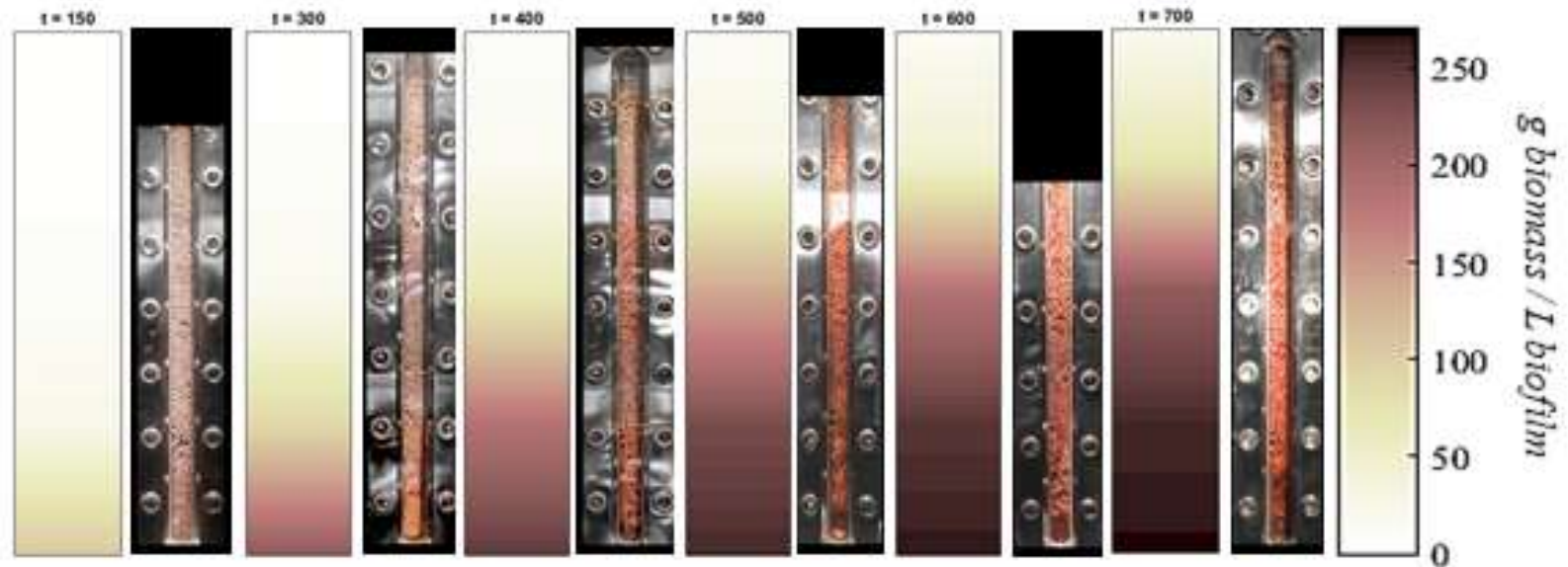
Figure 4-10. Fitting of the model predicted results and the visual comparison at different time points (t= 150, 300, 400, 500, 600 and 700 days).In each case a specific reproduction of the model (left) is compared with real image from that day in real culture. In the model results, legend for the interpretation of color distribution can be found on the right side of the picture.
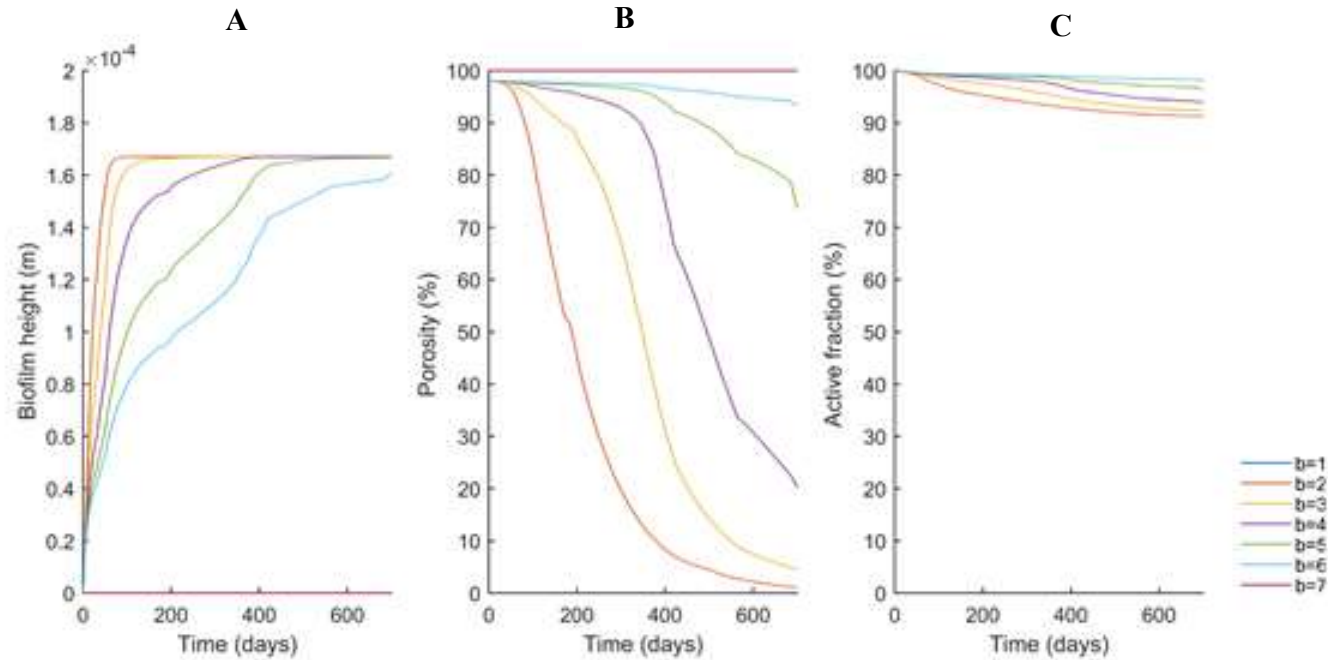
Figure 4-11. Results predicted by the model. Evolution of the main model variables describing biofilm evolution (biofilm height (A), porosity (B) and active fraction (C)) in the different n-tanks (b) described in the model definition. In this figure, b1 and b7 are the top and bottom sections of the packed-bed without packing material. Tanks b=2 to b=6 corresponds to the different volumes in which the packed bed is divided. As observed, evolution of the biofilm according to the model design implies the higher increase in porosity and inactive fraction in the bottom parts of the reactor.

4.5.3. Differential pressure evolution

The qualitatively reproduction of the biofilm evolution observed in previous section linked to the model results is also in agreement with the reproduction of the differential pressure increase during the operation (see Figure 4-12).
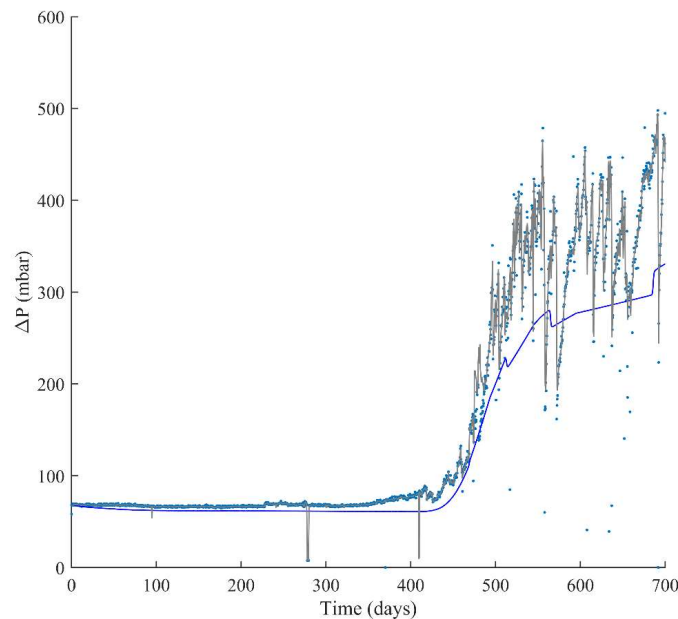
Figure 4-12. Packed-bed pressure drop comparison. Experimental results are shown as blue dots with mobile average value is represented as a black line. Model predicted results are shown in a blue line.

As explained in the experimental data discussion, the increase of differential pressure is normally linked to an increase of biomass concentration in the reactor that can lead to reactor clogging at long term operation. For this reason, having tools to anticipate this phenomenon could improve the operation of this reactor. In this context, the presented model predicts an increase of reactor differential pressure quite in agreement with the experimentally observed data, however the model does not reproduce the pattern of the experimental values at the end of the operation since it is affected by the performance of initial attempts of backwashing procedures (as already mentioned) that were not included in the model simulation.

Thus, the potential modelling of backwashing procedures in future versions of this model can improve the prediction of the reactor operation in more conditions.

In fact, this specific need to perform backwashing procedures at the end of the operation is also detected by the model regarding the distribution of different species (*Nitrosomonas*, *Nitrobacter* and inactive biomass) in the reactor height (see Figure 4-13). The predicted results show that bottom sections of the packed-bed reactor are more active than the upper sections at the beginning of the operation. However, evolution and consolidation of the biofilm in this bottom part is related to an increase of the inactive biomass content and therefore, to a concomitant increase of active microorganisms in the upper sections of the packed-bed. In this situation, the model predicts that, as observed experimentally, lower parts of the reactor will contain high amounts of biomass at the end of operation. In this situation, the performance of regular backwashing procedures could be required as a tool to revert this stratification and avoid future possible reactor clogging. Thus, this evidence supports the validity of the general strategy used for the model definition.
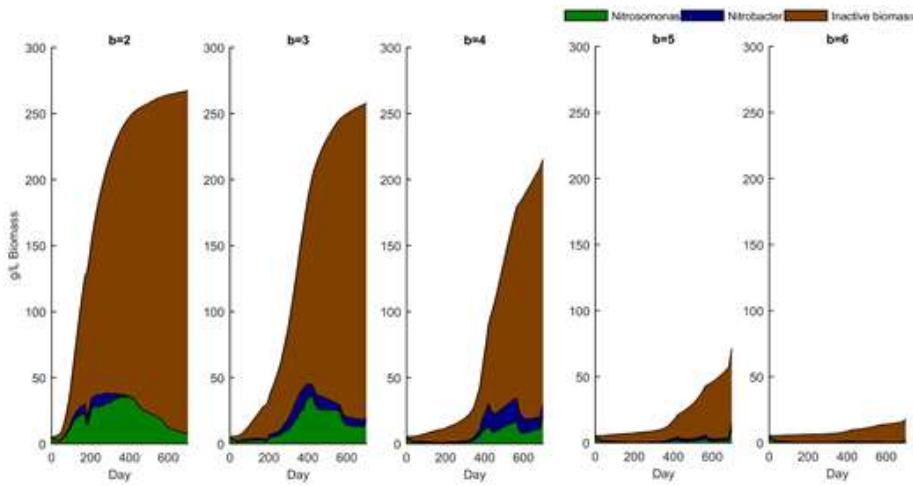
Figure 4-13. Evolution of the different species in the different packed bed reactor compartments during the 700 days of simulation. Different species are represented in the figure in different colors: Green for Nitrosomonas, blue for Nitrobacter and brown for Inactive biomass. As observed, stratification of total biomass is predicted during operation, with higher amounts of inactive biomass at the bottom parts of the reactor at the end of operation.

4.5.4. *Final biomass concentration profiles comparison*

The experimental biomass concentrations at the end of the reactor operation have been compared to results obtained with the model as a quantitative final way of comparing the fitting of biomass distribution data. As Figure 4-14 shows, values predicted by the model match reasonably well the experimental concentrations found. Thus, the correct fitting of model predictions with experimental visual observation and differential pressure evolution are corroborated by quantitatively fitting the final biomass concentrations at the end of operation. This evidence validates the general strategy used for the model definition, the quantitative capacity to reproduce experimental results and is also a proof of concept of the model validity.
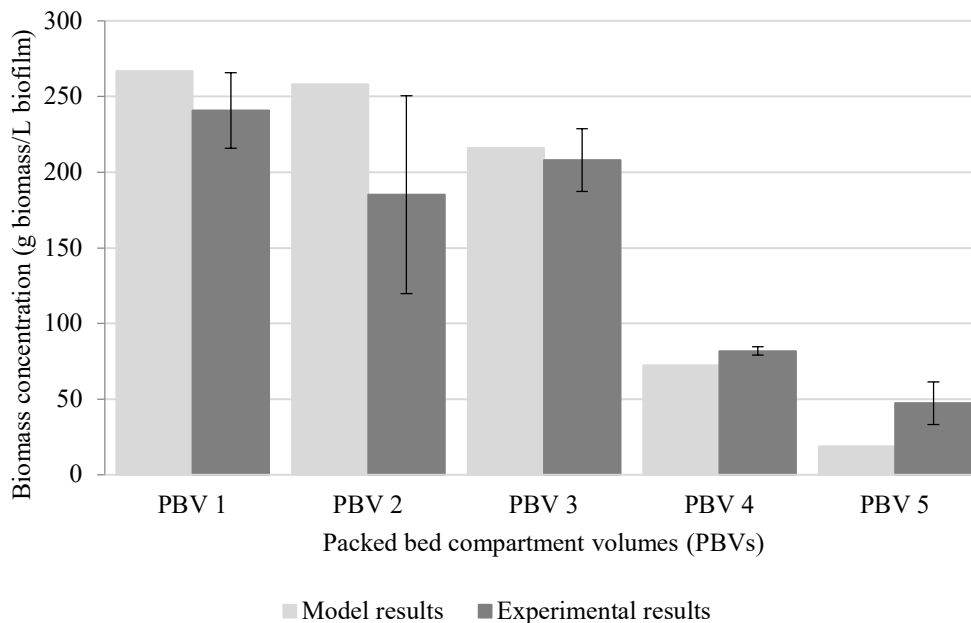
Figure 4-14. Comparison between the final biomass concentrations in the biofilm (g biomass/L biofilm) at the end of the experimental operation compared to the model predicted results).

4.6. CONCLUSIONS

In this chapter, the application of the mathematical model presented in Chapter 3 to describe the axenic operation of a nitrification packed-bed reactor during 700 days of continuous operation has been presented. In global terms, it can be concluded that the model provides an accurate representation of the experimental data, with a very good fitting in most of the period of operation. This is especially significant considering limitations of sampling linked to axenic operation of the packed-bed, particularly limiting the sampling of biofilm. Still, the model provides a plausible description of the evolution of the biofilm and its several species along the operation that in turn is coherent with the final measurements performed in the biofilm once the operation has been completed. Additionally, results of the model predict the requirement to perform backwashing procedures at the end of the operation. Thus, the use of this model for future simulations could potentially be used as a prediction of the global reactor behavior in order to avoid future reactor collapse.

Finally, the proposed model implies a reduction of the computational effort since the global biofilm evolution is correctly modelled on the basis of a macroscopic model based on a simplified calculation of the biofilm diffusion equations. For this reason, the present work presents a new simplified way to model biofilms evolution and a step forward in the biological understanding of the nitrifying compartment in the MELiSSA loop

4.7. BIBLIOGRAPHY

1. Pérez, J. Application of *Nitrosomonas* and *Nitrobacter* in biofilm form to allow for biologic nitrification in packed-bed reactors. (Universitat Autònoma de Barcelona, 2001).

2. Forler, C. *Development of a fixed bed pilot reactor for a continuous aexnic coculture of Nitrosomonas europae and Nitrobacter winogradsky.* (1994).

3. Zeghal, S. *MELiSSA Technical Note TN1 - Nitrification compartment.* (1992).

4. Walter, E. *MELiSSA internal report: Étude de la nitrifcation en condition axénique. Fixation et limitation soufre.* (1993).

5. Pérez, J., Poughon, L., Dussap, C., Montesinos, L. & Go, F. Dynamics and steady state operation of a nitrifying fixed bed biofilm reactor : mathematical model based description. *Process Biochemistry* 40, 2359–2369 (2005).

6. Montras, A. *et al.* Distribution of Nitrosomonas europaea and Nitrobacter winogradskyi in an autotrophic nitrifying biofilm reactor as depicted by molecular analyses and mathematical modelling. *Water Research* 42, 1700–1714 (2008).

7. Arnau, C., Peiro, E., Gòdia, F. & Lamaze, B. MELiSSA technical note *TN 108.3. Test Proocol for Start-up and Stand-alone characterization of CIII compartment.* (2016).

8. Arnau, C., Peiro, E., Gòdia, F. & Lamaze, B. *MELiSSA Technical Note TN 108.12. Work package III. Test Protocol.* (2017).

9. Cogne, G., Lehmann, B., Dussap, C. & Gros, C. G. Uptake of Macrominerals and Trace Elements by the Cyanobacterium Spirulina platensis (Arthrospira platensis PCC 8005) Under Photoautotrophic Conditions : Culture Medium Optimization. *Biotechnology and Bioengineering* 81, 588–593 (2003).

10. Perez, J., Montesinos, J. & Albiol, J. Nitrification by immobilized cells in a micro-ecological life support system using packed-bed bioreactors: an engineering study. *Journal of Chemical Technology and Biotechnology* 79, 742–754 (2004).

11. Laspidou, C. S. & Rittmann, B. E. Evaluating trends in biofilm density using the UMCCA model. *Water Research* 38, 3362–3372 (2004).

12. Casey, E. Tracer measurements reveal experimental evidence of biofilm consolidation. *Biotechnology and Bioengineering* 98, 913–918 (2007).

13. Arnau, C., Peiro, E. & Godia, F. *MELiSSA technical note. Test report for volumetric mass transfer coefficient (kLa) determination in C3 compartment (TN 87.2.9.).* (2012).

14. Poughon, L., Duchez, D., Cornet, J. F. & Dussap, C. G. *MELiSSA Technical note (TN-63.2).* (2002).

15. Poughon, L., Dussap, C., Perez, J., Montesinos, L. & Godia, F. Dynamics and steady state operation of a nitrifying fixed bed biofilm reactor: mathematical model based description. *Process Biochemistry* 40, 2359–2369 (2005).

16. Steinhaus, H. *Mathematical Snapshots.* (1999).

17. Farges, B. *et al.* Axenic cultures of *nitrosomonas europaea* and *nitrobacter winogradskyi* in autotrophic conditions: A new protocol for kinetic studies. *Applied Biochemistry and Biotechnology* 167, 1076–1091 (2012).

4.8. Supplementary Materials

4.8.1. Estimation of final biofilm height at the end of operation

In this section, details of specific calculations performed for the determination of final biofilm height at the end of the operation are summarized.

Table 4-6. Biofilm height at the end of the operation. Calculations

Parameter	Value	Units	Calculation
Bioreactor diameter	0.125	m	-
Initial packed-reactor height	0.556	m	-
Packed bed height reduction	0.13	m	-
Beads initial diameter	0.0041	m	-
Beads density	40000	g/m^3	
Total number of beads in the reactor	113445	-	
Sphere maximum packing efficiency	26	%	
Initial void fraction	40	%	
Final void fraction	5.7	%	
Bead volume at the end of operation	$3.41 \cdot 10^{-5}$	L	Calculated by considering the final reactor dimensions with packed bed height reduction, number of beads in the reactor and 26% sphere packing efficiency
Final biofilm volume	1.06	L	Calculated by considering the final reactor dimensions with packed bed height reduction with 5.7% void volume (beads and biofilm volume) minus the beads volume (volume of one bead x nº beads)
Bead + biofilm radius	0.00218	m	Volume of biofilm is divided by the number of beads. Then, radius of "bead+biofilm" is isolated by considering that the biofilm volume of one bead is calculated resting the volume of bead and biofilm minus the volume of the bead alone
Biofilm final height	169.3	μm	Calculated by resting the radius of the "bead+biofilm" minus the radius of the bead

4.8.2. Biofilm experimental concentration at the end of operation

In this section, specific calculations performed with experimental data at the end of operation to determine the effective biofilm volumes in the different five compartments of the packed bed are summarized. To do that, experimental void fraction of each compartment was also assessed. Specific experimental procedures used for the determination of the experimental void fraction and the final biofilm concentrations are shown in Section 4.2.6 of materials and methods section of this chapter.

In order to determine specific biofilm volume and concentration, first step was to determine experimental void fraction of the five representative sampling points in the reactor at the moment this analysis was performed. For this reason, 40 mL of solid material (beads and biofilm) were extracted and introduced to specific recipient of 40 mL. This packed material was introduced in the recipient without additional compression. Then, water was added to the recipient and the weight of water required to fill the final 40 mL volume was calculated. With this information, void fraction of specific packed bed sampling point was calculated by dividing the amount of water added by the final volume (40 mL). Table 4-7 shows the results obtained.

Table 4-7. Experimental packed bed void fraction (end operation)

Packed bed compartment volume (PBV)	Sample ID	Total volume (mL)	Volume of water added to completely fulfill 40 mL	Void fraction (fraction of non-solid volume)
1	1.1	40	14	35%
	1.2	40	14	35%
	1.3	40	12	30%
2[1]	2.1	40	15	38%
	2.2	40	15	38%
3	3.1	40	12	30%
	3.2	40	12	30%
	3.3	40	13	32%
4	4.1	40	13	33%
	4.2	40	13	33%
	4.3	40	15	38%
5[1]	5.2	40	14	31%
	5.3	40	10	30%

1- Sampling points 2.3. and 5.1. could not be analyzed due to an operational mistake in during sampling

With this experimental determination, the specific concentration of biomass in the biofilm was determined for each representative sampling point as summarized in Table 4-8. Thus, as stated in Section of materials and methods, the weight equivalent to a final volume of 15 mL of solid material was analyzed for each sampling point. Calculations performed are explained here. To do that, Sample 1.1 is taken as a reference case. In this case 785.8 mg of biomass were weighted. Then, the specific sample number of beads was calculated by considering an experimental void fraction of this sampling point of 35% (See Table 4-7), the radium of the original beads (0.0041 m), the specific biofilm height (169 μm) and the specific formula for a sphere volume. In this specific case being 225 beads.

With this number of beads, specific beads volume and weight in the 15 mL sample was assessed by considering the specific beads radium and the beads density (4000 g/m^3). Thus, the mass and volume of biofilm in this 15 mL sampling volume could be calculated by considering the weight and volume of the beads alone and the complete solid matrix of beads and biofilm. With this information, the complete biofilm volume was calculated. In this case being 228.58 mg/mL.

Table 4-8. Specific details on the calculation of experimental biofilm concentrations at the end of operation

Packed bed compartment volume (PBV)	Sample ID	Weight of total solid fraction (biomass and beads)	Exp. void fraction (%)	Exp. analyzed volume (mL)	Exp. solid volume (beads and biofilm)	Beads in 15 mL sample			Biofilm			
						Number of beads estimation	Volume (mL)	Weight (mg)	Weight (mg)	Volume (mL)	Concentration (g/L)	
1	1.1	785.8	35%	15	9.75	225	7.65	306.0	479.8	2.10	228.58	240.81±24.87
	1.2	777.1	35%	15	9.75	225	7.65	306.0	471.1	2.10	224.43	
	1.3	938.6	30%	15	10.50	242	8.24	329.6	609.0	2.26	269.43	
2[1]	2.1	574.6	38%	15	9.38	216	7.36	294.3	280.3	2.02	138.90	185.13±65.38
	2.2	761.2	38%	15	9.38	216	7.36	294.3	466.9	2.02	231.36	
3	3.1	810.9	30%	15	10.50	242	8.24	329.6	481.3	2.26	212.94	207.99±20.78
	3.2	840.1	30%	15	10.50	242	8.24	329.6	510.5	2.26	225.86	
	3.3	726.8	32%	15	10.20	235	8.00	320.2	406.6	2.20	185.19	
4	4.1	497.5	33%	15	10.05	232	7.89	315.5	182.0	2.16	84.14	81.81±2.73
	4.2	493.9	33%	15	10.05	232	7.89	315.5	178.4	2.16	82.48	
	4.3	453.3	38%	15	9.38	216	7.36	294.3	159.0	2.02	78.80	
5[1]	5.2	408.2	31%	15	10.35	239	8.12	324.9	83.3	2.23	37.40	47.30±14.01
	5.3	458.9	30%	15	10.50	242	8.24	329.6	129.3	2.26	57.21	

1) Sampling points 2.3. and 5.1. could not be analyzed due to an operational mistake in during sampling

4.8.3. Specific dimensions of the packed bed reactor

In this section a drawing of specific dimensions of the packed-bed reactor is attached

138
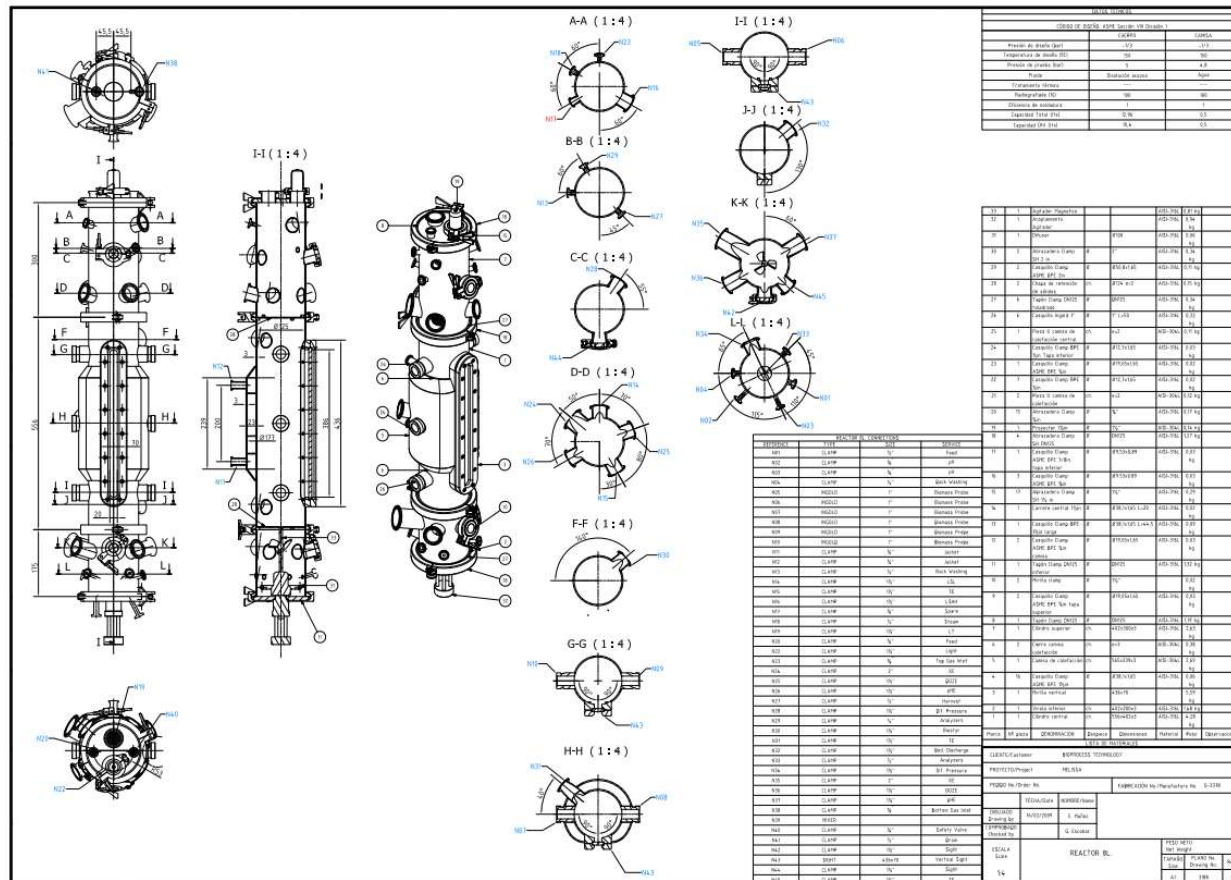
4.8.4. Specific dimensions and information on the packing material

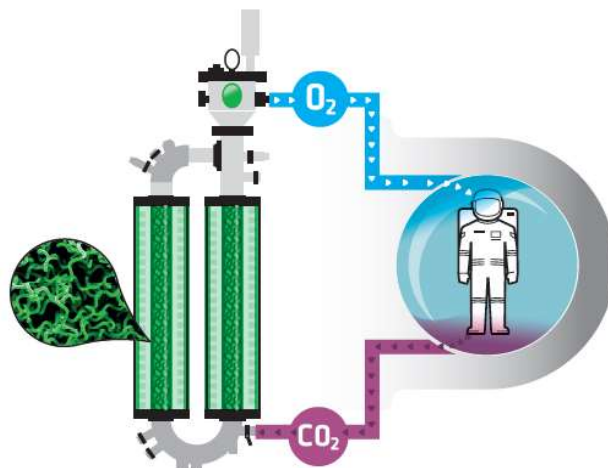In this section specific information of the packing material is provided in this section

Table 4-9. Specific characteristics of Biosty® material

Parameter	Value
Type of flow to be used	Up-flow
Support	Polystyrene
Specific gravity	0.04-0.05
Size (mm diameter)	0.0041
As (m^2/m^3)	1000

CHAPTER 5

Integration of the photobioreactor and animal compartment in gas close loop. Model description

5.1. Introduction

The work presented in Chapter 5 focuses on the development of a mathematical model of two compartments in the loop: the C4a (PBR, colonized with the cyanobacteria *Limnospira indica* [1], previously known as *Arthrospira platensis*) and the C5 (animal compartment, an isolator with rats as mock of the crew). These two compartments are used in the first integration package (WP1) where they are connected by the gas phase in a closed loop. In this integration, a specific control system is used for the control of both systems. Therefore, the mathematical model developed in this chapter includes a specific model for each compartment and also includes the basis used in the MPP control system for the control of such interphase. In this way, the series of experimental results obtained in the WP1 integration package can be used for the complete model validation presented in Chapter 6.

In this introduction, the modelling background for both PBR and animal compartments is provided.

<u>C4a modelling background</u>

Similarly to a terrestrial ecosystem, microalgae cultivation (C4a) is of high importance in the MELiSSA loop since the photosynthetic step is critical in the loop for the provision of food, oxygen and water purification together with the cultivation of plants (C4b) [2]. In the MPP, C4a design considers the use of an air-lift PBR since the use of these highly controlled closed-culture systems allows better operating conditions when compared to other alternatives [3]. The adopted external loop air-lift PBR in the MPP is a good option to provide good mixing and gas-liquid mass transfer in a hydrodynamic regime minimizing cell mechanical stress in comparison to alternative configurations like stirred tanks [4–6]. This is a very relevant aspect to maintain the required cell morphology. On top, the selected configuration, with a double glass column, allows to maximize the volume of bioreactor under illumination, a very relevant parameter in order to maximize the reactor productivity. Finally, also important for continuous operation, the bioreactor can be steam sterilized to guarantee axenic operation.

However, the complexity of these systems is relevant and this implies that their characterization and modeling require the consideration of several aspects: light distribution and availability, cell growth, and hydrodynamic aspects, such as PBR geometry, gas-liquid transfer rates, gas bubble size and mixing in order to correctly describe microalgal growth, CO_2 consumption and O_2 production. Indeed, reliable mathematical models describing the interaction between these variables are fundamental to the development of the corresponding control approaches [7,8].

This is achieved in current literature by coupling the macroscopical modelling of the photobioreactor with the microscopical reproduction of biological phenomena [9]. The first part of this modelling (macroscopical) includes a description of the PBR in terms of volumetric mass transfer coefficients and fluid hydrodynamics based on previous experimental data. Then, microscopical modelling of phenomena occurring at the cell level are also considered. These phenomena include the definition of the corresponding kinetics describing microalgae growth and physical phenomena such as light distribution in the liquid. Description of the microalgae kinetics can be performed with a basic kinetic equation (primary models: Malthusian, logistic and Gompertz models) expressing cell growth with the lowest number of parameters at their respective growth phases or dynamic kinetic equations (secondary models: Monod and Droop models) that describe microalgae cell growth dynamics as function of environmental conditions. In this category, Monod model express the kinetics of microalgae under a limited nutrient concentration environment. However, Monod model has low accuracy in predicting microalgae cell growth rate due to the high uptake of nutrients by microalgae [10]. On the contrary, Droop models relates microalgae growth rate with internal nutrients concentrations. In all cases, these kinetics can be modified to include limitations of carbon sources availability, nutrients concentration or light intensity among others [11,12]. In fact, modifications of Monod models with the integration of multiple factors allow to complete the model and achieve greater accuracy [9]. Specifically, one of the factors that can improve this accuracy is the description of the influence of light availability on microbial growth. Indeed, the efficiency of photosynthesis is directly related to the amount of light absorbed by the microalgae. Moreover, the fact that illumination is

provided externally around the glass surface of the illuminated columns and the light is absorbed by the cells growing in the liquid, create a light attenuation profile across the reactor radius. Thus, higher illuminated zones are located in the external part of the illuminated columns and lower illuminated zones are located in the inner part. This light distribution depends on the concentration of microalgae (g/L), the light transmitted in the PBR surface ($\mu mol/(m^2\ s^1)$) and the specific pigment content and shape of each specie [13]. According to literature, three different scenarios are possible regarding light adsorption in a photobioreactor: a) Photo-limited regime: where the entire photon flux transmitted is adsorbed by microalgae. This normally corresponds to cases with high microalgae residence time or concentration and causes that in part of the liquid culture, cells are in respiration metabolism instead of photosynthesis b) Strict physical limitation: where all light transmitted is absorbed but with a maximum use of the total reactor volume. Thus, maximizing the performance of the PBR, and c) Kinetic regime: where part of the light is transmitted but not absorbed, especially at low residence times or concentrations which can lead to a non-optimal use of the PBR.

Light attenuation has been represented historically by Beer-Lambert equation using a extinction coefficient representing the biomass light absorption [14]. However, this simple law does not consider the effects of light scattering by the cells. This issue was adressed by Cornet et al. [7,8] who proposed to describe light attenuation considering specific coefficients for light absorption by pigments (Ea) and light scattering by the cell (Es). With these coefficients, a fraction between light radiant energy at different points of the PBR radius and external light flux can be calculated for a cylindrical reactor geometry. Then, this light radiant energy flux is integrated into a Monod kinetic scheme to represent microalgae growth up to radiant energy levels above the compensation point (Cp), where photosynthesis becomes inefficient.

<u>C5 modelling background</u>

The possibility of future planetary bases allowing for a permanent human presence in space implies a number of challenges due to the impact of radiation and microgravity on human health [15]. For this reason, the monitoring of astronauts' health and spacecraft

habitability (temperature, air quality, lighting and noise) during space missions, is performed in high accuracy. In this aspect, the control of oxygen and carbon dioxide concentrations is especially relevant since it is a common feature that can lead to cardiovascular, neurological or immune health problems, as well as astronauts hypoxic/hypercapnic responses in toxicity levels [16,17]. This reason, and the fact that tools to potentially solve this problem can be studied in a terrestrial level are the explanation for the high monitoring of this aspect in the long-term terrestrial experiments of CELSS performed so far [18].

In this context, the MELiSSA project also considers the control of the final spacecraft habitability a priority. However, a stepwise approach of these habitability variables control with an intermediate step regarding the scale of the compartments is considered critical for the correct integration of all the technologies required for the complete loop completion at the final scale. This is the reason why MPP has been designed to provide the requirements for one human by using 60 rats as mock-up of the crew. This strategy allows for the intermediate scalability testing of the photosynthetic compartments (C4a and C4b) according to their expected contribution in the final production/consumption of oxygen by modifying the number of rats used for the experiments since rats have a respiratory quotient (RQ) similar to humans.

Additionally, the introduction of rats as mock-up of the crew allows to consider the impact of the living organisms metabolism in the operation of the loop by requiring the consideration of different zones for higher or lower oxygen consumption according to different activity of the rats [19–21]. This prevalence of daily rhythms in the metabolisms of mammals has been intensive research in the past years, with the consumption of oxygen being one of the most vital elements of these rhythms since it is primarily consumed in mitochondria through oxidative phosphorylation [22,23]. In this context, the use of rats as a simplified mock-up of the crew allows to work on the development of models that consider, in a simplified way, these activity periods in terms of oxygen consumption that are expected to be reproduced with a real human crew in a higher complexity.

Based on these studies, in this chapter, the dynamics of these rat's crew inside the C5 compartment is analyzed to determine a model to predict the estimated consumptions of oxygen and productions of carbon dioxide in a set of different oxygen target conditions defined (19-22%) by considering the compartment as a perfectly mixed reactor.

5.2. Materials and methods

The integration of the model equations with time has been implemented in MATLAB's Simulink, using the ode23tb solver with a variable timestep. This solver employs the TR-BDF2, a two-stage integration scheme: the first stage consists of an implicit Runge-Kutta algorithm with a trapezoidal rule step, while in the second stage, a backward differentiation formula of order two is considered. This method is typically used for solving stiff differential equations systems and so it is appropriate for modelling the global reactor bulk operation, for which, despite changes occur in a short timescale, the interest is on its long-term evolution.

5.3. Assumptions used for the model development

In this section, the main assumptions for specific C4a and C5 compartment model design are summarized.

5.3.1. Animal compartment.

The model proposed for the animal compartment is based on the use of potentially real crew oxygen and carbon dioxide consumption/production rates in all the activities performed during the day for a more precise adjustment of the global spacecraft oxygen consumption. In the MPP, this potential human crew is mimicked by using Laboratory Wistar rats to achieve a final total consumption of oxygen equivalent to one human. The selection of these animals to be used in the MPP was related to the fact that they are animal easy to accommodate [24] and with a similar respiratory quotient (RQ) than humans. Additionally, the higher specific oxygen intake between rats (13.5 mL/min/kg) and humans (3.51 mL/min/kg) [25,26] is due to the difference in weight. This difference is compensated in the MPP by using 60 rats to achieve the equivalent respiration needs of one human and also

145

allows for the use of a specific number of rats to test specific contribution of the different photosynthetic compartments in the loop in the global oxygen demand. Particularly, the integration of the PBR (C4a) with the animal isolator (C5) in the gas phase is expected to produce approximately the 5% oxygen of the respiration of a 20-50 years old human. Therefore, for the purpose of this integration, three rats were used to mimick this 5% oxygen requirement as detailed in Table 5-1.

**Table 5-1: Sizing of C5 compartment for WP1 integration tests**

	Rats	Humans
Age	14-30 weeks	20-50 years
Weight (approximate, kg)	0.2-0.4	50-70
Oxygen intake (mL O_2/min/kg)	13.5	3.51
Oxygen consumption (mL O_2/min)	2.7-5.4 (1 rat)	8.8-12.3 (5% body weight)
	8.1-16.2 (3 rats)	

In these conditions, the Oxygen and carbon dioxide consumption/production rates for each hour of the day were experimentally determined with three rats in C5. In order to perform the analyses, punctual data of rats' oxygen consumption and carbon dioxide production were analyzed while maintaining different oxygen set-points (19-22%) taken from the values accepted in space missions. For these analyses, the animal compartment was assumed to be a perfectly mixed reactor (see Supplementary material section 5.7.1 for more details on the calculations performed).

The obtained results are shown in Figure 5-1. The specific consumption/production rates were determined to be independent of the oxygen set-point in the range studied (19-22%). This independency indicates that in the range of oxygen tested, an increase of oxygen consumption is not observed as typically found in hypoxia situations [27]. In fact, as observed in Figure 5-1, the rats oxygen consumption profile is consistently divided in two specific periods: a high consumption activity period (20 pm to 8 am every day) and a lower consumption period (from 8 am to 20 pm every day). This pattern of consumption corresponds

to the day/night cycle established in the pilot plant for the illumination of the animal compartment and agrees with the fact that rats are nocturnal animals. For this reason, it was considered that the best approach would be to consider only two different states regarding oxygen consumption and carbon dioxide production.

This strategy allows for a simpler approach that can be potentially improved in future tests by including a more complex matrix of consumption/production coefficients to include a wider pattern of activities in the consumer compartment.
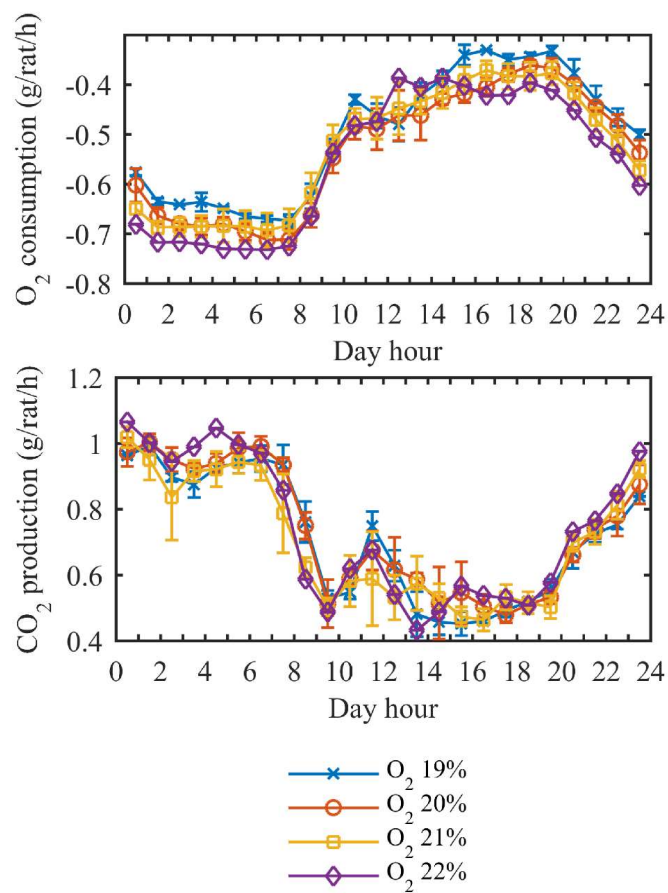
Figure 5-1. Oxygen consumption and carbon dioxide production by rats (mock crew) in the animal compartment at different oxygen set points. Blue 19% oxygen (n=2), orange: 20% oxygen (n=3), yellow: 21% oxygen (n=5), purple 22% oxygen (n=1).

A simplification of the obtained results in these 12h day/night activity periods is detailed in Table 5-2 (oxygen) and Table 5-3 (carbon dioxide) in volume or weight of compound per time and rat weight (mL/min/kg rat). Additionally, also a mean value of both oxygen consumptions and carbon dioxide production are shown in the same table, being equivalent to the mean values reported in the literature (13.5 mL O_2/min/kg [25,26] for a rat of approximately 14-30 weeks old with an average weight of 0.4 kg). Finally, reported values of RQ are also shown in the carbon dioxide table compared to the experimentally observed ones. In this case also equivalent values are obtained.

Table 5-2. Determination of rats' oxygen consumption rates

	Experimental value	Reference value
Rat weight	0.4 kg	
Night consumption (20 pm to 8 am)	0.66 g O_2/rat/h 19.3 mL O_2/min/kg	NA
Day consumption (8 am to 20 pm)	0.42 g O_2/rat/h 12.3 mL O_2/min/kg	NA
Average consumption	15.8 mL O_2/min/kg	13.5 mL O_2/min/kg

Table 5-3. Determination of rats' carbon dioxide production rates

|	Experimental value	Reference value
Rat weight	0.4 kg	
Night production (20 pm to 8 am)	0.94 g CO_2/rat/h 19.9 mL O_2/min/kg	NA
Day production (8 am to 20 pm)	0.53 g CO_2/rat/h 11.2 mL O_2/min/kg	NA
Average production	15.6 mL CO_2/min/kg	13.8 mL CO_2/min/kg
Average RQ (mol CO_2/mol O_2)	0.98	0.97 [28]

5.3.2. Photobioreactor compartment.

The characterization and modelling of photobioreactors requires the consideration of several fundamental aspects to describe microalgae growth and also carbon dioxide consumption and oxygen production [29–31]: light distribution and availability, cell growth, and hydrodynamic aspects, such as PBR geometry, gas-liquid transfer rates, gas bubble size and mixing. Figure 5-2 shows a scheme of the PBR reactor used in the MPP with a simplified description of the physical and biological aspects considered for its modelling. As mentioned earlier, the PBR used is an external loop air-lift reactor, with two glass cylindrical columns and stainless-steel connections in the upper and lower parts. Air injection is performed at the bottom of the riser column and the liquid circulation in the PBR is caused by the difference of densities with the downcomer column.

Based on this scheme, the following criteria have been used in the modelling approach of this PBR:

- Gas transfer: gas bubbles that generate the air-lift flow are injected in the lower part of the upriser column and reach the upper part of the riser column due to the difference of density between them and the liquid solution. Then, they are disengaged from the liquid at the top section of the riser. In the conditions studied, no bubbles are visually observed in the downcomer of the reactor. For this reason, the gas-liquid mass transfer required for the exchange of oxygen and carbon dioxide between the liquid and gas phases is only considered to occur in the riser column of the reactor.

- Illumination: the model considers the transfer of light to the microalgae only in the illuminated zones of the PBR corresponding to the glass columns of the riser and the downcomer. Thus, calculations of light provision as well as the performance of photosynthesis are only considered inside the cylindrical glass columns. The dark parts of the reactor are not considered to be illuminated. Additionally, the potential use of carbon source to perform respiration in these zones is not considered in the model kinetics.

No gas bubbles are present
in this part of the reactor

Air OUT

Liquid OUT

Liquid IN

Air IN

1,5 m | 2 m
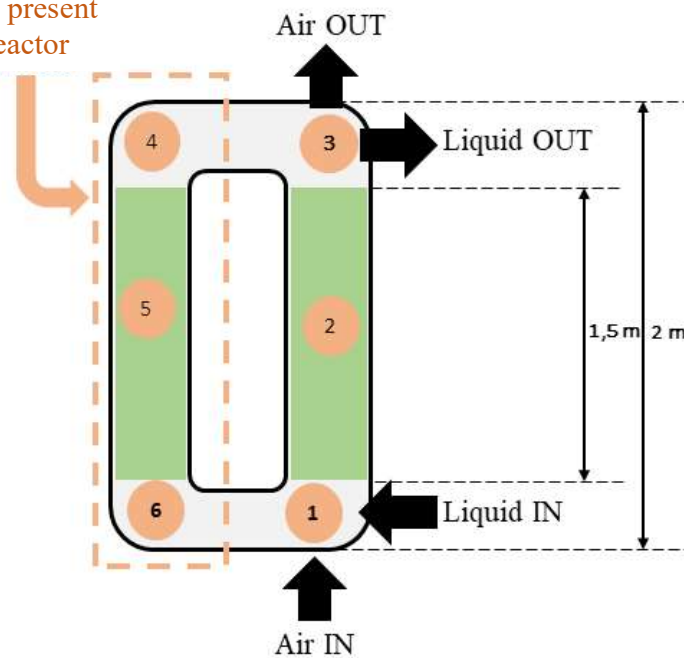
Reactor zone number						
	1	2	3	4	5	6
Reactor element	Riser			Downcomer		
Gas-liquid mass transfer	YES			NO		
Photosynthesis and growth	No	Yes	No	No	Yes	No

Figure 5-2. Description of the PBR discretization scheme applied for the simulation with specific operational characteristics to be taken into consideration. In this scheme, number 1/2/3 correspond to the areas of the riser and numbers 4/5/6 are related to the areas of the downcomer. Additionally, number 2 and 5 are the part subjected to light transference and therefore responsible to perform the photosynthesis.

150

In the sections below, the description of the model formulation is provided for the following parts: PBR light transfer (section 5.3.2.1), biomass growth kinetics (section 5.3.2.2) and hydrodynamic properties (section 5.3.2.3). Finally, the general model design is presented at the end of this section.

5.3.2.1. PBR light transfer assumptions

Light intensity transfer limitations are modeled in the PBR as described in previous work within the MELiSSA project [7,8]. This previous model was specially conceived for cylindrical PBRs with light as the limiting factor. It correlates the profile of radiant energy ($4\pi J_r$) with incident radiant flux intensity (F_r) at the external surface as defined in Equation 5-1.

$$\frac{4\pi J_r}{F_r} = 2 \cdot \frac{Bessel\ (0,r)\delta r}{Bessel(0,r)\delta R + \alpha Bessel(1,r)\delta R} \qquad \text{5-1}$$

This equation evaluates Bessel functions at different radius ($0 < r < R$) by considering the specific parameters α and δ defined in Equation 5-2 and Equation 5-3 respectively, that are function of the absorption (E_a), the scattering (E_s) coefficients and the biomass concentration (C_x).

$$\alpha = \left(\frac{E_a}{E_a + E_s}\right)^{\frac{1}{2}} \qquad \text{5-2}$$

$$\delta = [E_a \cdot (E_a + E_s)]^{\frac{1}{2}} \cdot C_x \qquad \text{5-3}$$

The specific parameters related to the PBR light transfer model for *Limnospira Indica* are provided in Table 5-6 at the end of the chapter.

5.3.2.2. Cell growth kinetics assumptions

Cell growth in the PBR has been represented by a modified Monod equation considering light intensity as the limiting substrate. To note, in the MELiSSA pilot plant PBR working conditions, inorganic carbon

concentration is more than 5 times higher (0.88-2.64 g/L) than the Monod saturation constant values published for similar cyanobacteria [32,33].

For this reason, growth has been considered to depend only on the light availability. The following equations define the complete (Equation 5-4) and simplified (Equation 5-5, considering carbon source not limiting the growth) kinetic expression used for the biomass growth. The simplified approach (Equation 5-5) has been used in the model definition according to the rationale presented.

$$r_x = C_x \mu_{max} \cdot \frac{C_{CO_2}}{K_{CO_2} + C_{CO_2}} \cdot \frac{1}{\pi R^2} \int_{R_{il}}^{R} 2\pi r \cdot \frac{4\pi J_r}{K_J + 4\pi J_r} dr \qquad 5\text{-}4$$

$$r_x = \frac{C_x \mu_{max}}{\pi R^2} \int_{R_{il}}^{R} 2\pi r \cdot \frac{4\pi J_r}{K_J + 4\pi J_r} dr \qquad 5\text{-}5$$
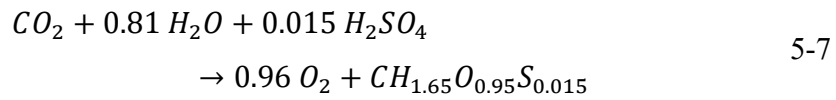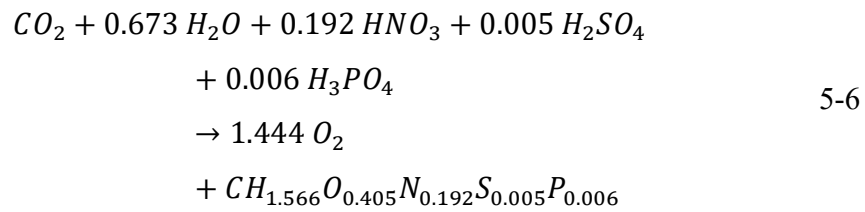
In these equations, K_J is the saturation constant for light and R_{il} is the illuminated radius of the PBR, $4\pi J_r$ is the profile of light radiant energy, μ_{max} is the maximum specific growth rate, C_x is the biomass concentration, C_{CO_2} is the concentration of carbon dioxide in the liquid phase, R is the reactor radius and r is the radial distance.

This kinetic simplified equation (Equation 5-5) is applied in the model for the calculation of the growth of *Limnospira indica.* However, this cyanobacteria cultivated in a PBR produces an exopolysaccharide in different quantities depending on the culture conditions [34].

For this reason, the current model considers two different compounds to be produced by this cyanobacteria and links the production of each compound to two different subtypes of biomass as a simplification: the active biomass (the amount of biomass of a given culture that is actively growing and it is mainly formed of proteins, lipids, carbohydrates and nucleic acids) and the inactive biomass (the amount of biomass of a given

culture that is producing exopolysaccharides that are compounds secreted by the culture into the surrounding environment).

Each subtype of biomass has their own stoichiometric equation and its own kinetic parameters in terms of light limitation (μ_{max} and K_J) that were calculated in experimental data by analyzing the content of the biomass in terms of proteins, fat, carbohydrates and exopolysaccharides in different radiant flux conditions [34]. The stoichiometric equations for both cases are detailed in Equation 5-6. and Equation 5-7 whereas kinetic parameters for the cyanobacteria growth to in each case are summarized in Table 5-6 at the end of the chapter.

$$
\begin{aligned}
CO_2 + 0.673\ H_2O &+ 0.192\ HNO_3 + 0.005\ H_2SO_4 \\
&+ 0.006\ H_3PO_4 \\
&\rightarrow 1.444\ O_2 \\
&+ CH_{1.566}O_{0.405}N_{0.192}S_{0.005}P_{0.006}
\end{aligned}
\tag{5-6}
$$

$$
\begin{aligned}
CO_2 + 0.81\ H_2O &+ 0.015\ H_2SO_4 \\
&\rightarrow 0.96\ O_2 + CH_{1.65}O_{0.95}S_{0.015}
\end{aligned}
\tag{5-7}
$$

Taking this into consideration, the model considers a total biomass variable (considering the active and inactive biomass) and a specific variable for the inactive biomass. The equations defining the growth of both variables can be found also in Table 5-7 at the end of the chapter.

5.3.2.3. Hydrodynamic characterization assumptions

An analysis of previous hydrodynamic work performed in this bioreactor at the MELiSSA Pilot Plant [35] was performed, focusing on the following parameters: a) mixing and circulation times, b) dimensionless Bodenstein number (Bo) and c) gas-liquid mass transfer rate. This section summarizes the results obtained and the main conclusions used for the mathematical model definition.

a) Mixing and circulation times determination

As detailed in previous studies [35], circulation and mixing time was studied in the gas flow rate operation range (0.75-4.25 L/min) by the introduction of an HCl pulse (see Supplementary material section 5.7.2 for more details). The obtained results are presented in Figure 5-3.
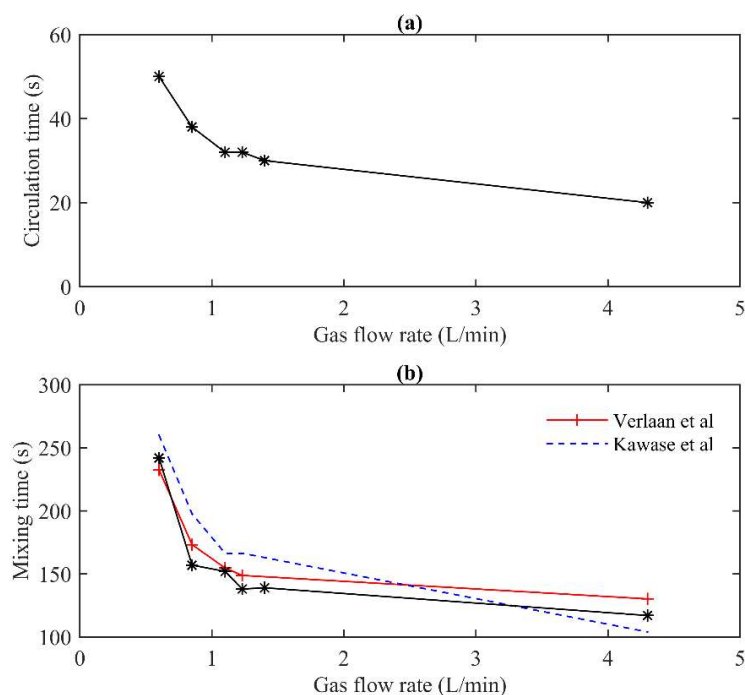
Figure 5-3. PBR hydrodynamic study. Determination of a) Circulation time (Tc) and b) Mixing time (Tm) in the operational gas flow rate studied (0.75-4.25 L/min). Operational conditions during the operation of the PBR is approximately 2.8 L/min.

As observed, Tm and Tc values are in agreement with well-established correlations [36,37] and show an exponential decay for increasing input gas flow rates reaching constant values at flow rates higher than 1.5 L/min as observed by other authors [38,39].

Based on these data, the ratio between Tm and Tc (dimensionless mixing time (DMT)) was calculated as shown in Figure 5-4. This dimensionless parameter is broadly used to evaluate the degree of mixing in air-lift PBRs. As previously reported in literature [40], this parameter typically does not depend on the gas velocity, being mainly affected by geometry and axial dispersion [41]. The results obtained show that dimensionless mixing time oscillate at an average constant value in lower gas flow rates but increases at higher gas flow rates. These results seem to show a slight decrease of axial dispersion at higher flow rates.
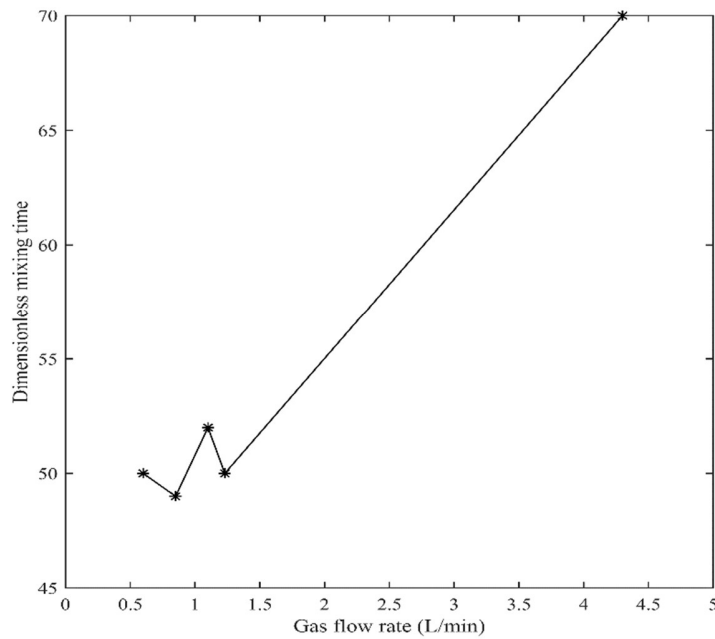
Figure 5-4. PBR hydrodynamic study. Determination of dimensionless mixing time (DMT) in the operational gas flow rate studied (0.75-4.25 L/min). Operational conditions during the operation of the PBR is approximately 2.8 L/min.

155

b) Dimensionless Bodenstein number (Bo)

PBR hydrodynamic characterization was performed by determination of the Bodenstein number (Bo) by fitting an axial dispersion-based model to the experimental data as detailed in [35]. Specific details on the dispersion model applied as well as the experimental data obtained is shown in section 5.7.2. This dimensionless number is directly related to the degree of mixing and is inversely proportional to the dispersion. The Bo number tends to zero for complete mixing while its value increases as the flow pattern approaches an ideal plug-flow behavior.

The Bo number is described as detailed in Equation 5-8 where "v" is the liquid velocity ($m \cdot s^{-1}$), "L" is the characteristic length (m) and "D" the dispersion coefficient ($m^2 \cdot s^{-1}$).

$$Bo = (v \cdot L) \cdot D^{-1} \qquad \qquad \text{5-8}$$

The results obtained are shown in Figure 5-5. As a general rule, a perfect mixing is considered when values of Bo below 20 are obtained [40] while values higher than 20 tend to describe a decrease in the axial dispersion of the reactor. It should be noted that this figure is also representing the previous DMT data detailed in the previous section since both parameters are related to the study of axial dispersion in the PBR.

The results obtained with the analysis of this dimensionless number reflect the same conclusions obtained with the analysis of DMT distribution in the gas flow rate studied: lower values of gas flow rate oscillate in an average of Bo numbers around 45. This number is slightly higher than the stablished limit for perfectly mixed reactors. However, it still reflects a good degree of mixing of the reactor. Additionally, values of Bo number obtained increase in higher flow

rates up to 60 and therefore, a decrease of the mixing and axial dispersion is also observed at this higher flow rates.
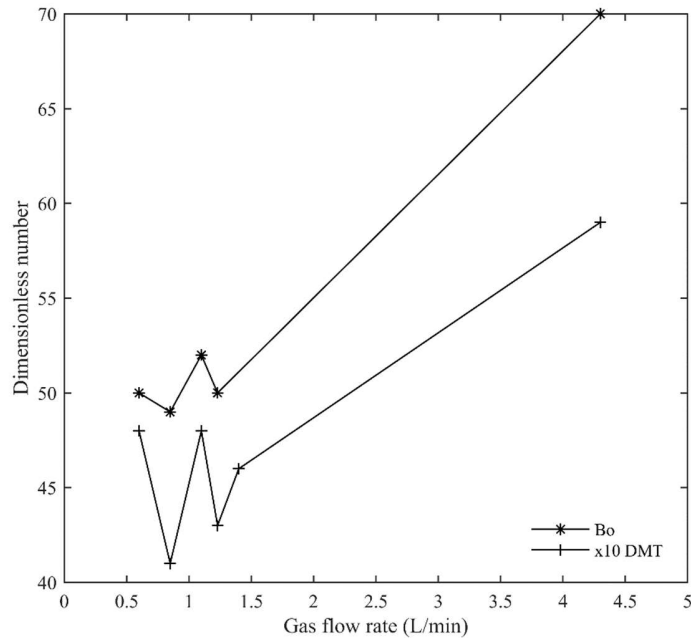
Figure 5-5. PBR hydrodynamic study. Determination of dimensionless mixing time (DMT) and Bo number in the operational gas flow rate studied (0.75-4.25 L/min). Operational conditions during the operation of the PBR is approximately 2.8 L/min.

It should be noted that, in general, comparisons between the gas-lift reactor in this study and in earlier work in the literature are somewhat difficult; the reactor used in this work offers unique characteristics due to its function, particularly a very low superficial gas velocity and an external loop geometry with both columns of equal diameters, intended to maximize the ratio of illuminated to total volume in the photobioreactor. It should be mentioned here that in many cases, external loop airlift bioreactors are built with different diameters for riser and downcomer. Nevertheless, a similar case was previously reported [41] in which an airlift with columns of equal diameter and lower velocity was designed (0.002-0.01 m/s). The hydrodynamic

results obtained in both reactors are comparable. In fact, the mixing degree was almost equal when the mentioned PBR was optimized by means of swirling flow induction. However, for the same Bo values, circulation and mixing times obtained in this reactor are approximately four times lower. Based on this comparison, the results point out that while the mixing degree in [41] was achieved by increasing the axial and radial dispersion by swirling flow induction, the current reactor geometry with low frictional loss allows the same mixing degree optimizing the bulk flow inside the reactor.

c) Residence time distribution

The distribution of residence time was determined by injecting a pulse of acid [35] into the photobioreactor and analyzing the proton concentration at the outlet, in continuous operation mode with a liquid flow rate of 2.8 L/h and aeration gas flow of 1.2 L/min (See section 5.7.2 for more detailed information of the experimental determination of this parameter). The obtained results are shown in Figure 5-6.

The obtained results reflect the behavior of the reactor as a correctly mixed reactor. The most plausible cause for this well-mixed behavior is probably the notable difference between the reactor circulation time (20-50 seconds range) and the residence time (approximately 28 hours). It should be noted that this well mixed behavior is observed at a lower gas flow rate where the results of dimensionless parameters also showed better mixing results but considered representative of real operational conditions due to the small difference in Bo and DMT values shown in the analysis.
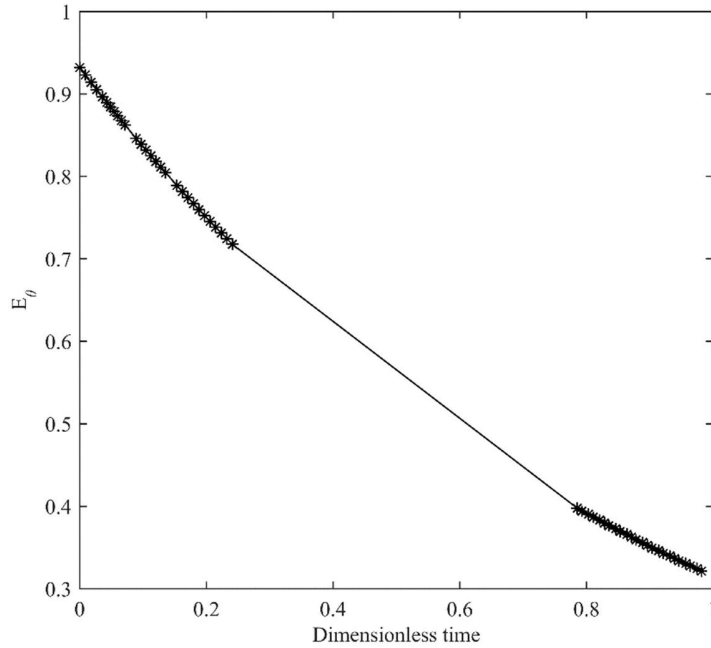
Figure 5-6. PBR hydrodynamic study. Determination of the residence time distribution (liquid flow rate 2.8 L/h, gas flow rate 1.2 L/min). In this graphic, dimensionless time is calculated by dividing the time by the residence time and the values in Y axis correspond to the normalized tracer concentration by considering the quantity injected.

d) Gas-liquid mass transfer term

The description of the gas-phase transport rates is defined in the proposed model based on conventional $k_l a$ treatment as described in Equation 5-9.

$$N = k_l a \cdot (C^* - C_L) \qquad\qquad 5\text{-}9$$

where N is the mass transfer rate from one phase to another, k_{la} is the mass transfer coefficient, C^* is the saturation concentration of dissolved species in the liquid calculated based on Henry's law and their partial pressure in the gas phase [42] and C_L is the molar concentration of the species in the liquid phase.

159

This coefficient is determined experimentally in the pilot plant PBR for oxygen and then estimated as a 0.91 [43,44] proportion of the value established for oxygen in the case of carbon dioxide. Additionally, for the carbon dioxide case, the specific carbon dioxide concentration in the liquid phase will be calculated from the equivalent concentration of carbon dioxide from all inorganic carbon forms, the equilibrium constants, pH and temperature [45].

Specific experimental determination of oxygen gas liquid mass transfer coefficient (k_{la}) values for oxygen in the air-lift PBR determined by the dynamic method [37] are shown in Figure 5-7. The results obtained could be interpreted with a linear dependency as function of gas flow rate ($k_{la} = 0.5257 \cdot x^{0.8484}, R^2 = 0.987$ where x is the gas velocity in m/s. See Supplementary materials section 5.7.2 for a more detailed information on the experimental performed).
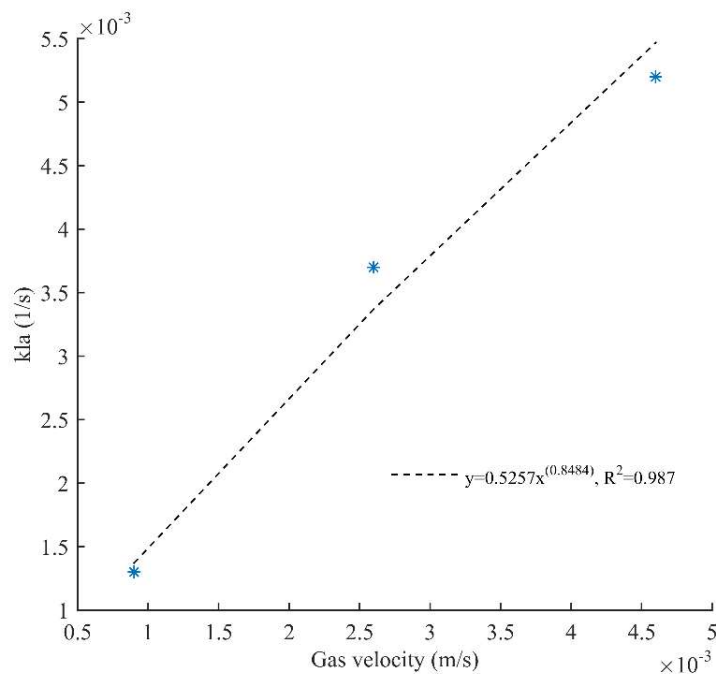

Figure 5-7. Experimental determination of gas liquid mass transfer for oxygen in different gas flow rates.

160

The analyses of all the parameters above mentioned show that the PBR has the behavior of a well-mixed tank in the liquid phase for all the gas flow-rate conditions evaluated. However, the analysis of the reactor flow also points to a slight decrease in the axial dispersion at higher gas flow rates. Therefore, if only the liquid phase of the reactor needs to be simulated, a perfectly mixed tank would probably provide a good reactor description. However, the present reactor has also a gas phase that is bubbling in the riser part of the reactor where a gas-liquid mass transfer is being performed. Thus, this particular case needs to be taken into consideration in the global reactor model since the consideration of this gas phase implies certain characteristics of plug flow since the experimental concentrations for O_2 and CO_2 in the gas phase decrease/increase from the bottom to top of the riser column where most of the gas-liquid transfer takes place, according to experimental measurements.

For this reason, the proposed model includes a PBR discretization (see Figure 5-8) in a low number of N-tanks in series (n=22) to allow for the liquid mixing and the gas phase plug flow reproduction in the riser part of the PBR.

Additionally, this discretization also allows for the differentiation of specific illuminated/non illuminated zones and gas-transfer/non gas-transfer zones in the different N-tanks of the model. As detailed in Figure 5-8, the N-tanks corresponding to dark zones in the PBR are modelled as non-illuminated (estimated as 36% of the total reactor volume) without cyanobacteria growth whereas the N-tanks corresponding to the downcomer side of the PBR do not consider the presence of gas bubbles and therefore gas-liquid mass transfer.
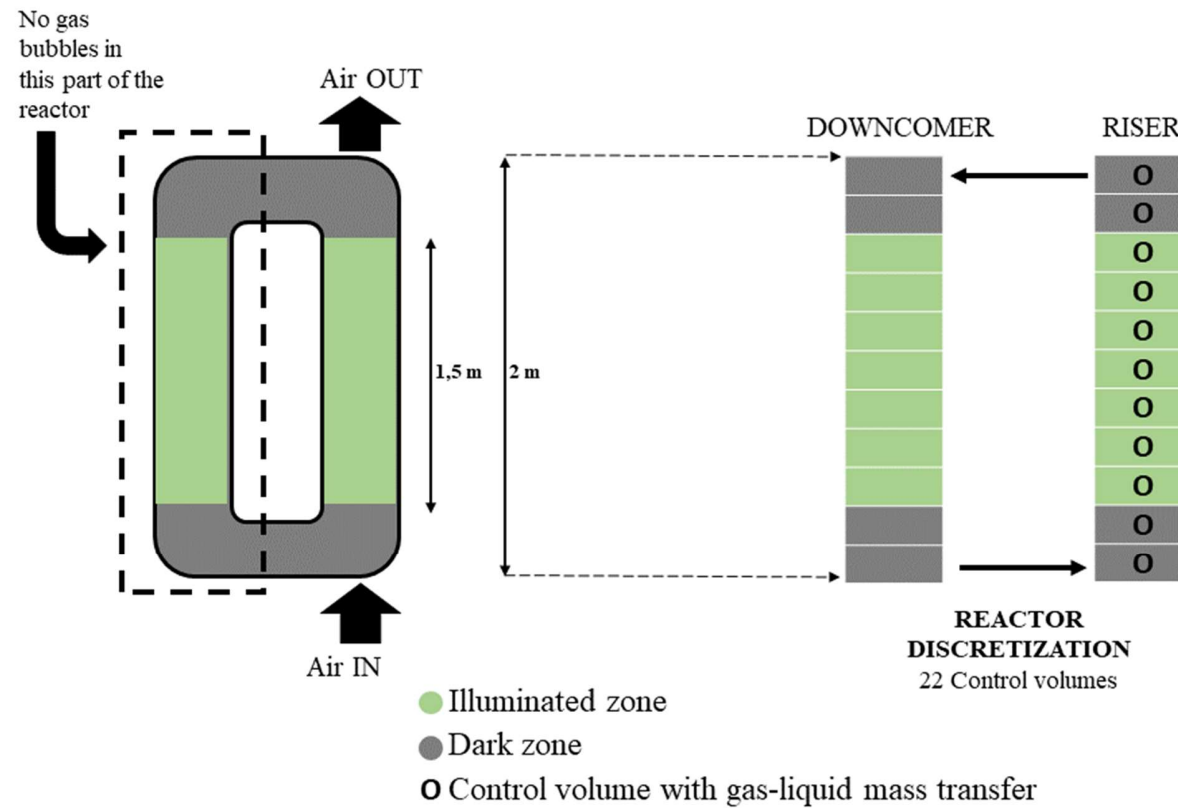
Figure 5-8. Scheme of the discretization proposed for the PBR modelling. Grey zones correspond to non-illuminated zones of the PBR whereas green zones correspond to illuminated zones of the PBR. In the right part of the picture, the theoretical scheme of the PBR is described in the N-Tanks in series discretization where tanks with gas-liquid mass transfer are highlighted with a circle.

5.3.3. Control system

A model based predictive control architecture was designed for the MPP with a master-slave control scheme to manipulate the light in the PBR compartment so that the desired setpoint of oxygen in the animal compartment was reached. Specifically, the master controller manipulates the PBR oxygen setpoint according to an animal compartment setpoint value. Then, the light intensity in the PBR is manipulated in the slave controller to regulate the oxygen concentration in the PBR. The specific mechanism of action of this controller is detailed in Figure 5-9. The control system designed for the MPP was applied to the proposed model to allow the reproduction of the observed intercompartment dynamics.
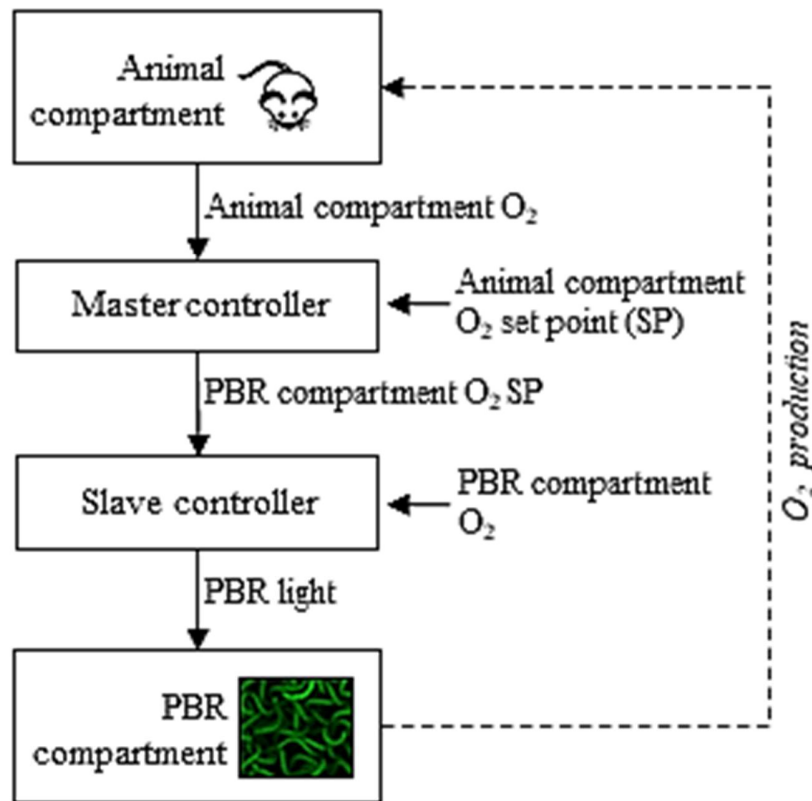
Figure 5-9. Simplified block diagram of the control system implemented in the integration tests of C4a and C5

5.4. Mathematical development

This section describes the mathematical development performed of the specific equations of the proposed model.

5.4.1. Animal compartment (C5)

The animal compartment was modeled as a single reactor in which a global mass balance was performed considering the active-inactive consumption coefficients obtained from the experimental data as explained in Section 5.3.1. The definition of the coefficients used can also be found in at Table 5-4.

In these conditions, the mass balance is provided in Equation 5-10.

$$\frac{\partial x_i}{\partial t} V = F_{in} \cdot x_{i_{in}} - F_{out} \cdot x_i + C_i \cdot N \qquad \text{5-10}$$

where V is the animal compartment volume, x_i is the species concentration in mol/L, $x_{i_{in}}$ is the species concentration at the inlet in mol/L, F_{in} is the animal compartment input flow in L/h, F_{out} is the output flow in L/h, C_i is the species consumption/production rate in mol/(rat·h) and N the number of rats.

The main parameters used for the model are provided in Table 5-4 whereas the final equations considering the main species (O_2 and CO_2) that describe the animal compartment model are provided in Table 5-5.

Table 5-4. Description of parameters related to animal compartment's model

Parameter	ID	Units	Value	Source
Volume	V	L	1600	Experimental
Carbon dioxide production coefficient (active)	$C_{active_{O_g}}$	g CO_2/(rat·h)	0.94	Detailed in the model based on experimental evidence
		mol CO_2/(rat·h) x 1000	21.4	
Carbon dioxide production coefficient (inactive)	$C_{inactive_{O_g}}$	g CO_2/(rat·h)	0.53	
		mol CO_2/(rat·h) x 1000	12.0	
Oxygen consumption coefficient (active)	$C_{active_{C_g}}$	g O_2/(rat·h)	0.66	
		mol CO_2/(rat·h) x 1000	20.6	
Oxygen consumption coefficient (inactive)	$C_{inactive_{C_g}}$	g O_2/(rat·h)	0.42	
		mol CO_2/(rat·h) x 1000	13.1	

Table 5-5. Equations applied to animal compartment

Variable			Equation
Oxygen (gas)	O_g	Active condition	$$\frac{\partial O_{g_a}}{\partial t}V = F_{in} \cdot O_{g_{in}} - F_{out} \cdot O_g + C_{active_{O_g}} \cdot N$$
		Inactive condition	$$\frac{\partial O_{g_i}}{\partial t}V = F_{in} \cdot O_{g_{in}} - F_{out} \cdot O_g + C_{inactive_{O_g}} \cdot N$$
Carbon dioxide (gas)	C_g	Active condition	$$\frac{\partial CO_{2_{g_a}}}{\partial t}V = F_{in} \cdot CO_{2_{g_{in}}} - F_{out} \cdot CO_{2_g} + C_{active_{C_g}} \cdot N$$
		Inactive condition	$$\frac{\partial CO_{2_{g_i}}}{\partial t}V = F_{in} \cdot C_{g_{in}} - F_{out} \cdot C_g + C_{inactive_{C_g}} \cdot N$$

5.4.2. Photobioreactor model (C4a)

One-dimensional finite volume discretization of the PBR was performed solving the mass balance equation for each species in each of the 22 N-Tank in order to model the partial plug flow behavior. It should be noted that axial dispersion was neglected during the development of equations according to the previous hydrodynamic study in order to simplify the model resolution. Thus, the general equation solved for each N-Tank (k) and each species (i) corresponds to Equation 5-11.

$$
\int_{V^{(k)}} \frac{\partial x_i^{(k)}}{\partial t} dV = \int_{S_{in}^{(k)}} v x_i^{(k-1)} dS - \int_{S_{out}^{(k)}} v x_i^{(k)} dS
$$
$$
+ \int_{V^{(k)}} R_i^{(k)}\left(x_j^{(k)}\right) dV \qquad \text{5-11}
$$
$$
+ \int_{V^{(k)}} T_i^{(k)}\left(x_j^{(k)}\right) dV
$$

where $V^{(k)}$ is the k-th N-Tank's volume, $S_{in}^{(k)}$ is the N-Tank's flow input area, $S_{out}^{(k)}$ is the N-Tank's flow output area, $x_i^{(k)}$ is the concentration of the species i in the N-Tank k, t is the time variable, v is the flow velocity (assumed constant), $R_i^{(k)}\left(x_j^{(k)}\right)$ is a function describing the reaction term and $T_i^{(k)}(x_j^{(k)})$ is a function describing the gas-liquid transfer term.

Table 5-6 shows the definition of model parameters related to PBR model. Table 5-7 summarizes the model reaction and gas-liquid mass transfer functions as well as the main model variables (active biomass (X), inactive biomass (X_{eps}), oxygen concentration in the liquid or gas phase (O_l or O_g), carbon dioxide in the gas phase (C_g) and the equivalent carbon dioxide in the liquid from the main inorganic forms of carbonate, bicarbonate and carbon dioxide (C_l), calculated according to the equilibrium constants, temperature and pH [45]).

Table 5-6: PBR model parameters definition

Parameter		ID	Units	Origin
Physical characteristics of the PBR	Photobioreactor radius	R	m	0.038
	Photobioreactor liquid volume	$V_{iliquid}$	L	83
	Photobioreactor gas volume	V_{igas}	L	0.83
PBR light transfer	Absorption mass coefficient	E_a	m²/kg	150 [46]
	Scattering mass coefficient	E_s	m²/kg	200 [46]
Gas-liquid mass transfer	Oxygen gas-liquid mass transfer constant	k_{la}	1/h	Figure 5-7
Kinetic of subtypes of biomass	Active biomass maximum growth constant	μ_{maxX}	1/h	0.073 [46]
	Light saturation constant for active biomass	K_{Jx}	W/m²	20 [46]
	Stoichiometric coefficients	h_{C_l}, h_X, h_{O_l}	Calculated based on growth equations defined in Equation 5-6	
	Inactive biomass maximum growth constant	$\mu_{maxXeps}$	1/h	0.3 [46]
	Light saturation constant for inactive biomass	K_{Jxeps}	W/m²	750 [46]
	Stoichiometric coefficients	$h_{C_l}, h_{X_{eps}}, h_{O_l}$	Calculated based on growth equations defined in Equation 5-7	

Table 5-7: PBR model variables and reaction ($R_i^{(k)}(x_i)$) and gas-liquid transfer ($T_i^{(k)}(x_i)$) term associated description

Variable		Equation	
Total biomass (addition)	X	$-(\mu_{maxX} \cdot (X - X_{eps}) \cdot \frac{1}{\pi R^2} \int_{R_{il}}^{R} 2\pi r \cdot \frac{4\pi J_r}{K_{Jx} + 4\pi J_r} \, dr + \mu_{maxXeps} \cdot X_{eps} \cdot \frac{1}{\pi R^2} \int_{R_{il}}^{R} 2\pi r \cdot \frac{4\pi J_r}{K_{Jxeps} + 4\pi J_r} \, dr$	$R_i^{(k)}(x_i)$
Non-active biomass	X_{eps}	$(\mu_{maxXeps} \cdot X_{eps} \cdot) \cdot \frac{1}{\pi R^2} \int_{R_{il}}^{R} 2\pi r \cdot \frac{4\pi J_r}{K_{Jxeps} + 4\pi J_r} \, dr \cdot$	$R_i^{(k)}(x_i)$
Carbon dioxide estimated as an equivalent from all the inorganic forms available (liquid)	C_l	$\frac{-h_{C_l}}{h_X} \cdot \mu_{maxX} \cdot (X - X_{eps}) \cdot \frac{1}{\pi R^2} \int_{R_{il}}^{R} 2\pi r \cdot \frac{4\pi J_r}{K_{Jx} + 4\pi J_r} \, dr \cdot - \frac{h_{C_l}}{h_{X_{eps}}} \cdot \mu_{maxXeps} \cdot X_{eps}$ $\cdot \frac{1}{\pi R^2} \int_{R_{il}}^{R} 2\pi r \cdot \frac{4\pi J_r}{K_{Jxeps} + 4\pi J_r} \, dr$	$R_i^{(k)}(x_i)$
		$k_{la} \cdot 0.91 \cdot \left(\frac{C_g}{K_i} \cdot 55.555 - \frac{C_l}{frac}\right)$ where $Frac = \frac{K1(T)}{10^{-pH}} \cdot \left(1 + \frac{K3(T)}{10^{-pH}}\right)$ K1(T) and K3(T) are the equilibrium constants for the reactions of the carbon dioxide-carbonate-bicarbonate equilibrium calculated as function of temperature [45]	$T_i^{(k)}(x_i)$
Oxygen (liquid)	O_l	$\frac{-h_{O_l}}{h_X} \cdot \mu_{maxX} \cdot (X - X_{eps}) \cdot \frac{1}{\pi R^2} \int_{R_{il}}^{R} 2\pi r \cdot \frac{4\pi J_r}{K_{Jx} + 4\pi J_r} \, dr \cdot + \frac{-h_{O_l}}{h_{X_{eps}}} \cdot \mu_{maxXeps} \cdot X_{eps}$ $\cdot \frac{1}{\pi R^2} \int_{R_{il}}^{R} 2\pi r \cdot \frac{4\pi J_r}{K_{Jxeps} + 4\pi J_r} \, dr \cdot$	$R_i^{(k)}(x_i)$
		$k_{la} \cdot \left(\frac{O_g}{K_i} * 55.555 - O_l\right)$	$T_i^{(k)}(x_i)$
Carbon dioxide (gas)	C_g	$k_{la} \cdot 0.91 \cdot \left(\frac{C_g}{K_i} - \frac{C_l}{frac}\right) \cdot \frac{V_{iliquid}}{V_{igas}}$	$T_i^{(k)}(x_i)$
Oxygen (gas)	O_g	$k_{la} \cdot \left(\frac{O_g}{K_i} - O_l\right) \cdot \frac{V_{iliquid}}{V_{igas}}$	$T_i^{(k)}(x_i)$

The main process variables are active biomass (X), inactive biomass (X_{eps}), equivalent carbon dioxide concentration in the liquid phase from all of the total inorganic forms (C_l), carbon dioxide concentration in the gas phase (C_g) and oxygen concentration in the liquid or gas phase (O_l or O_g). b) Illuminated radius (R_{il}) is defined as the photobioreactor radius where the light reaches the compensation point and ($4\pi J_r$) is the profile of light radiant energy determined according to [7,8].

5.4.3. Control system implementation

As detailed in section 5.3.3, the specific control system designed for the MPP was applied to the final proposed model to allow for the reproduction of the observed intercompartment dynamics. This model is based in the predictive control architecture and contains a master-slave control scheme. Master controller manipulates the PBR oxygen setpoint according to an animal compartment setpoint value. Then, the light intensity in the PBR is manipulated in the slave controller to regulate the oxygen concentration in the PBR.

For each controller, a reference trajectory is computed by a first order system with a closed loop response time (CLRT). This CLRT is the specification requested to the controller to achieve 95% of the process variable change to reach a defined setpoint. This reference trajectory is then compared to a first order prediction model defined as a representation of the behavior between the manipulated and process variable with a model gain (KM) and a time constant (T.C.). The slave controller required application of a conversion from the light intensity output in (%) to the current units used in the PBR model (W/m^2). It should be noted that the parameters used for each control system are those used currently in the MPP and summarized in Table 5-8. As observed, the time constants and CLRT for the slave controller are markedly lower than the those for the master controller. These differences are related to the efficiency of the photosynthetic conversion of CO_2 into O_2 and the difference in compartment volumes.

169

Table 5-8: Control system parameters definition

	Parameter	ID	Units	Value	Source
Master control	Closed Loop Response Time (CLRT)	CLRT	h	7	Current values in the MPP
	Model gain (KM)	KM	$\dfrac{\Delta O_2\ crew\ comp.\ (\%)}{\Delta O_2 PBR\ (\%)}$	1	
	Time constant (T.C.)	T.C.	h	9	
	Manipulated variable (O$_2$ PBR) maximum	M.V.max	%	18	
	Manipulated variable (O$_2$ PBR) minimum	M.V.min	%	25	
Slave control	Closed Loop Response Time (CLRT)	CLRT	min	20	
	Model gain (KM)	KM	$\dfrac{\Delta O_2 PBR\ (\%)}{\Delta\ light\ (\%)}$	0.028	
	Time constant (T.C.)	T.C.	h	0.15	
	Manipulated variable (O$_2$ PBR) maximum	M.V.max	%	95	
	Manipulated variable (O$_2$ PBR) minimum	M.V.min	%	0	

5.5. Conclusions

Accurate mathematical models describing the different elements of a biological life-support system can provide very valuable tools supporting their continuous operation under appropriate control strategies. In this chapter, a mathematical model to describe the operation of two of the compartments in the MELiSSA system has been developed: the animal compartment hosting rats and the photobioreactor colonized with *Limnospira indica* culture. This model is based on the observations made in the configuration and characterization of both compartments at the MPP and the characteristics of the two biological systems. It also considers the critical phenomena involved in their operation and the control component that regulates the change in the PBR operation to provide the oxygen needs in the animal compartment. In the next chapter, the accuracy of the model in the description of the results obtained in experimental campaigns at the MPP will be tested to provide a proof of concept of the validity and reliability of the proposed model.

5.6. Bibliography

1.   Nowicka-krawczyk, P., Mühlsteinová, R. & Hauer, T. Detailed characterization of the Arthrospira type species separating commercially grown taxa into the new genus *Limnospira* (Cyanobacteria). *Nature* Scientific, 1–11 (2019).

2.   Hendrickx, L. *et al.* Microbial ecology of the closed artificial ecosystem MELiSSA (Micro-Ecological Life Support System Alternative): Reinventing and compartmentalizing the Earth's food and oxygen regeneration system for long-haul space exploration missions. *Research in Microbiology* 157, 77–86 (2006).

3.   Wang, B., Lan, C. Q. & Horsman, M. Closed photobioreactors for production of microalgal biomasses. *Biotechnology Advances* 30, 904–912 (2012).

4.   Brennan, L. & Owende, P. Biofuels from microalgae — A review of technologies for production , processing , and extractions of biofuels and co-products. *Renewable and Sustainable Energy Reviews* 14, 557–577 (2010).

5.   Misra, N., Panda, P. K., Parida, B. K. & Mishra, B. K. Way forward to achieve sustainable and cost-effective biofuel production from microalgae: a review. *International Journal of Environmental Science and Technology* 13, 2735–2756 (2016).

6.   Pruvost, J., Cornet, J.-F. & Pilon, L. Large-scale production of algal biomass: Photobioreactors. in *Algae Biotechnology* (eds. Chisti, Y. & Bux, F.) 41–66 (2016).

7.   Cornet, J. F., Dussap, C. G., Gros, J. B., Binois, C. & Lasseur, C. A simplified monodimensional approach for modeling coupling between radiant light transfer and growth kinetics in photobioreactors. *Chemical Engineering Science* 50, 1489–1500 (1995).

8.   Cornet, J. F., Dussap, C. G. & Dubertret, G. A structured model for simulation of cultures of the cyanobacterium *Spirulilna platensis* in Photobioreactors: I. Coupling between light transfer and growth kinetics. *Biotechnology and Bioengineering* 40, 817–825 (1992).

9.   Khoo, C. G., Lam, M. K. & Lee, K. T. Chapter 1 - Microscale and macroscale modeling of microalgae cultivation in photobioreactor: A review and perspective. in *Advances in feedstock conversion technologies for alternative fuels and bioproducts. New technologies, challenges and opportunities* (ed. Majid Hosseini) 1–19 (Woodhead Publishing Series in Energy (Elsevier Inc), 2019).

10.   Torzillo, G. & Vonshak, A. Effect of light and temperature on the photosynthetic activity of the cyanobacterium spirulina platensis. *Biomass and Bioenergy* 6, 399–403 (1994).

11.   Takache, H., Gwendoline, C., Cornet, J.-F. & Pruvost, J. Experimental and theoretical assessment of maximum productivities for the microalgae Chlaydomonas reinhardtii in two different geometries of photobioreactors. *Biotechnology Progress* 26, 431–440 (2010).

12.   Legrand, J., Artu, A. & Pruvost, J. Review on photobioreactor design and modelling for microalgae production. *Reaction chemistry and engineering* 6, 1134–1151 (2021).

13.   Takache, H., Pruvost, J. & Cornet, J.-F. Kinetic modeling of the photosynthetic growth of Chlamydomonas reinhardtii in a photobioreactor. *Biotechnology Progress* 28, 681–

692 (2012).

14. Choul-Gyun, L. Calculation of light penetration depth in photobioreactors. *Biotechnology and Bioprocess Engineering* 4, 78–81 (1999).

15. Chancellor, J. C., Scott, G. B. I. & Sutton, J. P. Space Radiation: The number one risk to astronaut health beyond low earth orbit. *Life* 4, 491–510 (2014).

16. Krohn, T. C., Hansen, A. K. & Dragsted, N. The impact of low levels of carbon dioxide on rats. *Laboratory animals* 37, 94–99 (2003).

17. Krohn, T. C. & Hansen, A. K. Carbon dioxide concentrations in unventilated IVC cages. *Laboratory animals* 36, 209–212 (2002).

18. Alling, A. *et al.* Lessons Learned from Biosphere 2 and Laboratory Biosphere Closed Systems Experiments for the Mars On Earth Project. *Biological Sciences in Space* 19, 250–260 (2005).

19. Mortola, J. Breathing around the clock: an overview of the circadian pattern of respiration. *Journal of applied physiology* 91, 119–129 (2004).

20. Adamovich, Y., Ladeuix, B., Golik, M., Koeners, M. & Asher, G. Rhythmic oxygen levels reset circadian clocks through HIF1alpha. *Cell Metabolism* 25, 93–101 (2017).

21. Emans, T., Janssen, B., Joles, J. & Krediet CTP. Circadian rhythm in kidney tissue oxygenation in the rat. *Frontiers in Physiology* 8, 205 (2017).

22. Akram Muhammad. Citric acid cycle and role of its intermediates in metabolism. *Cell biochemistry and biophysics* 68, 475–478 (2014).

23. Wilson, D., Rumsey, W., Green, T. & Vanderkooi, J. The oxygen dependence of mitochondrial oxidative phosphorylation measured by a new optical method for measuing oxygen concentration. *Journal of biological chemistry* 263, 2712–2718 (1988).

24. COE. *ETS 123: Protection of Vertebrate Animals, 18.III.1986. Cets* 123 (1986).

25. Vidal, S. & Vergara, P. *MELiSSA technical note (MPP-TN-08-5001): Animal model for MELiSSA pilot plant.* (2014).

26. Gonzalez, N. C. & Kuwahira, I. Systemic oxygen transport with Rest, Exercise and Hypoxia: A comparison of Humans, Rats and Mice. *Comprehensive physiology* 8, 1537–1573 (2018).

27. Fukuda, Y. Changes in ventilatory response to hypoxia in the rat during growth and aging. *Eurpopean Journal of Physiology - Pflügers Archives* 421, 200–203 (1992).

28. Jørgensen, H., Hansen, C. H., Mu, H. & Jakobsen, K. Protein and energy metabolism of young male Wistar rats fed conjugated linoleic acid as structured triacylglycerol. *Archives of Animal Nutrition* 64, 322–336 (2010).

29. Acién, F. G., Fernández, J. M. & Molina, E. Photobioreactors for the production of microalgae. *Reviews in Environmental Science and Bio/Technology* 12, 131–151 (2013).

30. Posten, C. Design principles of photo-bioreactors for cultivation of microalgae. *Engineering in Life Sciences* 9, 165–177 (2009).

31. Huang, Q., Jiang, F., Wang, L. & Yang, C. Design of Photobioreactors for Mass Cultivation of Photosynthetic Organisms. *Engineering* 3, 318–329 (2017).

32. He, L., Subramanian, V. R. & Tang, Y. J. Experimental analysis and model-based optimization of microalgae growth in photo-bioreactors using flue gas. *Biomass and Bioenergy* 41, 131–138 (2012).

33. Pegallapati, A. K. & Nirmalakhandan, N. Modeling algal growth in bubble columns under sparging with CO2-enriched air. *Bioresource Technology* 124, 137–145 (2012).

34. Cornet, J., Dussap, C. & Gros, J.B. *MELiSSA Technical note: Modeling of physical limitations in photobioreactors. Applications to simulation and control of the Spirulina compartment of the MELiSSA artificial ecosystem (TN 19.1).* (1993).

35. Vernerey, A. Conception, contróle et fonctionnement d'un photobioréacteur pour la culture en mode continu de la cyanobacterie spirulina platensis. (Universitat Autònoma de Barcelona, 2000).

36. Kawasse, Y. & Tsujimura, M. Enhancement of oxygen transfer in highly viscous non-newtonian fermentation broths. *Biotechnology and Bioengineering* 44, 1115–1121 (1994).

37. Verlaan, P., Van Eijs, A. M. M., Tramper, J. & Van't Riet, K. Estimation of axial dispersion in individual sections of a gas-lift loop reactor. *Chemical Engineering Science* 44, 1139–1146 (1989).

38. Merchuk, J. C., Contreras, A., García, F. & Molina, E. Studies of mixing in a concentric tube airlift bioreactor with different spargers. *Chemical Engineering Science* 53, 709–719 (1998).

39. Miron, A. S., Garcia, M. C. C., Camacho, F. G., Grima, E. M. & Chisti, Y. Mixing in bubble column and airlift reactors. *Chemical Engineering Research and Design* 82, 1367–1374 (2004).

40. Chisti, Y. *Airlift Bioreactors*. (Elsevier Science Publishing CO, 1989).

41. Loubière, K. *et al.* A new photobioreactor for continuous microalgal production in hatcheries based on external-loop airlift and swirling flow. *Biotechnology and Bioengineering* 102, 132–147 (2008).

42. Wilhem, E., Battino, R. & Wilcok, R. J. Low-pressure solubility of gases in liquid water. *Chemical Reviews* 77, 219–262 (1977).

43. Hulatt, C. J. & Thomas, D. N. Productivity, carbon dioxide uptake and net energy return of microalgal bubble column photobioreactors. *Bioresource Technology* 102, 5775–5787 (2011).

44. Contreras, A., García, F., Molina, E. & Merchuk, J. C. Interaction Between CO_2-Mass Transfer, Light Availability and Hydrodynamic Stress in the Growth of Phaeodactylum tricornutum in a Concentric Tube Airlift Photobioreactor. *Biotechnology and Bioengineering* 60, 317–325 (1998).

45. Edwards, T., Maurer, G., Newman, J. & Prausnitz, J. Vapor-liquid-equilibra in multicomponent aqueous-solutions of volatile weak electrolytes. *AIChE J.* 24, 966–976 (1978).

46. Cornet, J.-F., Dussap, C. G. & Gros, J. B. *MELiSSA technical note (MPP-TN-19.2).* (1993).

47. Poughon, L., Dussap, C., Perez, J., Montesinos, L. & Godia, F. Dynamics and steady state operation of a nitrifying fixed bed biofilm reactor: mathematical model based description. *Process Biochemistry* 40, 2359–2369 (2005).

5.7. Supplementary materials

These supplementary materials are composed of the following sections:

Section 5.7.1.   Extended explanation of the methodology used for the determination of oxygen consumption and carbon dioxide production by the rats in the animal compartment.

Section 5.7.2.   Extended explanation of the methodology used for the determination of hydrodynamic parameters.

5.7.1. Methodology for the determination of oxygen/carbon dioxide consumption/production rates in the animal compartment

This section summarizes an explanation on the rationale behind the definition of the different oxygen/carbon dioxide consumption/production rates in the animal compartment.

In order to estimate this values, more than 13000 online measurements of oxygen and carbon dioxide concentrations were analyzed. These concentrations corresponded to independent trials where oxygen concentration in the animal compartment was maintained constant during a minimum of a week at different set points from 19-21% (n=11 tests). The maintenance of the oxygen set point was achieved by the introduction of air obtained from the operation of the MPP photobioreactor in a closed loop when the control system applied to this pilot plant was implemented. Thus, in these tests, oxygen concentration in the animal compartment was maintained constant as a requirement of the control system whereas the concentration of carbon dioxide was evolving as a balance between the consumption of the PBR microalgae and the production of the rats. Specific details on the number of runs performed at each set point is detailed in Table 5-9.

Table 5-9. Number of tests performed at each animal compartment set point

Oxygen set point test in animal compartment (%)	Number of runs performed
19	2
20	3
21	5
22	1

Additionally, the mentioned measures of online concentration of oxygen and carbon dioxide were performed at the entrance of the animal compartment and inside the animal compartment. Figure 5-10 details the specific location of these gas concentration on-line analyzers used for these independent tests.
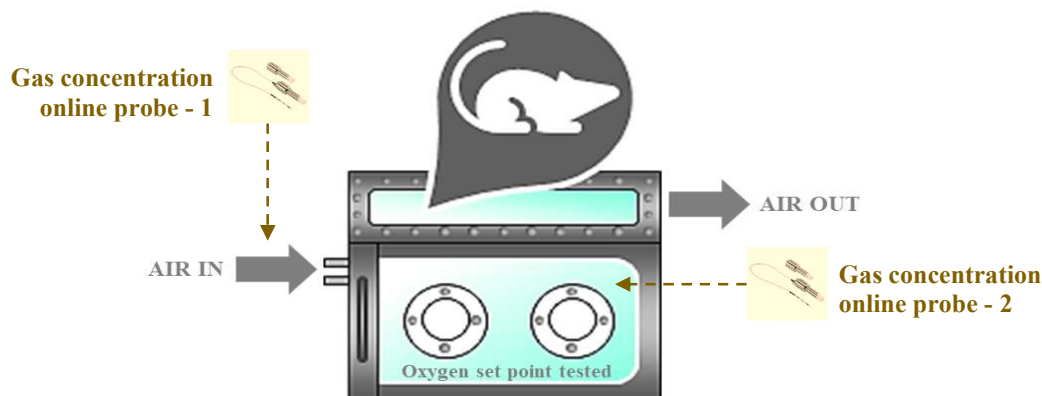
Figure 5-10. Scheme of the animal compartment with the location of the online probes for oxygen and carbon dioxide concentrations determination in the gas phase.

In this condition and for both cases (carbon dioxide and oxygen), an analysis of the mass balance of each specific compound was performed by considering the animal compartment as a perfectly mixed reactor in continuous operation.

For this analysis, the animal compartment could be considered as a perfectly mixed tank at steady state conditions once the specific oxygen set point was reached.

In these conditions, it was possible to perform a mass balance between the difference in the input ($F_{in} \cdot O_{g_{in}}$; calculated with results of online probe 1 and a mean flow rate of 160 L/h) and the output ($F_{out} \cdot O_g$; calculated with results of online probe 2 and a mean flow rate of 160 L/h) of the system. Once the specific mass flow in each hour of the day was determined, the difference between each hour and the previous one was taken as a rate of consumption/production of that variable ($\frac{\partial O_g}{\partial t} V$). In these conditions, specific consumption of the rats (n=3) could be calculated by considering the expressions detailed in Table 5-5. This exercise was performed for oxygen and carbon dioxide.

176

The results obtained from this analysis are provided in Figure 5-11 and are summarized in the upper part of the figure for oxygen and in the lower part of the figure for carbon dioxide). However, in Figure 5-11A and Figure 5-11C, the values provided are obtained by considering that the system is at a steady state for that compound in the range studied. Therefore, the value of the calculated accumulation term ($\frac{\partial O_g}{\partial t} V$ for oxygen) is approximated to zero. This is not considered for Figure 5-11B and Figure 5-11D. As observed, results obtained for the oxygen can be considered equivalent when steady state assumption is performed whereas the results obtained for carbon dioxide are not in agreement with oxygen consumption results when this steady state assumption is done. This is related to the fact that the control system applied in the MPP only controls (as expected) the concentration of oxygen by regulating the light in the PBR compartment. Therefore, the evolution of carbon dioxide in the system is completely linked to the balance between the consumption in the PBR and the production by the rats. For this reason, when the rate/accumulation term is considered, a profile equivalent to the one observed for the oxygen concentrations is obtained. Thus, these preliminary results suggest that the global system (PBR + animal compartment) could be capable of compensating for the fluctuation produced in the animal compartment regarding carbon dioxide despite lacking active external control.

For this reason, the final O_2 consumption and CO_2 production rates obtained for each hour of the day are considered by assuming a steady state for oxygen concentration and without assuming a steady state for the carbon dioxide concentration in the analysis of these data. A summary of these production/consumption rates is found in Table 5-10 (carbon dioxide) and Table 5-11 (oxygen). It should be noted that this estimation implies the conversion of the original data obtained from the on-line analyzer to g of gas / L volume. In order to do that, ideal equation of gases has been used as reference with the operational pressure (1.002 bar) and temperature (295 K).
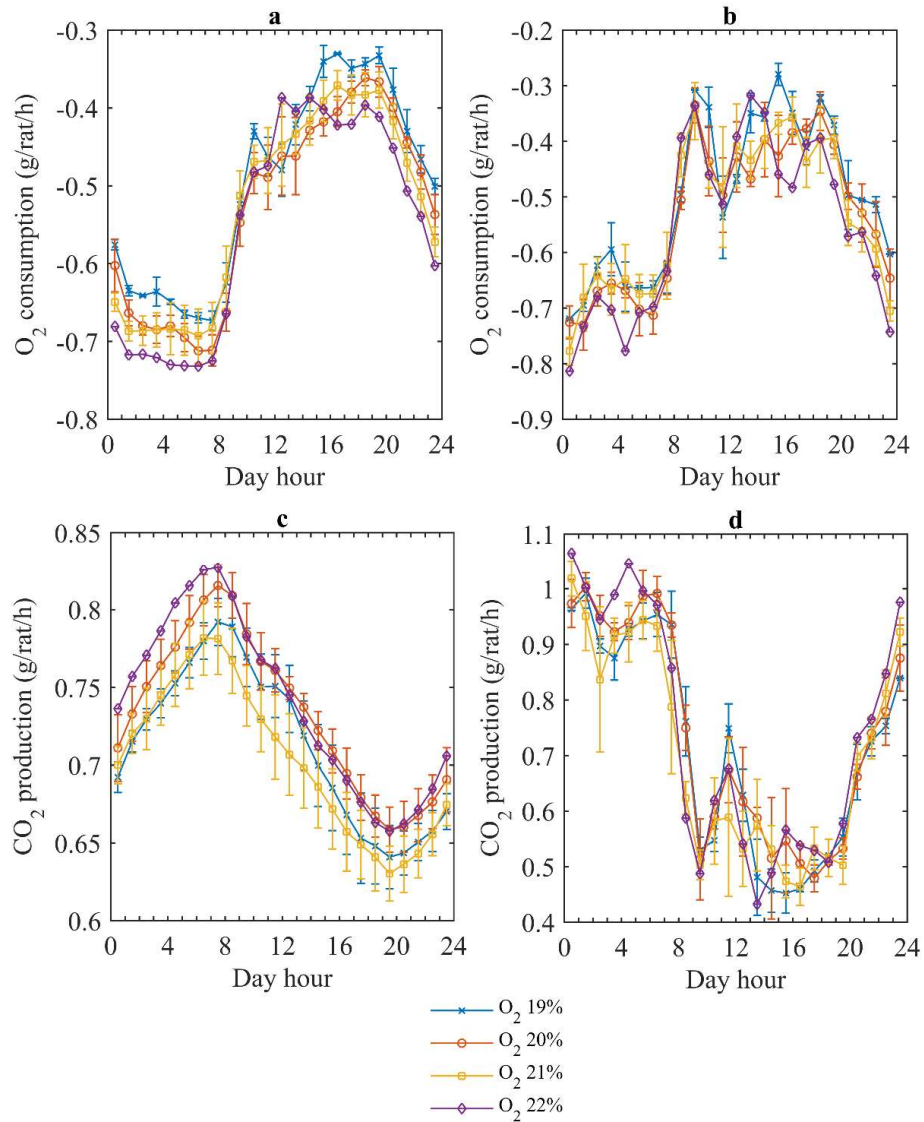
Figure 5-11. Oxygen and carbon dioxide consumption/production rates in the different hours of the day. Figures in the left part of the picture consider the establishment of a steady state for the mentioned variables in the time range studied when performing the calculations. Figures in the left part of the picture, however, do not consider the establishment of this steady state and consider accumulation term for the calculations.

178

Table 5-10. Carbon dioxide production rates (g/rat/h) in the different trials performed in the animal compartment

Oxygen set point (%)			21						19				20					22	Average mean
Test number (n)	1	2	3	4	5	Mean	Desvest	1	2	Mean	Desvest	1	2	3	Mean	Desvest	1		
0	1.06	0.98	1.03	0.99	1.04	1.02	0.03	0.97	0.96	0.96	0.00	0.97	0.92	1.03	0.97	0.04	1.07	**1.00**
1	0.83	1.01	0.97	0.96	0.98	0.95	0.06	1.02	0.97	0.99	0.03	1.02	1.02	0.97	1.00	0.03	1.00	**0.98**
2	0.58	0.89	0.90	0.90	0.92	0.84	0.13	0.88	0.91	0.90	0.01	0.91	1.00	0.95	0.95	0.04	0.94	**0.87**
3	0.91	0.91	0.96	0.93	0.87	0.92	0.03	0.84	0.91	0.88	0.04	0.90	0.92	0.94	0.92	0.02	0.99	**0.91**
4	0.87	0.88	0.88	0.99	0.98	0.92	0.05	0.94	0.91	0.93	0.01	0.90	0.95	0.97	0.94	0.03	1.05	**0.93**
5	0.88	0.95	0.93	0.98	0.98	0.94	0.04	0.91	0.97	0.94	0.03	0.97	0.94	1.05	0.99	0.05	1.00	**0.95**
6	0.86	0.91	0.93	0.96	1.00	0.93	0.05	0.91	0.99	0.95	0.04	0.96	1.03	0.99	0.99	0.03	0.97	**0.95**
7	0.81	0.89	0.55	0.85	0.84	0.79	0.12	0.88	1.00	0.94	0.06	0.93	0.96	0.91	0.93	0.02	0.86	**0.86**
8	0.60	0.68	0.61	0.63	0.60	0.62	0.03	0.70	0.82	0.76	0.06	0.70	0.80	0.75	0.75	0.04	0.59	**0.68**
9	0.48	0.50	0.49	0.56	0.50	0.50	0.03	0.51	0.55	0.53	0.02	0.41	0.58	0.55	0.51	0.07	0.49	**0.50**
10	0.50	0.47	0.63	0.65	0.65	0.58	0.08	0.53	0.57	0.55	0.02	0.57	0.62	0.58	0.59	0.02	0.62	**0.57**
11	0.45	0.70	0.61	0.78	0.40	0.59	0.14	0.70	0.79	0.75	0.04	0.72	0.71	0.59	0.67	0.06	0.68	**0.65**
12	0.56	0.54	0.51	0.63	0.42	0.53	0.07	0.58	0.68	0.63	0.05	0.75	0.57	0.53	0.62	0.10	0.54	**0.58**
13	0.55	0.49	0.57	0.54	0.73	0.57	0.08	0.41	0.55	0.48	0.07	0.59	0.61	0.56	0.59	0.02	0.43	**0.54**
14	0.46	0.56	0.57	0.56	0.50	0.53	0.04	0.42	0.50	0.46	0.04	0.46	0.42	0.67	0.52	0.11	0.49	**0.50**
15	0.44	0.49	0.46	0.45	0.52	0.47	0.03	0.42	0.49	0.45	0.04	0.43	0.65	0.56	0.55	0.09	0.57	**0.49**
16	0.45	0.41	0.47	0.49	0.50	0.46	0.03	0.47	0.45	0.46	0.01	0.46	0.55	0.51	0.51	0.04	0.54	**0.47**
17	0.60	0.49	0.51	0.52	0.56	0.53	0.04	0.47	0.51	0.49	0.02	0.49	0.45	0.50	0.48	0.02	0.53	**0.51**
18	0.47	0.57	0.52	0.51	0.50	0.52	0.03	0.52	0.52	0.52	0.00	0.52	0.50	0.52	0.51	0.01	0.51	**0.52**
19	0.54	0.46	0.54	0.46	0.50	0.50	0.03	0.59	0.52	0.55	0.03	0.51	0.53	0.56	0.53	0.02	0.58	**0.53**
20	0.70	0.67	0.69	0.75	0.68	0.70	0.03	0.72	0.62	0.67	0.05	0.65	0.64	0.69	0.66	0.02	0.73	**0.69**
21	0.74	0.68	0.79	0.70	0.75	0.73	0.04	0.75	0.70	0.73	0.03	0.72	0.72	0.78	0.74	0.03	0.77	**0.73**
22	0.86	0.75	0.84	0.83	0.78	0.81	0.04	0.74	0.77	0.75	0.01	0.77	0.71	0.86	0.78	0.06	0.85	**0.79**
23	0.92	0.89	0.97	0.92	0.93	0.92	0.03	0.84	0.84	0.84	0.00	0.83	0.84	0.96	0.88	0.06	0.98	**0.89**

(Row label column: Day hour)

Table 5-11. Oxygen consumption rates (g/rat/h) in the different trials performed in the animal compartment

Oxygen set point (%)		21%							19%				20%					22%	Average mean
Test number (n)		1	2	3	4	5	Mean	Desvest	1	2	Mean	Desvest	1	2	3	Mean	Desvest	1	
Day hour	0	-0.65	-0.65	-0.65	-0.66	-0.63	-0.65	0.01	-0.58	-0.57	-0.58	0.01	-0.58	-0.58	-0.65	-0.60	0.03	-0.68	**-0.62**
	1	-0.67	-0.71	-0.69	-0.69	-0.67	-0.69	0.01	-0.64	-0.63	-0.63	0.01	-0.65	-0.65	-0.69	-0.66	0.02	-0.72	**-0.67**
	2	-0.66	-0.71	-0.68	-0.70	-0.67	-0.69	0.02	-0.64	-0.64	-0.64	0.00	-0.67	-0.70	-0.68	-0.68	0.01	-0.72	**-0.68**
	3	-0.65	-0.71	-0.69	-0.71	-0.67	-0.69	0.02	-0.62	-0.65	-0.64	0.02	-0.66	-0.71	-0.68	-0.68	0.02	-0.72	**-0.68**
	4	-0.64	-0.71	-0.70	-0.72	-0.65	-0.68	0.03	-0.65	-0.65	-0.65	0.00	-0.66	-0.69	-0.68	-0.68	0.01	-0.73	**-0.68**
	5	-0.64	-0.72	-0.67	-0.72	-0.67	-0.69	0.03	-0.67	-0.66	-0.67	0.01	-0.67	-0.69	-0.72	-0.70	0.02	-0.73	**-0.69**
	6	-0.64	-0.73	-0.67	-0.73	-0.69	-0.69	0.03	-0.66	-0.68	-0.67	0.01	-0.69	-0.72	-0.73	-0.71	0.02	-0.73	**-0.69**
	7	-0.63	-0.71	-0.67	-0.72	-0.68	-0.68	0.03	-0.66	-0.69	-0.67	0.01	-0.69	-0.74	-0.71	-0.71	0.02	-0.72	**-0.69**
	8	-0.56	-0.67	-0.66	-0.61	-0.59	-0.62	0.04	-0.60	-0.65	-0.62	0.03	-0.63	-0.69	-0.66	-0.66	0.02	-0.66	**-0.63**
	9	-0.48	-0.56	-0.52	-0.52	-0.48	-0.51	0.03	-0.51	-0.54	-0.52	0.01	-0.51	-0.59	-0.54	-0.55	0.03	-0.54	**-0.52**
	10	-0.44	-0.50	-0.46	-0.48	-0.46	-0.47	0.02	-0.44	-0.42	-0.43	0.01	-0.48	-0.52	-0.45	-0.48	0.03	-0.48	**-0.47**
	11	-0.40	-0.53	-0.47	-0.49	-0.45	-0.47	0.04	-0.44	-0.49	-0.46	0.02	-0.53	-0.50	-0.43	-0.49	0.04	-0.47	**-0.47**
	12	-0.40	-0.52	-0.42	-0.50	-0.39	-0.45	0.05	-0.45	-0.51	-0.48	0.03	-0.52	-0.47	-0.40	-0.46	0.05	-0.39	**-0.46**
	13	-0.42	-0.47	-0.41	-0.46	-0.40	-0.43	0.03	-0.40	-0.45	-0.42	0.03	-0.52	-0.47	-0.40	-0.46	0.05	-0.40	**-0.44**
	14	-0.40	-0.47	-0.41	-0.43	-0.37	-0.42	0.03	-0.37	-0.40	-0.39	0.02	-0.44	-0.42	-0.42	-0.43	0.01	-0.39	**-0.41**
	15	-0.37	-0.44	-0.38	-0.39	-0.37	-0.39	0.03	-0.32	-0.36	-0.34	0.02	-0.39	-0.44	-0.42	-0.42	0.02	-0.40	**-0.39**
	16	-0.36	-0.40	-0.35	-0.38	-0.37	-0.37	0.02	-0.33	-0.33	-0.33	0.00	-0.38	-0.43	-0.40	-0.40	0.02	-0.42	**-0.38**
	17	-0.41	-0.40	-0.34	-0.39	-0.37	-0.38	0.03	-0.36	-0.34	-0.35	0.01	-0.38	-0.40	-0.36	-0.38	0.01	-0.42	**-0.38**
	18	-0.38	-0.44	-0.35	-0.38	-0.37	-0.38	0.03	-0.35	-0.34	-0.34	0.01	-0.37	-0.37	-0.35	-0.36	0.01	-0.40	**-0.37**
	19	-0.38	-0.42	-0.36	-0.38	-0.35	-0.38	0.02	-0.34	-0.32	-0.33	0.01	-0.38	-0.38	-0.34	-0.37	0.02	-0.41	**-0.37**
	20	-0.43	-0.45	-0.40	-0.41	-0.39	-0.42	0.02	-0.40	-0.35	-0.38	0.03	-0.42	-0.39	-0.39	-0.40	0.01	-0.45	**-0.41**
	21	-0.45	-0.50	-0.47	-0.49	-0.44	-0.47	0.02	-0.46	-0.40	-0.43	0.03	-0.43	-0.45	-0.45	-0.44	0.01	-0.51	**-0.46**
	22	-0.50	-0.54	-0.52	-0.53	-0.48	-0.51	0.02	-0.48	-0.45	-0.47	0.02	-0.47	-0.46	-0.51	-0.48	0.02	-0.54	**-0.50**
	23	-0.56	-0.58	-0.59	-0.59	-0.54	-0.57	0.02	-0.51	-0.49	-0.50	0.01	-0.51	-0.52	-0.57	-0.54	0.03	-0.60	**-0.55**

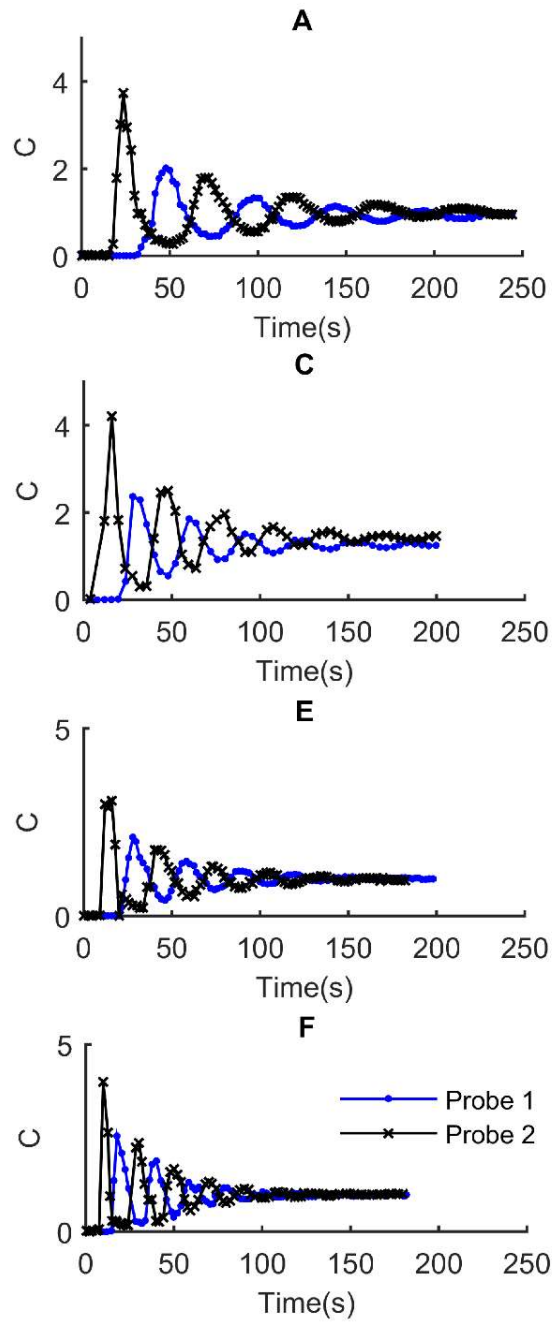### 5.7.2. *Methodology followed for the determination of hydrodynamic parameters*

This section summarizes the results obtained during the photobioreactor hydrodynamic characterization. These results include the mixing and circulation time determination, the modelling of the liquid flow behavior, the residence time distribution determination (RTD) and the gas-liquid mass transfer coefficient determination (k_la).

5.7.2.1. Mixing and circulation time determination

Mixing time was determined by an HCl pulse as previously described [37] since low volumes are required and air bubbles do not affect the measurements. 1 mL of HCl was injected into the reactor at 25ºC filled with 50 mM KCl and the proton concentration response was registered by two pH probes located at the beginning of the downcomer and the end of the riser with a time period of 2 seconds. The nonlinearity response to the pulse was corrected by means of a calibration of H^+ concentration in a KCl solution for pH 3.5-6.2 ($C_i = 2.03 \cdot 10^{-5} \cdot pH^4 - 4.47 \cdot 10^{-4} \cdot pH^3 + 36.7 \cdot 10^{-4} \cdot pH^2 - 1.33 \cdot 10^{-2} \cdot pH + 1.82 \cdot 10^{-2}$). Gas rates tested were 0.6, 0.9, 1.2, 1.3 and 4.5 L·min^{-1}, representing the minimal flow rate with good fluid circulation and the maximal flow rate due to physical limitations of the reactor. Numerical results of the mixing (95% homogeneity) and circulation times are summarized in Table 5-12 whereas the tracer concentration evolution over time is observed in Figure 5-12.

Table 5-12. Hydrodynamic study parameters. Different gas flow rates

ID	Inlet gas flow rate (l·min^{-1})	Superficial gas velocity ($*10^3$ m·s^{-1})	Circulation time (s)	Mixing time (s)	Bo number
A	0.6	0.6	50	242	50
B	0.9	0.85	38	157	49
C	1.2	1.1	32	152	52
D	1.3	1.23	32	138	50
E	1.5	1.4	30	139	-
F	4.5	4.3	20	117	70

Figure 5-12. Representative figure of the mixing time determination test results. Evolution of normalized tracer concentration with respect to time. Letters denote experimental conditions as described in Table 5-12 where each experiment is identified with a different letter.

182

5.7.2.2. Liquid flow behavior modeling

Characterization of the liquid flow behavior of the bioreactor in the riser and the downcomer was performed by numerically fitting an axial dispersion-based model to the experimental data. The fluid dispersion model used was based on Fick's diffusion law and involved consideration of the axial dispersion [37], according to the following equation:

$$C_\theta = \left(\frac{Bo}{4\pi\theta}\right)^{1/2} \sum_{x=1}^{\infty} \exp\left[\frac{-(x-\theta)^2 Bo}{4\theta}\right]$$
5-12

where θ is the dimensionless time (θ= time·circulation time-1), x is the axial coordinate and Bo is the Bodenstein number :

$$Bo = (v \cdot L) \cdot D^{-1}$$
5-13

Which relates the liquid velocity (v , m·s^{-1}) the length of the tube (L, m) and the dispersion coefficient (D, m^2·s^{-1}). The dimensionless Bodenstein number, Bo, is directly related to the degree of mixing and is inversely proportional to diffusion. The Bo number tends to zero in a complete mixing situation while its value increases as the flow pattern approaches an ideal plug flow behavior. Results obtained are summarized in Table 5-12.

5.7.2.3. Residence time distribution (RTD) determination

Residence time distribution was determined by a pulse method using acidic dye (bright red 'Duasyn' 4 RC Hoechst, Germany) in the photobioreactor operating in continuous mode at liquid flow rate of 2.8 L·h^{-1} and aeration gas flow of 1.2 L·min^{-1}. The tracer pulse was injected at the beginning of the downcomer and RTD monitoring was performed at the outlet of the reactor. The tracer concentration was determined at 507 nm optical density and converted to tracer concentration using a previously obtained calibration curve of absorbance as function of bright red concentration ($C = 0.0316 \cdot Abs - 0.0001 / r^2$: 0.9999).

With these data, mean residence time was calculated using an equation obtained directly from a mass balance for the tracer in a continuously stirred tank reactor (CSTR).

$$C = C_0 \exp\left(-\frac{t}{\bar{t}}\right) \qquad 5\text{-}14$$

Parameter evaluation was performed by least-squares curve fitting, using the following linearized flux model, given by Levenspiel (1972) for a CSTR:

$$\ln C = \ln C_0 - \frac{t}{\bar{t}} \qquad 5\text{-}15$$

where C is tracer concentration, C_0 is the initial tracer concentration after pulse introduction and $\bar{t}$ is the liquid residence time. Normalized curves were obtained by using the following dimensionless variables:

$$\theta = \frac{t}{\bar{t}} \qquad 5\text{-}16$$

$$E_\phi = (liquid\ flow) \cdot \frac{[tracer\ concentration]}{quntity\ of\ tracer\ injected} \cdot \qquad 5\text{-}17$$

Non-linear curve fitting was performed, representing the dimensionless exit age distribution function (Eθ) as a function of dimensionless time (θ). This allowed the calculation of experimental residence time. The obtained value was compared to theoretical residence time obtained from the liquid flow rate and reactor volume. The results are shown in Table 5-12.

184

5.7.2.4. Overall volumetric gas liquid mass transfer coefficient (kla) determination

The gas liquid mass transfer coefficient (kla) values were determined by the dynamic method. N_2 was introduced at the entrance of the reactor until a steady state was reached. Afterwards O_2 was sparged. The increase in total dissolved O_2 concentration was measured online by a polarographic oxygen probe (Mettler Toledo, Inpro 6800, Columbus, Ohio, US) located in the upper part of the riser.

In these determinations, the dynamics of the oxygen electrode must be taken into account. For this, the sensor response time was estimated to be 40 seconds. The electrode was alternatively submerged in two vessels, one sparged with air and another one with nitrogen gas. The electrode signal, Cm(t), was assumed to follow first-order dynamics:

$$\frac{dC_m}{dt} = \frac{C - C_m}{\tau}$$

5-18

Response time constant was taken as the time necessary to reach 63.2 % of the response and was calculated by nonlinear least-squares fitting to the step data.

For the determination of kla, the oxygen concentration in the aqueous liquid phase was monitored as a function of time after a step change in the supplied gas from nitrogen to air. The rate of oxygen absorption is given by:

$$\frac{dC}{dt} = k_l a \cdot (C^* - C)$$

5-19

where C* is the oxygen concentration in the gas-liquid interface at equilibrium with the gas concentration. A combination of Equation 5-18 and Equation 5-19 followed by integration yields the expression for the theoretical signal at time t.

185

$$C_m = \frac{C \cdot \left(1 - e^{-k_l a \cdot t} - k_l a \cdot t \cdot \left(1 - e^{-\frac{t}{\tau}}\right)\right)}{1 - k_l a \cdot \tau}$$

5-20

The kLa coefficient can thus be calculated by non-linear least squares fitting of the above equation to the experimentally measured electrode signal. This determination was performed at three different gas flow rates (1.0, 2.8 and 5.0 L/min) and the following correlation was stablished ($y = 0.5257 \cdot x^{0.8484}$, $n = 3$, $R^2 = 0.987$). [47]

CHAPTER 6

Integration of the photobioreactor and the animal compartment in gas close loop: Experimental results and model validation

6.1. Introduction

The work following to the development of the mathematical model presented in Chapter 5 consist on its application to validate different series of experiments performed in the MPP as part of the global integration strategy. Particularly, Chapter 6 presents the results related to the connection between the PBR compartment (C4a), colonized with *Limnospira indica*, previously known as *Artrospira platensis*, and the animal isolator (C5), corresponding to the WP1 of the integration strategy for the MPP.

As previously described, the demonstration scenario for the MPP proposes an intermediate scale for the different bioreactors that conform the complete loop with the objective to produce the oxygen equivalent to the respiration needs of one human, with 20-40% concomitant production of food. For this reason, laboratory Wistar rats were selected as a mock of a human member of the crew. This selection was based on the fact that they are animal easy to accommodate [1] with a similar RQ than humans. Additionally, the existing differences (related to the different weight) between oxygen intake in rats (13.71 mL/min/kg) and humans (3.51 mL/min/kg) [2,3] could be compensated by increasing the number of rats used. However, this defined final oxygen production scenario is expected only to be reached when the complete loop integration is connected and will require the use of 60 rats for the final closure scenario. Meanwhile, in the intermediate phases of the integration, different aspects need to be taken into consideration. For example, in some of the initial steps of the integration not all the oxygen equivalent to one human is expected to be produced. In this context, the use of rats implies a major advantage, since the number of rats in each experiment can be changed according to the expected oxygen production of the specific integration loop tested. This allows for the specific challenge of the integration at the expected oxygen production target according to the loop design.

Particularly, in this chapter the integration of the PBR compartment (C4a) and the animal isolator compartment (C5) in the gas phase was expected to produce approximately 5% oxygen of the respiration corresponding to a 20-50 years old human.

Therefore, as explained in Chapter 5, in this case three rats are required to live in the animal compartment based on the oxygen intake and weight of both rats and humans.

Two tests of 50 and 30 days duration respectively were performed to demonstrate the integration between both compartments, targeting different set-points of oxygen in the animal isolator (19-22% according to acceptable oxygen concentration variation ranges in ISS) while regulating the light in the photobioreactor to achieve the oxygen production required to match the oxygen consumption by the rats. This experimental design allowed for the challenge of the PBR light regulation capacity to achieve oxygen production at different oxygen set-points and the inherent changes of the activity of the rats according to their metabolism oscillations and day-night cycles. However, in order to test the light regulation capacity of the PBR, the potential influence of a limiting carbon source in the liquid phase needed to be eliminated. For this reason, an extra supply of carbonate in the liquid media was applied with concentrations in the liquid phase that exceed the saturation constant for the microalgae kinetics.

In this chapter, the results obtained from these tests have been used for the validation of the model described in Chapter 5.

6.2. Materials and methods

This section summarizes the specific procedures and analysis used for the photobioreactor (C4a) and animal compartment (C5) monitoring and operation.
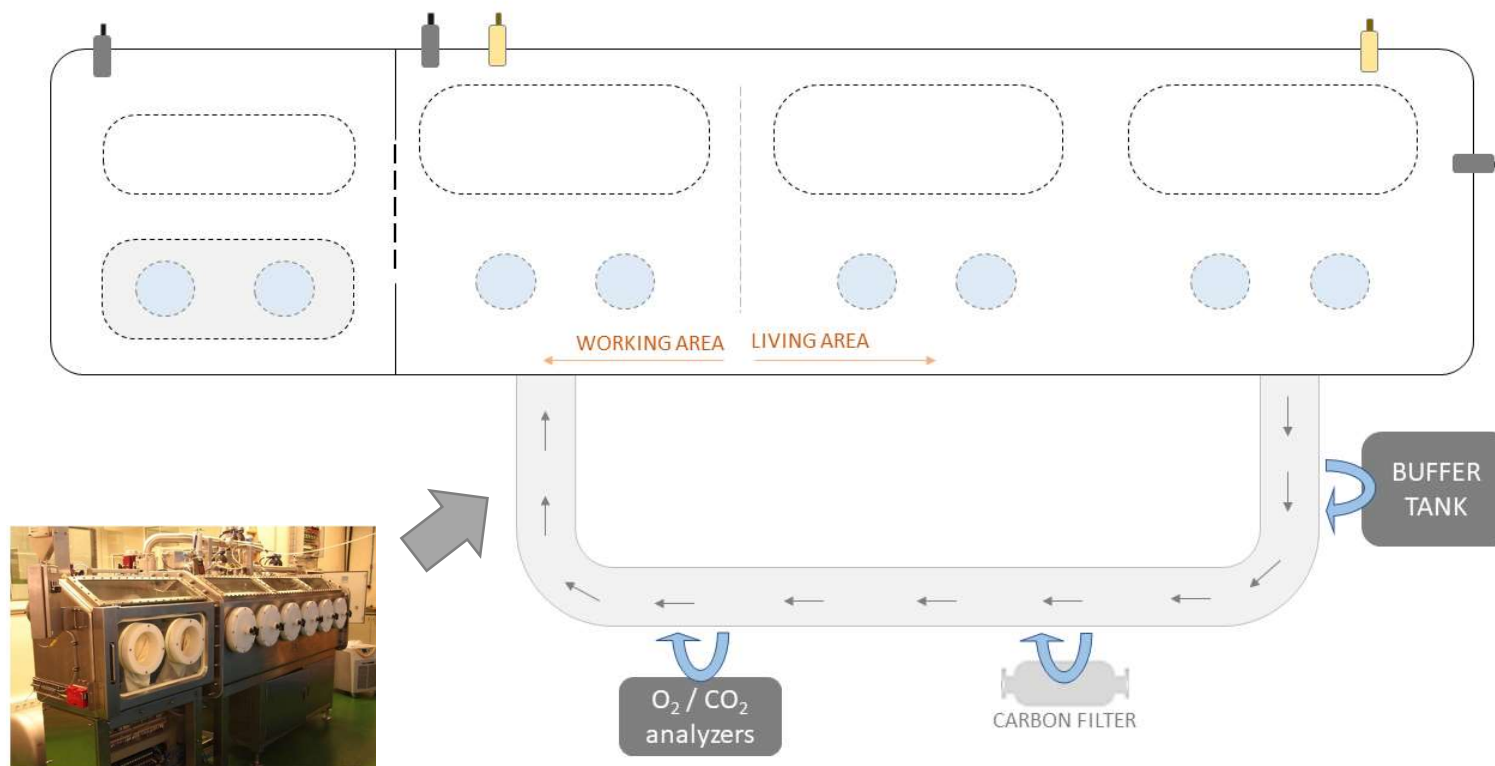
6.2.1. Animal isolator (C5)

A 1600 L modular isolator (Hosokawa Micron LTD, Preston Brook, United Kingdom) was designed and manufactured to host the cohort of rats. In the current step of the integration process, the modules used in the MPP were designed to host a cohort of 20 rats (A third of the maximum capacity required for the complete loop integration, 60 rats). This isolator was connected to the PBR at the entrance and output of the compartment so that a closed gas loop was established by using a diaphragm vacuum pump (GAST manufacturing, 22D1180-202-1005, Benton

Harbor, Michigan, USA). This isolator was configured into three main zones: main chamber, transfer airlock and gas recirculation loop.

The main chamber had a volume of 1600 L and was designed to host the animal crew with artificial light at periods of 12-12 hours day-night and included six 250 mm round gloveports at the front of the isolator to manipulate the animals. In the main chamber, an overpressure of 200 Pa was maintained by pressure control through two pressure transmitters (Emerson Electrics Rosemount, 2051 CG1, Shakopee, Minnesota, USA). An external 250 L buffer tank was connected to the isolator to compensate for the effects of atmospheric pressure changes. A gas recirculation loop was designed to ensure good mixing in the main chamber and the maintenance of the proper environmental conditions using a recirculation flow of 90 m^3/h^{-1} (temperature, humidity, level of contaminants) through heat exchanger equipment (Secomak, HT571, Hertfordshire, United Kingdom), humidity control equipment (HRS, K-series, Hertfordshire, United Kingdom) and an active carbon filter (Bioconservación, Bi-On® ACPA, Barcelona, Spain). Temperature and humidity in the isolator were monitored by the use of two transmitters (Vaisala, HMT337, Vantaa, Finland) and controlled at 22°C and 55%, respectively.

Additionally, carbon dioxide and oxygen were measured on-line with an IR and paramagnetic analyzers, respectively (SICK-Maihak, GSM810, Hamburg, Germany). Finally, the transfer airlock was designed with an independent pressure control (Emerson Electrics Rosemount, 2051 CG1, Shakopee, Minnesota, USA) to allow the entry and exit of materials without influencing the main chamber variables. Figure 6.1 shows a scheme of the C5 compartment.

190

Figure 6.1. The animal isolator (C5) at the MPP. Scheme of the compartment design. The animal isolator is configured of the transfer airlock (left part of the scheme) and the main chamber (right part of the scheme). In this main chamber two different zones are differentiated: the working area and the living area. Pressure probes are represented in grey and temperature/humidity probes are represented in yellow in the figure. An air recirculation system is located in the main area. This recirculation system is also connected to the 250 L buffer tank, the oxygen and carbon dioxide analyzers and the carbon filter.

6.2.2. Laboratory Wistar rats

During these experiments, three female adult white Laboratory Wistar rats (*Rattus norvegicus*, 13-14 weeks old, 200-250 g initial weight) were used as mock-up of the crew to simulate the 5% oxygen respiration needs of one human. The age of the rats was selected to achieve a more stable oxygen consumption since at 13-14 weeks these animals can be considered adult individuals.

These rats were exposed to light-dark cycles of 12 hours and were kept inside the isolator in a cage of 940 cm^2(480 x 265 x 210 mm) with a drinking bottle that was replaced twice a week. Rats were fed with an a*d libitum* 2914 Teklad Irradiated Diet (Envigo, Santa Perpètua de Mogoda, Spain).

Physico-chemical and biological controls were performed to the rats at the beginning and the end of the experiments (haematology, gasometry and biochemistry blood analysis) and their behavior/physical conditions were assessed by qualified veterinaries once a week in terms of general appearance, food and water intake, hair, eyes and mucous membranes exam, motor activity, urination and defecation activity and body weight gain.

6.2.3. Photobioreactor (C4a)

A 83 L external-loop gas lift PBR (Bioengineering Ag, Wald, Switzerland) was designed as previously described in [4] to provide approximately 5% of oxygen requirements for one human. The reactor consisted in two glass cylindrical tubes of 15 cm diameter and 1.5 m height with an illuminated volume of 55 L (estimated to be approximately a 64% of the total volume). The upper and lower parts of the tubes were connected by curved stainless steel (A316L) sections that allowed liquid circulation and heat exchange through an external jacket for temperature control with 0.3 m^2 total heat exchange area and 20% glycol as refrigerating fluid. In this system, the gas phase was injected at the bottom of the right column (riser) and was exiting from the top of that same column, creating a difference of density driving the fluid circulation to flow through the left column (downcomer)

(see Figure 6.2). By this, a constant internal liquid circulation and mixing was obtained in the bioreactor by means of the gas injection.

For the continuous operation of the reactor, the input liquid medium was pumped at constant flow rate of 0.75 L/h into the reactor by means of a variable speed gear pump (Lewa, EEC0002S11, Hispania S.L., Leonberg, Germany) followed by a sterile filtration (0.22 μm ZCSGB-020Z-PS1, Domnick Hunter, Gateshead, United Kingdom).

Air supply during operation was measured and regulated at 2.8 L/min by means of three mass-flow meters/controllers (Bronkhorst, F-202D-FA, AK Ruurlo, Netherlands). Composition of the gas phase was measured on-line by an IR analyzer for CO_2 coupled to a paramagnetic analyzer for O_2 (600 series, California Analytical Instruments, Orange, California, USA) and sterile filtered at the input and output of the reactor prior its entrance in the C5 compartment (Bioprocess-Dominick hunter, 0.2 μm High flow Tetpor ZHFT/AT, Gateshead, United Kingdom). pH was measured by means of a conventional sterilizable glass pH probe connected to a pH amplifier (Inpro 3, Mettler Toledo, Greifensee, Switzerland). Control of pH was performed by addition of NaOH (2 M) or H_2SO_4 (2M) as required.

Regarding illumination, a total of 350 halogen lamps (Sylvania, MR16HM, (12 V, 20 W), Quebec, Canada) homogeneously distributed around the illuminated volume were used for the bioreactor illumination. Light intensity was modified directly on the 380 V AC power line and transformed to 12 V CC. This system allowed a simpler light regulation as required for illumination control.
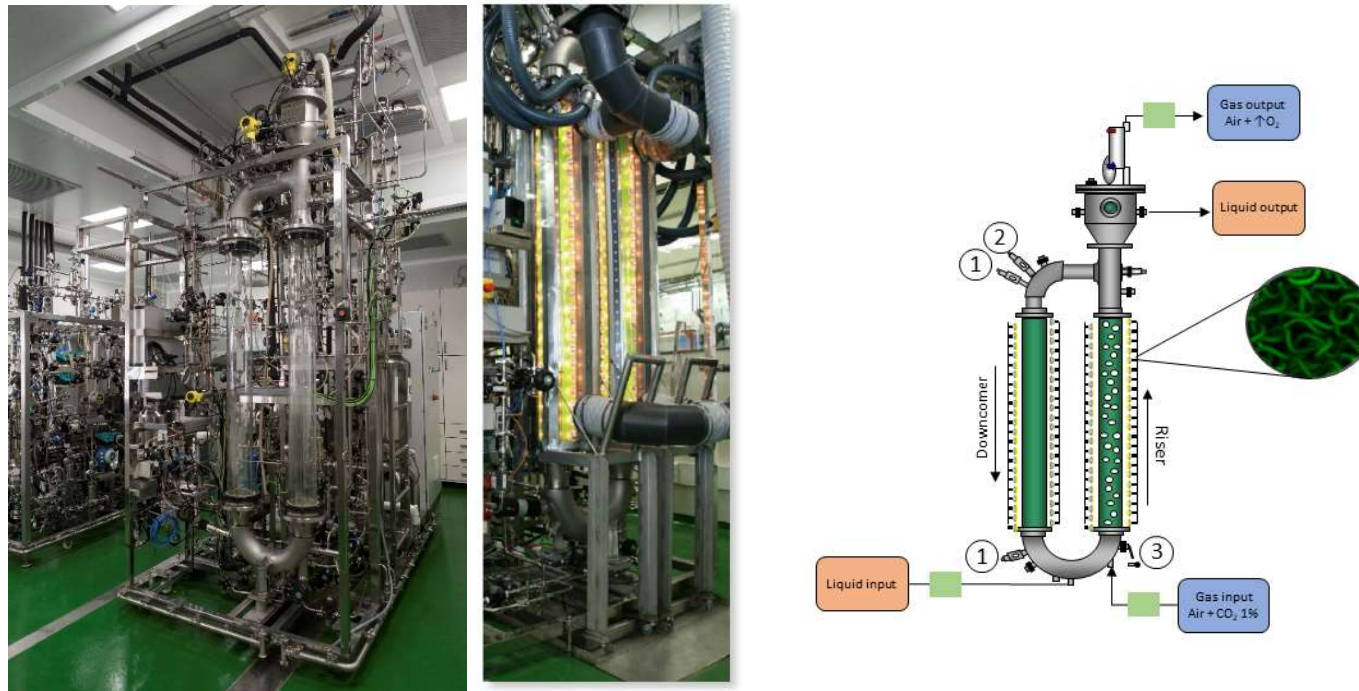
Figure 6.2. The photobioreactor (C4a) at the MPP. In the scheme, liquid (orange) and gas (blue) input and output lines are highlighted. Sterile filters applicable to liquid and gas lines can be seen in the scheme as a green square. Finally, an identification is shown for the different control elements: 1) pH probes, 2) Oxygen measurement probe and 3) sampling port.

6.2.4. Limnospira indica culture

An axenic strain of the cyanobacteria *Limnospira indica* PCC 8005 was used. This strain was cultured in a modified Zarrouk medium (2.5 g of $NaNO_3$, 1 g of K_2SO_4, 1 g of NaCl, 0.08 g of $MgSO_4 \cdot 7H_2O$, 0.04 g of $CaCl_2 \cdot 2\ H_2O$, 0.01g of $FeSO_4 \cdot 7H_2O$, 0.09 g of $EDTA \cdot 2H_2O$, 0.5 g of K_2HPO_4, 10.5 g of $NaHCO_3$, 7.6 g of Na_2CO_3, 0.23 mg of $MnCl_2 \cdot 4H_2O$, 0.11 mg of $ZnSO_4 \cdot 7H_2O$ and 0.03 mg of $CuSO_4 \cdot 5H_2O$) as previously reported [5]. The operational conditions for continuous operation of the photobioreactor were stablished according to previous work [4]. A pH value of 9.5 and a feed flow rate of 0.75 L/h were maintained during the whole continuous operation.

For the initial batch inoculation, 8 L inoculum with 1.1 optical density was used to initiate bioreactor operation in order to obtain an initial optical density of 0.1 AU. These conditions were selected to achieve a biomass concentration at the end of the batch step of approximately 1 g/L in about 8 days considering a specific cyanobacteria growth rate of 0.012 h^{-1}.

The inoculum was previously grown in 1 L flasks containing modified Zarrouk medium [5] and kept under constant illumination at 30 $\mu mol \cdot m^{-2} \cdot s^{-1}$ provided by fluorescent tubes to avoid photoinhibition at low cyanobacteria concentration [6,7] and guarantee a specific growth rate of 0.007 h^{-1}. Flasks were incubated and stirred at 26°C (F-4 incubator, ASL-IBERCEX, Alcalá de Henares, Spain).

6.2.5. Biomass concentration determination

Biomass concentration was estimated by dry mass determination. 25 mL of culture broth were filtered through 47 mm-glass microfiber filter (GMFC-52047, Scharlau, Barcelona, Spain), incubated until constant weight in the oven at 105ºC and then weighed. Determinations were performed in triplicate.

6.2.6. *Measurement of* total *inorganic carbon*

Total inorganic carbon (TIC) was determined by chemical oxidative digestion (kit LCK380, Hach Lange GMBH, Berlin, Germany).

6.2.7. *Statistical evaluation of the results*

In each series of experiments, and for a set of fixed operational conditions, the experimental results obtained were compared to those predicted by the mathematical model and the quality of the fitting was taken as a sign of the validity of the model to describe the proposed system.

For the results evaluation, a statistical analysis was performed based on the evaluation of the residuals for the main variables and the calculation of average root mean squared error (RMSE) according to Equation 6-1 [8]. Additionally, Pearson correlation coefficient [8] (Equation 6-2) and Willmott-d-index [9] (Equation 6-3) were also calculated.

$$\text{RMSE} = \sqrt{\frac{1}{n} \cdot \sum_{t=1}^{n} (x_t - y_t)^2} \qquad \text{6-1}$$

$$r = \frac{\sum_{t=1}^{n}(x_t - \bar{x})(y_t - \bar{y})}{\sqrt{\sum_{t=1}^{n}(x_t - \bar{x})^2}\sqrt{\sum_{t=1}^{n}(y_t - \bar{y})^2}} \qquad \text{6-2}$$

$$\text{Willmott} - \text{d} - \text{index} = 1 - \left(\frac{\sum_{i=1}^{n}(y_t - x_t)^2}{\sum_{i=1}^{n}(y_t' + x_t')^2}\right) \qquad \text{6-3}$$

Where: x_t are the experimental values, $\bar{x}_t$ is the mean of the experimental values, y_t are the simulated values, $\bar{y}_t$ is the mean of the experimental values, y_t' and x_t' are the difference between the punctual experimental or simulated data and the data average and n the total number of experimental data.

6.3. Summary of experimental results

This section summarizes the main experimental results. First, the experimental campaign results are provided. Then, the results related to the gas phase analysis are presented for both compartments. Finally, the results of the liquid phase of the PBR are also detailed.

6.3.1. Experimental design conditions

Two experimental campaigns with gas-phase integration between C4a and C5 were performed as part of the integration WP1. In these tests, the animal compartment hosted three rats and its oxygen concentration was maintained at different oxygen set points (19-22%). This regulation was performed by the control system adjusting the light in the photobioreactor compartment as a function of the oxygen production needs. Specifically, the control system adjusted the illumination in the PBR in order to reach the oxygen concentration desired in the animal compartment and to maintain it during day-night cycle responding to the physiological variations of the animal cohort.

The dynamics of the global system when moving from one oxygen set point to another, as well as the global system capacity to maintain a specific oxygen set point were tested. Table 6-1 details the specific animal compartment oxygen set points tested and the period of time that each set point was maintained.

**Table 6-1. Oxygen set-points defined in the animal compartment for integration periods**

Experimental condition	Test 1		Test 2	
	Oxygen set point in animal compartment (%)	Test period (days)	Oxygen set point animal compartment (%)	Test period (days)
1	21	1-7	21	1-5
2	19	7-14	19	5-9
3	20	14-21	20	9-15
4	21	21-28	21	15-23
5	22	28-35	22	23-30
6	20	35-42		
7	21	42-50		

6.3.2. Experimental results

The results obtained for the gas phase evolution are presented in Figure 6.3 (C5 Test 1), Figure 6.4 (C5 Test 2) Figure 6.5 (C4a Test 1) and Figure 6.6 (C4a Test 2). The oxygen concentrations in the animal compartment follow the oxygen concentration values according to the conditions presented in Table 6-1. It should be noted that the maintenance of each specific oxygen concentration in the gas phase of the animal compartment is reflected in slightly higher oxygen levels in the PBR compartment. This is achieved by regulating the light intensity in the PBR. For these reasons, the specific experimental periods corresponding to an increase of the oxygen concentration set-point in the animal compartment are linked to a short transition period with constant light intensity at the maximum value whereas periods corresponding to a decrease in the oxygen concentration set-point are reflected in a short transition period with no light intensity in the PBR.

On the other hand, carbon dioxide concentrations are reproducible, stable at approximately 10,000 ppm and always below a maximum toxicity limit of 20,000 ppm in the animal or the PBR compartment established according to previous data [10,11]. This final oxygen concentration is higher than the terrestrial desired levels but equivalent to previous CELSS tests where the volume of the crew compartment was comparatively higher compared to the dimensions of the MPP C5 compartment. However, it should be noted that the main purpose of these tests was the challenge of the PBR light regulation to achieve a desired production of oxygen by the microalgae allowing to achieve the oxygen target set points in C5 compartment defined in the experimental phase. For this reason, as explained in section 6.2.4, the defined composition of the media included the presence of carbonate salt to assure the presence of inorganic forms of CO_2 in the liquid phase at levels where microalgae growth was not limited by carbon lack. Thus, the potential maximum transference of oxygen from the gas to the liquid was also limited during the experiments and therefore, in these tests the maximum potential of the microalgae to reduce carbon dioxide concentration in the animal

compartment was not tested. However, results obtained are promising since even with additional carbonate supplementation levels of carbon inorganic forms in C4a media, the levels of carbon dioxide in the animal compartment are stable, controlled and below the toxicity limit. Thus, in future integrations, the stable baseline of carbon dioxide concentration is expected to be reduced in a significative factor, allowing for the maintenance of the system at lower concentrations.
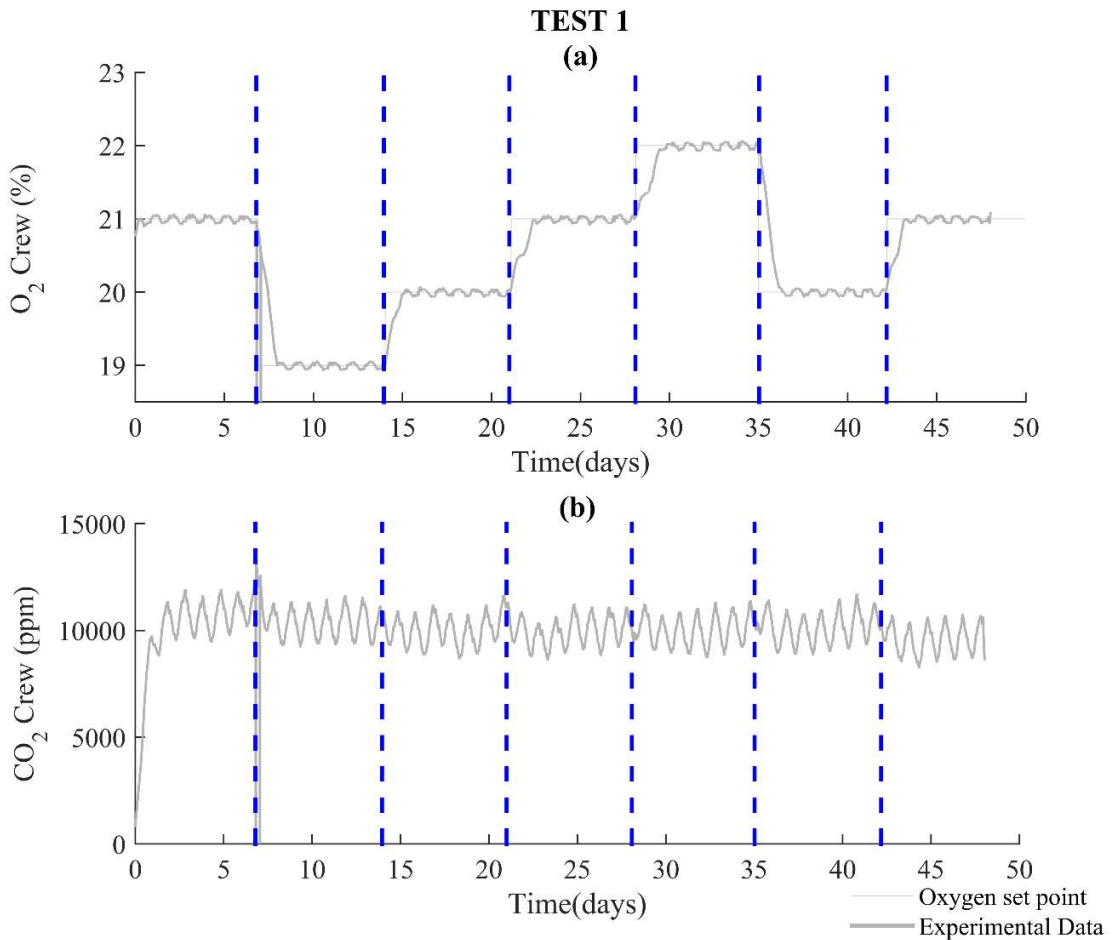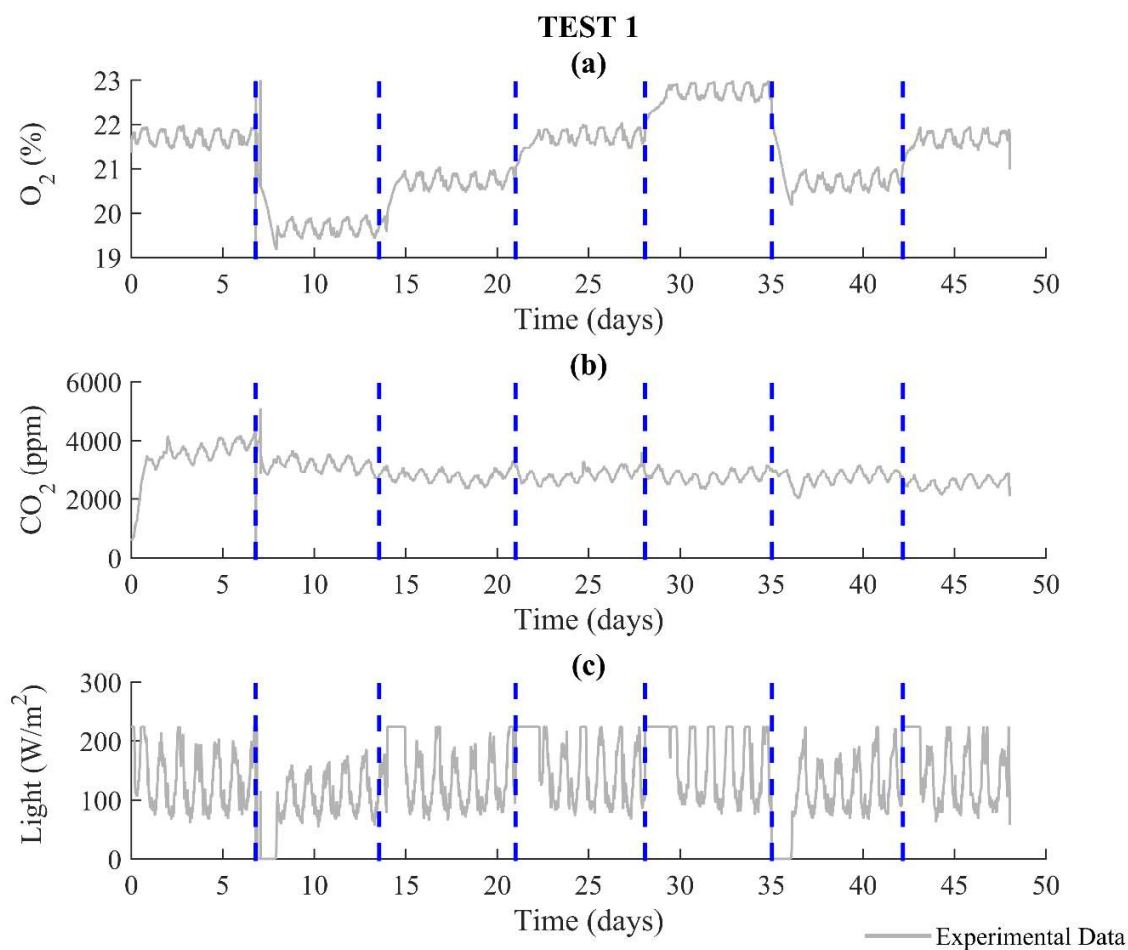

TEST 1

Figure 6.3. Concentration profiles in the gas phase of the animal compartment during Test 1. The experimental values include a) oxygen (%) and b) carbon dioxide (ppm) concentrations in the gas phase. In these figures, the specific times of change of oxygen set-point concentration in the animal compartment are indicated in blue dashed lines.
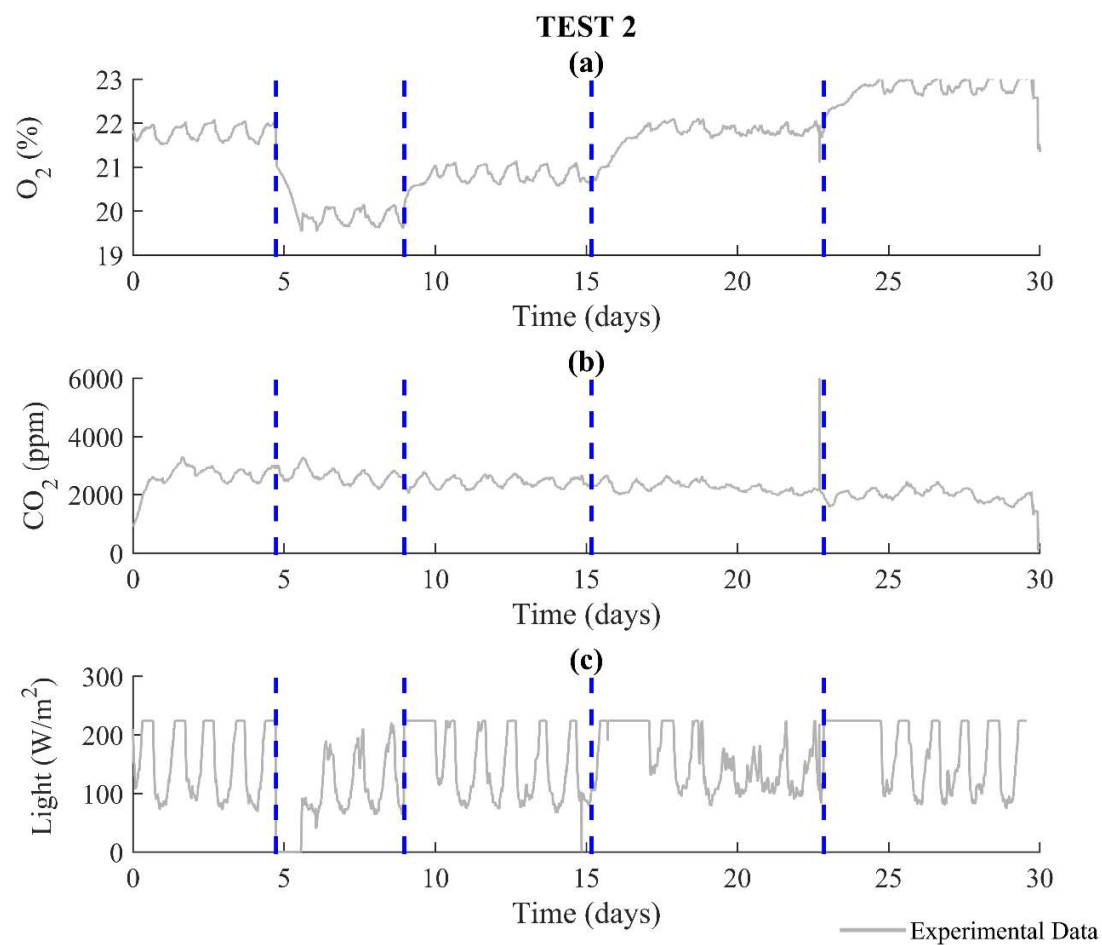
TEST 2

(a)

(b)
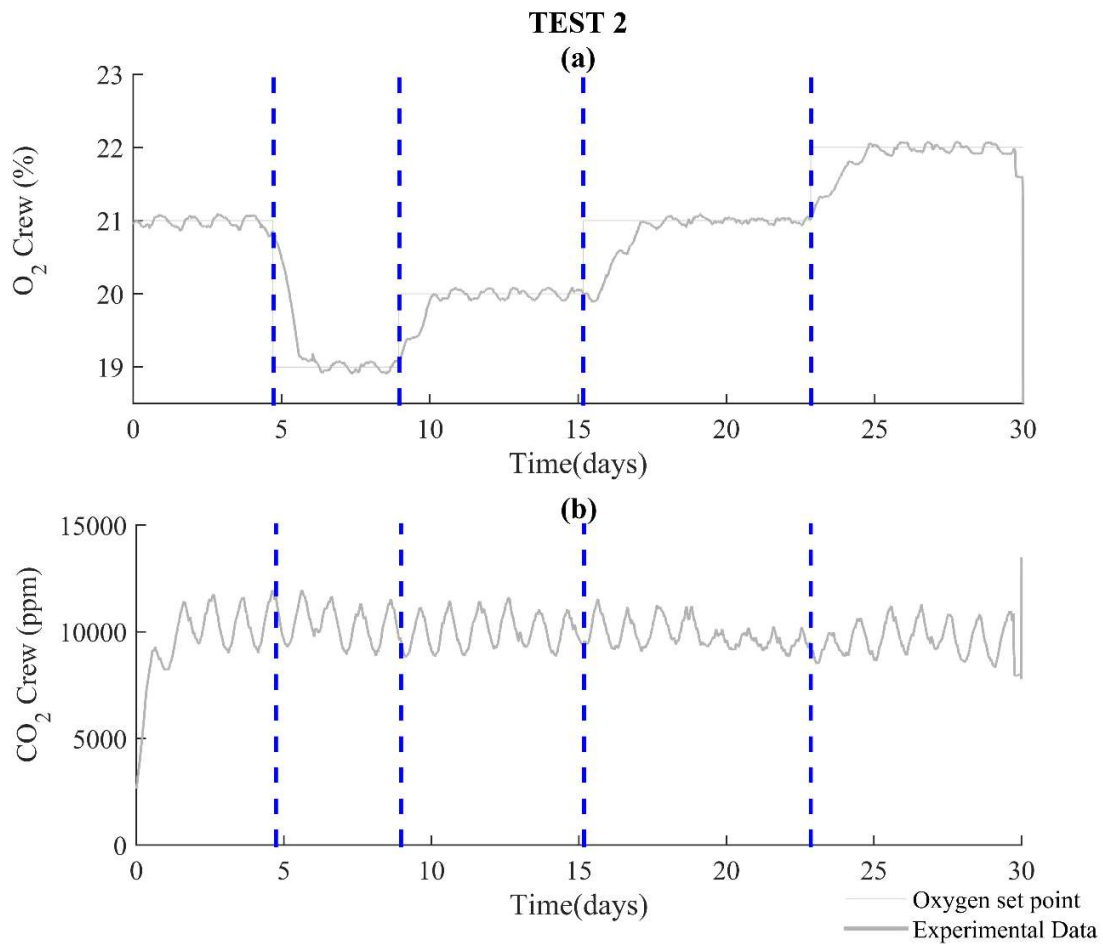
Figure 6.4. Concentration profiles in the gas phase of the animal compartment during Test 2. The experimental values include a) oxygen (%) and b) carbon dioxide (ppm) concentrations in the gas phase. In these figures, the specific times of change of oxygen set-point concentration in the animal compartment are indicated in blue dashed lines.
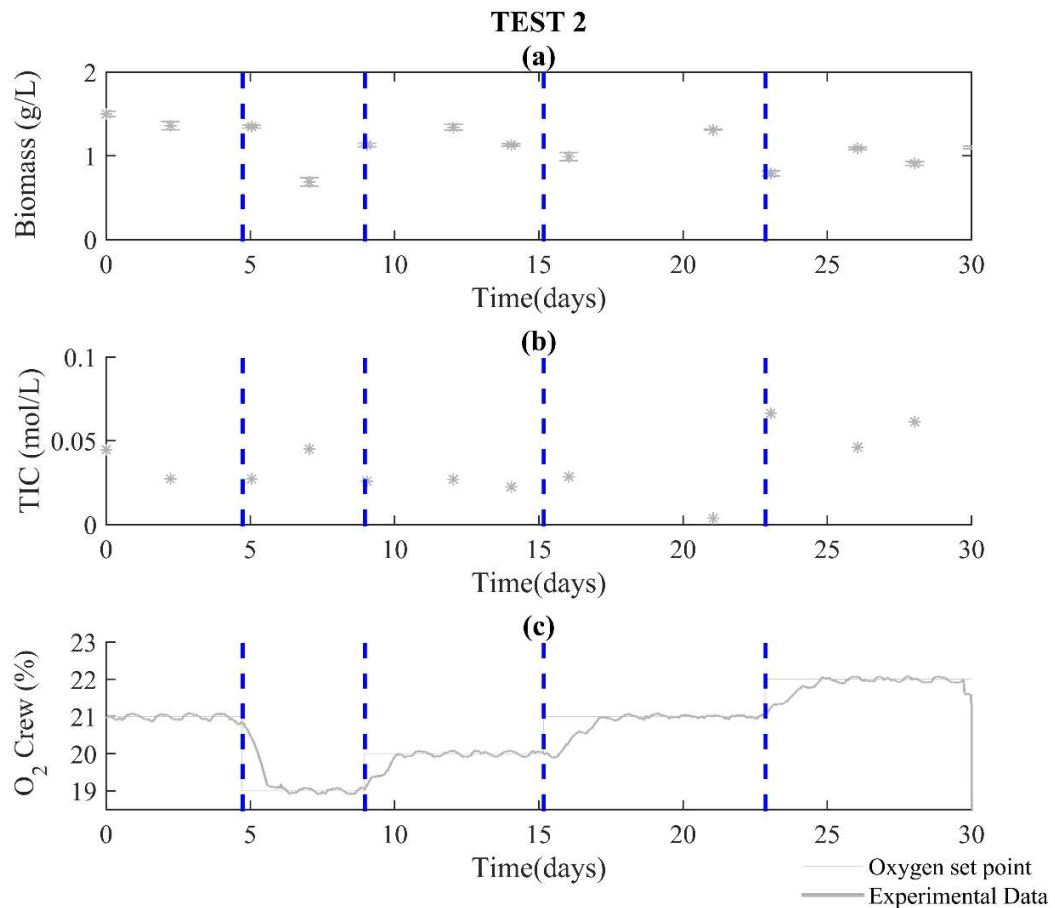
Figure 6.5. Concentration profiles in the gas phase of PBR compartment during Test 1. The experimental values include a) oxygen (%) and b) carbon dioxide (ppm) concentrations in the gas phase and c) light intensity (W/m²). In these figures, the specific times of change of oxygen set point concentration in animal compartment are indicated in blue dashed lines.

Figure 6.6. Concentration profiles in the gas phase of PBR compartment during Test 2. The experimental values include a) oxygen (%) and b) carbon dioxide (ppm) concentrations in the gas phase and c) light intensity (W/m²). In these figures, the specific times of changes of oxygen set point concentration in animal compartment are indicated in blue dashed lines.

202

The results obtained for the liquid phase in the PBR compartment are presented in Figure 6.7 (Test 1) and Figure 6.8 (Test 2). It should be noted that the biomass concentration is maintained around 1 g/L for all conditions tested. In these figures, the evolution of oxygen concentration in C5 has been included as additional information.
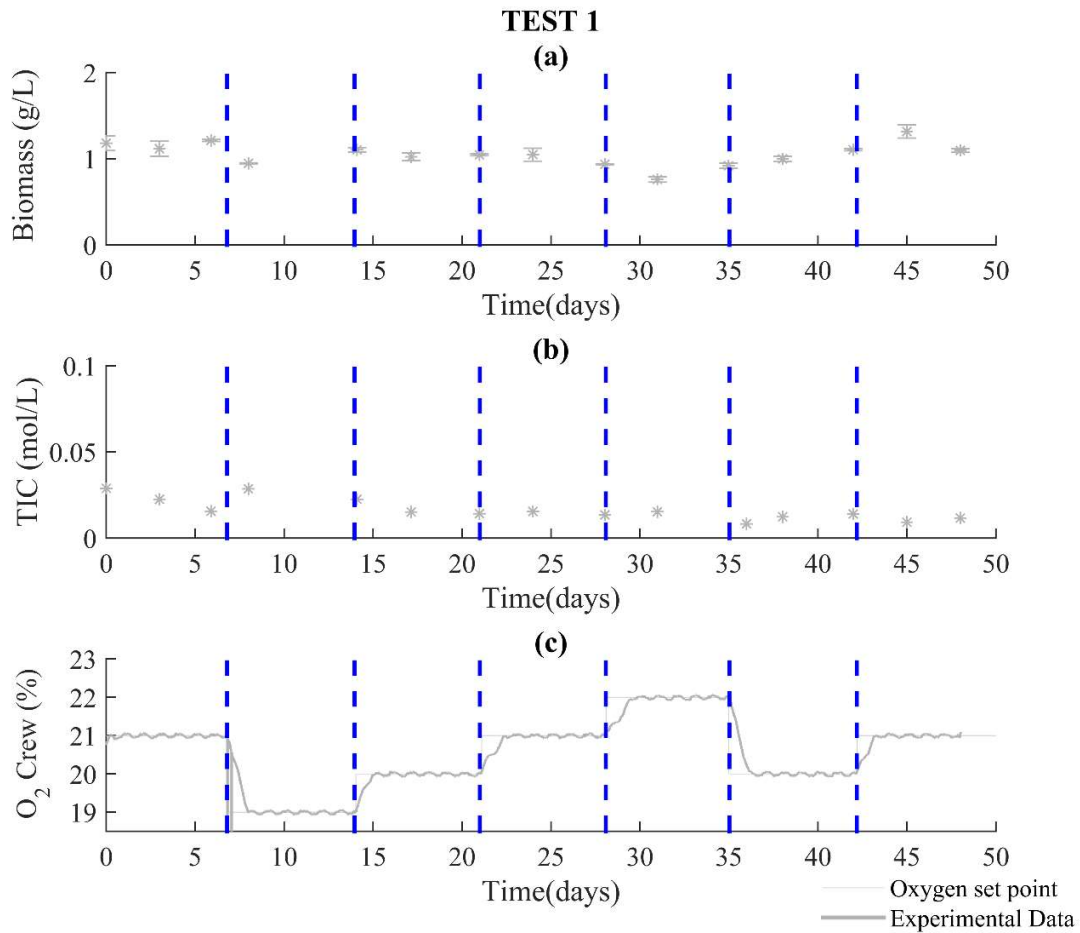
TEST 1

Figure 6.7. Concentrations profile in the liquid phase of the PBR in Test 1. The experimental values include a) biomass concentration (g/L) and b) total inorganic carbon (TIC (mol/L)) concentrations in the liquid phase. Additionally, the oxygen concentration in C5 has been included as additional information. In these figures, the specific times of changes of oxygen set point concentration in animal compartment are indicated in blue dashed lines

TEST 2

Figure 6.8: Concentrations profiles in the liquid phase of the PBR in Tests 2. The experimental values include a) biomass concentration (g/L) and b) total inorganic carbon (TIC (mol/L)) concentrations in the liquid phase. Additionally, the oxygen concentration in C5 has been included as additional information. In these figures, the specific times of changes of oxygen set point concentration in animal compartment are indicated in blue dashed lines

6.4. Model validation

This section summarizes the results obtained when the model described in Chapter 5 has been applied to reproduce the operation profiles presented previously for the two tests of the integration WP1 between the C4a and C5 compartments gas phase. In order to evaluate the fitting of these simulation into the experimental values, complete residuals data and statistical indexes have been calculated and are provided in Table 6-2. It should be noted that the relative values have been normalized in respect to the range of experimental data, to take into account the intrinsic oscillations of the variables due to day-night cycles. The discussion of this statistical analysis will be performed together with the discussion of the figures containing both, experimental and modelled data.

Table 6-2. Absolute and relative errors, Pearson correlation coefficient and Willmott-d-index for the main variables in WP1 tests.

| Variable		Compartment	Test	RMSE (Absolute)	RMSE (Relative)	Pearson correlation coefficient (r)	Willmott-d-index
Oxygen (gas %)	O_g	Animal compartment	1	0.2	0.03	0.99	0.99
			2	0.1	0.04	0.99	1.00
		PBR	1	0.2	0.03	0.98	0.99
			2	0.2	0.06	0.99	0.99
Carbon dioxide (gas %)	C_g	Animal compartment	1	584.5	0.08	0.74	0.85
			2	541.5	0.14	0.77	0.87
		PBR	1	417.0	0.18	0.61	0.68
Light intensity (W/m^2)	NA	PBR	1	37.2	0.17	0.85	0.91
			2	37.2	0.17	0.85	0.92

The results obtained for the gas phase are presented in Figure 6.9 (C5 Test 1), Figure 6.10 (C5 Test 2), Figure 6.11 (C4a Test 1) and Figure 6.12 (C4a Test 2). On one hand, it can be observed that the oxygen concentration profiles obtained with the mathematical model are very close to the experimental results. The low relative normalized residuals (lower than 0.06 in PBR and lower than 0.04 in animal compartment) as well as high values of Willmott-d-index and Pearson coefficient (≥ 0.98 in all cases) corroborate the remarkable performance of the model in describing the evolution of the main controlled

variable in the system. This is particularly relevant since the provision of oxygen to the crew is the main purpose in a closed life-support system.

On the other hand, reproduction of carbon dioxide concentrations by the model also predicts the maintenance of those concentrations below the given limit of 20,000 ppm in the animal and the PBR compartment, as found experimentally. In this case, calculated relative residuals show a good adjustment of the carbon dioxide concentrations in the animal (0.08 value for Test 1 and 0.14 value for Test 2) and the PBR compartment (0.18 value for Test 1). Additionally, values obtained for Pearson coefficient and Willmott-d-index are in the range of 0.61-0.68 for the photobioreactor and 0.74-0.87 for the animal compartment. These statistical results show a slightly lower adjustment for these variables but still an acceptable fit to experimental data. It should be noted that for Test 2, the statistical analysis in the PBR is not provided since a progressive drift of the CO_2 analyzer measurements was detected along the experiment and corroborated with re-calibration at the end of the test.

Additionally, the model also reproduces the day-night dynamics observed in the experimental data, as well as transient periods between a maximum evaluated range of 3% in oxygen concentration variation. The reproduction of these day-night dynamics and transient periods could be achieved by the use of the model control system law, that regulates light intensity in the PBR compartment to reach the desired oxygen concentrations. Transition periods corresponding to an increase or decrease in oxygen concentration are reflected in maximum or minimum light intensity in the PBR compartment. The robustness of the model when controlling the fluctuation of light intensity values is shown in Figure 6.11 and Figure 6.12 and leads to a normalized residual for this variable of 0.17 in both tests. As it can be observed in the figure, the illumination predicted by the model is slightly lower than the experimental values at lower intensities. However, the high values obtained for Pearson coefficients and Willmott-d-indexes (0.85-0.92) indicate high reproducibility. Thus, the error values detected are considered acceptable taking into account the sharp changes in the illumination when following the day and night cycles dynamics.

Therefore, the correlation of the light and gas phase model predictions and the experimental data corroborates the validity of the proposed model for each one of the compartments as well as for the control of the interfacing gas loop between them. Additionally, the reproducibility of the fluctuation of the different variables during transient periods together with the maintenance of the average gas concentrations imply that the proposed model is capable of reproducing the true compensation observed in the experimental data. This high degree of reproducibility is a proof of the high reaction capacity of the model. This result is especially relevant considering the high-volume ratio between both compartments of, approximately 200.
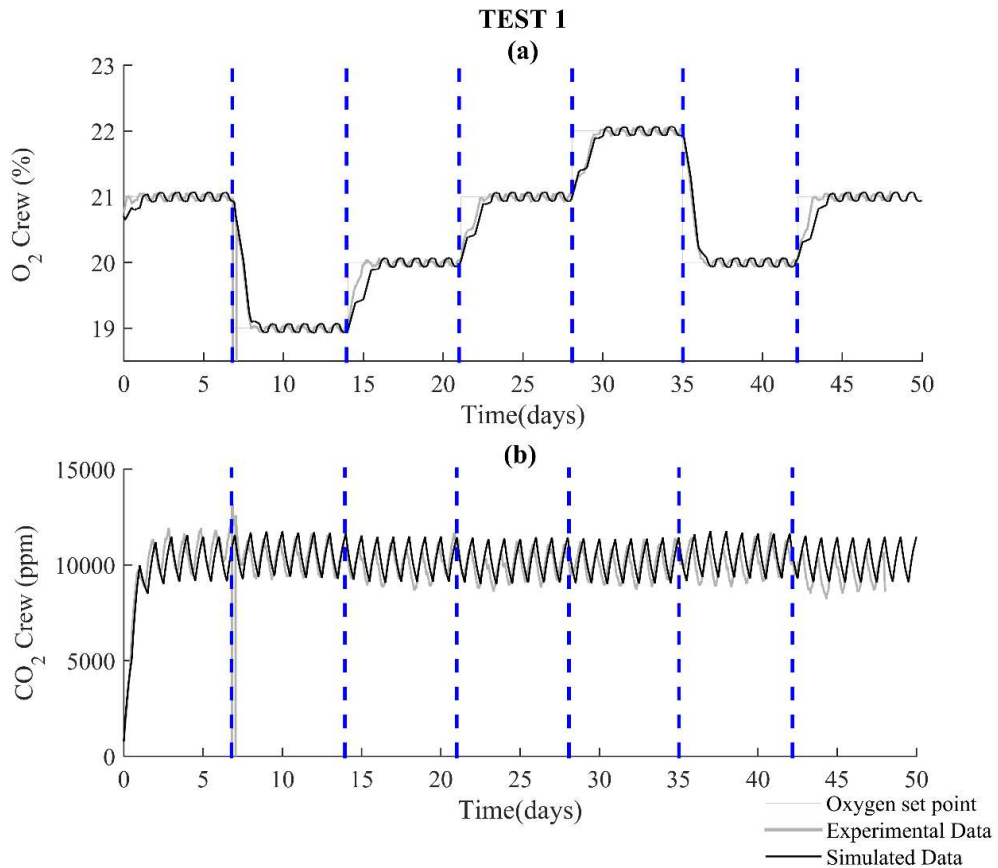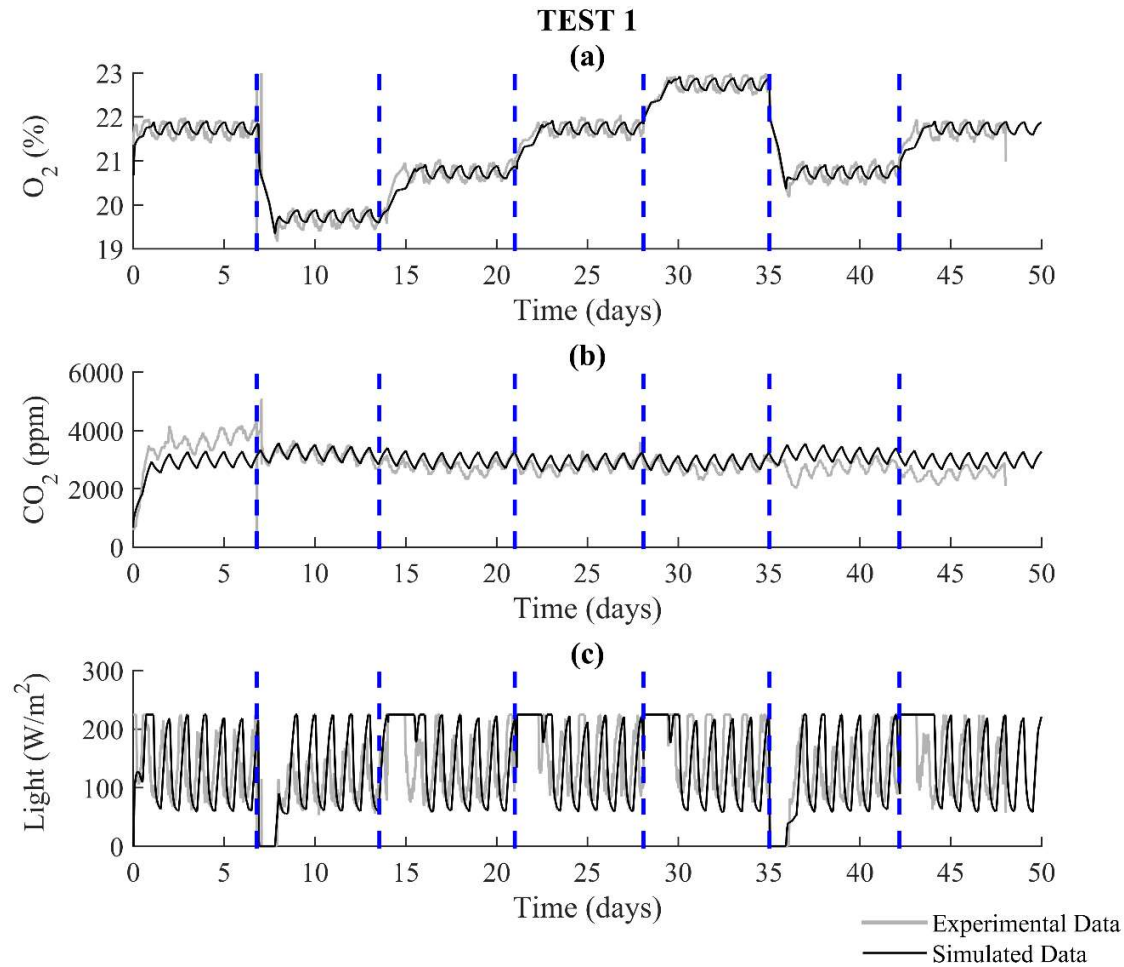

Figure 6.9. Concentration profiles in the gas phase of the animal compartment during Test 1. a) oxygen (%) and b) carbon dioxide (ppm) concentrations in the gas phase. Experimental profiles (grey) are compared with modelized profiles (black). Additionally, the specific times of change of oxygen set-point concentration in the animal compartment are indicated in blue dashed lines.
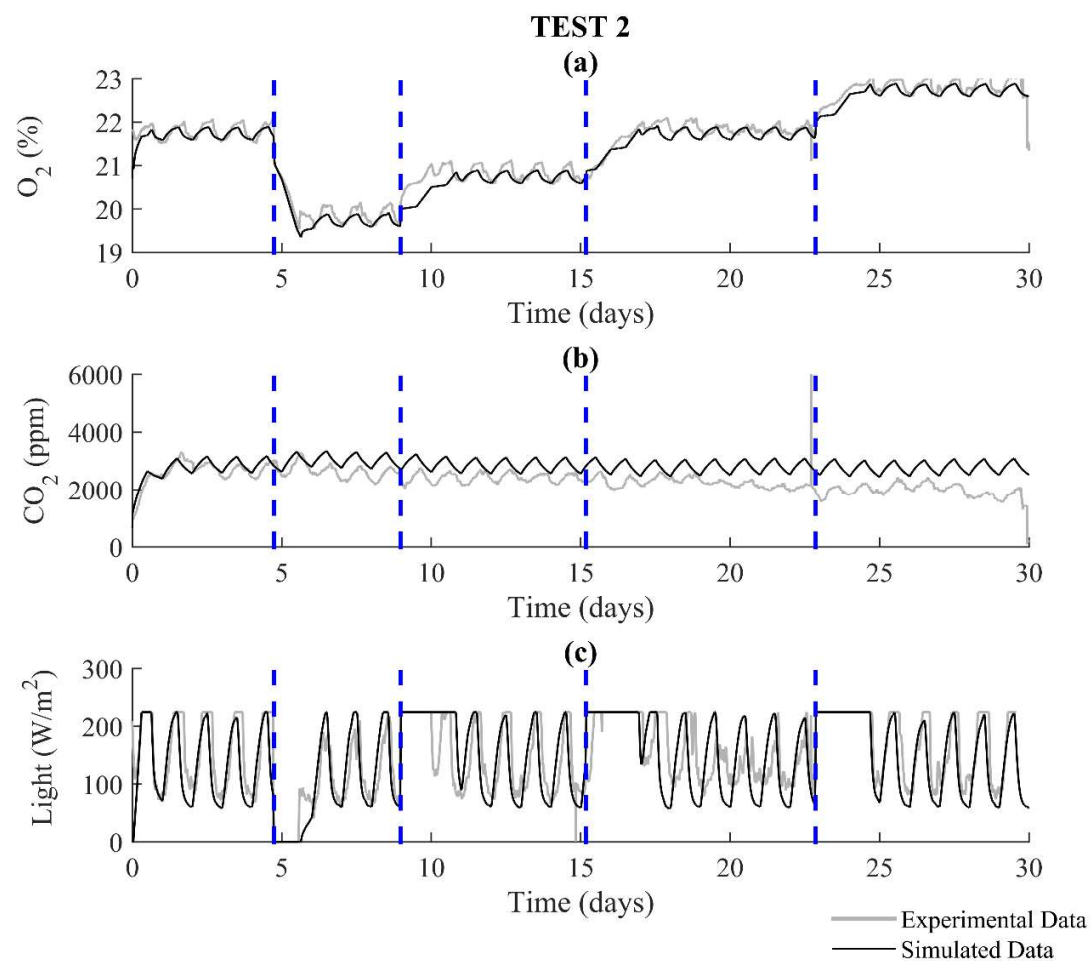
TEST 2

(a)

(b)
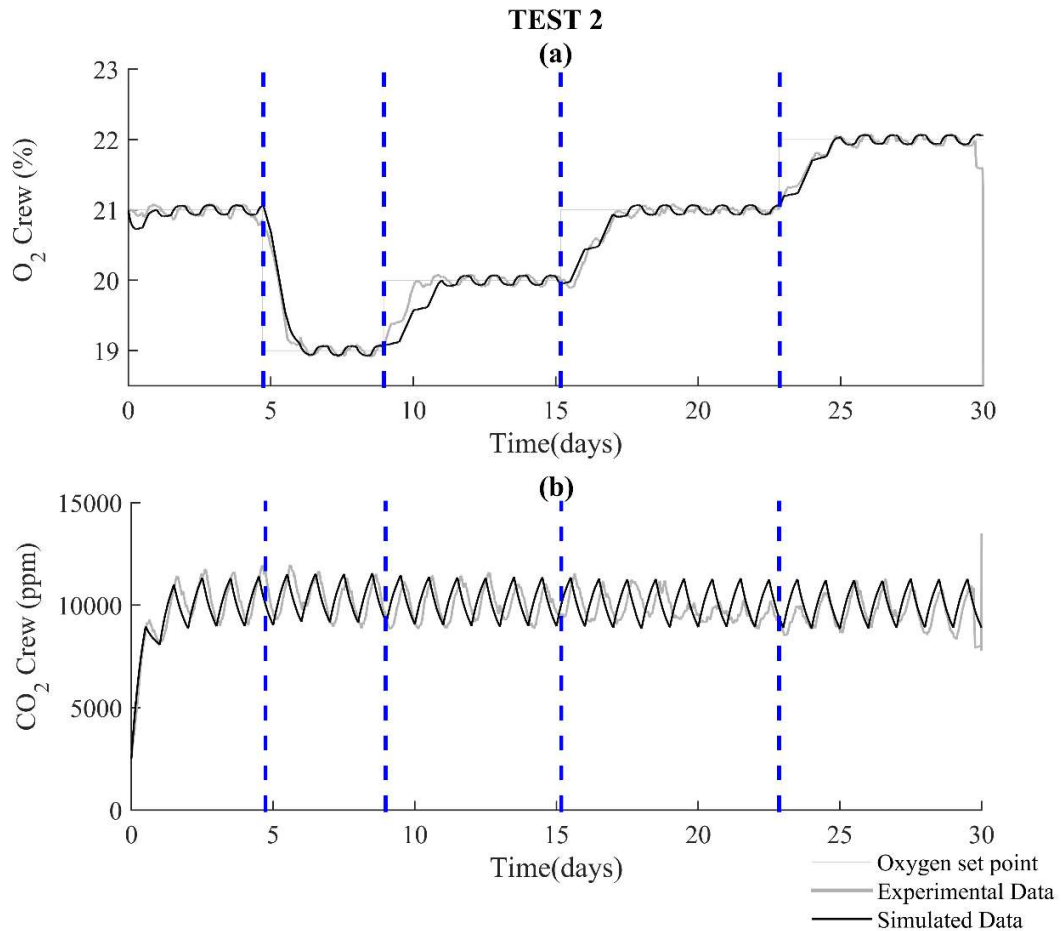
Figure 6.10. Concentration profiles in the gas phase of the animal compartment during Test 2. a) oxygen (%) and b) carbon dioxide (ppm) concentrations in the gas phase. Experimental profiles (grey) are compared with modelized profiles (black). Additionally, the specific times of change of oxygen set-point concentration in the animal compartment are indicated in blue dashed lines.
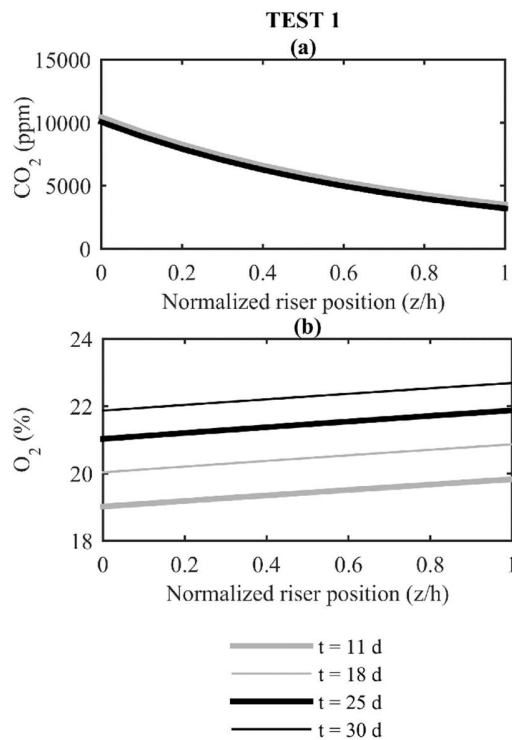
Figure 6.11. Concentration profiles in the gas phase of PBR compartment during Test 1. a) oxygen (%) and b) carbon dioxide (ppm) concentrations in the gas phase and c) light intensity (W/m²). Experimental profiles (grey) are compared with modelized profiles (black). Additionally, the specific times of change of oxygen set-point concentration in the animal compartment are indicated in blue dashed lines.

TEST 2

(a)

(b)

(c)

Figure 6.12. Concentration profiles in the gas phase of PBR compartment during Test 2. a) oxygen (%) and b) carbon dioxide (ppm) concentrations in the gas phase and c) light intensity (W/m^2). Experimental profiles (grey) are compared with modelized profiles (black). Additionally, the specific times of change of oxygen set-point concentration in the animal compartment are indicated in blue dashed lines.

210

Finally, Figure 6.13 (data corresponding to Test 1, but similar behavior observed in Test 2) provides the internal PBR profiles for the CO_2 and O_2 concentrations in the gas phase predicted by the model which agree with the model assumptions for the PBR hydrodynamics and particularly the fact that these concentrations change during the circulation of the gas phase through the PBR riser column. These profiles are especially relevant in the riser for oxygen and carbon dioxide and corroborate the difference in concentrations between inlet and outlet of the gas phase observed experimentally. While the oxygen concentration increases linearly with riser height, the carbon dioxide variation is not linear; therefore, gas-liquid mass transfer for the carbon dioxide case is not equivalent within the different N-tank volumes. Consequently, the need of a discretized model is corroborated.


Figure 6.13. Riser gas phase concentration profiles predicted by the model in different riser normalized positions (riser height (z) / riser total height (h)) in Test 1 where the maximum height corresponds to the riser air output. a) carbon dioxide concentrations (ppm). b) oxygen concentrations (%).

Additionally, the results obtained for the liquid phase in the PBR compartment are presented in Figure 6.14 and Figure 6.15. It should be noted that in this case, the statistical analysis of the obtained error has not been calculated given the reduced number of experimental data available.

As observed in these figures, the obtained biomass and TIC profiles reproduce the experimental results with an acceptable degree of accuracy. In general, the relation between liquid concentrations and light intensity predicted by the model is close to that observed experimentally as shown with the equivalence seen between the biomass curve and the C5 oxygen concentrations. Thus, the model allows the simulation of the gas control loop and the interactions in the liquid phase of the PBR with an acceptable degree of consistency. However, there is a deviation between experimental and modelized values on the last three experimental TIC determinations in Test 2 and the biomass concentration at the highest animal compartment oxygen set point (22%) in Test 1 that could potentially be due to a potential errors in sampling or measurement.
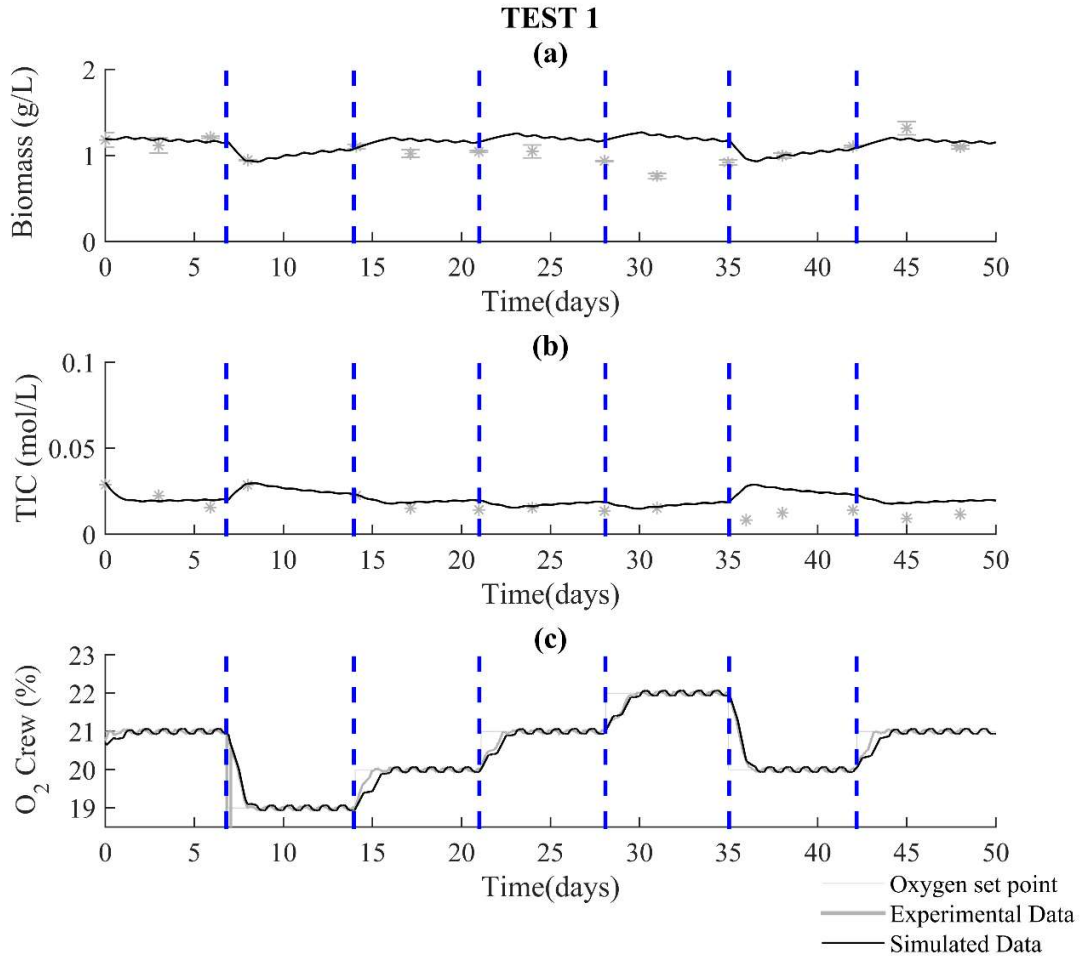
Figure 6.14. Concentrations profile in the liquid phase of the PBR in Test 1. a) biomass concentration (g/L) and b) Total inorganic carbon (TIC (mol/L)) concentrations in the liquid phase. Experimental profiles (grey) are compared with modelized profiles (black). Additionally, the oxygen concentration in C5 has been included as additional information. The specific times of change of oxygen set-point concentration in the animal compartment are indicated in blue dashed lines.

213
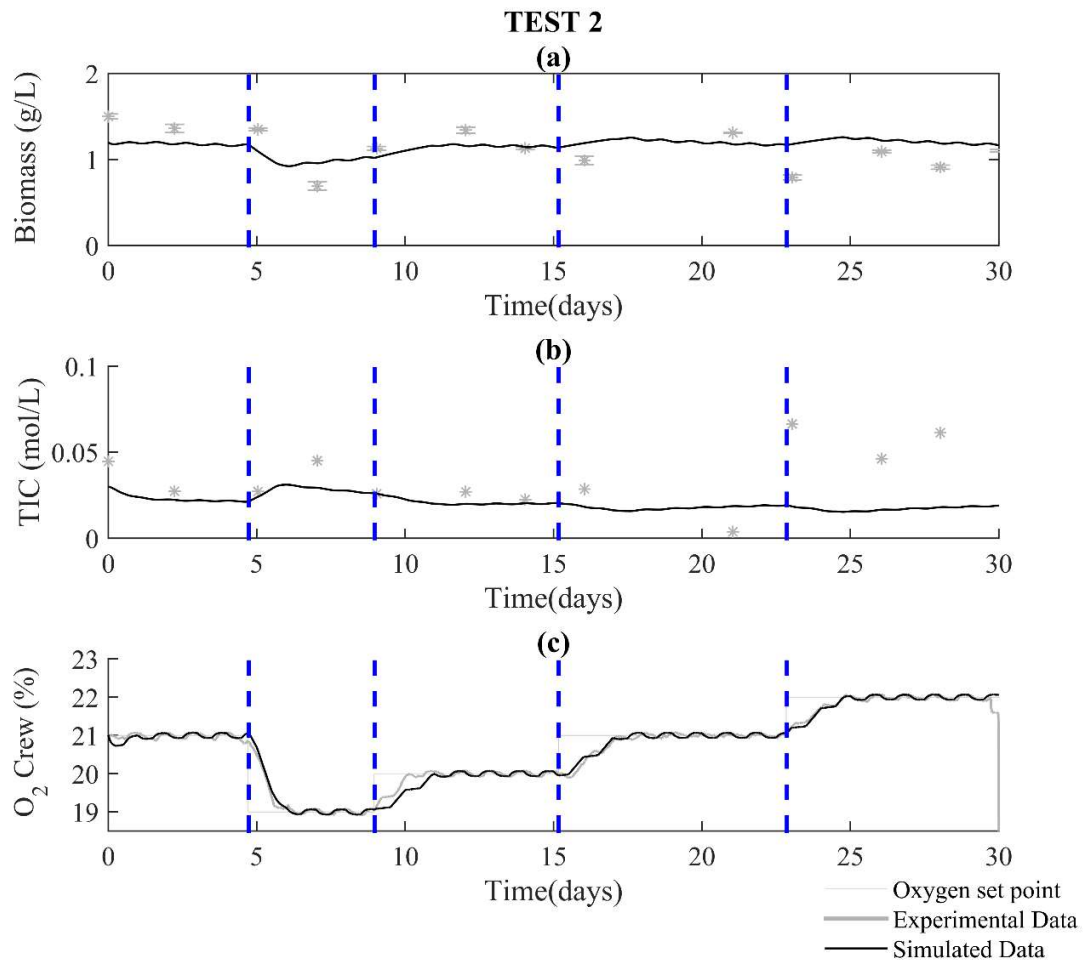
TEST 2

Figure 6.15. Concentrations profile in the liquid phase of the PBR in Test 2. a) biomass concentration (g/L) and b) Total inorganic carbon (TIC (mol/L)) concentrations in the liquid phase. Experimental profiles (grey) are compared with modelized profiles (black). Additionally, the oxygen concentration in C5 has been included as additional information. The specific times of change of oxygen set-point concentration in the animal compartment are indicated in blue dashed lines.

214

6.5. CONCLUSIONS

Accurate mathematical models describing the different elements of a biological life-support system can provide very valuable tools supporting their continuous operation under appropriate control strategies. Here, this approach has been demonstrated successfully for the close-loop operation of two elements in the MELiSSA system: the animal compartment hosting rats and the photobioreactor colonized with *Limnospira indica* culture. The results show that the model can reproduce the evolution of the main process variables in each compartment, the day-night global dynamics associated to the animal activity and the dynamics of imposed changes in oxygen set-point concentrations in the animal compartment. This demonstrates the model validity and robustness. Additionally, the accuracy shown for oxygen, the critical variable in the system (relative errors lower than 0.06 in all cases) as well as the controlled maximum carbon dioxide concentrations reached would potentially enable the application of such a system in real space missions. This represents a step forward in the development of life-support systems and particularly, in the future application of the MELiSSA project.

6.6. BIBLIOGRAPHY

1.   COE. *ETS 123: Protection of Vertebrate Animals, 18.III.1986. Cets* 123 (1986).
2.   Vidal, S. & Vergara, P. *MELiSSA technical note (MPP-TN-08-5001): Animal model for MELiSSA pilot plant.* (2014).
3.   Gonzalez, N. C. & Kuwahira, I. Systemic oxygen transport with Rest, Exercise and Hypoxia: A comparison of Humans, Rats and Mice. *Comprehensive Physiology* 8, 1537–1573 (2018).
4.   Vernerey, A. & Albiol, J. Scale Up and Design of a Pilot Plant Photobioreactor for the Continuous Culture of *Spirulina platensis*. *Biotechnology Progress* 17, 3 (2001).
5.   Cogne, G., Lehmann, B., Dussap, C. & Gros, C. G. Uptake of Macrominerals and Trace Elements by the Cyanobacterium Spirulina platensis (Arthrospira platensis PCC 8005) Under Photoautotrophic Conditions : Culture Medium Optimization. *Biotechnology and Bioengineering* 81, 588–593 (2003).
6.   Vonshak, A. & Guy, R. Photoadaptation , photoinhibition and productivity in the blue-green alga , Spirulina platensis grown outdoors. *Plant, cell and environment* 15, 613–616 (1992).
7.   Cheung, S. M., Vonshak, A. & Chen, F. Photoinhibition and Its Recovery of Spirulina Platensis in Photoautotrophic and Mixotrophic Cultures. in Photosynthesis: Mechanisms and Effects 4171–4174 (1998).
8.   Jachner, S. Boogaart, K & Petzoldt, T. Statistical Methods for the Qualitative Assessment of Dynamic Models with Time Delay (R Package qualV). *Journal of statistical software* 22, 1-30 (2007).
9.   Willmott, J. Some comments on the Evaluation of Model Performance. *Bulletin American Meteorological Society 63,* 1309-1313 (1982).
10.   Krohn, T. C., Hansen, A. K. & Dragsted, N. The impact of low levels of carbon dioxide on rats. *Laboratory Animals* 37, 94–99 (2003).
11.   Krohn, T. C. & Hansen, A. K. Carbon dioxide concentrations in unventilated IVC cages. *Laboratory Animals* 36, 209–212 (2002).

CHAPTER 7

Overall conclusions and future work

The integration of the different compartments of the MELiSSA loop is a challenging goal for the MELiSSA project and particularly for the MELiSSA Pilot Plant as a demonstrator of the complete concept and architecture. The present work is framed on the effort to understand and model the bioreactors configuring the loop and their solid, liquid and gas phases connections. Indeed, the complexity of the different bioreactors is related to the different biological, chemical and physical dynamics observed in each compartment. The formulation of mathematical models such as the ones developed here provide a knowledge-based tool describing the performance of the compartments. This is useful to describe the obtained experimental results with accuracy but, also important, to improve the understanding of their operation and to enable the prediction of their performance in other operating conditions through simulation.

The current thesis represents an important step-forward in the definition and application of these models since three of the six compartments in the loop have been studied: C3, nitrifying compartment; C4a, photobioreactor compartment; and C5, crew compartment.

On one hand, a complete model has been developed for the C3 packed-bed nitrifying reactor. The final proposed model is structured in three different levels: the global reactor hydrodynamics and the biofilm that considers the growth of the different species based on a simplified 1-D diffusion model and includes a simplified approach to simulate biofilm consolidation. The proposed model has been validated by the fitting of experimental data from the continuous operation of the compartment during a period of nearly 2 years in axenic conditions with good results. The good fitting of the model results with real experimental data is particularly relevant in this case considering the limitation to obtain biofilm samples during the long-term operation in order not to perturbate the packed-bed structure. Further, the use of this compartment model will be a very valuable tool for the simulation of its performance and the successful definition of the appropriate conditions in future integration of this reactor in next phases of the MPP development.

On the other hand, a complete model has been developed to describe the operation of the C4a photobioreactor compartment. In this case, a hydrodynamic model coupled to a light transfer model and microalgae growth kinetics has been developed. Moreover, the C4a model has been completed with another model describing the experimental behavior of the rats' oxygen consumption and carbon dioxide production together with a reproduction of the control system that defines the control of the C4a-C5 integration.

Then, this global model has been successfully applied to two sets of experimental data obtained from the integrated operation of both compartments at different oxygen set points in C5. In these conditions, the developed models reproduce with high accuracy the experimental profiles of each bioreactor and the global system dynamics associated to the introduction of a real living crew in continuous close gas loop connection to the photobioreactor. This provides a proof of concept that the use of these models can be usefully exploited in the simulation of future integration steps, by analyzing the potential compartment performance in a given operation scenario. For this reason, the models developed in this thesis can be further developed in a future interphase to analyze potential situations in future integration packages to be performed in the MPP, to simulate the impact of possible perturbances or even to identify the potential need for the introduction of a buffer tank or additional physicochemical interphases in the loop. Thus, the developed models are a strategic tool to identify the operational conditions for best loop functionality and safety in long-term operation. At the end, the objective will be to reduce the degrees of freedom in the system that will be paramount to its correct operation and control.

Additionally, all the developed models in this thesis can be used, apart from the improvement of the reactor operation control, as a simulation tool when considering potential new scenarios or design improvements related to the MELiSSA loop design or scalability. These scenarios include, among others, the future consideration of a real human crew with more activity periods in C5 and the potential modification of the proposed models to include future loop modifications (i.e. the introduction of urine in C3 or the potential limitation of carbon source in C4a). In all these conditions, developed models in this thesis are foreseen as potential key points that can be used as a prediction to faster the future experimental development of the project.

Finally, the inclusion of the developed models in an integrated control architecture is paramount to gain knowledge on the complete loop operation (one of the main aspects in the MELiSSA approach) and create the basis for the establishment of a model-based predictive control approach. In this scenario, the present thesis opens, as a final goal, the in-depth study of the different model integration prediction in different conditions that will be a requirement for the final definition of a control system with acceptable mathematical load able to fully predict the different compartments of such a complex system.

In the future steps to be performed in the MELiSSA Pilot Plant, the methodology followed in this work will be applied to more compartments and to more integration steps, following this multiple level approach: understanding the fundamental processes involved in each compartment (biological, physico-chemical, etc.), building models describing the performance of compartments with accuracy, using these models in the control of the compartments under integration and ultimately in the control of the final loop using them as tools to anticipate the performance of the individual compartments and the complete loop. The developed model will also be used as a design tool for future application of the MELiSSA loop to given scenarios of life support systems, either in Space or in Ground Demonstration Facilities.

CURRICULUM VITAE

Laura Alemany Juvanteny

LAURA ALEMANY JUVANTENY

**Biotechnologist, Msc Biological and environmental Engineering
PhD Candidate 2022 / ESADE EMBA Candidate 2024**
Product development, process scale-up, clinical lots manufacturing,
process transference, project management and production scale
manufacturing (GMP)

Barcelona area • Birth date: 06/08/1992 • 616572882 •
lalemanyj@gmail.com • *https://www.linkedin.com/in/laura-alemany-juvanteny/*

SUMMARY/PRESENTATION

I define myself as an enthusiastic professional motivated in applying my knowledge and always willing to expand it. Hard worker, persistent, constant and passionate in excelling in my work.

My professional career includes initially positions as of basic and applied investigation. However, my professional development in the pharmaceutical industry for over 8 years has allowed me to extendedly work in process development and final steps of industrial manufacturing implementation (clinical lots, conformance lots, new regulatory strategies implementation FDA; EMA) and process transference in plasma-derived protein purification as responsible personnel. The transversal role of my position has allowed me to deeply interact and coordinate different areas of the company (production, quality and R&D) to achieve successful implementation of new manufacturing plants into the company and successfully fixing derived manufacturing facilities incidences.

Additionally, the huge effort that has implied for me the performance of part-time PhD in such an interesting project as the MELiSSA closed loop bioregenerative life support system will hopefully proof my development as a researcher and consolidate my profile in the pharmaceutical and biotechnological sector.

EXPERIENCE

Process development technologies manager
Instituto Grifols, Parets del Vallès
November 2017 – Nowadays
Process development technologies. Specialist
Instituto Grifols, Parets del Vallès
February 2015 – November 2017

Validation assistant
Regulatory Affairs and Validation department. Diagnostic Grifols, Parets del Vallès
July 2014 – February 2015
Intern at R&D Instruments Diagnostic Grifols
Diagnostic Grifols, Parets del Vallès
July 2013 – February 2014
Intern at Chemical Engineering department
Autonomous University of Barcelona
July 2013 – February 2014

EDUCATION

PhD in bioprocess scale-up and computational simulation (Part time)
Collaboration with European Space Agency (MELiSSA project) in the context of life support systems.
Autonomous University of Barcelona (UAB).
2016 – July 2022

Master's Degree in Biological and environmental engineering UAB – Average grade 8.8 (2014-2016)

Bachelor's Degree in Biotechnology. Honor mention in bioprocess.
UAB - Average grade: 9.09 (2010-2014)

Intellectual Property and Biotechnology
Justus Liebig University Giessen (July 2013)

Professional grade in Music. Piano specialist
Vic Average grade: 9.00 (1997-2010)

LANGUAGES

Catalan; Native proficiency (C2)
Spanish: Native proficiency(C2)
English: Professional working proficiency(C2)
French: Intermediate level(B2)
German; Low-intermediate level (A2)
*2 Projects
*3 Oral communications in congresses

PUBLICATIONS, PROJECTS & AWARDS

*1 Publication. Located in the front page of Biochemical engineering Journal November 2019.
*2nd In the promotion (2015)
Master's degree in biological and environmental engineering
*Excellency Scholarship Collaborative Depart. (2013)
Bachellor degree in Biotechnology.
*16 Honors Qualification (2014)
Bachellor degree in Biotechnology.